



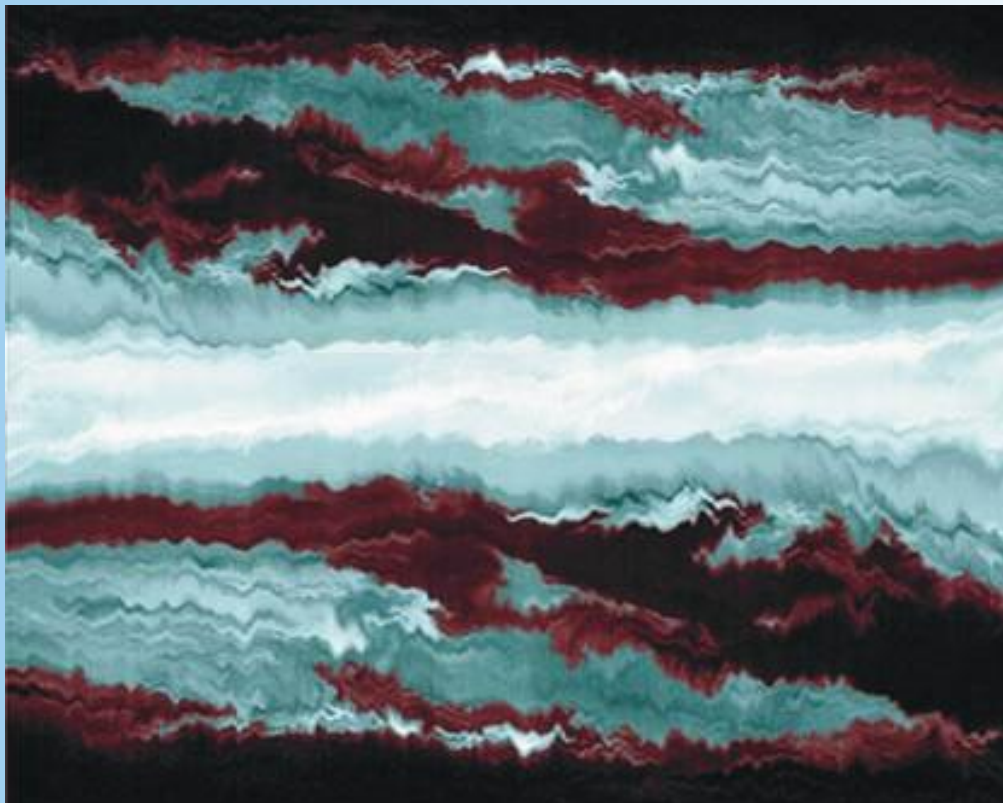
ISSN 1028-8546

Volume XVI, Number 1
March, 2010

Azerbaijan Journal of Physics

Fizika

www.elm.az/physics



G.M. Abdullayev Institute of Physics
Azerbaijan National Academy of Sciences
Department of Physical, Mathematical and Technical Sciences

Azerbaijan Journal of Physics

Fizika

*G.M.Abdullayev Institute of Physics
Azerbaijan National Academy of Sciences
Department of Physical, Mathematical and Technical Sciences*

HONORARY EDITORS

Arif PASHAYEV

Mahmud Kerimov

EDITORS-IN-CHIEF

Arif Hashimov
Chingiz Qajar

SENIOR EDITOR

Talat Mehdiyev

INTERNATIONAL REVIEW BOARD

Ivan Scherbakov, Russia
Kerim Allahverdiev, Turkey
Mehmet Onder Yetish, Turkey
Gennadii Jablonskii, Buelorussia
Rafael Imamov, Russia
Vladimir Man'ko, Russia
Eldar Salayev, Azerbaijan
Dieter Hochhaimer, USA
Victor L'vov, Israel
Vyacheslav Tuzlukov, South Korea

Firudin Hashimzadeh, Azerbaijan
Majid Ebrahim-zadeh, Spain
Anatoly Boreysho, Russia
Mikhail Khalin, Russia
Hasan Bidadi, Tebriz, East Azerbaijan, Iran
Mamed Emin Shahtakhtinskii, Azerbaijan
Maksud Aliyev, Azerbaijan
Bahram Askerov, Azerbaijan
Vali Huseynov, Azerbaijan
Javad Abdinov, Azerbaijan

Bagadur Tagiyev, Azerbaijan
Tayar Djafarov, Azerbaijan
Natiq Atakishiyev, Mexico
Talat Mehdiyev, Azerbaijan
Nazim Mamedov, Azerbaijan
Emil Guseynov, Azerbaijan
Ayaz Baramov, Azerbaijan
Tofiq Mamadov, Azerbaijan
Rauf Guseynov, Azerbaijan
Shakir Naqiyev, Azerbaijan

TECHNICAL EDITORIAL BOARD

Talat Mehdiyev, Elmira Akhundova, Narmin Babayeva, Nazli Guseynova, Sakina Aliyeva, Nigar Akhundova

PUBLISHING OFFICE

33 H.Javid ave, AZ-1143, Baku
ANAS, G.M.Abdullayev Institute of Physics

Tel.: (99412) 439-51-63, 439-32-23
Fax: (99412) 447-04-56
E-mail: joph@physics.ab.az
Internet: www.elm.az/physics

It is authorized for printing: 02.20.2010

Published at "ŞƏRQ-QƏRB"

17 Ashug Alesger str., Baku

Typographer : Aziz Gulaliyev

Sent for printing on: __.03. 2010
Printing approved on: __.03. 2010
Physical binding: _____
Number of copies: _____ 200
Order: _____

LASER CRYSTALLIZATION INDUCED MULTICRYSTALLINE SILICON THIN FILM SOLAR CELLS ON GLASS: EUROPEAN HIGH-EF PROJECT

F. ANTONI¹, E. FOGARASSY¹, A. SLAOU¹, Y. LEROY¹, Z. SAID-BACAR¹, F. FALK², E. OSE²,
S. CHRISTIANSEN², G. SARAU², J. SCHNEIDER³, N. LICHTENSTEIN⁴, B. VALK⁴,
M. LECLERCQ⁵, R. LEWANDOWSKA⁵, J. MICHLER⁶, X. MAEDER⁶,
A.-S. DEHLINGER⁷, J. LÁBÁR⁸, G. SÁFRÁN⁸,

¹*InESS-CNRS/UdS, Strasbourg, France*

²*IPHT, Jena, Germany*

³*CSG Solar AG, Thalheim, Germany*

⁴*Oclaro, Switzerland AG*

⁵*Horiba Jobin Yvon, Lille, France*

⁶*Swiss Federal Laboratories for Materials Testing and Research, Thun, Switzerland*

⁷*ALMA Consulting Group, Lyon, France*

⁸*Research Institute for Technical Physics and Materials Science Hungarian Academy of Science,
Budapest, Hungary*

The European project HIGH-EF is aimed at developing a unique process for silicon thin films based solar cells on glass substrate. To provide high solar cells efficiency (> 12 %), a combination of laser crystallization of a seed layer and an additional solid phase epitaxy of a thicker layer is realized. In a first step, the crystallization of the seed layer is obtained by scanning a focused in-line laser beam obtained by a specific optical lens system. In a second step, epitaxial growth of a large grains active silicon layer is achieved by solid phase epitaxy. Process optimisation is supported by numerical simulations of both melting and crystallization process of the seed layer as well as epitaxial solid phase crystallization.

1. INTRODUCTION

Photovoltaic (PV) cells can be divided in two main categories : wafer based crystalline silicon and thin film modules. Single or multicrystalline silicon bulk cells dominate the market (over 90%). The difficulty to secure a feedstock supply to produce conventional wafer-based solar cells has encouraged the industrial production of silicon thin film based solar cells [1]. The European HIGH-EF project aims to provide an unique process to obtain thin film solar cells allowing high efficiency (potential for > 12 %) at a very competitive cost. To obtain such a performance, the finalized thin film surface has to present large and low defective grains as well as low stress in the multicrystalline structure. The preparation process results from a combination of a laser crystallization of a very thin (less than 200 nm) amorphous silicon (a-Si) seed layer and an additional epitaxial thickening (up to 1.5 μm) obtained by Solid Phase Crystallization (SPC), corresponding to the absorbing layer of the finalized active cell. The a-Si layer as well as the epitaxial growth are deposited by Electron Beam Evaporation (EBE) at the rate of 300 nm/min. The substrate is a borosilicate glass.

2. EXPERIMENTAL DETAILS

The preparation of a large grains seed layer (over 100 μm long) is performed in the melting phase regime by scanning a focused in-line laser beam, obtained by a set of aligned power laser diodes. The focused beam should be able to treat the a-Si layer at a speed able to reach the crystallisation of an entire module in one pass (almost 1.4 m²) as they are available as an industrial product. Because of the dimension of such a panel, the treatment should be provided by an unique laser module able to scan a 1.1 m large a-Si covered glass substrate. The results shown in this report are obtained by a prototype system able to treat 10 cm large samples. To obtain the

required power to melt the a-Si layer and keeping in mind that the system has to remain at low cost, the high power laser diode modules presently used emit at a wavelength of 806 nm.

Electron backscattered diffraction (EBSD) has been used to characterize grains size and orientation as well as the crystalline properties of both the seed and thicker SPE layers. EBSD experiments were previously reported [2,3] for strain analysis in multi-crystalline semiconductors. In order to determine the laser power density needed to melt and crystallize the a-Si layer, numerical simulations were performed. A comprehensive numbers of parameters like absorption coefficient, surface reflection, boundaries conditions and all thermal parameters of the different layers of the whole structure were taken into account. A correlation between absorbed energy in the seed layer, energy density of the 806 nm diode laser beam and initial substrate temperature was investigated in order to optimize the crystallisation process.

3. CELL STRUCTURE

The substrate of the cell is a borosilicate glass panel (Schott borofloat, 3.3 mm thick) covered in a first step by a thin silicon nitride (SiN) barrier layer obtained by PECVD, which serves as an antireflective layer in the finalized cell. The incoming light reaches the active junction through the glass substrate. On the top of the barrier layer, the heavily doped a-Si thin film (50 to 400 nm), functioning both as a seed layer and as an emitter, is taking place. The thickness should be as reduced as possible in order to avoid light absorption. The active region of the cell is localized in the thick upper SPC layer. The doping of the different parts of the cell is obtained by additional evaporation of boron and phosphorus during the EBE growth process. The epitaxial

crystallization of the upper a-Si thick layer is performed by SPE at a temperature of 650°C. The final superstrate structure of the cell is shown in Fig. 1.

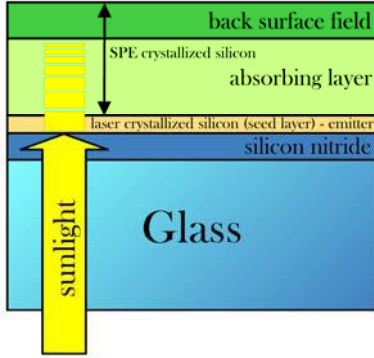


Fig. 1. Layered structure of the cell.

4. NUMERICAL SIMULATION

Process optimization is supported by numerical simulations of the laser melting and crystallization of the seed layer. Simulations are performed by the COMSOL MULTIPHYSICS© software and are based on finite difference and finite element methods. This paragraph reports simulation results of laser crystallisation of the seed layer, with or without the barrier layer between the substrate and the a-Si. The ultimate goal is the optimization of experimental conditions in terms of layer thicknesses and laser beam scanning velocity for an efficient crystallization of the seed layer.

The generalized heat equation is used to solve the melting of the a-Si layer:

$$\rho C_p \frac{\partial T}{\partial t} + \rho C_p v \nabla T - \nabla(k \nabla T) = Q$$

The transient term $\rho C_p \frac{\partial T}{\partial t}$ is neglected in order to consider the stationary heat equation where the temperature does not change in time. The duration required to reach the stationary state is supposed to be short as compared to the one required to irradiate the whole surface. The convective

term $\rho C_p v \nabla T$ is used to model the scanning of the laser. It is equivalent to the heat density deposited during the movement of the laser. In stationary case, the laser is fixed and the substrate is considered moving under the focused beam line. This way, we can reduce drastically the complexity of the simulated geometry.

Due to the fact that the laser beam is Gaussian and that the absorbance of the material follows the Beer-Lambert law, the expression of the heat source density Q is:

$$Q = D_0 \alpha (1 - R) \exp\left(\frac{-(x - x_0)^2}{2\sigma^2}\right) \exp(\alpha(y_0 - y))$$

This term is present only in absorbent layers (e.g. a-Si layers). In what follows, D_0 is always the resulting value of the power density required to reach the melting temperature of a-Si ($T_m=1420$ K). According to experimental results, the FWHM of the focused beam is 167 μm . The simulations compare two irradiation conditions: the laser beam comes

from the top of the a-Si layer (direct process) or through the glass substrate (flip process) as shown in Fig. 2.

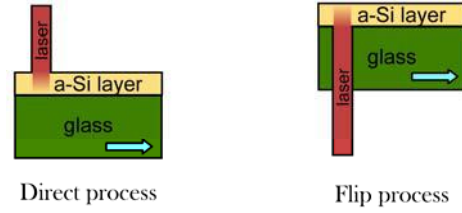


Fig. 2. The two considered cases of laser irradiation of the a-Si layer (becoming the seed layer) in the numerical simulations.

Because the fusion temperature of the glass is low (920 K) compared to silicon, all simulations show that the substrate is melted well under the melting threshold of the a-Si layer. Practically, a solution must be found to prevent stress and cracks at the interface during the solidification process. In order to reduce this effect, the initial substrate temperature was set at 900 K during the irradiation process. This has also been taken into account in all numerical simulations. Optical and physical parameters of the materials are obtained by experimental measurements as well as extracted from references [4,5,6]

As a first step, the power density needed to melt the a-Si layer was compared in the two cases of the direct and flip processes. Resulting from a change in the surface reflection coefficient from 0.39 to 0.23, a slight difference in the required energy is observed, as shown in Fig. 3.

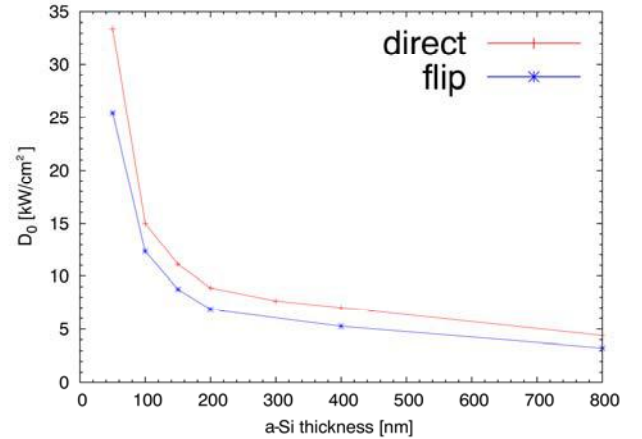


Fig. 3. Power density D_0 needed to melt the a-Si layer as a function of thickness.

We can also observe that this difference remains constant if the layer becomes thicker. The required power density decreases rapidly with increasing thickness. Actually, only 10.6% of the incoming laser energy is absorbed in a 50 nm thick a-Si layer. If the layer becomes 200 nm in thickness, this low percentage increases to 36.13% and reaches the value of 63% for 446 nm. This is the direct consequence of the low absorption coefficient of amorphous silicon at 806nm.

Fig. 4 shows the influence of the scanning velocity on the required power to melt a 50nm a-Si layer. This relation remains nearly linear with increasing speed. The simulation results show that scanning velocity, power density and thickness should be considered for finding optimum condition.

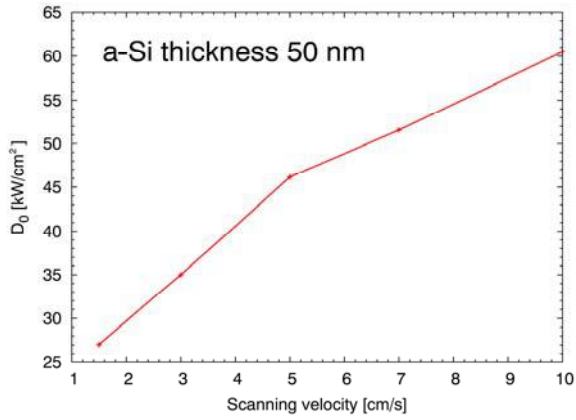
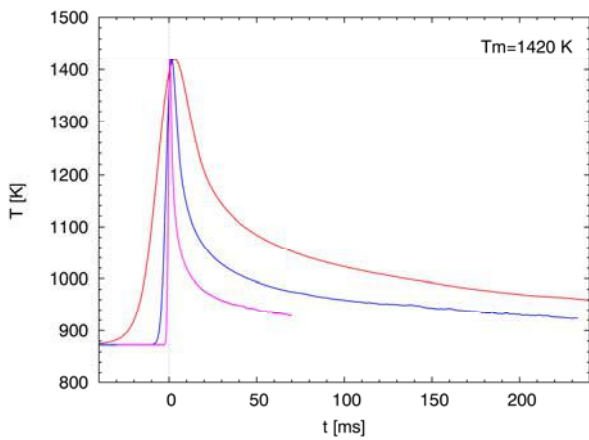
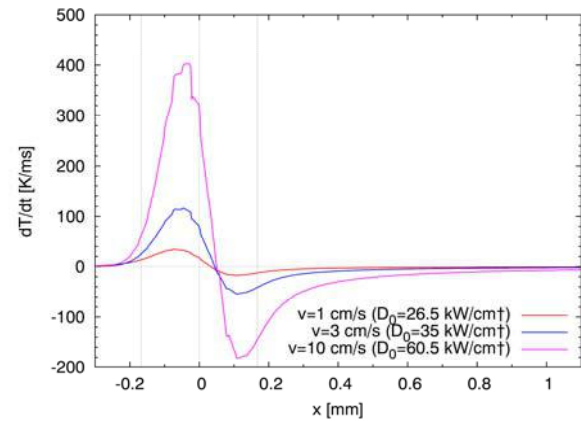


Fig.4. Power density D_0 required to melt a 50nm thick a-Si layer as a function of scanning velocity in the case of a direct process.



(a)



(b)

Fig.5. (a) Temperature evolution of a given point moving on the surface under laser irradiation at different scanning speeds and power density (b) corresponding heating and cooling rates.

In order to obtain large grain crystallization of the seed layer, heating and cooling rates are very critical parameters. Simulation attempts to correlate temperature variation as a function of time in the case of different scanning speeds (from 1 to 10 cm/s). As shown in Fig. 5, the required power density increases by a factor of two for an increase in the scanning speed by a factor of ten. The heating and cooling rates of the thin silicon layer are strongly related to the scanning speed, and must be carefully adjusted to ensure

optimal crystallization during the solidification of the seed layer.

5. RESULTS AND DISCUSSION

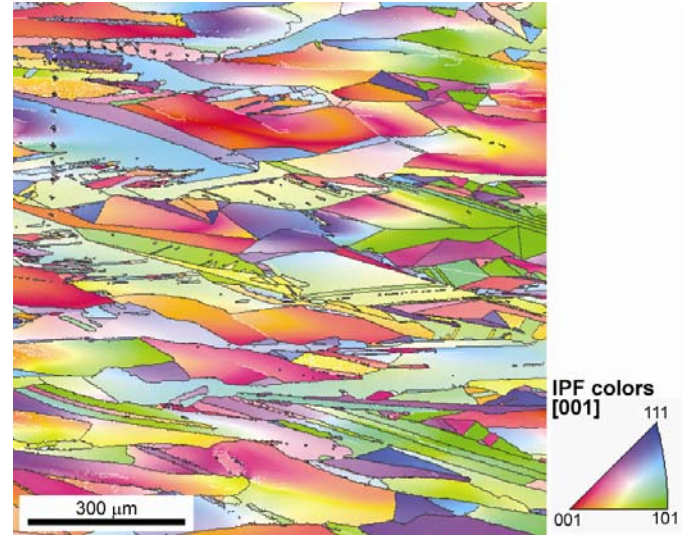


Fig. 6. EBSD picture of elongated grains obtained after laser irradiation of a 445 nm thick seed layer.

Experimental results show that a very thin a-Si layer is not optimal to obtain good seed layer crystallization. One of the explanation is that a dewetting effect occurs more easily in very thin layers. A fast increase of the temperature in the layer during irradiation is another inconvenient effect. Fortunately, during the melting phase, the reflectivity of the silicon is increased by a factor of two which helps to reduce the temperature variation in the liquid silicon. The grain size structure characterized by EBSD is shown in Fig. 6. The seed layer presented has 445 nm in thickness and reveals some grain length over 500 μm long. However, individual grains show a twist in the crystalline orientation. EBSD shows also that more than 50% of the boundaries are with a high angle change (> 15°).

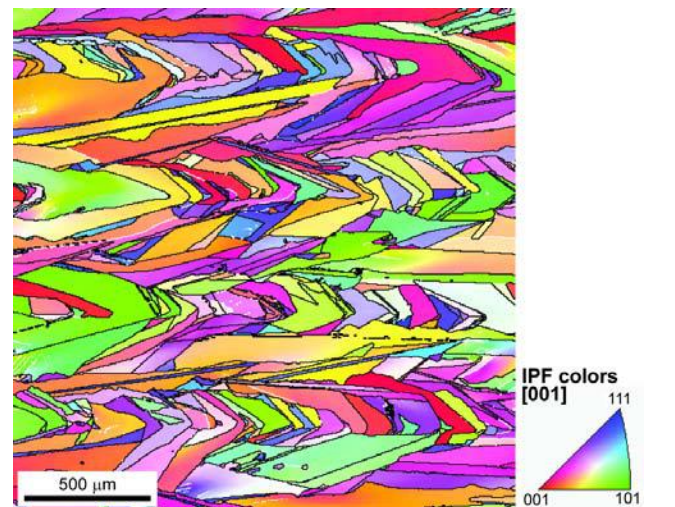


Fig.7. EBSD picture of elongated grains obtained after epitaxial growth of a 650 nm a-Si layer, after a furnace annealing at 650 °C during 9.5 hours.

Solid phase crystallization of the absorbing layer can only be considered successful if the crystalline structure is able to follow a grain size evolution corresponding to the seed layer. This clearly means that the EBE deposition of the absorbing thick layer should not present nuclei centers in its own. If the film is grown at a temperature over 400°C, a significant concentration of undesired nuclei centers induces a degradation in the grain size, despite of a higher crystallization rate. Deposition at room temperature need more time to obtain epitaxy. An optimal temperature during EBE growth seems to be around 300°C. SPC at a rate around 10 nm/s was made at a temperature of 650°C and resulted in a crystallization structure shown in Fig. 7. The EBSD picture clearly shows an epitaxial growth of the whole layer as confirmed by additional TEM experiments not shown here.

6. CONCLUSION

Numerical simulations are helpful in providing information of heating and cooling rates of the seed layer

during the laser induced crystallization process. A comprehensive study of temperature evolution depending on scanning speed, initial temperature and power density permits to find the optimum conditions during the whole deposition process.

Epitaxial growth obtained by SPC of a thick silicon layer over a laser crystallized seed layer is demonstrated. Experimental results show that a thick seed layer (around 400nm) induces a large grain structure after laser irradiation as it is confirmed by EBSD measurements. In addition, a limited temperature during the EBE deposition of the active layer is reducing drastically the presence of nuclei centres and permits also an efficient epitaxial growth during the SPC process.

7. ACKNOWLEDGEMENT

The HIGH-EF project is supported by the 7th Framework Programme under contract 213303.

-
- [1]. *M. Rogol, and B. Fisher*, Sun Screen II, CLSA Solar Power Sector Outlook Report (2005).
- [2]. *C. Trager-Cowan, F. Sweeney, P.W. Trimby, A.P. Day, A. Gholinia, N.-H. Schmidt, P.J. Parbrook, A.J. Wilkinson, and I.M. Watson*, Phys. Rev. B 75, 085301 (2007).
- [3]. *S. Christiansen, M. Nerding, J. Krinke, H.P. Strunk, P. Lengsfeld, and N.H. Nickel*, J. Appl. Phys. 89, 5348 (2001).
- [4]. *I. Chambouleyron, S. D. Ventura, E. G. Birgin, and J.M. Martinez*, J. Appl. Phys., 92 (6), 3093 (2002).
- [5]. *G. E. Jellison, Jr. and D. H. Lowndes*, Appl. Phys. Lett., 47 (7), 718 (1985).
- [6]. *N. M. Ravindra, and J. Narayan*, J. Appl. Phys, 60 (3), 1139 (1986).

TURKISH ACCELERATOR COMPLEX, FEL RESONATOR SYSTEM

HATICE DURAN YILDIZ

*Dumlupınar University, Faculty of Science and Arts, Physics Department,
Merkez Kampüs, 43100, Kütahya, Turkey*

Accelerator technology is an important tool for the development in almost all fields of science and technology. Considering the importance of accelerator technology, a feasibility report and conceptual design report (CDR) on Turkic Accelerator Complex (TAC) in Turkey has been completed in 2005. It is proposed that the complex will contain a collider, light sources (SR, FEL) and a proton accelerator. Beginning of 2006, third phase of the TAC project is started with the collaboration 10 Turkish Universities. There are three main goals of this phase: to built Institute of Accelerator Technologies, to write the Technical Design Report of TAC, and to construct linac based infrared free electron laser facility to use in basic, applied research, and to get experience on related technologies. TAC IR-FEL will be covered range of 2-250 microns that based on 15 - 40 MeV e-linac. The main system of TAC project is briefly presented while calculated resonator and mirror system parameters for TAC IR-FEL Resonator and optic cavity system such as maximum density, saturation density, power, pulse energy, RMS pulse length are obtained and explained in more detail. In this research, diffraction losses are calculated by using mirror parameters in GLAD Program. In order to maximize FEL efficiency, controlled optic cavity system, stability and beam quality of the out-coupled signal are needed. FEL parameters are given depending on electron beam parameters.

1. INTRODUCTION

Turkish Accelerator Center, Infrared Free Electron Laser (TAC IR-FEL) Project will contain an electron linac in 15-40 MeV energy range with two optical resonators in order to obtain FEL in 2.5-250 microns range. TAC IR-FEL is shown in figure 1. The optical resonators which will have same lengths but the undulators will have periods of 2.5 and 9 cm.

The facility will be located in Ankara University, Gölbaşı

Campus and the commissioning is planned to be by the middle of 2012.

2. ACCELERATOR

The electron beam with tunable energy in 15-40 MeV can be injected to undulator-1 and undulator-2 line independently. Linac structure of TAC IR-FEL is shown in figure 2 with other main equipments.

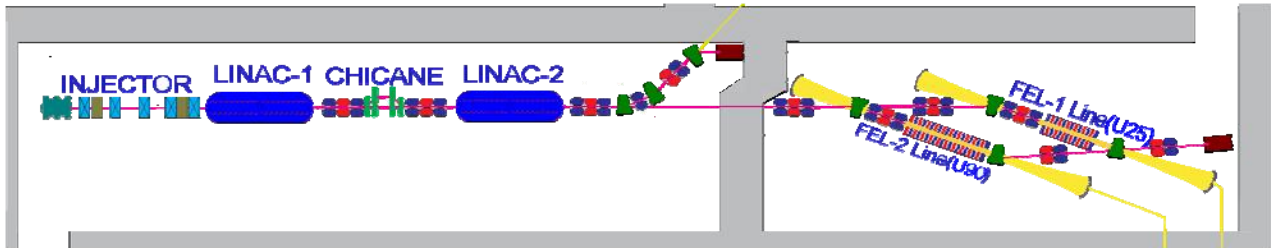


Fig.1. TAC IR-FEL Facility

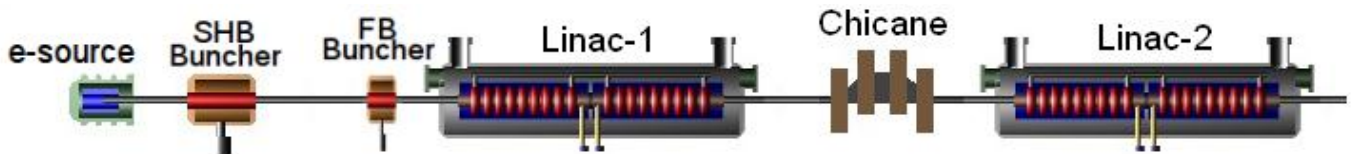


Fig.2. TAC IR-FEL linac

In order to obtain high quality FEL, the electron beam should have high peak current, short bunches, minimum energy spread, and low emittance [1]. In order to effective acceleration the bunch which has about 500 ps length after the gun needs to be compressed using two step buncher called subharmonic and fundamental buncher cavities which operates 260 MHz and 1.3 GHz, respectively [2]. The bunch after injector is compressed up to 10 ps and has 250 keV energy. A booster linac can be proposed which will be used for capturing and accelerating beam up to 1-2 MeV.

PARMELA code has been used to define the beam parameters at the entrance of undulators. In simulations, the beam was assumed as it has 30 mm.mrad total emittance and 100 pC bunch charge at the exit of the gun. For TAC IR-FEL, fundamental electron beam parameters are given in Table 1. As an average beam current, 1.6 mA is taken into account and it was accepted that preferred normalized RMS longitudinal emittance and normalized RMS transverse emittances are limited with same values.

3. OPTICAL RESONATORS

Two optical resonators will be used in Turkish accelerator Complex, IR-FEL System with same length which houses same family planar undulators. The undulators have different periods and housed between at the center of different kind mirrors with same distances.

Table 1: TAC IR-FEL electron beam parameters

Parameter	Value
Energy [MeV]	15-40
Bunch Charge [pC]	120
Average Beam Current [mA]	1.6
Bunch Repetition Rate [MHz]	260-13
Bunch Length [ps]	1-10
Norm. RMS Transverse Emittance [mm mrad]	<15
Norm. RMS Longitudinal Emittance [keV.ps]	<100
Pulse Duration	CW/tunable

Table 2: Fundamental parameters of SmCo type undulators

Parameter	Undulator-1	Undulator-2
Magnet Material of the undulator	SmCo	SmCo
Period Length (mm)	25	90
Number of periods	60	40
Magnet block dimensions (width*height*thickness)(mm)	74*26*10.5	90*90*35
Steel pole dimensions (width*height*thickness)(mm)	74*18*2	70*20*10
Magnetic gap (mm)	15	40
Effective field (T)	0.3591	0.4205
K_{rms}	0.71	2.5

UNDULATORS

Scanning large wavelength region is possible with wide tunable undulator's strengths as well as wider tunable electron beam energy according to FEL wavelength equation. Therefore, we have chosen 25 mm and 90 mm undulator periods for scanning 2.5-250 microns FEL wavelength with 15-40 MeV range electron beam in TAC IR-FEL System. SmCo magnet material hybrid-type undulators with iron poles is proposed. Fundamental parameters of undulators which are available in market are given in table 2.

The numbers of the undulator poles were determined with optimum gain and optimum intra cavity power. The strength

for undulator-2 is limited at 2.5 although it can be increased up to 3. The strength of undulator-1 is limited by the minimum gap. The beam pipe is considered to have 1.5 cm radius between the undulator-1 layers.

3.1. MIRROR PARAMETERS

In optical resonator electromagnetic fields can exist whose distribution of amplitudes and phases reproduce themselves upon repeated reflections between the mirrors. These particular field configurations compromise the transverse electromagnetic modes of a passive resonator. Oscillator FEL systems, which includes 2 mirrors, are mainly in Gaussian Mode, which is explained with TEM_{00} . Symmetric and concentric resonator types are chosen as optical cavity system. Symmetric and concentric systems have several advantages such as small waist, big mirror spot. The mirrors will be covered by Au or Cu materials and will have holes with the diameter between 0.5 and 2 mm to get light out and have reflectivity around %95 [3].

The distance of mirrors is related with the electron bunch repetition. In TAC IR-FEL system, the bunch repetition rate is 77 ns and corresponding mirrors distance is $L_c=11.53$ m. Minimum spot size for the lowest order TEM Mode occurs at the Rayleigh length ($Z_R \approx L_u / 2$) for an undulator length L_u . Beam waist, beam spot size, radius of curvature of the mirrors, spot size on mirrors, and Rayleigh length are obtained by the equations:

$$w(z) = w_0 [1 + (\frac{\lambda z}{\pi w_0^2})^2]^{1/2} \quad (1)$$

$$R(z) = z [1 + (\frac{\pi w_0^2}{\lambda z})^2] \quad (2)$$

$$\omega^2(0) = \omega_0^2 = \frac{\lambda_R}{2\pi} \sqrt{L_c(2R - L_c)} \quad (3)$$

$$Z_R = \frac{\pi \omega_0^2}{\lambda_R} \quad (4)$$

The main parameters of the optical resonator systems which consists the undulators that have 2.5 and 9 cm period lengths at the center between mirrors is given in table 3.

Table 3: The main parameters of optical resonators.

Parameter	Resonator-1	Resonator-2
Undulator period [mm]	25	90
Undulator length [m]	1.50	3.6
Optic cavity length, L_c [m]	11.53	
Resonator Type	Symmetric, concentric	
1 st Mirror, radius of curvature, R_1 [m]	5.92	6.51
2 nd Mirror, radius of curvature, R_2 [m]	5.92	6.51
Rayleigh length, Z_R [m]	0.97	2.07
Mirror Material	Au / Cu	Au / Cu
Radius of out coupling hole [mm]	2/3/4	2/3/4

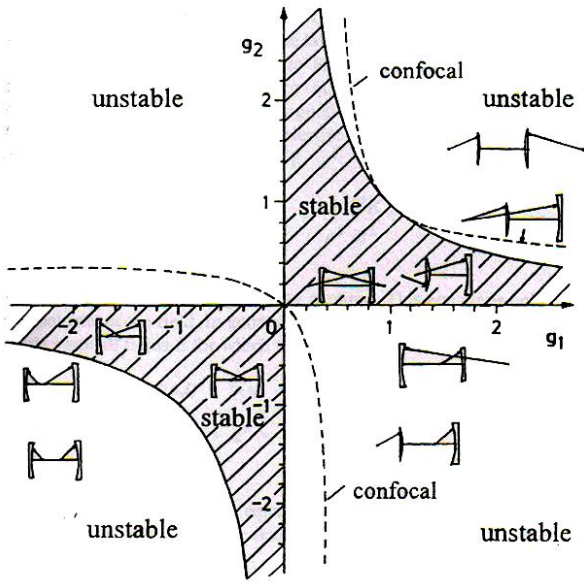


Fig. 3. g_1 , g_2 and resonator types

Stability condition for a stable resonator:

$$0 < \left(1 - \frac{L}{R_1}\right)\left(1 - \frac{L}{R_2}\right) < 1 \quad (5)$$

This condition is derived from a paraxial ray tracing in a periodic convergent lens sequence where $g_1=1-L/R_1$ and $g_2=1-L/R_2$. As one can see from the Figure 3, multiplication of the stability parameters, g_1 and g_2 , is housed in the stable area which is shaded.

3.3. MIRROR COATINGS

Mirror coating is important to obtain preferred transmitted

light and to know the reflected percent. In TAC IR-FEL System, metallic protected silver and gold are thought to be chosen as mirror material. The highest wavelength for coating is ZnS 0.38-25 micron, it has transparent region, and 2.55 diffraction index. For coating, Ion Beam sputtering is chosen in order to deposit dielectric coatings. This energetic process generate layers with bulk-like indices of refraction, resulting in a better durability of the coating [4, 5].

Table 4. Physical properties of coating materials used for laser mirrors

Material	Index of Refraction	Transparent Spectral Range
Na ₃ AlF ₆	1.35	0.20-14um
MgF ₂	1.37	0.22-2um
SiO ₂	1.46	0.20-8um
HfO ₂	1.95	0.22-12um
ZrO ₂	2.10	0.34-12um
Ta ₂ O ₅	2.16	0.30-10um
TiO ₂	2.25	0.35-12um
ZnS	2.55	0.38-25um

3.4. DIFFRACTION LOSSES

In TAC IR-FEL System, diffraction loss and energy losses are simulated with the GLAD 5.2 Code [6]. GLAD is written to calculate the performance of laser systems that have defined direction of propagation. By using GLAD 5.2 version, diffraction losses and energy passes are worked out and following histograms are obtained by using optic cavity and TAC IR-FEL parameters. Figure 4, the diffraction loss for 1.5 m undulator wavelength case with silver mirror coating. For silver 0.480 micron and for gold 0.650 micron have be taken for wavelength range.

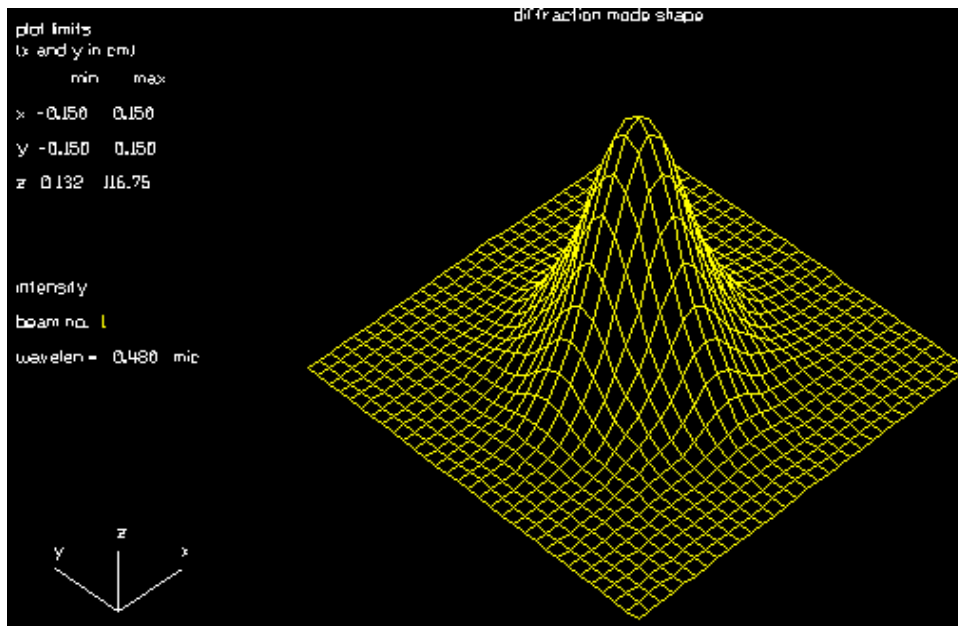


Fig.4. Diffraction mode shape for TAC IR-FEL System for silver coating

3.5. WAVE PROPAGATION

In TAC IR-FEL System, wave propagation in the resonator is studied with the Genesis 1.3 and Optical Propagation Code (OPC) programs [7-8]. Genesis simulates undulator in the resonator while OPC simulate the light fro the undulate through mirrors. From this simulation, one can obtain TEM Modes that suits the TAC IR-FEL Resonator System. From the equation $W_{pl}=C_{pl}\omega_0$, where $C_{00}=1$, $C_{01}=1.5$, $C_{10}=1.9$, $C_{11}=2.15$, $C_{20}=2.42$, $C_{21}=2.63$ and $\omega_0=0.002891$ m beam waist. W_{00} , W_{01} , W_{10} , W_{11} , and W_{20} TEM modes are smaller than the undulator gap, thus these modes can be attainable modes for Undulator-1 in TAC I-FEL System. In undulator-2, W_{00} , W_{01} , W_{10} can be obtained within the undulator gap where beam waist is 0.01121 m and Rayleigh length 2.078 m with the stability parameter, $g_0=-0.77$. These TEM_{pl} Modes related with the radial intensity of the beam which is given by Laguerre polynomials. The radial intensity distributions are normalized to the spot size of a Gaussian Beam profile.

4. TAC INFRARED-FREE ELECTRON LASER

For the Concentric resonator, the Filling factor is greater than (for $\lambda_u=2.5$ cm: $\lambda=2.5-27$ μ m and for $\lambda_u=9$ cm: $\lambda=11-250$ μ m) 50% in the output FEL wavelength. To obtain FEL in 2.5-250 microns range using 15-40 MeV energy electron beam inclined us to use undulators that have 2.5 cm and 9 cm period lengths which we call undulator-1 and undulator-2 respectively. In calculations we have taken in consideration the electron beam to have 1,6 mA average current , 1ps bunch length, 13 MHz repetition rate, 15 mm.mrad normalized transverse emittance and 100 keV.ps normalized longitudinal emittance. The obtained FEL wavelength is given by an analytical well known expression:

$$\lambda_r = \frac{\lambda_u}{2\gamma^2} (1 + a_u^2) \quad (6)$$

where λ_u is undulator period length, a_u is rms undulator strength parameter and γ is the Lorentz factor that is a measure of the electron energy. Small signal gain for planar undulators is calculated by using:

$$g_0 = \frac{16\pi}{\gamma} \lambda [m] \lambda_u [m] N^3 \frac{J \left[\frac{A}{m^2} \right]}{I_0 [A]} \xi f_b (\xi)^2 \quad (7)$$

where J shows Bessel Function while I_0 shows Alfven current. N stands for number of periods in the undulator and ξ shows undulator parameter which is related to the Bessel

Functions. Gain for single pass is:

$$G_{max} = 0.85 * g_0 + 0.19 * g_0^2 + 4.12 * 10^{-3} * g_0^3 \quad (8)$$

For TAC IR-FEL system, one can obtain small single gain as 0.006175 and gain for single pass is approximately found as 0.00645 for undulator-1 with 2.5 cm wavelength. Electron beam energy spread, finite emittance, longitudinal slippage and Chesworth filling method correction factors are used for calculating the ideal gain. It is considered %10 cavity losses, 120 pC bunch charge, %0.1 beam energy spread and 15 mm.mrad RMS transverse emittance for both undulator simulations. Only bunch lengths and cavity detuning were considered to be different for better coupling in the resonators.

5. CONCLUSION

Due to longer electron bunch length, for longer wavelength FELs the laser pulses are longer and reach up to 10 ps. The main parameters of the FEL which can be produced by undulator-1 and undulator-2 for 120 pC bunch charge are given in Table 5 as the results of analytical calculations, FELO, GENESIS and OPC simulation codes. For several FEL and other technology applications, in order to improve technology, industry and science in Middle East Area, it is volunterely decided to construct Turkish Accelerator Center, which includes IR-FEL System besides Synchrotron Radiation, Proton Accelerator, Particle Factory, and SASE FEL System.

Table 5: Expected Main Parameters of TAC IR-FEL for 1,6 mA average beam current

Parameter	Undulator-1	Undulator-2
Wavelength [μ m]	2.5-27	11-250
Micropulse repetition rate [MHz]	13	13
Max. Peak Power [MW]	~5	~2.5
Average Power [W]	0.1-40	0.1-30
Max. Pulse energy [μ J]	~10	~8
Pulse length [ps]	1-10	1-10

6. ACKNOWLEDGEMENT

This work is supported by the Turkish Atomic Energy Authority (TAEA) and Turkish State Planning Organization under the grant no. DPT2006K-120470. This work is also supported by TÜBİTAK under grant no. 105T442.

-
- [1]. *F. Ciocci, G. Dattoli, A. Torre, A. Renieri*, Insertion Devices for Synchrotron Radiation and Free Electron Laser (World Scientific, 2000), ISBN 981-02-3832-0.
- [2]. *D. C.Tyte*, In 'Advances in Quantum Electronics', Vol.1, (D.W. Goodwin, ed., Academic Press, New York, 1970).
- [3]. *W.W.Rigrod*, Journal of Appl. Physics, v34, pp.248 1965
- [4]. *H.Kogelnik, T.Li*, Proceedings of the IEEE, p.97 (1966).
- [5]. Laser Resonators and Beam Properties, *Normann Hodson*, (Optical Sciences, 2004).
- [6]. <http://www.aor.com/anonymous/pub/theory.pdf>
- [7]. <http://corona.physics.ucla.edu/~reiche/>
- [8]. <http://lpno.tnw.utwente.nl/project.php?projectid=21&submenu=16>

M² QUALIFY LASER BEAM PROPAGATION

ABDELHALIM BENCHEIKH, MOHAMED BOUAFIA

Applied Optics Laboratory, University Ferhat Abbas –Setif 19000 , Algeria

One of the most important properties of a laser resonator is the highly collimated or spatially coherent nature of the laser output beam. Laser beam diameter and quality factor M^2 are significant parameters in a wide range of laser applications. This is because the spatial beam quality determines how closely the beam can be focused or how well the beam propagates over long distances without significant dispersion. In the present paper we have used three different methods to qualify the spatial structure of a laser beam propagating in free space, the results are obtained and discussed, and we have found that the Wigner distribution function is a powerful tool which allows a global characterization of any kind of beam.

1. INTRODUCTION

The use of lenses and other optical elements is required by mainly laser applications so as to focus, modify, or shape the laser beam [1]. The adequate choice of the best optics for a particular laser application necessitates the knowledge of the basic properties of Gaussian beams. In most cases, the propagation of laser-beam can be approximated by assuming that the laser beam has an ideal Gaussian intensity profile, corresponding to the theoretical TEM_{00} mode.

In praxis, the real lasers output is not truly Gaussian. This discrepancy can be accommodated by using a quality factor M^2 (called the “M-square” factor). The quality factor M^2 has been defined to describe the deviation of the laser beam from a theoretical Gaussian one.

For a theoretical Gaussian beam $M^2 = 1$; but for a real laser beam $M^2 > 1$. In all cases, the M^2 factor, which varies significantly, affects the characteristics of a laser beam and cannot be neglected in optical designs [1-3].

Firstly, we will discuss the characteristics of a theoretical Gaussian beam $M^2 = 1$ and then we will show how these characteristics change as the beam deviates from its theoretical shape. In all cases, a circularly symmetric wave front is assumed, as would be the case for a helium neon laser. Diode laser beams are asymmetric and often astigmatic, which causes their transformation to be more complex. In order to gain an appreciation of the principles and limitations of Gaussian beam optics, it is necessary to understand the nature of the laser output beam. In TEM_{00} mode, the beam emitted from a laser is a perfect plane wave with a Gaussian transverse irradiance profile. The Gaussian shape is truncated at some diameter either by the internal dimensions of the laser or by some limiting aperture in the optical train. To specify and discuss propagation characteristics of a laser beam, we must give the theoretical aspect of laser beam propagation.

The aim of this paper consists on the use of a three techniques to evaluate the spatial structure of a laser beam; the first technique is based on the measurement of the width of the beam in different locations along the axis of propagation and then we plot the width as a function of the distance of propagation, from the curve we extract the spatial characteristics of the beam.

The second one is based on the measurement of the intensity moments in different locations along the axis of propagation, from these moments we extract the spatial characteristics of the beam, and we do that we have done with the first method.

The last technique is based on the measurement of the Wigner distribution function; this last gives access to the whole spatial characteristics of the laser beam. And finally we discuss the results and we will finish with a conclusion.

2. THEORETICAL ASPECTS

2.1 Gaussian beam

Gaussian beams are the simplest and often the most desirable type of beam provided by a laser source. As we will see in this section, they are well characterized and the evolution is smooth and easily predicted. The amplitude function representing a Gaussian beam can be deduced from the boundary conditions of the optical resonator where the laser radiation is produced. The geometrical characteristics of the resonator determine the type of laser emission obtained. For stable resonators, neglecting a small loss of energy, the amplitude distribution is self-reproduced in every round trip of the laser through the resonator. Unstable resonators produce an amplitude distribution more complicated than in the stable case. Besides, the energy is leaking in large proportion for every round trip. For sake of simplicity we restrict this first analysis to those laser sources producing Gaussian beams. The curvature of the mirrors of the resonator and their axial distance determines the size and the location of the region showing the highest density of energy along the beam. The transversal characteristics of the resonator allow the existence of a set of amplitude distributions that are usually named as modes of the resonator. The Gaussian beam is the lowest degree mode, and therefore it is the most commonly obtained from stable optical resonators [2, 3].

The propagation of Gaussian beams through an optical system can be treated almost as simply as geometric optics. Because of the unique self-Fourier Transform characteristic of the Gaussian, we do not need an integral to describe the evolution of the intensity profile with distance. The transverse distribution intensity remains Gaussian at every point in the system; only the radius of the Gaussian and the radius of curvature of the wave front change [4].

The set of modes is characterized in every point along the propagation axis by two functions: $R(z)$ and $w(z)$. The first describes the radius in the transverse plane for which the amplitude of the field has decreased by a factor $1/e$ with respect to the amplitude value along the propagation axis, while the second parameter, with respect to the fundamental mode TEM_{00} , gives the radius of curvature of the wave front that intersects the propagation axis. The transversal intensity

distribution of the laser beam (for the TEM_{00} only) has a Gaussian dependence, it is given by:

$$U(r, z) = A(z) \exp\left(-jk \frac{r^2}{2q(z)}\right) \quad (1)$$

And its radius $w(z)$ contracts to a minimum w_0 known as the waist of the beam. The two parameters $R(z)$ and $w(z)$ are determined by the waist size w_0 and by the distance z from the waist position, the complex ray of curvature between brackets is given as a function of the ray curvature of the wave front of the beam and of its width [1, 2, 3]:

$$\frac{1}{q(z)} = \frac{1}{R(z)} - j \frac{\lambda}{\pi w^2(z)} \quad (2)$$

The longitudinal beam profile determined by the function $w(z)$ is a hyperbola with asymptotes forming an angle with the propagation axis.

The equations describing the beam radius $w(z)$ and the wave front radius of curvature $R(z)$ are:

$$w^2(z) = w_0^2 \left(1 + \left(\frac{z}{z_R}\right)^2\right) \quad (3)$$

$$R(z) = z \left(1 + \left(\frac{z_R}{z}\right)^2\right) \quad (4)$$

The Rayleigh length and the divergence angle, respectively relate the beam waist to the wave length as follows:

$$z_R = \frac{\pi w_0^2}{\lambda} \quad ; \quad \theta = \frac{\lambda}{\pi w_0} \quad (5)$$

The beam size will increase, slowly at first, then faster, eventually increasing proportionally to z . The wave front radius of curvature, which was infinite at $z = 0$, will become finite and initially decrease with z . At some point it will reach a minimum value, and then increase with larger z , eventually becoming proportional to z .

2.2 Real aspect of laser beams and the intensity moments

In the most cases in practice the laser beam is not purely Gaussian because of the experimental limitations as; truncation, phase distortion, etc... (see fig.1)

The theory of Gaussian beam propagation is not sufficient to describe the evolution of the spatial characteristics of such beams as beam width and the divergence, the introduction of the intensity moments is very convenient in this case and the beam width and the divergence are given by (for the sake of simplicity we consider a circular beam with only one dimension x) [5]:

$$d(z) = 4\sqrt{\langle x^2 \rangle} \quad \theta(z) = 4\sqrt{\langle \theta^2 \rangle} \quad (6)$$

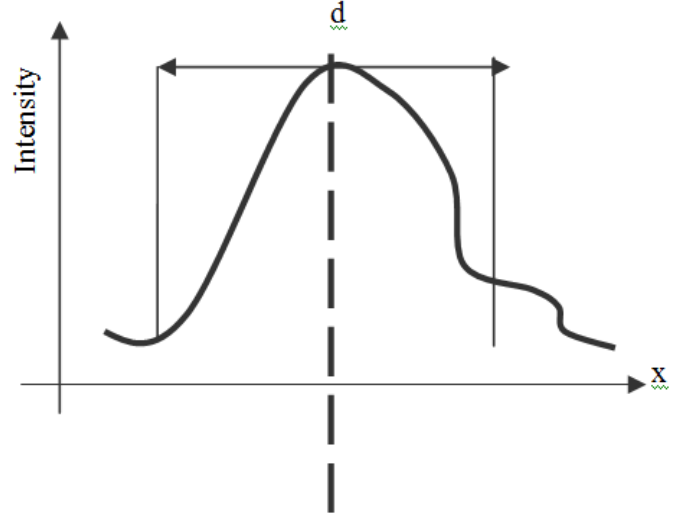


Fig.1: Intensity distribution of non Gaussian laser.

Here the second moments of the intensity distribution $I(x, y, z)$ at the location z are given by:

$$\langle x^2 \rangle(z) = \frac{\iint (x - \langle x \rangle)^2 I(x, y, z) dx dy}{\iint I(x, y, z) dx dy} \quad (7)$$

$$\langle \theta^2 \rangle(z) = \frac{\iint \langle \theta^2 \rangle \bar{I}(x, y, z) dx dy}{\iint \bar{I}(x, y, z) dx dy} \quad (8)$$

Here $\langle x \rangle$ is the first moment of the intensity distribution giving coordinates of the beam centre:

$$\langle x(z) \rangle = \frac{\iint \langle x \rangle I(x, y, z) dx dy}{\iint I(x, y, z) dx dy} \quad (9)$$

$$\langle \theta(z) \rangle = \frac{\iint \langle \theta \rangle \bar{I}(x, y, z) dx dy}{\iint \bar{I}(x, y, z) dx dy} \quad (10)$$

$$\langle x\theta(z) \rangle = \frac{\iint \langle x\theta \rangle I(x, y, z) dx dy}{\iint I(x, y, z) dx dy} \quad (11)$$

The invariant parameter and the quality factor M^2

We can introduce a matrix which describes the different spatial parameters of a laser beam (parameters of propagation), this matrix is called in the literature a beam matrix M , and it is given with the physical signification of each element of the matrix by:

$$M = \begin{pmatrix} \langle x^2 \rangle & \langle x\theta \rangle \\ \langle x\theta \rangle & \langle \theta^2 \rangle \end{pmatrix} = \begin{pmatrix} \text{Width} & \text{Curvature} \\ \text{Curvature} & \text{Divergence} \end{pmatrix} \quad (12)$$

The propagation of a given laser beam along the optical systems described by ABCD matrix, is given by [3, 5]:

$$\begin{pmatrix} \langle x_2^2 \rangle & \langle x_2\theta_2 \rangle \\ \langle x_2\theta_2 \rangle & \langle \theta_2^2 \rangle \end{pmatrix} = \begin{pmatrix} A & B \\ C & D \end{pmatrix} \begin{pmatrix} \langle x_1^2 \rangle & \langle x_1\theta_1 \rangle \\ \langle x_1\theta_1 \rangle & \langle \theta_1^2 \rangle \end{pmatrix} \begin{pmatrix} A & B \\ C & D \end{pmatrix}^T \quad (13)$$

We can write [5]:

$$\langle x_2^2 \rangle \langle \theta_2^2 \rangle - \langle x_2\theta_2 \rangle^2 = \langle x_1^2 \rangle \langle \theta_1^2 \rangle - \langle x_1\theta_1 \rangle^2 \quad (14)$$

Where, the sub notations 1 and 2 are for the input and out beam.

Finally we can show that the quantity $\langle x^2 \rangle \langle \theta^2 \rangle - \langle x\theta \rangle^2$ is invariant with propagation with lossless optical systems. This invariant is given by [3.5]:

$$\langle x^2 \rangle \langle \theta^2 \rangle - \langle x\theta \rangle^2 = \left(\frac{\lambda}{4\pi} M^2 \right)^2 \quad (15)$$

In the previous paragraph we have found that for the Gaussian beams there is a parameter which remains invariant along the propagation through ABCD optical systems. If we rearrange the equation (15) we find the famous quality factor known as M² factor [3, 5-9], given by:

$$M^2 = \frac{4\pi}{\lambda} \sqrt{\langle x^2 \rangle \langle \theta^2 \rangle - \langle x\theta \rangle^2} \quad (16)$$

This parameter gives a compact characterization of any kind of laser beams; it describes the deviation of the real laser beam from the ideal model which is the Gaussian one. The value of M² is 1 for the ideal case (Gaussian beam), and it become greater than 1 when the intensity distribution deviates from the Gaussian model.

2.3. Wigner distribution function

A partially-coherent light beam is described better by its second order functions. One of these functions is the cross spectral density function that, in the two dimensional case, can be written as [6, 7, 10, 11,12]:

$$\Gamma(x, s, z) = \left\langle E\left(x + \frac{s}{2}, z\right) E^*\left(x - \frac{s}{2}, z\right) \right\rangle \quad (17)$$

Where; $E(x, z)$ is the distribution of the electric field along the x axis at a given distance of propagation z, * means the complex conjugate and $\langle \rangle$ stands for an ensemble average.

The Wigner distribution is defined as the Fourier transform of the cross spectral density as follows [6, 7, 12].

$$W(x, u, z) = \int \Gamma(x, s, z) \exp(-2i\pi us) ds \quad (18)$$

The use of the Wigner distribution in optics has been deeply studied and it seems to be very well adapted to the analysis of partially coherent beam because it contains information about the spatial irradiance distribution and its angular spectrum at the same time, so it allows to give the local spatial frequencies at any location.

We define both the width, divergence and the curvature as functions of the second order moments of the Wigner distribution as [6-7, 10-12]:

$$\langle x^2 \rangle_w(z) = \frac{\iint (x - \langle x \rangle)^2 W(x, u, z) dx du}{\iint W(x, u, z) dx du} \quad (19)$$

$$\langle \theta^2 \rangle_w(z) = \frac{\iint (u - \langle u \rangle)^2 W(x, u, z) dx du}{\iint W(x, u, z) dx du} \quad (20)$$

$$\langle x\theta \rangle_w(z) = \frac{\iint \langle xu \rangle W(x, u, z) dx du}{\iint W(x, u, z) dx du} \quad (21)$$

3. EXPERIMENTAL RESULTS

The first step of the experiment is to take different caustics which correspond to the different propagating distances z by using the setup presented in the figure.2

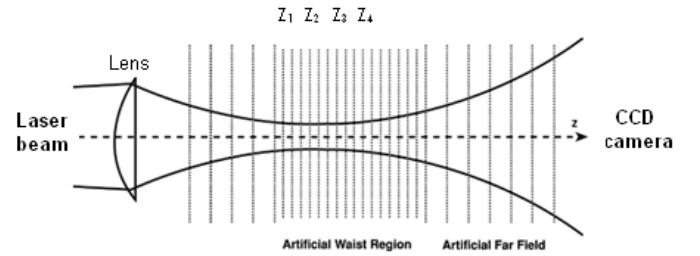


Fig.2. The record of the different caustics

We have a lens which focuses the laser beam, and then we take different images (caustics) in different locations along z axis of propagation. The images taken by a CCD camera are presented below:

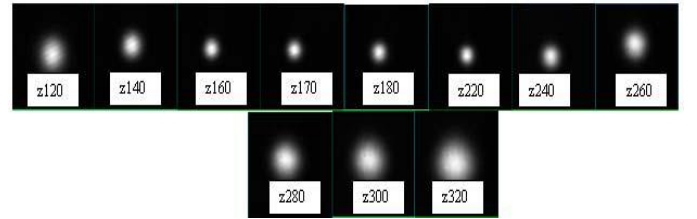


Fig.3. Caustics spots of laser beam in different z positions in mm.

With the three methods we use the same caustics (images) to characterize the spatial structure of the laser beam.

The first method:

The evolution of the width of laser beam along free space is represented in figure 4. From this curve we extract the beam waist and the divergence, and then the M^2 factor.

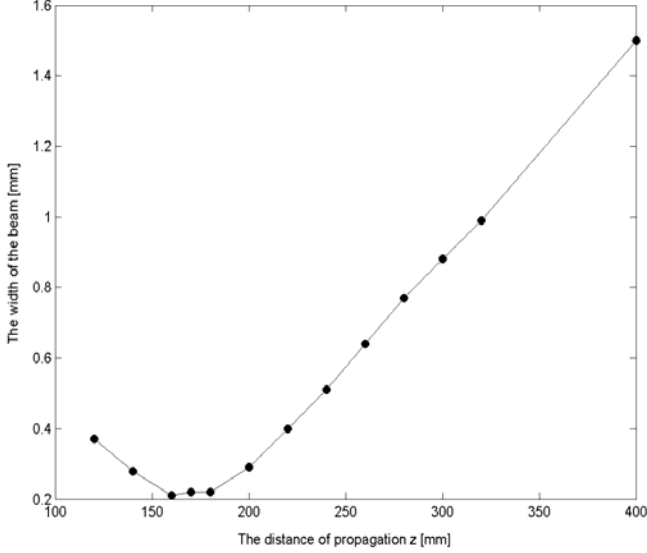


Fig.4. The evolution of laser beam width along free space. $d_0 = 2w_0 = 0.4\text{mm}$. The quality factor is found $M^2 = 1.77$

The second method "Moment method":

With the same manner as the first method, but in this one we measure the intensity second order moments at different distances of propagation z, we have plotted the curve by using 'Beam analyzer' software. The curve is given by the figure 5.

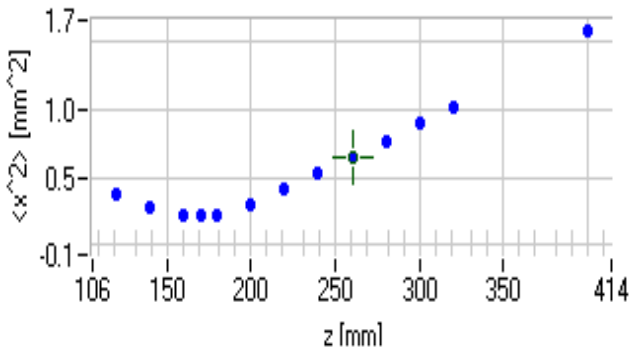


Fig.5. The evolution of the second order moment of laser beam along free space.

From the curve we extract the spatial characteristics as follows: the waist: $d_0 = 2w_0 = 4\sqrt{\langle x^2 \rangle} = 0.43\text{mm}$, and the divergence $\theta = 4\sqrt{\langle \theta^2 \rangle} = 2.83 \times 10^{-6}\text{rad}$. The quality factor is given by $M^2 = \frac{BPP}{(\lambda/4\pi)} = 1.77$

The third method "Wigner distribution":

For this method, we construct the Wigner distribution function from the different caustics, the reconstruction is based on the mathematical concept of Radon transform and filtered back projection theorem, in the present experiment we have reconstructed the Wigner distribution by using the 'Beam analyzer' software and the result is given bellow in the figure 6.

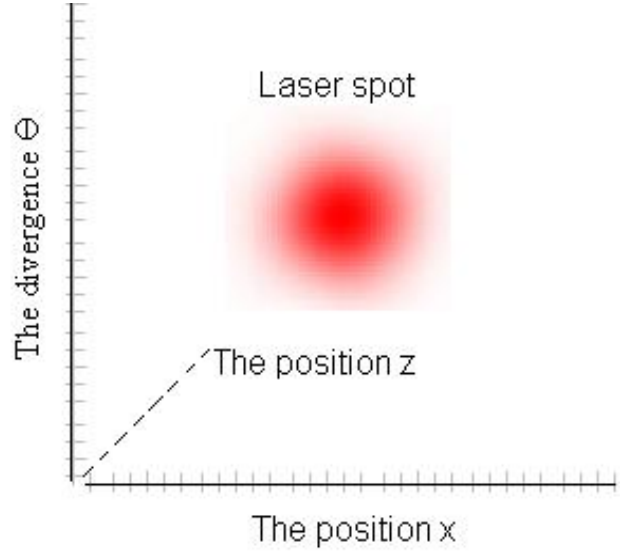


Fig.6. Wigner distribution of reconstructed caustics.

The software beam analyzer allows calculating the different moments (first, second and mixed orders) of the Wigner distribution function. It gives the results in a form of a (4*4) matrix.

The beam matrix is given by:

$$S = \begin{pmatrix} \langle x^2 \rangle & \langle xu \rangle \\ \langle xu \rangle & \langle u^2 \rangle \end{pmatrix} = \begin{pmatrix} \langle 2.84 \times 10^{-3} \rangle & \langle -4.76 \times 10^{-6} \rangle \\ \langle -4.76 \times 10^{-6} \rangle & \langle 2.83 \times 10^{-6} \rangle \end{pmatrix}$$

From this matrix we extract the waist $d_0 = 2w_0 = 4\sqrt{\langle x^2 \rangle} = 0.42\text{mm}$, and the divergence $\theta = 2.83 \times 10^{-6}\text{rad}$. Finally we get the value of the quality factor as $M^2 = \frac{BPP}{(\lambda/4\pi)} = 1.78$.

4. CONCLUSION

In this work three methods are used to characterize the laser beam quality. The results obtained from experiments show that the use of the Wigner distribution gives more information about the characteristics of laser such as coherence. The use of the Wigner distribution is more important in partially light characterization.

5. ACKNOWLEDGMENTS

The authors acknowledge support from the German Academic Exchange Service –DAAD–.

- [1]. *A.E.Siegman*, Lasers, (University Science Books, 1986).
- [2]. *H.Kogelnik and T. Li*, IEEE. 54, 1312 (1966).
- [3]. *N.Hodgson and H.Weber*, Laser Resonators and Beam Propagation, Fundamentals, Advanced Concepts and Applications, Second Edition, (Springer, 2004).
- [4]. *R.Martinez-Herrero, P.M Mejéas, H.Weber*. Opt. Quantum Electron. 25, 423 (1993)
- [5]. *P.A.Bélangier*, Optic Lett. 16, 196 (1991).
- [6]. *M.J. Bastiaans*, J. Opt. Soc. Am. 69, 1790 (1979).
- [7]. *M.J. Bastiaans*, J. Opt. Soc. Am. A 3, 1227 (1986).
- [8]. *A.E. Siegman*, IEEE J.Quantum Elec. 27,1146, (1991).
- [9]. *J.Alda*, Opt. Commun. 192, 199 (2001).
- [10]. *M.J. Bastiaans*, Optik. 88, 163 (1991).
- [11]. *M.J.Bastiaans*, Optik. 82, 173, (1989).
- [12]. *B.J.Neubert, B.Eppich*, Opt. Comm. 02, 38 (2005)

EFFECT OF CO₂ LASER FOCUSING ON GROOVE CUTTING INTO STEEL SURFACES

SULEYMAN BIYIKLI¹ AND JALE YILMAZKAYA SUNGU²

¹ *Mechanical Engineering Department,
Okan University, 34959 Istanbul /Turkey*

² *Faculty of Arts and Science, Department of Physics,
Kocaeli University, 41380 Kocaeli /Turkey*

High power CO₂ lasers with power outputs of 20 kW or more are being manufactured with such a power it is possible to build CNC machining centers to machine metals such as austenitic steels. Effect of lens focusing on evaporative laser groove forming on steel parts with a moving continuous wave laser is described by solving a heat transfer model. A three dimensional heat transfer model which was developed by Biyikli and Modest[13] subject to a number of assumptions such as negligible convective losses, no multiple reflections within the groove, and negligible beam channeling is modified for carbon steels for this study. This model is solved to analyze the lens focusing effects on the laser groove-cutting of steels. Evaporative removal of steel is achieved by heating the steel surface with a high-power CO₂ laser. The laser beam is highly-concentrated Gaussian Continuous-Wave at TEM₀₀ mode and it is focused by a lens through which the laser beam passes and behind which it converges to a minimum beam waist and subsequently expands. The resulting non-linear partial differential equations were solved numerically by an explicit-implicit method. The thermal properties of steel which are available in the literature are used in this model to study the focusing effects on the kerf geometry for a given scanning speed and laser power. The results of this model are used to investigate the effect of lens focusing on the groove depth, thickness, and shape for some typical laser parameters such as lens focal position, laser power, and scanning speed.

1. INTRODUCTION

High power CO₂ lasers have been used as a tool for material processing such as welding, trimming, scribing, cutting in many different industries. With the concentrated energy of the CO₂, at the focal point of the lens it is possible to heat, melt, and vaporize any known material including stainless steel. Laser cutting have many advantages over conventional cutting techniques which include high productivity, narrow kerf width, low roughness of cut surfaces, minimum metallurgical distortion, easy integration with the CNC machines, cutting complex geometries, non contact process for reducing vibration, and eliminating all the problems related to the cutting tools [1-3]. Laser cutting is a thermal process in which a cut kerf (slot or groove) is formed by the heating action of a focused traversing laser beam. The laser cutting process types, defined according to their dominant transformation process, include: laser fusion cutting (inert gas cutting), laser oxygen cutting and laser vaporization cutting. The laser fusion cutting process, also called inert gas melt shearing, is based on transformation of the material along the kerf into the molten state by heating with laser energy and the molten material is blown out of the kerf by a high-pressure inert gas jet. The principle of laser oxygen cutting is that the focused laser beam heats the material in an oxidizing atmosphere and ignites an exothermic oxidation reaction of the oxygen with the material which in turn improves the laser cutting process by providing additional heat in the cutting zone resulting into higher cutting speeds compared to laser cutting with inert gases. During laser vaporization cutting, the material is heated beyond its melting temperature and eventually vaporized. A process gas jet is used to blow the material vapor out of the kerf to avoid precipitation of the hot gaseous emissions on the workpiece and to prevent them from condensation within the developing kerf. Laser vaporization cutting has the lowest speed among other methods; however, it is suitable for very precise, complex cut geometries [4 -5]. The laser cutting parameters are dependent on the beam wavelength, power, beam quality, polarization, thermal properties and

thickness of the material to be cut, continuous wave (CW) or pulsed laser power, focal length of the lens, focal position of the lens relative to material surface, and the cutting speed [6].

Mathematical investigations in the area of laser material processing have treated cases with and without phase change and a variety of irradiation or source conditions have been studied both theoretically and experimentally. Material removal from the top surface of a solid by a high intensity laser beam was analytically treated by Dabby and Paek [7]. They calculated the material removal rate by vaporization from the solid surface and the temperature profile in the solid. Cline and Anthony [8] derived a model for laser heating and melting of materials for a Gaussian source moving at constant velocity for which they calculated the temperature distribution and depth of melting zone as a function of laser beam diameter, velocity and power. A three-dimensional heat transfer model was developed by Mazumder and Steen [9] for a laser beam striking the surface of an opaque substrate moving with a uniform velocity. The model was solved numerically for temperature distribution and melt depth. A model developed by Modest and Abakians [11] studied the formation of a groove by evaporation on a moving semi-infinite solid. Most of the analytical models reported in the literature assumed parallel laser beams which is a reasonable assumption only when there is no focusing of the beam, or when the focal length of the lens is many times the depth of the groove. In practical applications, material processing is achieved by melting or evaporating material with a Gaussian laser beam, which is focused by a lens to a small spot size around its focal point in order to increase the intensity of the laser beam. The radius of the focused beam waist and subsequent expansion of the beam depend on the characteristics of the laser beam as well as the type of lens being used. Both beam waist and expansion rate have profound effects on the size and shape of the laser cuts. Bar-Isaac and Korn [12] used a three-dimensional moving heat source model to describe the effect of a focused laser beam in the drilling process. They studied the effects of changing focal position of the beam on the motion of the evaporation

surface. Biyikli and Modest [13] studied the evaporative cutting of a semi-infinite material with a moving focused continuous-wave laser by solving numerically the non-linear partial differential equations. The results of these solutions for groove depth and shape were presented for a variety of laser and solid parameters. The partial differential equations were non dimensionalized and solved for general cases which did not apply for any materials. In the present work, evaporative groove forming were studied for austenitic stainless steel (grades AISI 304 and AISI 316). . The effect of focusing parameters such as position of lens focal point above or below the surface, minimum beam radius, and material removal rate are investigated.

2. THEORETICAL ANALYSIS

Steel groove cutting is achieved by evaporating steel with a focused Gaussian laser beam as a heat source. A Gaussian laser beam at TEM₀₀ mode is focused by a lens through which the laser beam passes and behind which it converges to a minimum beam waist around the focal point of the lens, as shown in Figure 1. In order to develop a mathematical model the physical description of the problem is given as follows; a focused Gaussian laser beam strikes the surface of an opaque semi-infinite steel material moving in the x-direction with a constant velocity as shown in Figure 1. There are three different regions on the surface of the material. Region I is that part of the surface that is still too far away to have reached evaporation temperature or too far away on the side to even reach evaporation but it is heating; Region II is the area close to the beam center where evaporation takes place; and finally, Region III is the surface where evaporation has been completed but it is cooling off.

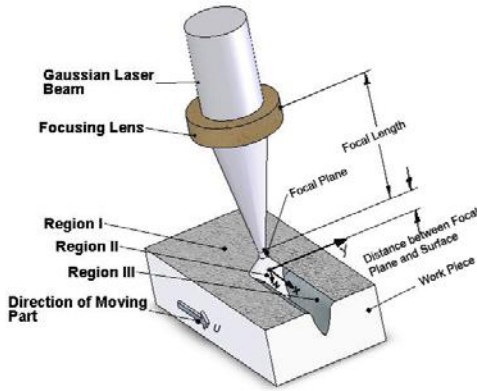


Fig. 1. Evaporative laser groove cutting by using a focusing lens with three different regions

Laser beam strikes with an intensity, F , to the surface of the material at an angle and starts evaporating and forming the groove which can be better visualized in Figure 2. The radius of the beam reaches to its minimum value at the focal plane and is expressed as the focal point radius, R_0 . Distance between the focal plane and the surface is expressed as, w , can be on the surface, above the surface, or below the surface. Laser beam intensity can be calculated by using $F = P / \pi R^2(z)$ where P is the laser power, and the $R(z)$ is the beam radius. Laser beam is striking at an angle when the groove is forming. Vector components of the laser beam intensity $F_x, F_y, F_z,$ and F_r are also shown in Figure 2.

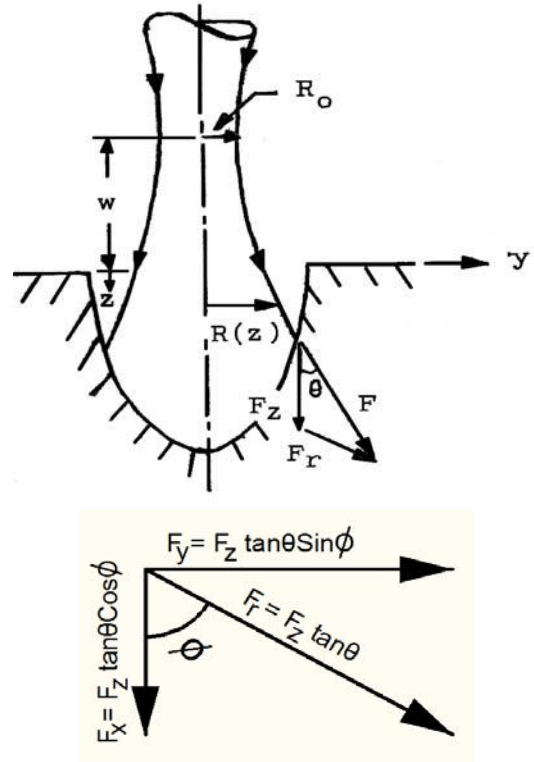


Fig.2. Evaporative laser cutting terminology used in the equations.

$R(z)$ is the laser beam radius away from the focal plane of the beam. An expression for the laser beam expansion, $R(z)$, is given by Self [14] as;

$$R(z) = R_0 \left[1.0 + \left(\frac{w+z}{\pi R_0^2 / \lambda} \right)^2 \right]^{1/2} \tag{1}$$

Laser beam intensity at the beam focal point can be calculated by using $F_0 = P / \pi R_0^2$ since the beam is striking at an angle when the groove is forming and also as the beam expanding, the beam intensity can be expressed by using the following equation;

$$\vec{F}(x, y, z) = (k + \tan \theta \cos \phi \vec{i} + \tan \theta \sin \phi \vec{j}) F_0 \frac{R_0^2}{R^2(z)} e^{-(x^2+y^2)/R^2(z)} \tag{2}$$

where $\vec{i}, \vec{j}, \vec{k}$ are the unit vectors in the x, y, z directions, respectively, after evaluating the angles by using analytic geometry, laser beam intensity can be written as;

$$\vec{F}(x, y, z) = \left[k + \frac{w+z}{(\pi R_0^2 / \lambda)^2 + (w+z)^2} (x \vec{i} + y \vec{j}) \right] F_0 \frac{R_0^2}{R^2(z)} e^{-(x^2+y^2)/R^2(z)} \tag{3}$$

The heat transfer model is developed by using the following assumptions, the more detailed discussion of the assumptions are given in reference [13].

1. The solid moves at constant velocity.
2. The solid is isotropic with constant thermal properties.
3. The material is opaque, i.e., the laser beam does not penetrate appreciably into the medium, with constant absorptivity.
4. Change of phase of the medium from solid to vapor occurs in one step at a single evaporation temperature.
5. The evaporated material does not interfere with the laser beam reaching the surface.
6. Multiple reflections of laser radiations within the groove are neglected.
7. Evaporation occurs as a quasi-steady laser cutting, for this case, the temperature does not change with time with respect to coordinate system attached to the moving heat source. Experimental results indicate that a state is reached when an observer positioned at the heat source or moving origin detects no change in the temperature distribution around the source [10].

By using the assumptions and a similar derivation developed by Modest and Abakians [11], the heat transfer model is governed by the following equation,

$$\rho c u \frac{\partial T}{\partial x} = k \nabla^2 T \quad (4)$$

Subject to the boundary conditions;

$$x \rightarrow \pm\infty, \quad y \rightarrow \pm\infty, \quad z \rightarrow +\infty, \quad T \rightarrow T_\infty$$

and at the surface, $z=0$;

$$\alpha(F \cdot \vec{n}) = -\rho h_{ig} u (\vec{i} \cdot \vec{n}) - k(\vec{n} \cdot \nabla T) \quad (5)$$

Where T is the temperature in the material, and u is the velocity in the x - direction. The boundary condition at the surface is obtained from energy balance on a surface element. Modest and Abakians [11] showed that the influence of convection and radiation losses on groove depth and shape is small, and for that reason it is assumed here that heat losses

to the outside are negligible. The unit surface normal, \vec{n} , is pointing into the medium and is given by the following equation;

$$\vec{n} = \frac{\frac{\partial s}{\partial x} \vec{i} + \frac{\partial s}{\partial y} \vec{j} + \vec{k}}{\sqrt{1 + \left(\frac{\partial s}{\partial x}\right)^2 + \left(\frac{\partial s}{\partial y}\right)^2}} \quad (6)$$

The boundary condition at the surface for Region I where there is no evaporation yet but it is heating by the laser beam can be expressed as;

$$\alpha F_o \frac{R_o^2}{R^2(0)} e^{-(x^2+y^2)/R^2(0)} = -k \frac{\partial T}{\partial z} \quad (7)$$

$$x < x_{\min}(y)$$

Where F_o is the intensity of the laser beam at beam center, R_o is the effective laser beam radius at the focal plane, $R(0)$ is the beam radius at the surface, $z=0$, which does not have the same value as R_o when the beam is below or above the surface. In this equation α is surface absorptivity, $x_{\min}(y)$ is the location where evaporation commences. Then the boundary conditions at the surface for Region II where evaporation is taking place are expressed as;

$$\begin{aligned} & \left[1 - \frac{w+s}{\pi R_o^2 / \lambda + (w+s)^2} \left(x \frac{\partial s}{\partial x} + y \frac{\partial s}{\partial y} \right) \right] \alpha F_o \frac{R_o^2}{R^2(s)} e^{-(x^2+y^2)/R^2(s)} \\ & = \rho h_{ig} u \frac{\partial s}{\partial x} - k \left(\vec{n} \cdot \nabla T \right) \sqrt{1 + \left(\frac{\partial s}{\partial x}\right)^2 + \left(\frac{\partial s}{\partial y}\right)^2} \\ & T = T_{ev}, \quad z = s(x, y), \quad x_{\min} < x < x_{\max}(y) \end{aligned} \quad (8)$$

where s is the local groove depth, \vec{n} is the unit surface normal pointing into the medium, and h_{ig} is the heat of sublimation of steel. Similarly, the boundary condition for Region III where the groove is fully established, laser beam moved away and there is no evaporation taking place but the material is cooling off.

$$\begin{aligned} & \left[1 - \frac{w+s_\infty}{\pi R_o^2 / \lambda + (w+s_\infty)^2} y \frac{\partial s_\infty}{\partial y} \right] \alpha F_o \frac{R_o^2}{R^2(s_\infty)} e^{-(x^2+y^2)/R^2(s_\infty)} \\ & = -k \left(\vec{n} \cdot \nabla T \right) \sqrt{1 + \left(\frac{\partial s_\infty}{\partial x}\right)^2 + \left(\frac{\partial s_\infty}{\partial y}\right)^2} \\ & z = s_\infty(y), \quad x > x_{\max}(y) \end{aligned} \quad (9)$$

3. METHOD OF SOLUTION

Equations (1- 9) are solved by using an explicit-implicit numerical method. In this study, thermal properties of steel are used in the governing equations in order to study the effect of lens focusing on the size and shape of a groove formed by laser evaporation. Table 1 lists the thermal properties of carbon steels which are reported by many investigators [15-16], these properties were used during solution of the governing equations.

Table 1 Thermal properties of Carbon Steel (Steel 304)

Thermal Properties	Values and Units
Density (ρ)	7870 kg/m ³
Melting Temperature (T_m)	1808 K
Ambient Temperature (T_∞)	298 K
Evaporation Temperature (T_{ev})	3023 K
Specific Heat of Solid Material (c_{ps})	0.452 kJ/kg K
Specific Heat of Liquid Material (c_{pl})	0.800 kJ/kg K
Specific Heat of Vapor Material (c_{pv})	0.450 kJ/kg K
Latent Heat of Melting (L_m)	272 kJ/kg
Latent Heat of Evaporation (L_{ev})	6088 kJ/kg
Heat of Sublimation (h_{ig})	8015 kJ/kg
Thermal Conductivity (k)	27 W/mK
Surface Absorptivity (α)	0.80

There was no reported value for heat of sublimation for steels that is why; the following formula is used to evaluate the value of heat of sublimation of steel.

$$h_{ig} = c_{ps}(T_m - T_\infty) + L_m + c_{pl}(T_{ev} - T_m) + L_{ev} \quad (10)$$

Calculations were based on a 10.6 μm wavelength 9.6 kW CO₂ laser with a beam size of 19 mm in diameter which has a focusing lens of 190 mm focal length that can reduce the beam size to 135 μm in diameter at the focal plane, and the scanning speed of 8.5 cm/s.

While only the solution to Regime II is of interest Regime I must be solved first in order to provide the boundary between the two regimes, $x_{\min}(y)$ and a beginning value for the conduction penetration depth. The equations for Regime I

can be solved analytically and the solution for the surface temperature distribution is;

$$(T - T_{\infty}) = \left[\frac{3\alpha^2 P^2 e^{-(x^2+y^2)/R^2}}{4\rho c u k \pi^{3/2} R^3} \left[1 + \operatorname{erf}\left(\frac{x}{R}\right) \right] \right]^{1/2} \quad (11)$$

Solving for y as a function of x in Eq(11) for T= T_{ev} establishes the boundary between Regions I and II. The groove depth s(x,y) is found from the equations for Region II using the Region I solution as boundary conditions by using explicit-implicit numerical method as described in details Biyikli and Modest [13].

4. DISCUSSION OF RESULTS

When a beam is focused by a lens, the resulting beam waist and subsequent expansion of the beam depends on the characteristics of the laser beam as well as the type of lens being used. Figure 3 shows top view of evaporating zone under a laser beam striking to the surface of a flat steel part.

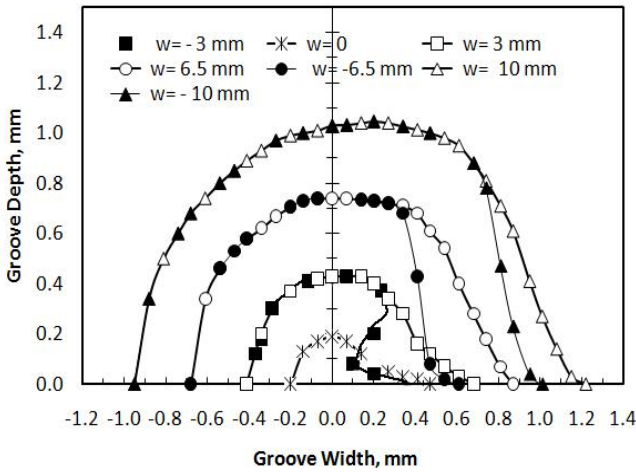


Fig. 3 Top view of the evaporation region when the beam focal point at different locations on the surface of the steel work piece.

The plots are actually symmetric around x-axis to give the complete view of the laser cut. It is seen that sizes and shapes of the evaporating zone change significantly with changing focal position of the beam on the material; w is negative for focal point of lenses below the surface of the material. The evaporating zone is smallest where the beam is focused on the surface I (w = 0). Changing the focal point of the lens above or below the surface of the material increases the area of evaporating zone.

The influence of beam waist position on fully developed groove shape and depth is shown in Figure 4 for focal points below the surface of the steel work piece. It is observed that the depth of the cuts increases and passes through a maximum when the beam is focused slightly inside the material. This type of behavior has also been observed by Bar-Isaac and Korn [12] for laser drilling. When the focal point is moved further into the material the groove becomes shallower. The increase in the groove depth by focusing the beam slightly inside the material is apparently due to better focusing of the laser energy in the center of the evaporating groove hence utilizing the energy more efficiently for

evaporation rather than for conduction; further moving the focal point into the material diverges the beam in the evaporating zone and increases the conduction losses.

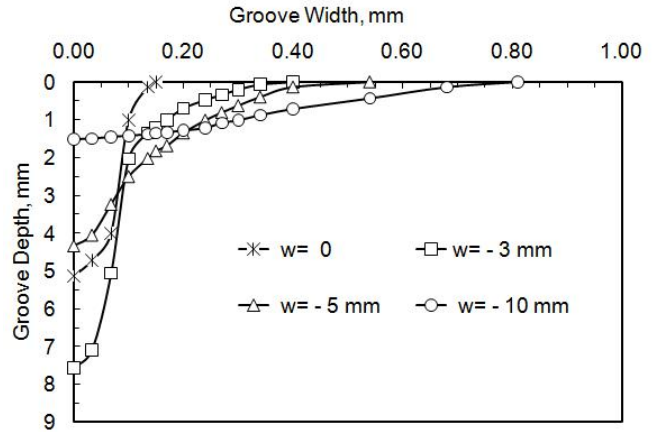


Fig.4. Effect of focal positions on the groove cross-section when focal point is in the steel, w shows the distances between the focal point of the lens and top surface of the steel.

Changes in the fully developed groove shape and depth when the beam is focused above the surface of the material are shown in Figure 5. The groove gets shallower and wider when the focal plane is moved up from the surface of the material, since the laser energy is less concentrated everywhere within the evaporating zone. As can be seen in Figures 4 and 5, the narrowest cuts are obtained when laser beams focused on the surface. This can be an important point to remember for some laser cutting operations.

The variation of fully developed maximum groove depth as a function of beam focusing distance, w, is shown in Figure 6 for different beam expansion rates. Maximum groove depth for parallel beams (w = 0) staying at focal point diameter is of course ideal case, in reality laser beam expands after the focal plane. In practice parallel beams coming from a laser are unfocused and are therefore have large beam diameters depending on the laser characteristics and are rarely strong enough to cause evaporation. In order to evaporate a material these beams need to be focused to a small diameter thus the parallel beam in Figure 6 corresponds to an ideal beam which has a diameter equal to the diameter of a focused beam at the focal plane showing a case of a lens with an infinite focal length.

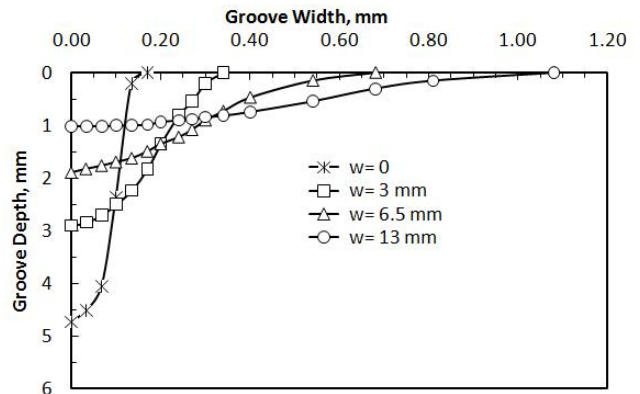


Fig.5. Effect of focal positions on the groove cross-section when focal point is above the steel surface, w shows the distances between the focal point of the lens and top surface of the steel.

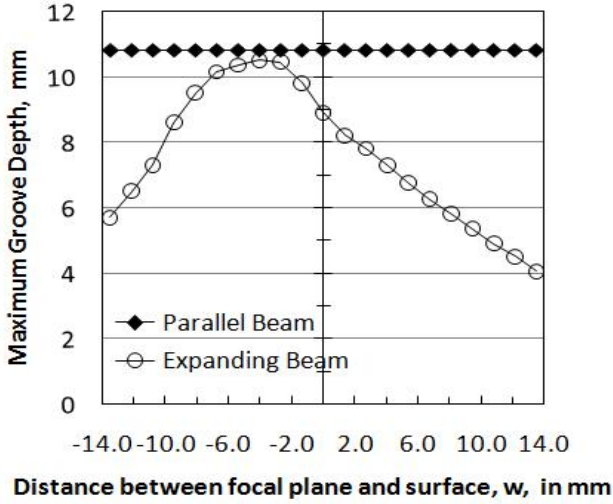


Fig.6. Variation of maximum groove depth as a function of focal plane position which can be above, below, or on the surface for parallel and expanding beams.

Figure 7 shows maximum groove depth as a function of laser power (or decreasing laser power) for different beam focusing rates. As expected for constant scanning speed the groove depth decreases significantly with decreasing laser power. This effect is the same for all focusing conditions. The effect of increasing laser speed on the groove depth for constant laser power is very similar to the variation of the groove depth in Figure 7 (not shown here).

Evaporated material removal rate varies with the distance between the lens focal plane and the surface of the work piece as shown in Figure 8.

The straight line in Figure 8 shows the maximum possible material removal rate meaning all the laser power is used just to evaporate steel, there are no other losses. When the lens is focused above or below the surface of the steel gives more material removal rate, when lens is slightly focused inside the surface ($w = -3$ mm) gives the highest removal rate.

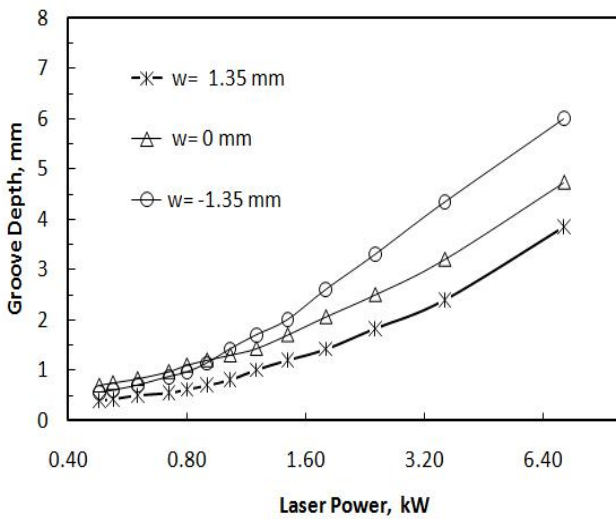


Fig.7. Variation of Maximum Groove Depth with laser power at a scanning speed of 8.5 cm/s.

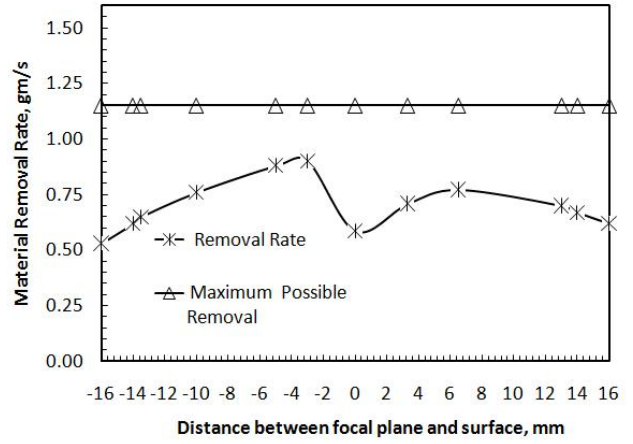


Fig.8. Variation of material removal rate with the distance between lens focal plane and the surface of the work piece

5. CONCLUSIONS

A heat transfer model for evaporative cutting of a semi-infinite body with a moving continuous wave laser has been solved numerically to investigate the effects of beam focusing on the size and shape of a groove. The study of the results indicated some interesting aspects. The depth of the groove increases and passes through a maximum when the beam is focused slightly in the material. The groove depth decreases when the beam is focused above the surface of the material. The groove depths can be increased by using lenses with long focal lengths. Longer focal length lens give a larger minimum beam radius at focal plane. Smallest width cuts are obtained when the beams are focused exactly on the surface.

Heat Affected Zone(HAZ) is defined as the temperature at which the material will experience a change in properties, for carbon steels the critical temperature is eutectoid temperature which is at 723°C . Heat Affected Zone for carbon steels for the evaporating zone can be upto 2.4 mm from the evaporating surface.

6. NOMENCLATURE

- c - specific heat, kJ/kg.K
- F_0 - laser intensity at center of a beam, W/m^2
- F_x, F_y, F_z, F_r are the components of the intensity, W/m^2
- h_{ig} - heat of sublimation, kJ/kg
- n - unit vector normal to the groove
- k - thermal conductivity, J/s.m.K
- P - laser power, W
- R - effective laser beam radius, mm
- R_0 - laser beam radius on focal plane, mm
- s - groove depth, mm
- s_{max} - maximum groove depth, mm
- s_{∞} - established groove cross section, mm
- T_{ev} - evaporation temperature, K
- T_{∞} - ambient temperature, K
- u - laser scanning speed, cm/s
- w - distance between the focal plane and surface, mm
- α - absorptivity
- ρ - density, kg/m^3
- λ - laser wave length, μm

- [1]. *N.Rajaram, J. Sheik-Ahmad and S. H.Cheraghi*, "CO₂ laser cut quality of 4130 steel", International Journal of Machine Tools & Manufacture Volume 43, 2003, pp. 351-358.
- [2]. *I.P. Shkarofsky*, "Review on Industrial Applications of High Power Laser Beams III", RCA Review, Vol. 36, 1975, pp. 338-368.
- [3]. *H.Golnabi and M.H. Mahdieh*, "Trend of laser research developments in global level", Optics & Laser Technology, Volume 38, Issue 2, 2006, pp. 122-131.
- [4]. *D.Petring*, "Laser Cutting", LIA Handbook of Laser Materials Processing, First Edition, 2001, Laser Institute of America, ISBN 0-912035-15-3, pp. 425-433.
- [5]. *J.Powell*, "CO₂ Laser Cutting", 1993, Springer Verlag, ISBN 3-540-19786-9, pp. 83-184.
- [6]. *J.C.Ion*, "Laser Processing of Engineering materials", ISBN 0 7506 6079 1, pp. 347-365.
- [7]. *F.W. Dabby, and U. Paek*, "High Intensity Laser-Induced Vaporization and Explosion of Solid Material", IEEE J. of Quantum Electronics, Vol. QE-8, No.2, 1972, pp. 106-111.
- [8]. *H.E. Cline, and T.R.Anthony*, "Heat Treating and Melting Material with Scanning Laser or Electron Beam", Journal of Applied Physics, Vol. 48, No.9, 1977, pp. 3895-3900.
- [9]. *J. Mazumder and W.M.Steen*, "Heat Transfer Model for CW Laser Material Processing", Journal of Applied Physics, 51(2), 1980, pp. 941-947.
- [10]. *E.Kannatey-Asibu*, "Principles of Laser Materials Processing", Wiley, 2009, pp231-280.
- [11]. *M. F. Modest and H.Abakians*, "Evaporative Cutting of a Semi-Infinite Body with a Moving CW Laser", ASME Journal of Heat Transfer , Vol. 108, 1986, pp. 602-607.
- [12]. *C.Bar-Isaa, and U.Korn*, "Moving Heat Source Dynamics in Laser Drilling Process", Appl. Phys., Vol. 3,1974, pp. 45-54
- [13]. *S.Bryikh and M.F.Modest*, "Beam Expansion and Focusing Effects on Evaporative Laser Cutting", Journal of Heat Transfer, 110, (1988), 529-532.
- [14]. *A.S. Self*, "Focusing of Spherical Gaussian Beams", Applied Optics, Vol. 22, No 5, 1983, pp 658-661.
- [15]. *M.J. Hsu and P.A.Mollian*, " Thermo chemical modeling in CO₂ laser cutting of carbon steel" Journal of Materials Science 29 (1994) 5607-5611.
- [16]. *B.S. Yilbas, S.B. Mansoor, R. Mansoor*, "Laser pulse heating: Cavity formation into steel, nickel and tantalum surfaces", Optics & Laser Technology 40 (2008) 723-734.

PRELIMINARY RESULTS FROM THE NEW MULTIWAVELENGTH AEROSOL LIDAR IN TURKEY

K. R. ALLAKHVERDIEV^{1,2}, **T. BAYKARA**¹, **M. BEKBOLET**³, **M. F. HUSEYINOGLU**^{1,3*},
S. OZBEK¹, **Z. SALAEVA**^{1,2}, **A. SECGIN**¹, **S. VARTAPETOV**⁴,
I. VESELOVSKII⁴, **M. KORENSKII**⁴

¹*TUBITAK, Marmara Research Center, Materials Institute, P.K. 21, 41470 Gebze/Kocaeli, Turkey*

²*Institute of Physics ANAS, 370143, Baku, Azerbaijan*

³*Bogazici University, Institute of Environmental Sciences, P.K. 34342, Bebek/Istanbul, Turkey*

⁴*Physics Instrumentation Center of General Physics Institute, Troitsk, Moscow region, 142190 Russia*

The multiwavelength Mie-Raman lidar based on a tripled Nd:YAG laser becomes an important tool for profiling aerosol physical parameters in the planetary boundary layer (PBL) and troposphere. Such lidar quantifies three aerosol backscattering and two extinction coefficients and from these optical data the particle parameters such as concentration, bimodal size distribution and complex refractive index are retrieved through inversion with regularization. In this paper, the description of new multiwavelength lidar installed in TUBITAK, MRC, Materials Institute, K09 Lab., Turkey is explained, and the first results obtained from the data acquired during the summer of 2009 are presented.

1. INTRODUCTION

Atmospheric aerosols originating either naturally from sources as diverse as marine spray, desert dust, volcano eruptions, natural grassland or forest fires, or generated from anthropogenic activities like fossil fuel burning or industrial activities, affect the Earth's radiation balance by absorbing or scattering the fluxes of either solar or terrestrial radiation. This change leads to radiative forcing of the atmosphere. Scattering and absorption tend to cool the atmosphere and it is called the aerosol direct effect. Moreover, they modify the cloud properties effecting rainfall patterns and this is called the aerosol indirect effect. Since the effect on the radiative forcing isn't immediately followed by a change in the climate, there is a major uncertainty with the predictions. On the report of the Intergovernmental Panel on Climate Change (IPCC) in 2002, it was stated that aerosol indirect effect is the most important source of error in climate modeling. At the same time, the level of understanding of the influence of aerosols onto the global mean radiative forcing is poorly understandable at present time [1].

With the lidar system, aerosol optical and physical properties like the spatial and temporal distribution, morphological characterization, particle size distribution and complex refractive index can be calculated. Also, important atmospheric data like cloud height, and characteristics as well as aerosol extinction and backscattering coefficients can be obtained by the remote sensing instrumentation technology of lidars. This information has uppermost importance regarding a better understanding of the atmosphere and its constituents [2].

The aim of this paper is to demonstrate the first results of homemade lidar sounding over the industrial zone of Gebze, Kocaeli district, Turkey (Gebze is located at the shore of Marmara Sea, Gulf of Izmit, about 40 km East from Bosphorus).

2. EXPERIMENT

Lidar is a highly sophisticated instrument able to obtain in-depth important data from the troposphere. Therefore every lidar is designed precisely for the certain purpose which it will be used. Briefly the technical characteristics of the lidar designed and developed in a joint project by the

TUBITAK, Marmara Research Center, Materials Institute (Turkey) and the Physics Instrumentation Center of General Physics Institute, Troitsk, Moscow region (Russia) are as follows: The transmitting unit is a QUANTEL BrilliantB Q-switched Nd:YAG laser emitting 855 / 400 / 240 mJ in a pulse at 1064 / 532 / 355 nm wavelengths, respectively. Laser repetition rate is 10 Hz. Laser beam is collimated by off axis parabolic mirrors with high reflecting dielectric coating at all three wavelengths. Laser beam diameter after collimation is 40 mm and divergence is below 0.2 mrad. Laser and collimator are mounted on top of the telescope allowing operation at an adjustable desired angle to the horizontal. Scattered radiation is collected by 400 mm aperture Newtonian telescope with the focal length of 1.2 m. The optical signals are separated and analyzed in 7-channel spectrum analyzer. In the process of measurements, elastic backscatters (355, 532, 1064 nm), depolarization at 355 nm, Raman signals of nitrogen (387, 608 nm) and water vapor (408 nm) are detected. The scheme of the telescope and the mounted laser is shown in figure 1.

The optical data is converted to digital signals by Hamamatsu analog-to-digital converters (ADC) inside the 7 photo-multiplier-tubes (PMT) situated on the spectrum analyzer. The digital data is acquired by the Licel transient recorder and then transferred to a computer to be pretreated and interpreted.

After the light which is backscattered by the atmospheric particles arrive the pinhole of the spectrum analyzer, it is separated into several channels and the analog signal is converted to digital data by three different types of instruments, 2 different photomultiplying Hamamatsu analog-to-digital converters and Avalanche converters. This digital data is acquired by Licel software. The acquired data is pretreated by custom made analyzing program. On this step backscattering and extinction coefficients can be calculated. Next step is the retrieval of data and this is achieved by another custom made program. On this next step, aerosol microphysics is resolved by inversion with regularization to obtain the aerosol parameters. Complex refractive index, particle size distribution (PSD), Angström component, particle volume distribution and surface area concentration

can be retrieved. The photo of the homemade lidar installed at the TUBITAK, MRC is presented in Fig. 2.

3. RESULTS AND DISCUSSION

In lidar measurements aerosol backscatter β and extinction α coefficients, attributed to particle size distribution $f(r)$ by means of integral equation can be determined using the following formulae.

$$\beta(\lambda) = \int_{r_{\min}}^{r_{\max}} f(r)K_{\beta}(r, m, \lambda)dr \quad (1)$$

$$\alpha(\lambda) = \int_{r_{\min}}^{r_{\max}} f(r)K_{\alpha}(r, m, \lambda)dr \quad (2)$$

where r – particles radius, m – refraction index and λ - wave length. The nuclei of the aerosol particles represented with $K_{\beta,\alpha}$ for spherical particles are calculated on the grounds of Mie theory. The principle of multiwave sounding is based on measurements of $\beta(\lambda)$ and $\alpha(\lambda)$ spectral dependences. Change of particle parameters, such as average size or mass,

leads to $\beta(\lambda)$ and $\alpha(\lambda)$ spectrum change. If $\beta_i(\lambda)$ or $\alpha_i(\lambda)$ exsecants, corresponding to different aerosol parameters, are linearly independent, the identification of these parameters becomes possible [3].

With our Multiwavelength Mie-Raman lidar α and β at multiple wavelengths are converted to microphysical properties of aerosols through mathematical inversion. The retrieved data contains parameters of size distribution, particle radius (r), volume (V), number density (N), complex refractive index (m_R-im_I). The most practical configuration ($3\beta+2\alpha$) is based on tripled Nd:YAG laser with backscattering (β) at 355, 532, 1064 nm wavelengths and extinction (α) at 355, 532 nm wavelengths. Acceptable input errors are estimated not more than 10% and the uncertainties of retrieval: number density –40%; volume, radius –20-30%. The retrieval for the aerosol parameters is realized by Tikhonov’s Inversion with Regularization method [4] and further developed by I. Veselovskii et al [3, 5]. The first successful application of regularization to Raman lidar is realized by D. Muller et.al. in 1998 [6].

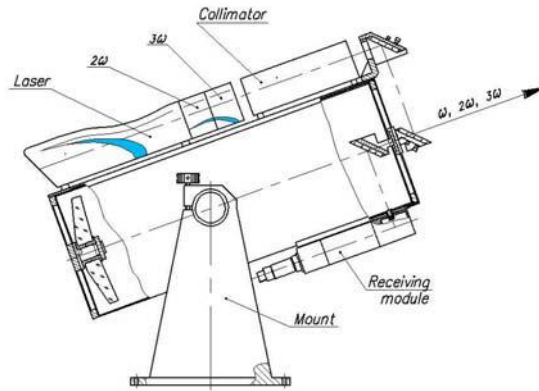


Fig.1. The scheme of the telescope and the laser on the angle adjustable mount is situated in a monostatic configuration, i.e., the transmitter (laser) and the receiver (telescope) are collocated.



Fig. 2. The picture of the lidar set-up at TUBITAK MRC, Materials Institute, K09 Laboratory during a night-time Mie and Raman scattering data acquisition. The unit on the right is the power supply and cooling unit for the transmitting unit, QUANTEL BrilliantB laser. Next is the laser mounted on top of the receiving unit, the telescope and the electronics which consist of a LICEL recorder, power supply units for the PMT’s and necessary equipment for the calibration like oscilloscope and pulse generator is situated left to the telescope.

First experimental results from Gebze region were detected on the 13th of May 2009. Obtained results were presented at the 17th International Conference on Advanced Laser Technologies, Antalya, Turkey [7]. The color maps detected during a clear night sky on June 30, 2009 is shown in Fig. 3. Please note that the term “color map” is frequently

used and the graphics is not in color. In the original versions of these color maps, colors extend from blue to red, including all the shades of green and yellow, however for the requirements of Azerbaijan Journal of Fizika, they are converted as a grey scale starting from white to black, using all shades of grey.

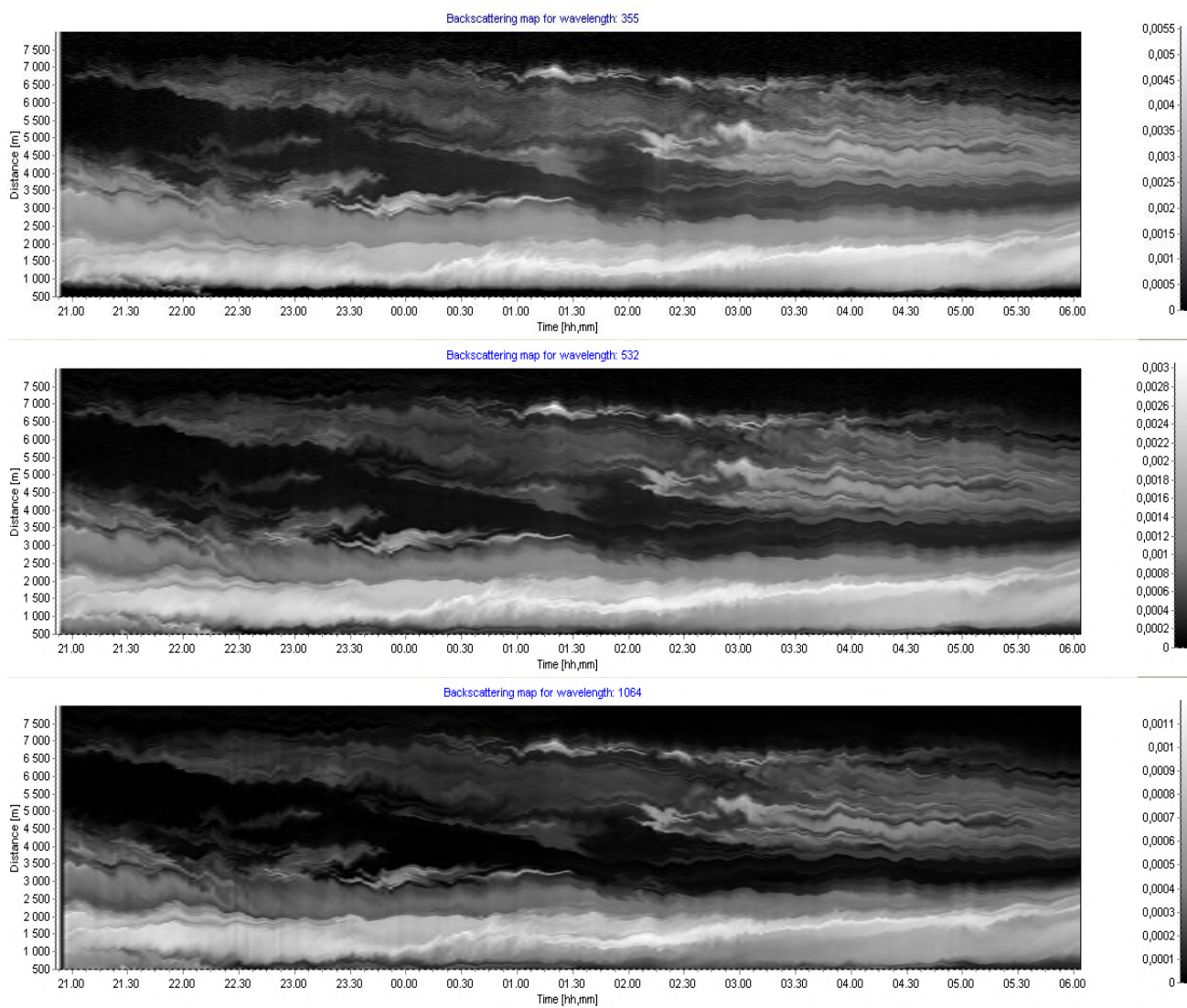


Fig. 3. The color map represents the results of lidar data obtained on June 30, 2009 during a night from 21:00 PM to 6:00 AM.

With the retrieval of data from lidar, 3 dimensional color maps can be drawn. Here, on each three parts of the figure, the vertically situated numbers on the left denotes the distance from the lidar, and since the lidar is angled 30 degrees with the horizon, to be able to calculate the real heights, the distance on the color map should be divided by 2 ($\text{Sin } 30^\circ$ is $1/2$). On the left, vertical numbered scale is given, and the horizontal numbers on the bottom of each graph denote the time. In this backscattering to distance ratio, presented in the 3-D color map for the interval of 9 hours on the x-axis, the aerosol layer at 1000 to 1500 meters kilometres was easily detected. Also, after midnight, another weaker layer is present between 6500 and 4000 meters. The three wavelengths (355, 532 and 1064 nm's) from the laser

are transmitted simultaneously, and the color maps belong to these three wavelengths respectively.

4. CONCLUSION

Homemade multiwavelength Mie-Raman lidar provided the opportunity to obtain important data of the aerosols in the troposphere layer of Gebze. These first results serve as the beginning of a greater understanding of the atmospheric constituents and their affects on cloud formation and cloud lifetime in general, and especially in the region of Bosphorus and Marmara Sea.

The main directions of coming lidar research are the study of seasonal and diurnal variations of aerosol characteristics in Gebze and Bosphorus region; separation of atmospheric aerosols of anthropogenic and natural origin; investigation of

African dust transport; study of fuel burning aerosol distribution over the area; comparison of aerosol parameters retrieved from lidar data with data from other instruments; application of aerosol lidar data for estimation of climate forcing.

5. ACKNOWLEDGMENTS

The authors are indebted to the State Plan Committee (DPT) of Turkey for the support.

-
- [1]. IPCC Third Assessment Report – Working Group I, Summary for Policy Makers, http://www.grida.no/publications/other/ipcc_tar/?src=/climate/ipcc_tar/wg1/005.htm
- [2]. C. Weitkamp, (ed) Lidar: Range-Resolved Optical Remote Sensing of the Atmosphere, (Springer, New York, 2002).
- [3]. I. Veselovskii, A. Kolgotin, V. Griaznov, D. Müller, U. Wandinger, and D. N. Whiteman, *Appl. Opt.* **41**, 3685 (2002).
- [4]. AN. Tikhonov, 1963, *Soviet Math Dokl* 4, 1035, English translation of *Dokl Akad Nauk SSSR* 151, 501 (1963)
- [5]. I. Veselovskii, A. Kolgotin, V. Griaznov, D. Müller, K. Franke, and D. N. Whiteman, *Appl. Opt.* **43**, 1180–1195 (2004).
- [6]. D. Müller, U. Wandinger, D. Althausen, I. Mattis, and A. Ansmann, *Appl. Opt.* **37**, 2260–2263 (1998).
- [7]. K. Allahverdiev, T. Baykara, M. Bekbolet, F. Huseyinoglu, S. Ozbek, Z. Salaeva, A. Secgin, S. Vartapeov and I. Vesselovskii, Proceedings of the 17th International Conference on Advanced Laser Technologies, Antalya, Turkey, 26 September- 1 October 2009 <http://alt09.kocaeli.edu.tr>

NEAR IR LASER LIGHT VISUALIZATORS USING NONLINEAR GaSe AND OTHER LAYERED CRYSTALLITES

K. R. ALLAKHVERDİEV^{a,b*}, M. Ö. YETİS^a, T. B. BAYKARA^a, S. ÖZBEK^a, E. Yu. SALAEV^b
^aTUBITAK, Marmara Research Center, P.K. 21, 41470 Gebze/Kocaeli, Turkey
^bInstitute of Physics, ANAS, 370143, Baku, H.Javid ave., 33, Azerbaijan

Two methods of preparation of the devices for visualization of pulsed and continuous near-IR (near infrared) are described and the results of conversion of pulsed and continuous IR (800-1360 nm) laser radiation into the visible range of spectra (400-680 nm) by using a transparent substrate covered with the particles (including nanoparticles) of effective nonlinear materials of GaSe_xS_{1-x} (0.2 ≤ x ≤ 0.8) are presented. Converted light can be detected in transmission or reflection geometry as a visible spot corresponding to the real size of the incident laser beam. Developed device structures can be used for checking if the laser is working or not, for optical adjustment, for visualization of distribution of laser radiation over the cross of the beam and for investigation of the content of the laser radiation. Low energy (power density) limit for visualization of the IR laser pulses with 2-3 ps duration for these device structures are: between 4.6 – 2.1 μJ (3·10⁻⁴ – 1·10⁻⁴ W/cm²) at 1200 nm; between 8.4 – 2.6 μJ (4.7·10⁻⁴ – 1.5·10⁻⁴ W/cm²) at 1300 nm; between 14.4 – 8.1 μJ (8.2·10⁻⁴ – 4.6·10⁻⁴ W/cm²) at 1360 nm. Threshold damage density is more than 10 MW/cm² at λ = 1060 nm, pulse duration τ = 35 ps. The results are compared with commercially existing laser light visualizers.

1. INTRODUCTION

Near IR laser light converters are essential components in optical communication systems. These devices should have low power density limit (high energy sensitivity), high threshold damage, linear response and longer spectral sensitivity. Two types of converters are in use for visualization of the near IR radiation. First type is a commercial beam detector plates of KDP [KH(PO₄)₂-potassium dihydrogen phosphate], KTP [KTiOPO₄-potassium titanium phosphate] or ceramic ABO₃ [eg. PZT, Pb_x(Zr_{0.53}Ti_{0.47})O₃]. They consist of pressed microcrystals (fine powder) of KDP, KTP or PZT in a crystalline form. In this type of devices the second harmonic generation (SHG) effect is used for visualization. Second type of converters (IR laser sensors) are commercially distributed by LASER 2000 [2] and consist of a special phosphor material (different materials for wavelength from 250 nm to 1800 nm; standard from 750 to 1300 nm) buried in a plastic foil. In these type of devices a fine powder (microcrystals) in a crystalline form is buried in a plastic foil. The physical principle of light conversion is different in the second type of devices and based on the phosphorescence phenomenon.

Both type of these converters reveal strong and weak points. Among them are:

- first type permits to visualize the distribution of the intensity of laser radiation over the cross section of laser beam and to investigate a content of laser radiation. The sensitivity is limited, they do not give a possibility to visualize a weak radiation (less than 40 μJ power in a 1/e beam diameter of 1.5 mm) at 1053 nm and radiation at wavelength more or equal to 1200 nm.
- second type, in comparison with the first type, permits to visualize the laser radiation at 1053 nm and also at wavelength up to 1800 nm. The response is highly nonlinear, they do not give the real spot size of the laser beam due to fluorescence of the regions of material which are close to the excited spot region. Besides this, the second type of converters do not give a possibility for visualization of distribution of the intensity of radiation over the cross section of laser beam and for investigation of content of laser radiation. Furthermore the second type of converters must be charged by a short exposure to a daylight or

fluorescent light prior to use. The sensitivity decreases after exposure as a function of time.

All the above-mentioned, attracted our attention to the class of crystals with GaSe- type structure. It is well known, that highly anisotropic GaSe (chemical family – metal selenide, including GaS, InSe, GaTe) and GaSe_xS_{1-x} (0.2 ≤ x ≤ 0.8) semiconductors possess several outstanding physical properties, the best known of which is a very high non-linear susceptibility χ(2) and a wide optical transmission range that is used for phase-matched second harmonic generation in a middle-IR and THz range of spectra [3 and references therein]. The optical band gap of this class of crystals is well suited for investigations with available lasers and is also convenient for testing the spectral response of the detection system (optical band gap for GaSe (red color) is ΔE = 2.02 eV at room temperature (RT), for GaS (yellow) ΔE ≈ 2.9 eV (RT)).

χ(2) is mostly expressed in the ε-GaSe polytype, which belongs to non-centrosymmetric space group D_{3h}¹ [3]. This polytype is predominantly obtained by crystal growth from the melt and is used in our research. Other modifications, such as γ-GaSe and δ-GaSe are typically present as inclusions in grown crystals and exist as extended stacking faults in the layer plane (across to crystal c-axis which coincides with the direction of crystallographic z- axis).

The aim of the present research was to overcome negative sides of existing types of laser light converters by using only one device. To achieve the aim, we developed the method of preparation and investigated the properties of laser radiation converters which permit to visualize continuous and pulsed laser radiation in the spectral range from 900 nm to 1300 nm. As a basic material for converters we used GaSe and GaSe-GaS solid solutions.

2. METHOD OF PREPARATION, DATA PERFORMANCE, RESULTS AND DISCUSSION

All measurements were carried out with the crystals grown by the Bridgman method. The details of preparation of device structures was described in Ref. [4]. In addition to that given in Ref. [4], in the present work we describe also the method of preparation based by using the nanoparticles of nonlinear materials. Briefly these three methods are as follows:

Method A: 1. Preparation of microcrystals (fine powder) which can be obtained by hand or mechanical grinding of poly- or single crystalline material in agate or any other mortar; 2. Preparation of colloidal suspension of fine powder (microcrystals) in any liquids, which do not have chemical interaction with the materials (for example for class of materials studied in the present work it may be: water, methanol, ethanol, acetone, octan, hexan and other liquids); 3. Mixing the colloidal suspension with any mixer; 4. Putting some drops of suspension onto the surface of substrate up to the full covering the surface of substrate; 5. Drying the substrate with coverage; 6. Covering the surface of substrate containing microcrystals (fine powder) with any plastic foil solved in corresponding solvent (the foil should be optically transparent at least in the 450– 1360 nm range); 7. Drying the device structure covered with plastic foil in air, under vacuum or inert atmosphere.

Method B: In principle the converters can be also made by preparation of colloidal suspension of microcrystals in any polymers (plastics) solved in corresponding solvent.

As one can see there are not too much differences between these two methods. In devices prepared by Method B the microcrystals (fine powder) are embedded in polymer (plastic) matrix, whereas in the devices prepared by Method A the microcrystals (fine powder) are covered with polymer (plastic) film.

Method C: We prepared converters also by fabrication of nanoparticles onto the substrate by laser ablation with KrF excimer laser. In this case the size of dots was successfully controlled: by the selection of experimental parameters of rare gas pressure; gas species of Ar or He; power of the laser pulse, and also the distance between the target and the substrate. The size distribution was studied: by TEM measurement (JEOL - JEM100C) and scanning SEM (JSM - 840) microscopes, the experimental results of the optical absorption (Perkin Elmer Lambda9 faring spectrometer), Raman scattering (home made confocal microspectrometer, He-Ne 632.8 nm line, 16 mWt) and infrared absorption (IR Fourier transform spectrometers (Perkin Elmer Spectrum 1 FTIR and Bomem DA-3). Not going too deep into the details of nano- particle formation and analysis of their optical properties we can summarize: **a)** size of the nano particles becomes larger with the increase of the rare gas pressure, and the size distributes wide with the increase of rare gas pressure; **b)** absorption edge shift with size is interpreted by the weak confinement effect on GaSe (also in the solid solutions of GaSe-GaS) Wannier-Mott type exciton taking into account the anisotropy of interlayer and intralayer forces; **c)** Raman scattering spectra of nano particles are analyzed with the Campbell-Fauchet analysis for the phonon confinement [5] taking into account the anisotropy of interlayer and intralayer forces. From the low frequency Raman data, decrease of the force constants of ca. 15% due to the formation of the nano dots are estimated.

It is worth to mention, that the conversion characteristics for the devices prepared by all three methods are nearly the same.

Two kind of experiments were performed to investigate conversion characteristics of thin crystalline microcrystals (fine powder) in devices prepared by above mentioned three methods (hereinafter we will discuss the results obtained on GaSe).

First, the second harmonic conversion of laser radiation from 1053 nm up to 1400 nm was examined. The results were compared with a commercial beam detector plate of KDP.

Second, the second harmonic efficiency of our devices was examined in a transmission experiment.

As a laser source we used Nd:glass laser system with the following parameters: laser wavelength – 1053 nm; pulse duration – 2-3 ps; single pulse energy – 1.37 mJ; 1/e beam diameter – 1 mm.

A travelling wave dye laser was used as tunable light source with the next parameters: wavelength range: 1200 – 1400 nm; pulse duration: 3 ps; single pulse energy: 18 μJ (at 1200 nm); beam diameter: ca. 1 mm.

All energy measurements were made with a pyroelectric detector with an accuracy of typical ± 10 %.

Examination at 1053 nm: SHG efficiency was examined as a function of the energy of the incident laser pulse (69, 38, 26 and 12 μJ). The detection of the second harmonic converted signal was made visually. Our devices were examined in comparison with commercially existed plate of KDP converter.

At pulse energy ≤ 69 μJ commercially available plates showed weak second harmonic signal, whereas our devices showed already well noticeable green signal. Moreover, commercial plates do not convert the laser light at 1053 nm wavelength with energies less or equal 40 μJ, whereas the low energy limit for our converters was about 12 μJ. This result is expected taking into account the fact that nonlinear constant (determines the efficiency of the SHG signal) of GaSe is about $d_{22} = 72 \pm 6$ pm/V was determined at 1579 nm [6], whereas for KDP it is only about 0.5 pm/V [1]. Moreover, our converters allow to detect converted signal not only in reflection geometry, as in case of commercial plates, but also in the transmission geometry, which is very useful, for example, for optical alignment.

Examination between 1200 and 1400 nm: were made at: 1200 nm (18, 8.3, 4.6 and 2.1 μJ pulse energy); 1300 nm (26.8, 8.4 and 2.6 μJ pulse energy); 1340 nm (21.4 μJ); 1360 nm (14.4 μJ); 1380 nm (8.1 μJ) and 1400 nm (4.3 μJ).

No converted signal was observed with commercial KDP plates at wavelength of the incident laser pulses of more than or equal to 1200 nm. At the same time, our devices permitted to visualize the laser pulses up to the wavelength 1360 nm. Low energy limit for visualization of the IR laser pulses using our devices were: between 4.6 – 2.1 μJ at 1200 nm; 8.4 – 2.6 μJ at 1300 nm and 14.4 – 8.1 μJ at 1360 nm.

Conversion efficiency: the IR (1053 nm) and second harmonic (526.5 nm) intensity was measured with an avalanche diode (high voltage 1.3 kV). IR signal pulse energy was 1.37 mJ. The measurements were performed according to the following experimental setup as follows:

IR laser beam → Visualizator → Second Harmonic Signal → IR Blocking Filter → Avalanche Diode

A conversion efficiency (number of photons as the second harmonic divided by the number of photons at incident IR laser light) of about 10^{-7} was obtained.

3. CONCLUSIONS

New type of visualizators for conversion of pulsed and continuous IR (900 - 1360 nm) laser radiation into the visible

range (450 – 680 nm) of spectra are suggested. Device consists of the crystallites of GaSe- type semiconductor materials embedded into the transparent matrix and covered onto the surface of glass (or any other transparent) plate. It can be used in reflection as well as in transmission geometries. The visualizers are based on the GaSe and GaSe-GaS solid solutions and may be used for checking if the laser is working or not, for optical adjustment, for visualization of distribution of the intensity of laser radiation over the cross of the beam and for investigation of the content of the laser radiation. Specifications for suggested devices are as follows: visualizer gives integral lightness in the green range of spectra (526 – 527 nm) when excited with 2 – 3 ps laser pulses ($\lambda = 1053$ nm) with a power density of excitation of $7 \cdot 10^{-4}$ W/cm² (12 μ J, 1/e beam diameter 1.5 mm). Low-

energy power density limit for visualization of the IR laser pulses with 2 – 3 ps duration for these devices are: between 4.6 – 2.1 μ J ($3 \cdot 10^{-4}$ – $1 \cdot 10^{-4}$ W/cm²) at 1200 nm; between 8.4 – 2.6 μ J ($4.7 \cdot 10^{-4}$ – $1.5 \cdot 10^{-4}$ W/cm²) at 1300 nm; between 14.4 – 8.1 μ J ($8.2 \cdot 10^{-4}$ – $4.6 \cdot 10^{-4}$ W/cm²) at 1360 nm. Threshold damage density is more than 10 MW/cm² at $\lambda = 1060$ nm, pulse duration $\tau = 35$ ps.

4. ACKNOWLEDGMENTS

The authors are gratefully acknowledge financial support from the Scientific and Technical Research Council of Turkey (TÜBİTAK, project TBAG-U78 (103T092)) and the Turkish State Planning Committee (projects DPT No. 5045901 and 5075810).

-
- [1]. Encyclopedia of Lasers and Optical Technology, Robert A. Meyer, Editor, Academic Press, Inc., Harcourt Brace Jovanovich Publishers, San Diego, N. Y., Boston, London, Sydney, Tokyo, Toronto, 1991, p. 343.
- [2]. LASER 200 News, Neue Sensorkarten zum Nachweis von Infrarot-Strahlung, List of Products 1997, LASER 200 GmbH, Benzstrasse 30, 8039 Puchheim, Germany.
- [3]. K. R. Allakhverdiev, M. Ö. Yetis, S. Özbek, T. K. Baykara, E. Yu. Salaev, Laser Phys., **19**, 1092 (2009).
- [4]. K. Allakhverdiev, E. Salaev, D. Haarer, A. Seilmeier, Method of Preparation of Laser Radiation Converters by the Use of Nonlinear Optical Materials, Patent No97/00784, Registered 11.08.97 by Patent Institute, Ankara, Turkey.
- [5]. I. H. Campbell and P. M. Fauchet, Sol. State. Com., **58**, 739 (1976).
- [6]. L. Kador, M. Braun, K. R. Allakhverdiev, E. Yu. Salaev, Optics. Commun., **114**, 333 (1995).

THE EROSIVE LASER PLUME IONS COMPONENT RESEARCHES AT THE SILICON ABLATION IN VACUUM

E.V.KHAYDUKOV, V.V.ROCHEVA, A.A. LOTIN,
O.A.NOVDVORSKY, V.Ya.PANCHENKO

*Institute on Laser and Information Technologies of the Russian Academy of Sciences (ILIT RAS),
1 Svyatoozerskaya St., 140700 Shatura, Moscow Region, Russia*

For the first time it is informed on engineering of the modified crossed-beam pulsed laser deposition method (CBPLD) which allows operating deposited particles energy in a wide range. By the Langmuir probe technique silicon ions time-of-flight curves (TFC) for the plasma beam formed by the crossed plumes from two silicon targets and the erosion plume from one silicon target are received. It is shown that ions TFC of the erosion plume approximate by the sum of one-dimensional Maxwell velocity distributions. Ions concentration change in initial plumes as a result of interaction is measured. Energy spectrum change of the plasma beam formed by the crossed plumes by means of angle change between them is shown.

1. INTRODUCTION

Silicon is widely applied in electronics and optoelectronics devices. Engineering of cheap technology of the ultrathin silicon films deposition would allow to introduce multilayer (which includes silicon layers) structures creation process (materials for spintronics, solar cells) in already existing silicon technologies [1,2]. One of the advantageous processes of the epitaxial thin films production is the pulsed laser deposition method (PLD) [2,3].

It is necessary to avoid drops falling on the substrate at the thin silicon films creation by the PLD method [2,4-6].

Efficient method of drops separation in the PLD method is the crossed plumes scheme of two erosive plumes [7,8]. Plume particles energy is rendered significant influence on properties of the received film (type of crystal structure, crystals size, adhesion, epitaxy, etc.) besides drops [9]. Therefore the important characteristics of the pulsed laser deposition process are a plume energy spectrum monitoring and control in particular an ions energy spectrum [3,9-11] directly during the thin film growth. It is especially important to control the energy spectrum at the multilayer ultrathin films deposition [12].

In the present work by the Langmuir probe technique ions velocity distributions of the plume at one silicon target ablation and of the plasma beam formed by the crossed plumes at two silicon targets ablation by radiation of the first harmonic of the solid-state laser ($\lambda = 1,06 \mu\text{m}$) are investigated. The ions time-of-flight curves (TFC) are received at the probe-to-target distances in the 25-120 mm range. TFC approximation by the sum of one-dimensional Maxwell velocity distributions for several ions groups is spent. For the first time ions energy spectrum control possibility at the crossed plumes method by means of angle changing between initial plumes axes is shown.

2. EXPERIMENTAL SETUP

The experimental setup scheme is presented on fig. 1. Experiments were performed in the vacuum chamber which was pumped by turbo-molecular pump to 10^{-6} Torr pressure. Disk form targets from monocrystalline silicon were fixed in the holder and rotated for homogeneous target yield. Laser erosion plasma from the silicon target was formed by the influence of the first harmonic Q-switching YAG:Nd³⁺ laser radiation. Pulse duration made 15 ns, pulse energy was 50 - 500 mJ. The beam divides into two equal parts which radiation was focused on the targets surface.

Langmuir probe of 5.5 mm length was fabricated from 0.16 mm diameter tungsten wire. The probe placed perpendicularly plume axes. Probe moving in the vacuum chamber was carried out along the erosion plume axis in 25-120 mm range. The probe potential could change in limits from 0 to -20 V. As a source of the probe variable voltage was the storage battery which through a potentiometer was connected by one pole to the probe and by other pole through the pull-up resistor was earthed. For the probe potential stabilization during current flow the source of variable voltage was bridged by 2.5 μF capacity. The probe current was registered on 1 k Ω pull-down resistor with use of a high-speed AT-5102 (International Instruments) analog-to-digital converter (ADC) and saved to the PC. Charges time of arrival to the probe reading was performed from the laser pulse generation moment registered by the photodiode the signal from which delivered on the ADC starting channel.

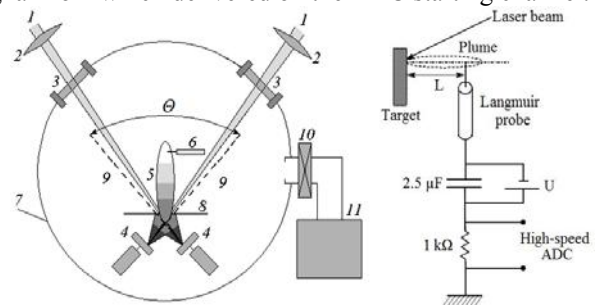


Fig.1. Experimental setup scheme and electrical schematic of the plasma beam probe researches at the silicon ablation: 1 – YAG:Nd³⁺ laser radiation, 2 – focusing lenses, 3 – window of the vacuum chamber, 4 – target, 5 – plasma beam, 6 – Langmuir probe, 7 – vacuum chamber, 8 – diaphragm, 9 – erosion plume axis, 10 – vacuum seal, 11 – turbo-molecular pump.

In the crossed plumes mode the angle between targets and accordingly between plumes axes changed from 180° to 70°. Targets rotation axes placed in one plane. The fixed shield with an aperture mounted perpendicularly bisector of the angle formed by the plumes axes. The aperture diameter selected such to exclude direct visibility of the targets ablation areas from the probe location than the direct hit on the probe of the charged particles from initial plumes was excluded. At one of initial plumes research the signal of the probe located on the plume recession axis was registered, the second plume was blocked, the shield was not mounted.

3. RESULTS AND DISCUSSION

In the spent experiments the ions probe current TFC have been received in a case of the silicon ablation at various probe-to-target distances at different laser radiation energies. On fig. 2 are demonstrated the TFC at 32 J/cm² energy density on the target, time was counted from the ablation moment. At energy density decrease on the silicon targets the form of the TFC does not change.

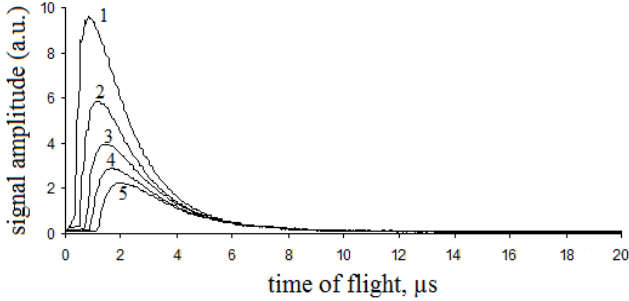


Fig. 2. Probe time-of-flight curves of the erosion plume from one target at various probe-to-target distances: 1 – 35 mm, 2 – 55 mm, 3 – 75 mm, 4 – 95 mm, 5 – 115 mm. Probe potential -18 V.

The ions TFC for have one strongly pronounced maximum with sharp rise-up portion and more flat descending part which is receding to zero approximately of 15 μs. All TFC have been received in the time range from 0 to 50 μs but on fig. 2 time interval is reduced to 20 μs for the best resolution. The TFC signal amplitude at probe-to-target distance increase decreases inversely to probe-to-target squared distance as a result of plume expansion.

From fig. 2 it is visible that the rise-up portion signal delay is proportional to probe-to-target distance. The ions leading group times of arrival from probe-to-target distance in 25-115 mm range have been determined. Time of arrival was determined by the delay between the targets ablation moment and the maximum of the probe signal. At three various energy densities on the target this dependence has linear character. The received dependences are demonstrated on fig. 3.

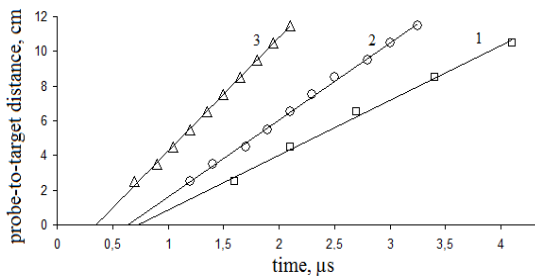


Fig.3. The time-of-flight curves peak time of arrival dependence on probe-to-target distance of the erosion plume from one target at the various energy density: 1 - 10 J/cm², 2 - 16 J/cm², 3 - 32 J/cm².

From fig. 3 it is visible that the silicon ions lead group recession velocity does not depend on distance to the target and at 32 J/cm², 16 J/cm², 10 J/cm² energy density makes 53 km/s, 31 km/s, 25 km/s accordingly.

Asymmetry of the probe curves presented on fig. 2 is connected with nonequilibrium ions velocity distribution in the plume [10]. All the received TFC are well approximated by the sum of several Maxwell curves with different positions of maxima:

$$I(t) = KLt^{-4} \exp\left[-\frac{2(L/t)^2}{v^2}\right], \quad (1)$$

where K – proportionality coefficient; v – the most probable velocity; L – probe-to-target distance, t – time. Approximation was spent from the assumption that at the plume there are singly charged ions with m weight and the charged particles with nm weights, where $n = 2,3,4 \dots$. So for the plume from one target at 32 J/cm² energy density for all the measured probe-to-target distances the TFC are approximated by the sum of six groups of positive charged particles spreading with the velocities: 57.7 km/s; 40.8 km/s; 33.3 km/s, 28.9 km/s, 25.8 km/s and 23.6 km/s.

On fig. 4 are presented the TFC for 65 and 105 mm probe-to-target distances and their approximation by the sum of six Maxwell curves. It is visible that the total curves are labeled on fig. 4 by circles coincide with the experimental TFC.

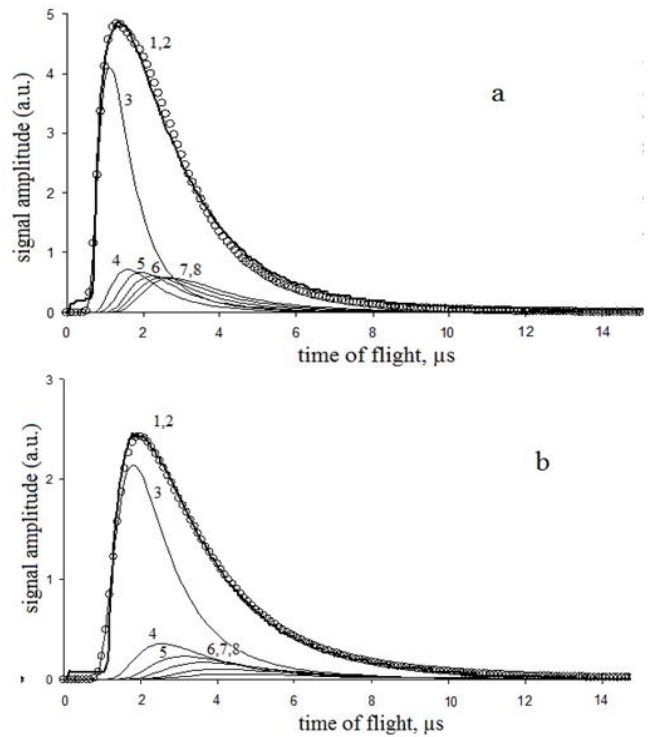


Fig.4. Experimental time-of-flight curves of the erosion plume from one target for 65 mm (a) and 105 mm (b) probe-to-target distances and their approximate by the sum of six Maxwell curves. By thick firm line is labeled experimental curve 1, by circles is labeled theoretical curve 2 that be the sum of Maxwell curves 4, 5, 6, 7 and 8 with 57.7 km/s, 40.8 km/s, 33.3 km/s, 28.9 km/s, 25.8 km/s and 23.6 km/s velocities.

The TFC of the deflected beam formed by the crossed plumes (fig. 1) at different angles and at various energy densities on the silicon targets have been received. The probe

moved along the deflected beam axis, the distance was measured from diaphragm position. On fig. 5 are presented the experimental TFC of the deflected beam formed after the initial plumes crossing at 90 degrees angle at different probe positions relative to the diaphragm. The TFC amplitude decreased inversely to squared distance as well as for the case of the plume from one target.

The TFC maximum time of arrival as well as for the case of the plume from one target changes linearly at change of the probe position (insert on fig. 5) that indicate of inertial recession of the beam charged particles.

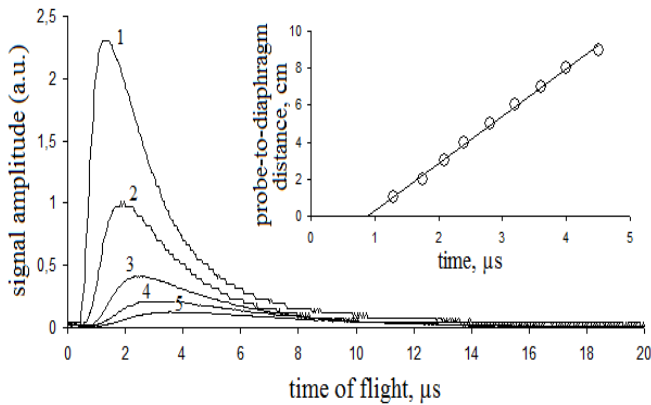


Fig.5. Probe time-of-flight curves of the plasma beam formed by the crossed plumes at various probe-to-diaphragm distances: 1 – 10 mm, 2 – 30 mm, 3 – 50 mm, 4 – 70 mm, 5 – 90 mm. Angle Θ between plumes axes made 90° . Probe potential -18 V. Energy density - 32 J/cm^2 . On insert: the time-of-flight curves peak time of arrival dependence on probe-to-diaphragm distance.

Comparing the ions TFC of the erosion plume from one target (fig. 2) and the beam spreading on the bisector between initial plumes axes (fig. 5) it is possible to see that not all ions which are present at initial plumes deflect at interaction. From TFC of the probe placed on one of the plumes recession diagram axis behind the plumes crossing area at 120 mm distance from the target (at the diaphragm 8 absence, fig. 1) ions concentration was determined at presence and absence of the second plume (insert on fig. 6). The Θ angle between plumes axes made 90° . Such probe location excluded hit on it of the charged particles from the second plume. The results are presented on fig. 6 where the curve 1 shows concentration distribution in the plume from the A target at the B target ablation absence, the curve 2 shows concentration distribution in the plume from the A target at the A and B targets ablation. The difference between curves corresponds to the deflected part of the plume. It is visible that the considerable part of the plume deflects.

At the angle change between initial plumes axes the TFC maximum of the deflected beam moves, the probe position is fixed (6 on fig. 1). Fig. 7 demonstrates the shift of the deflected beam TFC maximum at the Θ angle change between initial plumes axes from 90° to 170° . It is possible to calculate velocities of the deflected ions after interaction considering plumes recession velocity till the crossing moment and knowing a way passed by ions before and after crossing.

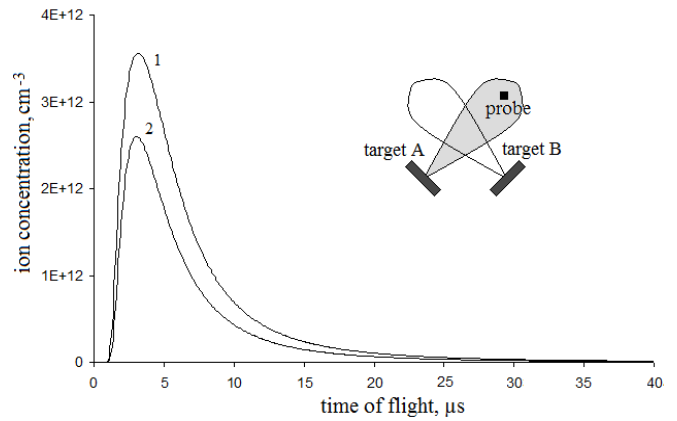


Fig.6. Ions concentration change in the plume at 120 mm probe-to-target distance. 1 – probe on plume axis at the A target ablation, 2 - probe on plume axis at the A and B targets ablation. Angle Θ between plumes axes made 90° . On insert: scheme of the experiment.

At the angle change between initial plumes axes the TFC maximum of the deflected beam moves, the probe position is fixed (6 on fig. 1). Fig. 7 demonstrates the shift of the deflected beam TFC maximum at the Θ angle change between initial plumes axes from 90° to 170° . It is possible to calculate velocities of the deflected ions after interaction considering plumes recession velocity till the crossing moment and knowing a way passed by ions before and after crossing.

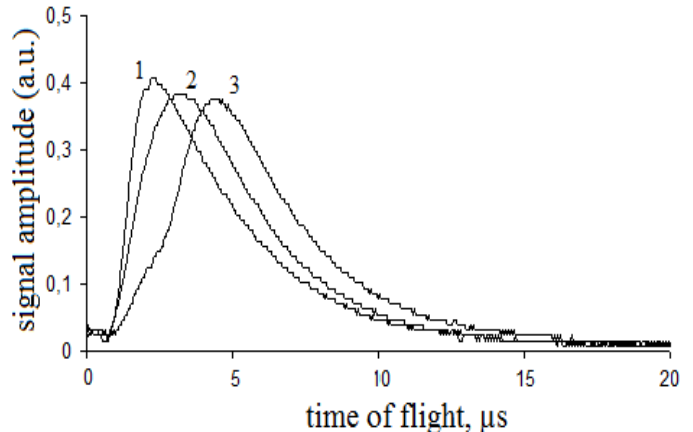


Fig.7. Probe time-of-flight curves at the angle change between initial plumes axes. 1 – 170° , 2 – 130° , 3 – 90° at 50 mm probe-to-diaphragm distance. Probe potential -18 V. Energy density - 32 J/cm^2 .

It allows to determine kinetic energy change of the leading ions in the deflected beam at the angle change between initial plumes axes. Kinetic energy change of the leading ions from the angle between initial plumes axes is presented on fig. 8.

From fig. 8 it is visible that at angle change from 170 to 70 degrees between plumes axes the ions leading group energy changes from 92 to 480 eV at 32 J/cm^2 energy density on the target. For comparison on fig. 8 value of the ions leading group energy which is equal 677 eV is presented at one silicon target ablation (it is labeled by triangle on fig. 8) at other similar conditions.

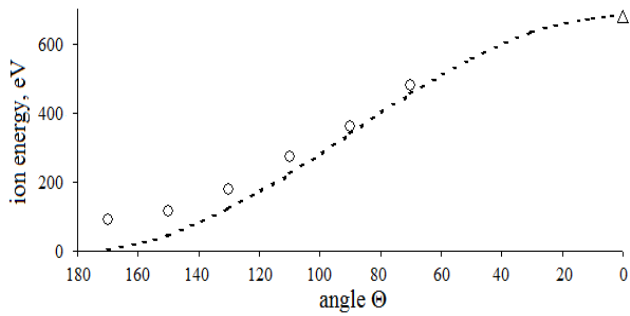


Fig.8. Ions leading group energy change for the plasma beam formed by the crossed plumes from the angle between initial plumes axes at 32 J/cm² energy density on the silicon target.

In the figure by the dotted line is presented a theoretical curve for the particles energy in the deflected beam with the assumption of conservation of the ions initial velocity tangential component at the collisional process. Character of the deflected ions energy change qualitatively is matching to the offered model. Quantitative mismatching of the experimental data is connected with presence of particles recession angle dispersion in the initial plumes. The additional energy increase of the deflected beam particles can

be caused by heating of the initial plumes crossing area at inelastic collision.

4. CONCLUSIONS

By the Langmuir probe technique the erosion plume characteristics at silicon ablation by the Q-switching YAG:Nd³⁺ laser are investigated.

Silicon ions lead group recession velocity does not depend on distance to the target at one silicon target ablation and in plasma beam formed by the crossed plumes at two silicon targets ablation.

The TFC are received at the probe-to-target distances in the 25-120 mm range. TFC approximation by the sum of one-dimensional Maxwell velocity distributions for several ions groups is spent. For the first time it is informed on engineering of the modified crossed-beam pulsed laser deposition method which allows operating deposited particles energy in a wide range.

4. ACKNOWLEDGMENTS

Work is executed with support of RFBR grants 09-08-00291, 09-02-12108, 09-08-01053, 09-02-01298, 09-07-12151.

-
- [1]. *M.Bolduc, C.Awo-Affoud, A.Stollenwerk, et al.*, Phys. Rev. B. 71, 033302-033305 (2005).
 - [2]. *S.Yasuda, T.Chikyow, S.Inoue, N.Matsuki, K.Miyazaki, S. Nishio, M.Kakahana, H.Koinuma*, Appl. Phys. A. 69, S925-S927 (1999).
 - [3]. *V.Ya.Panchenko, O.A.Novodvorsky, V.S.Golubev*, Science and technology in industry. 4(1), 39-51 (2006).
 - [4]. *E.V.Khaydukov, A.A.Lotin, D.N.Melnikov, O.A.Novodvorsky, V.Ya.Panchenko*, Proceedings of IX Interuniversity scientific school of young experts «The concentrated energy streams in the space technology, electronics, ecology and medicine», 127-131 (2008).
 - [5]. *A.Masuda, K.Matsuda, S.Usui, T.Minamikawa, T.Shimizu, A.Morimoto, Y.Yonezawa*, Mater. Sci. Eng. B. 41, 161-165 (1996).
 - [6]. *E.V.Khaydukov, A.A.Lotin, O.A.Novodvorsky, V.Ya.Panchenko, V.V.Rocheva*, The Collection of scientific and technical sections reports theses of the International Forum on Nanotechnology, Part 1, 771-772 (2008).
 - [7]. *M.D.Strikovskiy, E.B.Klyuenkov, S.V.Gaponov, J.Schubert, C.A.Copetti*, Appl. Phys. Lett. 63 (8), 1146-1148 (1993).
 - [8]. *A.Gorbunov, A.Tselev, W.Pompe*, Proc. SPIE 3688, 351-358 (1999).
 - [9]. *K.L.Saenger*, J. Appl. Phys. 70, 5629-5635 (1991).
 - [10]. *R.Eason*, Pulsed laser deposition of thin films: Applications-LED growth of functional materials, N.J.:Wiley-Interscience, Hoboken, (2007).
 - [11]. *O.A.Novodvorsky, E.O.Filippova, O.D.Khramova, A.K.Shevelev, C.Wenzel, J.W.Bartha*, Quantum Electronics. 31(2), 159-163 (2001).
 - [12]. *H.Mai, R.Dietsch, T.Holz, S.Voellmar, S.Hopfe, R.Scholz, Peter Weissbrodt, R.Krawietz, B.Wehtner, H.Eichler, H.Wendrock*, Proc. SPIE 2253, 268-279 (1994).

EXPERIMENTAL INVESTIGATION OF DIFFERENT REFINING STAGES INFLUENCES ON OPTICAL AND ULTRASONIC SIGNALS IN PAPER PULP SUSPENSIONS

JAN NIEMI

*Department of Computer Science and Electrical Engineering
Luleå University of Technology, SE-97187 Luleå, Sweden*

An important parameter to control in papermaking is the fibre mass fraction in the pulp suspension. Poor control of the mass fraction leads to an unstable process that compromises the production, quality and the energy efficiency in the pulp mill. Using optical or ultrasound measurement techniques can obtain estimation of the mass fraction. Refining is an important operation in preparing the fibres for the paper machine. Refining influence the properties of the fibre by crushing the fibre, roughens the fibre surface and occasionally cut fibres and removes parts of the outer fibre wall leading to an increasing amount of short fibres (fines). Since refining is used to give the fibres desirable properties, its impact on the fibres with respect to light and sound is investigated. Two different types of chemical pulp is considered; bleached hardwood and unbleached softwood pulp. A freeness tester was used to verify the changes in fibre properties at four different refining levels. The result shows that for unbleached softwood pulp the used measurement techniques are influenced by refining. For bleached hardwood pulp the influence of refining intensity on the tested measurement techniques either were not observable or minor. The results indicate that refining can potentially influence accurate consistency estimation for unbleached softwood pulp but for bleached hardwood pulp the influence is believed to be minor using the investigating measurement techniques.

INTRODUCTION

The papermaking process is today a fully automated process. This has put high demand on the sensors for controlling the papermaking process in order to produce the desired paper quality. Also have the demands for an environmentally friendly process and effective use of raw materials and energy increased the complexity of controlling the process. By improving the process control, the demands for efficiency and quality can be met.

An important control parameter in the papermaking process is the mass fraction or consistency of cellulosic materials in the pulp suspension [1]. Poor control of the mass fraction leads to an unstable process that compromises the production, quality and the energy efficiency in the pulp mill. Today, consistency is estimated with mainly three different techniques, shear force sensors, microwave sensors and optical sensors. It is believed that no commercial product uses ultrasound to measure pulp consistency. Although, Löfqvist [2] showed that ultrasound have the potential to estimate consistency. In Törmänen et al. [3] a method based on a combination of optical and ultrasonic techniques was proposed. They showed that short fibre fragments (fines) are the predominant source for optical scattering. Further, the long fibres are the predominant source for attenuation of ultrasonic waves. By combine the two techniques the mass fraction of fines and the mass fraction of fibres in a pulp sample could be determined, respectively.

The different sensor techniques have their advantages and disadvantages. Different process treatment and location in the process chain favour different sensors. All sensors used today estimate the consistency by measure something that relates the measured signal to the consistency. The calibration is recognised as the key to accurate consistency measurements [1], [4]. Optical sensors can be accurate with proper calibration [5]. However, optical sensors are sensitive to pulp composition [1]. Changing the properties of the pulp compared to the calibration samples, might compromise the consistency estimation.

Manufacturing of paper involves different treatment on the pulp suspension. The refining process is an important

operation in preparing the fibres for the paper machine. The degree of beating or refining of the fibres influence the elastic properties of the fibre by split and crush the fibre. Refining also roughens the fibre surface, creating hair-like fibrils, which increase the specific surface area of the fibre. Further, refining also occasionally cut fibres and removes parts of the outer fibre wall leading to an increasing amount of fines in the suspension [6].

The motivation for this study is to examine the influence of refining on light and sound waves and thereby compromise accurate consistency control based on the investigated measurement techniques.

EXPERIMENTAL METHODS

This study concern two different measurement techniques, optical and ultrasound. The examined optical properties are light intensity and the time-of-flight of the received light pulse that has travelled through the pulp sample. The examined ultrasonic property is the attenuation of a sound pulse that has travelled through the pulp sample.

Light pulses propagating through random inhomogeneous medium are temporally divided into ballistic, snake and diffuse components [7]. Depending on the number of scattering particles one or the other components is dominating. In a turbid sample, where multiple scattering occur, diffusion light will dominate. The propagation time for a photon through a medium is due to number of scattering events and speed. With increasing scattering events in the medium the photon density reduces and the probability for a photon to be absorbed increases. These two factors decrease intensity as the light propagates through the medium. Hence, both time-of-flight (TOF) and light intensity for a propagating pulse is affected by number of scattering events in a low absorbing highly scattering medium.

The ultrasonic attenuation is due to absorption and scattering of the sound waves as they propagate through the medium [8]. Absorption is the conversion of sound energy to other forms of energy (heat). Scattering is the reflection of the sound in directions other than its original direction of propagation. The sound attenuation in a pulp suspension is a

function of frequency. The frequency-dependent attenuation in this study is calculated as:

$$\alpha_s(f) = \ln[|P_w(f)|/|P_s(f)|]/(2d) + \alpha_w(f) \quad (1)$$

where $\alpha_s(f)$ is the attenuation in the suspension, d is the distance between the transducer and the steel reflector, $|P_w(f)|$ is the amplitude in the frequency domain of the water reference echo, $|P_s(f)|$ is the amplitude in the frequency domain of the sample echo and $\alpha_w(f)$ is the attenuation in pure water and is assumed to be $25 \cdot 10^{-15} f^2$, where f is the frequency [8].

EXPERIMENTS

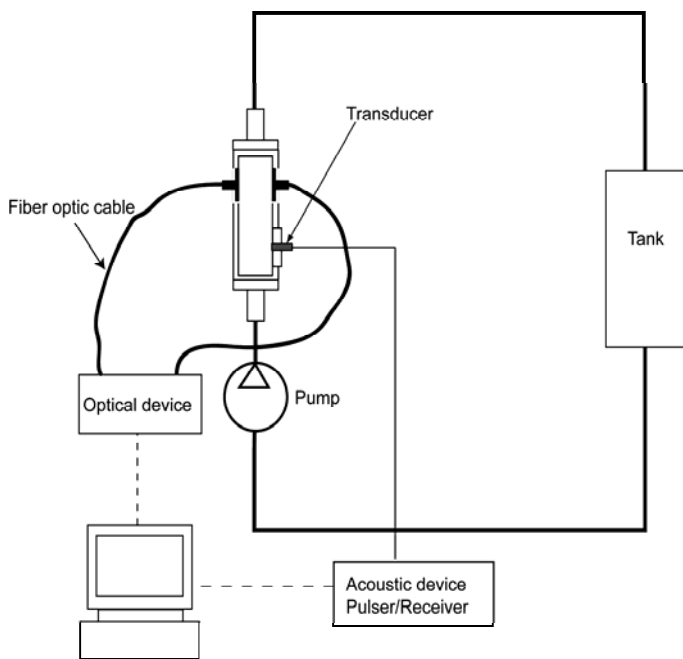


Fig. 1 Illustration of the experimental set-up

The measurement cell is designed to allow measurements of the two techniques simultaneously. Figure 1 shows an illustration of the measurement cell and also the experimental setup. The inner dimension of the measurement cell is $10 \times 3 \times 3$ cm.

The light was generated and measured by a custom designed LIDAR system CMP3 from Noptel Oy, Finland. The light was coupled to the measurement cell by optical fibres with a 0.39 NA and a core diameter $600 \mu\text{m}$. The light is directed onto the incident window of the cell, containing the flowing pulp. The light beam that emerges on the opposite side passes a parallel plane window and is directed onto an optical fibre, which is connected to the optical device. The optical device register both intensity and time-of-flight (TOF) of the receive light. The device is connected to a computer for storing of the measured properties. The wavelength of the light is 905 nm . With a repetition rate of 4000 Hz the average of 1024 measurements was captured and stored in the computer. The procedure was repeated 200 times to improve the statistical significance of the measurement. In this study we present TOF as the remaining time in picoseconds, after the TOF value for pure water is

subtracted. The received light intensity is presented as voltage.

The ultrasound wave was measured in a pulse-echo setup. The propagating ultrasonic wave is travelling through the suspension and reflected back at a polished steel reflector and thereafter captured by the transducer. A PZT transducer from Panametrics, Waltham, USA generated the ultrasound signal, with a center frequency of 15 MHz . The transducer was excited and amplified by a dual pulser/receiver model DPR500 from JSR Ultrasonics, NY, USA. The captured ultrasonic signal from the pulser/receiver was digitised with an oscilloscope card (CompuScope 12400 from GageScope) sampling at 100 MHz with a 12 bit resolution. For each pulp sample, 200 ultrasonic pulses were recorded and averaged using an averaging procedure that reduces timing jitter [9]. A digital thermometer monitored the temperature in both the water and the room. The temperature range in the pulp samples during the course of experiments was $19.60 \pm 1.5^\circ\text{C}$. The travelling distance for the ultrasonic wave was calculated from the theoretical speed of sound in water given by the pure water sample temperature [10] and the time-of-flight of the ultrasonic wave that has travelled back and forth once respectively twice in the cell using cross-correlation technique. The distance d was found to be 29.7 mm .

The pulp was delivered by Smurfit Kappa Kraftliner, Piteå, Sweden. Two different types of chemical pulp were considered; bleached hardwood and unbleached softwood pulp aimed for kraftliner production. The pulp samples stems from before between and after three refiners connected in series, resulting in four different refining intensity levels. From each refining level pulp samples of four different mass fractions were mixed. The mass fraction ranged from 0.3% to 1.3% for unbleached softwood pulp and 0.25% to 1.5% for bleached hardwood pulp. Altogether, a set of 16 pulp samples with four refining levels and four mass fraction levels for each pulp type was investigated.

The rate of drainage, which is related to the work done on the fibres during refining was measured in a laboratory at the pulp mill with a freeness tester and is presented in MSR (Modified Shopper-Riegler) values. Freeness testing is a standard method for determines the degree of refining of pulp. The relation between refining intensity and MSR, is that increased refining intensity give a increased MSR value. In this study the MSR values ranged from 18 (unrefined) to 37 after the last refiner for unbleached softwood pulp. For bleached hardwood the MSR value increased from 31 (unrefined) to 54 after the last refining level.

RESULTS

UNBLEACHED SOFTWOOD PULP

Figure 2 shows the received light intensity converted into millivolt at different consistency levels as a function of MSR, i.e. refining intensity, for unbleached softwood pulp. The standard deviation of each measurement is shown as error bars in the figure.

The trend in all mass fraction levels is that the amplitude decreases with increasing refining. Figure 3 shows TOF plotted against MSR at the different consistency levels. The trend is that the propagation time for the light pulse in the suspension increases with refining intensity. In the mass fraction level 0.3% , the trend is not observable as the values are within the uncertainty of the measurements.

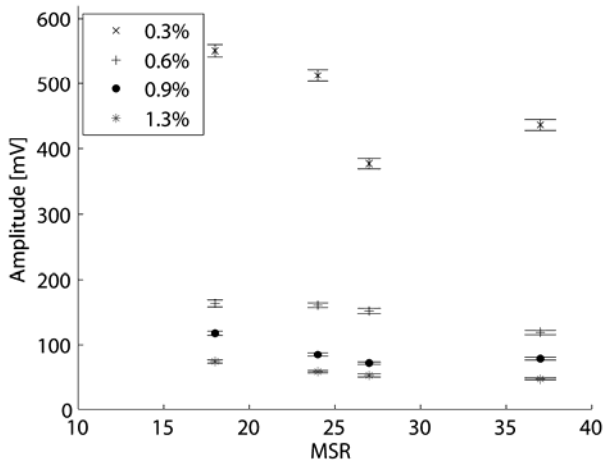


Fig. 2 Received light intensity as function of MSR at different consistency levels for unbleached softwood pulp

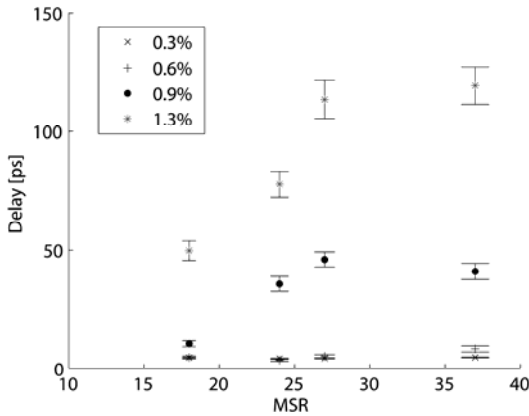


Fig. 3 Time-of flight as function of MSR at different consistency levels for unbleached softwood pulp

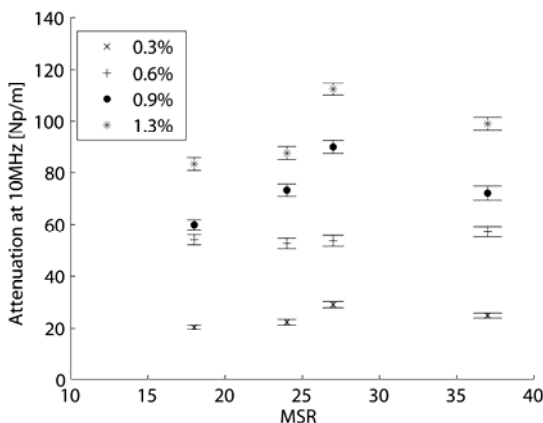


Fig. 4 Ultrasonic attenuation at 10 MHz plotted against MSR at different consistency levels for unbleached softwood pulp

Figure 4 shows the ultrasonic attenuation in Neper/m at 10 MHz for unbleached softwood pulp. A trend is noticed, sound attenuation increases weakly with refining intensity. But the results also show a large variation between the measurements, especially in pulp samples at higher

consistency levels and refining intensities. It is believed that it is caused by inhomogeneity in the pulp suspension, likely due to floc formation in the suspension. During the experiment it was noted that floc formation was more evident in high-refined pulp samples and at higher consistencies levels. These flocs cause variations in the received signal since the floc represents a locally higher concentration of fibres blocking the optic or acoustic signal path. Further, in the area close to the flocs there will be a locally lower concentration of fibres. Although, steps were taken to reduce floc formation, it is believed that the measurements were conducted on a pulp consistency other than the expected. The floc formation in pulp suspension is well known and has been discussed by others [1], [11] as a source of error.

These results for unbleached softwood pulp confirm the assumption that refining change the specific surfaces of the fibres and also an increase the amount of small particles (fines) in the suspension.

BLEACHED HARDWOOD PULP

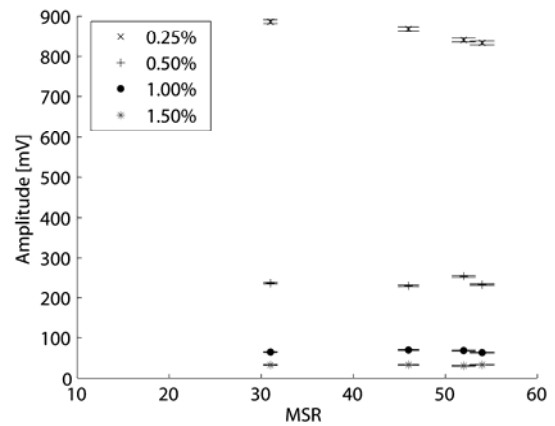


Fig. 5 Received light intensity as function of MSR at different consistency levels for bleached hardwood pulp

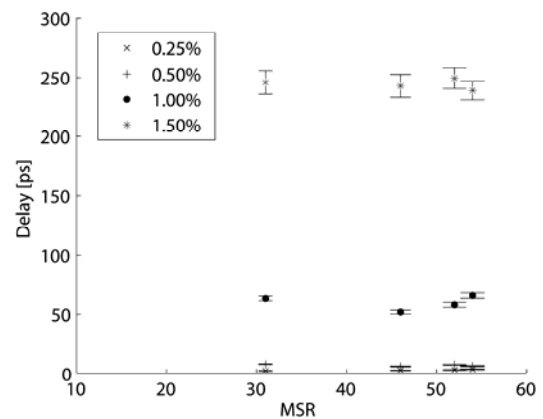


Fig. 6 Time-of flight as function of MSR at different consistency levels for bleached hardwood pulp

Figure 5 shows the received light intensity as a function of MSR. In this case the influence of refining on the amplitude is not apparent or minor. Figure 6 shows the TOF values as function of MSR here the influence of refining

intensity are not noticeable. Figure 7 shows the ultrasonic attenuation at 10 MHz plotted against the MSR value. There is no clear indication on the ultrasonic attenuation that the fibres have been affected by the refining intensity.

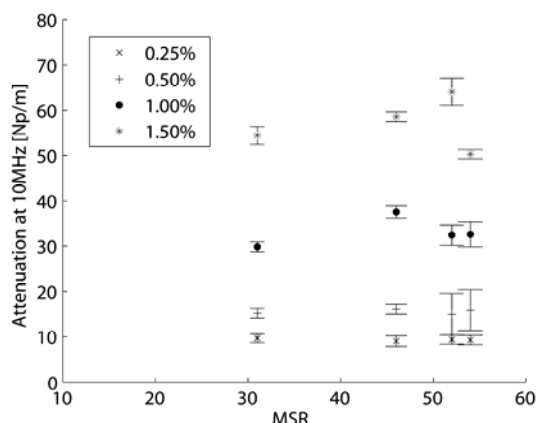


Fig. 7 Ultrasonic attenuation at 10 MHz plotted against MSR at different consistency levels for bleached hardwood pulp

These results indicate that changes in terms of fibre surface development or increasing amount of fines during refining on bleached hardwood pulp are not detectable with the used methods.

CONCLUSION

In this study we have presented experimental results on different refining stages influences on optical and ultrasonic signals in paper pulp suspensions.

The results show that for unbleached softwood pulp the optical amplitude decreases as refining intensity increases. The time-of-flight of the light pulse increases with refining intensity. For the ultrasound attenuation there is a weak trend for increased attenuation as refining intensity increases. For bleached hardwood pulp the influence of refining intensity on the tested measurement techniques was not observable or minor.

The results indicate that refining potentially can influence accurate consistency estimation for unbleached softwood pulp but for bleached hardwood pulp using the investigating measurement techniques the influence is minor or negligible. However, it should be noted that the variation in MSR used in this study is well beyond the normal variation in a pulp mill. Hence, under normal conditions the influence of refining on accurate consistency estimation is believed to be less evident than the results indicate for unbleached softwood pulp.

ACKNOWLEDGEMENT

We wish to express our appreciation to Smurfit Kappa Kraftliner, Piteå, Sweden, for providing the pulp samples and measurement on drainage rate.

-
- [1]. *I. Janson*, Accurate consistency: A handbook of consistency measurement in pulp and paper processing. (Säffle: BTG Pulp & Technology AB, 1999).
 - [2]. *T. Löfqvist*, "Ultrasonic wave attenuation and phase velocity in a paper-fibre suspension," in (*Proc.IEEE Ultrasonics Symposium*, 1997), pp. 841-844.
 - [3]. *M. Törmänen*, *J. Niemi*, *T. Löfqvist*, and *R. Myllylä*, *Measurement Science and Technology*, vol. 17, no. 4, pp. 695-702, (2006).
 - [4]. *J. Tornberg*, "Special measurements in pulp and paper processes," in *Papermaking Science and Technology*. (Helsinki, Finland: Fapet, 1999).
 - [5]. *L. Montonen*, *Svensk Papperstidning*, vol. 5, pp. 38-40, (1995).
 - [6]. *C. Fellers. and B. Norman*, *Pappersteknik*. (Stockholm: Tekniska högskolan i Stockholm. Institutionen för pappers- och massateknik, 1996).
 - [7]. *J. Saarela*, *Photon migration in pulp and paper*. (University of Oulu,Finland, 2004).
 - [8]. *L. E. Kinsler*, *A. R. Frey*, *A. B. Coppens*, and *J. V. Sanders*, *Fundamentals of Acoustics*. (New York, USA: John Wiley and Sons Inc., 2000).
 - [9]. *J. Martinsson*, *Measurement Science and Technology*, vol. 19, no. 2, p. 025101, (2008).
 - [10]. *N. Bilaniuk and G. S. K. Wong*, *The Journal of the Acoustical Society of America*, vol. 93, no. 4, pp. 2306-2306, (1993).
 - [11]. *Z. Zhao*, *M. Törmänen*, and *R. Myllyä*, *Measurement Science and Technology*, vol. 17, no. 1, pp. 128-134, (2006).

TREE MAPPING USING A TIME-OF-FLIGHT 3D CAMERA

ARTTU V.H. OLLIKKALA, ANSSI J. MÄKYNEN
*Measurement and Sensor Laboratory, University of Oulu
Technology Park 127, 87400 Kajaani, Finland*

The purpose of this work was to study the use of a time-of-flight (TOF) 3D camera for tree mapping. The main idea was to measure a panoramic range image of the surrounding environment and use suitable segmenting algorithm to find standing sticks that were modeling trees in laboratory environment. Also real trees were measured in outdoor environment. The possible affect of different weather conditions to distance values measured by the 3D camera were also tested.

1. INTRODUCTION

The need to map trees is to make an inventory of the biomass of the forest and also to plan the tree harvesting. The conventional way to plan the tree harvesting is done with a human eye. To make the harvest planning more accurate, tree measurement system is needed. Previous researches have used 2D or 3D laser range finder (LRF) based measurement systems [1]-[2]. 3D LRF systems scan the desired area in a few minutes. However, they are expensive. TOF 3D cameras such as those manufactured by PMD Tech, Canesta and Mesa Imaging, for example, are low-cost non-scanning (staring) range imagers based on CMOS imager chips that are capable of providing range images at full video speed. TOF offers a direct depth data acquisition, whereas LRF involves a great amount of computational power for the same 3D image. Because of the progress in TOF-vision systems, current 3D matrix cameras can be manufactured and be used for many applications such as robotic, automotive, industrial, navigation, safety, medical and multimedia applications. For all application areas new accurate and fast algorithms for 3D measuring and surface recognition are needed. In this paper a tree measurement, particularly the measurement of location using a TOF 3D camera in forest environment, is explored.

measurement speed of 10 to 25 frames per second and allows averaging and suitable filtering. Unambiguous measuring range is depended on the modulation frequency. For example using 20 MHz modulation frequency unambiguous measuring range is 7.5 m. More specific information on the characterization of the 3D camera has been done and published before [5].

The 3D camera was set on a pan-tilt unit, which main specifications are:

- Tilt range: -47° to $+31^{\circ}$ from level
- Pan range: $\pm 159^{\circ}$ ($\pm 180^{\circ}$ with extended range mode enabled)
- Tilt resolution: $0,003^{\circ}$
- Pan resolution: $0,013^{\circ}$

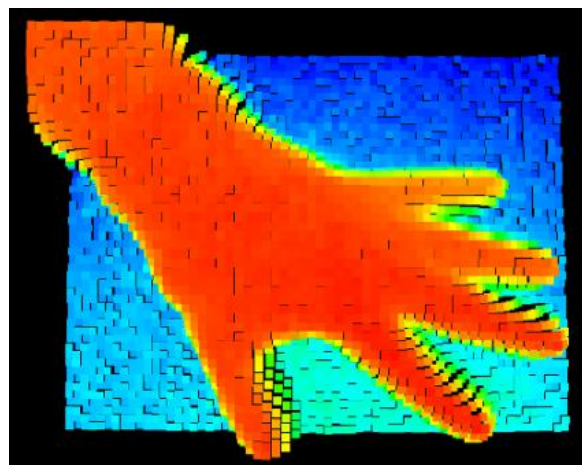


Fig. 2. Range image taken with the 3D camera.



Fig. 1. PMD [vision][®] 3k-S 3D video range camera

2. MEASURING SYSTEM

2.1 Equipment

The 3D camera (PMD [vision][®] 3k-S) produces a two-dimensional range image by measuring 3072 distances simultaneously using a 64×48 pixel array [3]-[4]. The 3D camera has a field-of-view of 22.5° . The range image is generated by illuminating the entire field-of-view with sine modulated light produced by LEDs and measuring the phase delay of reflected light concurrently in each pixel. It attains a

2.2 Panoramic range image

To attain a panoramic range image, the 3D camera has to be panned around to 16 different angles to reach 360 degrees. The 3D camera was set on a pan-tilt unit to make possible accurate movement of the camera. Range images are stored to data files and later on processed. All the data handling is performed as offline computing on MATLAB.

A room was measured in ten different angles to test the panoramic range image construction. The point clouds, shown in Fig. 3, are represented from above and are measured using a field of view of 225 degrees. The point clouds formed from the single range images are fitting correctly to the geometry of the room.

2.3 Spatial resolution

The number of the pixels in the array of the 3D camera is relatively small when compared to common camera

technology (usually 1000×1000 or even more). In tree map measurement low spatial resolution can make the determination of the tree location difficult when the trees are far away. It can also have an effect on the accuracy of the tree location. Especially low spatial resolution affects on the accuracy of the tree width estimation. However spatial resolution can be increased by overlapping two or more range images. In measuring situation this means that the angle of the 3D camera is changed horizontally less (half, one-fourth etc.) than the angle formed by single pixel. The disadvantage of the overlapping method is that it also increases the measuring time.

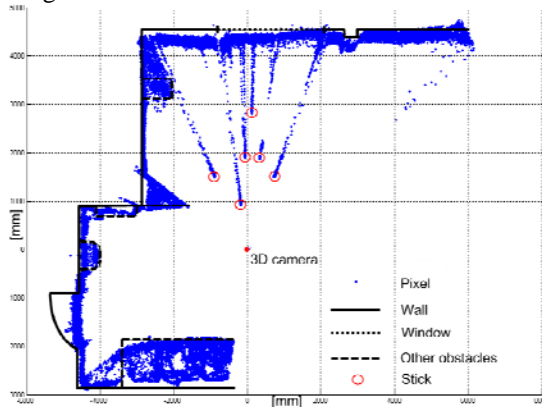


Fig. 3. A room measured with the 3D camera.

2.4 Segmenting algorithm

To detect right objects from the measured data, segmenting algorithm has to be used. The algorithm uses different kind of thresholds. The thresholds have to be set manually to fit to different measuring targets. The following threshold criteria were used:

- The distance difference of the adjacent points
- The maximum distance of a point to origin
- The distance of a point to another point
- The maximum width of a group of points.

3. EXPERIMENTS

In outdoor environment, measuring conditions are not ideal. Measurements done outside can be interfered by the weather (rain, snowfall, mist, sun etc.) and cause error to the measuring results. On the other hand the forest environment is its own problem. Well managed pine tree forests would be the easiest measuring target, but in the worst case the underbrush and branches make the tree measurement more difficult or even impossible.

3.1 Weather

The effects of the weather to measurements were tested in cloudy and sunny daylight, rain, snowfall and dark night time. Rain and snowfall effects were measured only in daylight. The 3D camera was pointed outside through a window. The target was placed outside to about 6 m from the 3D camera. The 3D camera and the target were kept ready for the measurements whenever the weather was right.

Measurements showed that distance results were a few centimeters longer on a rainy day than in clear weather conditions. This is due to reflections and refractions of light in drops of water. This kind of behavior can be compared to the effect of the multipath propagation of light. Snowfall didn't have any effect on the distance results. Although the

3D camera suppresses the background illumination, there was a slight, but almost insignificant, difference between the measurements made in the daylight and in dark conditions. In these measuring situations the sun was shining behind the target towards the camera. The worst case was realized when the target was enlightened by the sun. Error of tens of centimeters was induced to the distance values making the distance values longer.

3.2 Indoor

In the indoor setup 25 mm wide sticks were used to model trees. The sticks were placed approximately to the distances of 1 - 3 m from the 3D camera. This setup corresponds to 25 cm wide tree trunks on distances of 10 - 30 m.

The point clouds, shown in Fig. 4, are measured using field of view of 67.5 degrees. In Fig. 4.a), two range images have been overlapped, which means double amount of measuring points horizontally compared to Fig. 4.b). Corresponding segmented data is shown in Fig. 5. Measurements were done using six sticks in the field of view of the 3D camera. All of the sticks were found when better resolution was used. However, the segmenting algorithm does not detect the stick farthest away (3 m distance) when the resolution is lower (Fig. 5.b)). This happens because the pixel size is about the same as the width of the stick. In this case the segmenting algorithm using the distance difference of the adjacent pixels can't reliably distinguish the sticks from other possible objects. The stick in 3 m distance can be detected, when increasing the threshold, but can also cause false detections. Fig. 5 shows that with better resolution, the segmenting algorithm detects more right data points also in vertical direction which improves the reliability of the detection.

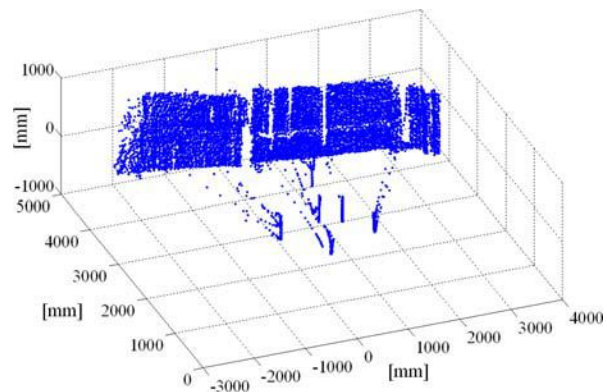
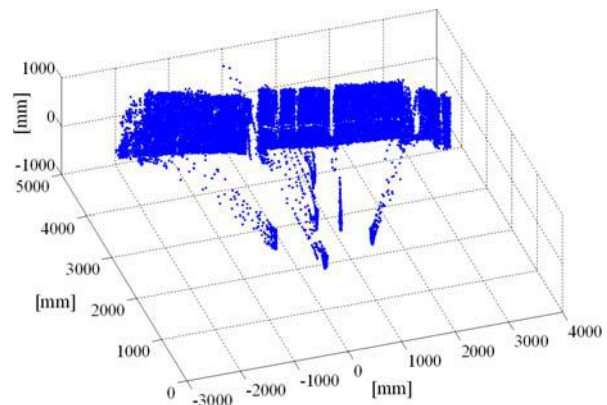


Fig.4. Point clouds using a) better resolution b) lower resolution.

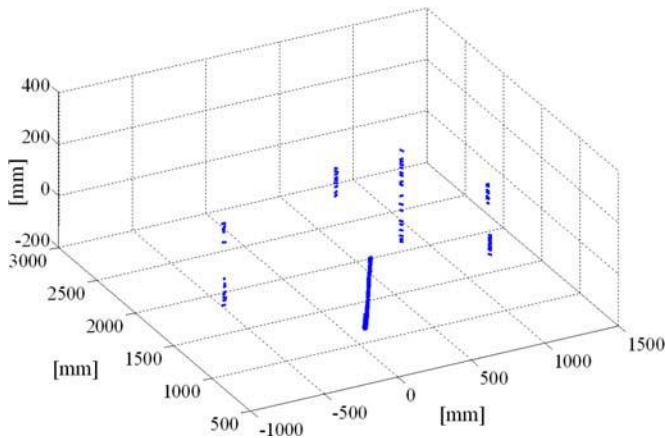
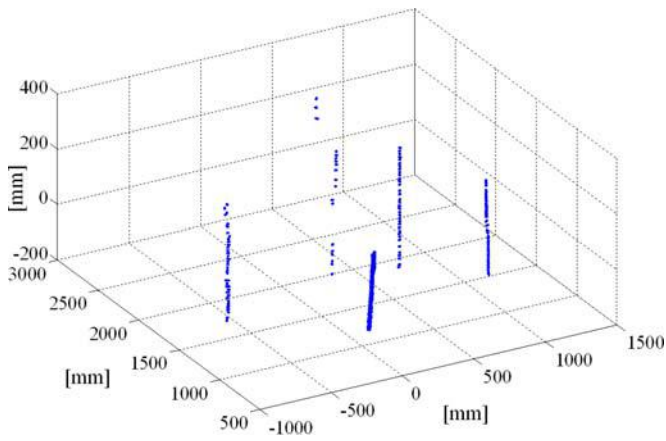


Fig.5. Segmented point clouds using a) better resolution b) lower resolution.

3.3 Outdoor

Outdoor experiments were done in a well-kept grass area (Fig. 6). Because the distances outside were much longer, the modulation frequency of the 3D camera was changed to 5 MHz, which extends the unambiguous measuring range to 30 m. Fig. 7 shows the results of the measurements done outside. The individual measuring points, shown in Fig. 7.b), are branches which the segmenting algorithm didn't cut away. The segmenting algorithm detects just the trees seen in front in Fig. 6. This maybe results from the function of the 3D camera, which didn't work as expected. The main reason was that the sun was shining to trees while the measurements were done.

4. CONCLUSION

In this paper, the use of a time-of-flight (TOF) 3D camera for tree measurement was explored. The paper also discussed the problems in tree measurement. The research shows that it is possible to use 3D camera technology in this kind of application. More work has to be done to get the system to work properly. In future larger forest area is wanted to be mapped. Covering larger area needs measuring trees in several locations and therefore needs map matching. Also the calculation of the width of the tree will be added.



Fig. 6. Outdoor measurement area with trees.

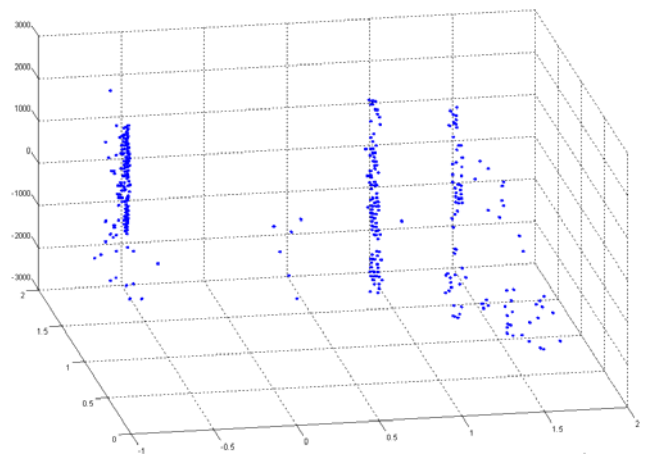
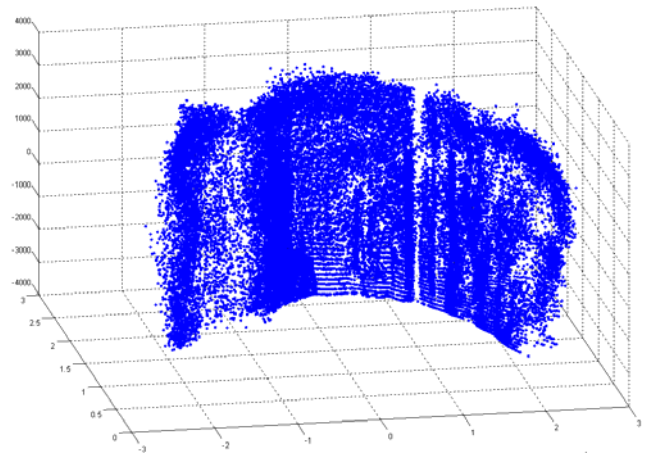


Fig.7. Point clouds from forest environment a) raw data b) segmented data.

5. ACKNOWLEDGEMENT

The authors would like to thank Finnish Funding Agency for Technology and Innovation (TEKES) and European Regional Development Fund (ERDF) for funding this research.

- [1]. *J. Jutila, K. Kannas, and A. Visala*, “Tree Measurement in Forest by 2D Laser Scanning”, in: Proceedings of the 2007 IEEE International Symposium on Computational Intelligence in Robotics and Automation, Jacksonville, FL, USA, June 20-23, 2007, pp. 491-496.
- [2]. *P. Forsman, and A. Halme*, “3-D Mapping of Natural Environments with Trees by Means of Mobile Perception”, in: IEEE Transactions on Robotics, vol. 21, no. 3, June 2005, pp. 482-490.
- [3]. *T. Möller, H. Kraft, J. Frey, M. Albrecht, and R. Lange*, “Robust 3D Measurement with PMD Sensors”, Proceedings of the First Range Imaging Research Day at ETH Zurich, ISBN 3-906467-57-0, 2005.
- [4]. *Z. Xu, R. Schwarte, H. Heinol, B. Buxbaum, and T. Ringbeck*, “Smart pixel - photonic mixer device (pmd) New system concept of a 3d-imaging camera-on-a-chip”, Tech. rep., PMDTec (2005).
- [5]. *A. Ollikkala, and A. Mäkynen*, “Range Imaging Using a Time-of-Flight 3D Camera and a Cooperative Object”, in: Proceedings of 12MTC 2009 - International Instrumentation and Measurement Technology Conference, Singapore, 5-7 May 2009, pp. 817-821.

THE OPTICAL AND STRUCTURAL PROPERTIES OF QUANTUM WELLS $\text{Mg}_{0.27}\text{Zn}_{0.73}\text{O}/\text{ZnO}$ PRODUCED BY PULSED LASER DEPOSITION

A.A. LOTIN, O.A. NOVODVORSKY, L.S. PARSHINA,
E.V. KHAYDUKOV, O.D. KHRAMOVA, V.Ya. PANCHENKO

*Institute on Laser and Information Technologies,
Russian Academy of Sciences (ILIT RAS)
Shatura, Moscow Region, Russia*

The multiple quantum wells (MQW) $\text{Mg}_{0.27}\text{Zn}_{0.73}\text{O}/\text{ZnO}$ have been grown by pulsed laser deposition method with different well width L_w . The optical and structural characteristics of MQW $\text{Mg}_{0.27}\text{Zn}_{0.73}\text{O}/\text{ZnO}$ have been investigated. The quantum confinement effect showing up in the blue shift of exciton peak in low temperature (8 K) photoluminescence spectra at well width reduction has been studied. It is established that intensity exciton peak I_{ex} and Einstein's characteristic temperature Θ_E increase at reduction of well width L_w . It is revealed that the discontinuity ratio of conduction and a valence bands in heterostructure $\text{Mg}_{0.27}\text{Zn}_{0.73}\text{O}/\text{ZnO}$ is 0.65/0.35 that corresponds to the literature.

1. INTRODUCTION

The semiconductor two-dimensional structures, such as quantum wells and the superlattices, serve for more than a decade as a basis for a wide spectrum of optoelectronic devices. Recently the great attention is given to $A^{II}B^{VI}$ (or $A^{III}B^V$) wide gap semiconductors because the optoelectronic devices based on them are capable of working in ultra-violet and visible ranges of wavelengths [1-5]. Of particular interest in this range of semiconductors is zinc oxide, thanks to wide band gap $E_g=3.37$ eV and high exciton binding energy (60 meV) that provides effective exciton emission at higher temperatures on comparison with III-V optical semiconductors [6]. High heat conductivity, effective luminescence, as well as mechanical and chemical stability allow the ZnO based devices to work under most extreme conditions [7]. The excitons in the quantum wells (QW) based on ZnO have higher stability on comparison with III-V QW because of exciton binding energy increase and exciton-phonon interaction reduction, caused by quantum confinement. Thanks to these effects, the excitons should play the important role in such processes as stimulated radiation in the multiple quantum wells (MQW) based on zinc oxide even at a room temperature [6].

In the present work the series $\text{Mg}_{0.27}\text{Zn}_{0.73}\text{O}/\text{ZnO}$ MQW with different well widths has been grown. The quantum confinement effect showing up in the blue shift of exciton peak in photoluminescence spectra (PL) is investigated at well width reduction. It is established that the intensity of exciton peak and Einstein's characteristic temperature increase at well width L_w reduction. The values of conductivity and valence bands discontinuity in heterostructure $\text{Mg}_{0.27}\text{Zn}_{0.73}\text{O}/\text{ZnO}$ have been defined. The research of structural properties of $\text{Mg}_{0.27}\text{Zn}_{0.73}\text{O}/\text{ZnO}$ has been conducted.

2. EXPERIMENTAL TECHNIQUE

The series of multiple quantum wells $\text{Mg}_{0.27}\text{Zn}_{0.73}\text{O}/\text{ZnO}$ with a well width range from 1.04 nm to 20 nm was grown on sapphire substrates (00.1) by pulsed laser deposition method. The growth of MQW was carried out in a high vacuum chamber with initial vacuum not worse than 10^{-7} Torr. The ablation of ceramic targets was made by excimer laser LC-7020 at pulse repetition frequency of 10 Hz ($\lambda=248$ nm, $\tau=15$ ns), the energy density of laser radiation on the

target being 3 J/cm^2 . The detail of experimental setup we already reported in [8].

As the mismatch of a -parameter of ZnO lattices and the sapphire (00.1) substrate is $\sim 18\%$ the buffer layer $\text{Mg}_{0.27}\text{Zn}_{0.73}\text{O}$ of thickness ~ 50 nm was preliminarily grown on the substrate. The thickness b of individual barrier layers $\text{Mg}_{0.27}\text{Zn}_{0.73}\text{O}$ and the total thickness $m \cdot L_w$ of ZnO layers was constant for all the MQW ($b=6$ nm and $m \cdot L_w=40$ nm, m – the number of periods). The substrate temperature during growth was maintained in the range $(450 \pm 5)^\circ\text{C}$. The substrates were mounted within 7 cm from the targets. For achievement of an atomic-smooth surface, the substrates with the grown on them buffer layer $\text{Mg}_{0.27}\text{Zn}_{0.73}\text{O}$ were annealed for 2 hours in oxygen atmosphere at the temperature 1000°C . The oxygen (O_2) was used as buffer gas; its pressure in the chamber was 5 mTorr.

To study the optical properties of MQW $\text{Mg}_{0.27}\text{Zn}_{0.73}\text{O}/\text{ZnO}$ the low temperature (8 K) spectra of a photoluminescence were measured in the short-wave area. The PL excitation was carried out by a continuous He-Cd laser ($\lambda=325$ nm, $W=23$ mW) and a pulsed-periodical KrF excimer laser, the PL spectra were registered by Ocean Optics HR4000 spectrometer. The research of structural characteristics, diffusion processes and interface quality of multiple quantum wells $\text{Mg}_{0.27}\text{Zn}_{0.73}\text{O}/\text{ZnO}$ was performed by the multi-purpose X-ray diffractometer D8 Discover (Bruker-AXS). The surface morphology was investigated by an atomic force microscope (AFM) DME DualScope 2401.

3. RESULTS AND DISCUSSION

The research of surface morphology of the buffer layer $\text{Mg}_{0.27}\text{Zn}_{0.73}\text{O}$ by the atomic force microscopy method has shown that the surface roughness after the deposition is 5-12 nm. To reduce the surface roughness the substrates with buffer layers were subjected to thermal annealing at various temperatures in oxygen atmosphere. From Fig.1 it is seen that the minimum roughness of the surface not exceeding 1 nanometer is reached at annealing temperature 1000°C .

The band gap of the buffer and barrier layers $\text{Mg}_{0.27}\text{Zn}_{0.73}\text{O}$ was 3.57 eV, and for the active layer ZnO it was 3.36 eV. The X-ray analysis of ZnO and $\text{Mg}_{0.27}\text{Zn}_{0.73}\text{O}$ films has indicated that their lattice mismatch does not exceed 0.66 %. A study has been made of the low temperature photoluminescence spectra (at 8K) of multiple quantum wells $\text{Mg}_{0.27}\text{Zn}_{0.73}\text{O}/\text{ZnO}$.

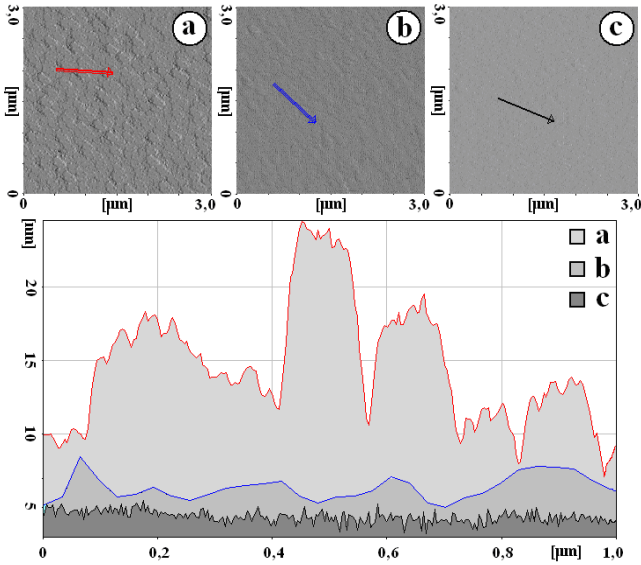


Fig.1. The surface morphology of buffer layer $Mg_{0.27}Zn_{0.73}O$ on a sapphire substrate (00.1): (a) – before annealing, (b) – annealed at $800^{\circ}C$, (c) - annealed at $1000^{\circ}C$, and cross-section profiles of corresponding surfaces (below).

On Fig.2 the photoluminescence spectra of the $Mg_{0.27}Zn_{0.73}O/ZnO$ MQW series with the well width L_w varying from 1.04 nm to 20 nm are presented. The PL spectrum of 70 nm ZnO film is presented in this figure for comparison. The monotonous nonlinear blue shift of the UV peak position with the quantum well width reduction characterizes the quantum confinement effect in the two-dimensional structures $Mg_{0.27}Zn_{0.73}O/ZnO$ [6,9-11].

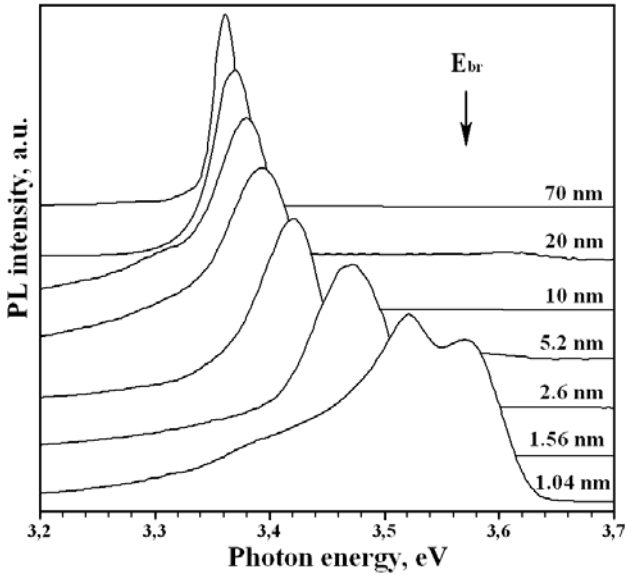


Fig.2. The low temperature photoluminescence spectra of MQW $Mg_{0.27}Zn_{0.73}O/ZnO$ with various well width L_w .

The important parameter in designing heterostructures is the value of energy band discontinuity in the conduction and valence bands. The solution of the Schrödinger equation for a finite square potential well under the condition of symmetry and continuity of the wave function in the conduction and valence bands is possible to obtain as follows [12]:

$$\tan\left[\sqrt{\frac{2m_{1(e,h)}^*E_n^{(e,h)}(L_w)}{\hbar^2}}L_w\right] = \sqrt{\frac{m_{2(e,h)}^*(\Delta E_{(C,V)} - E_n^{(e,h)}(L_w))}{m_{1(e,h)}^*E_n^{(e,h)}(L_w)}}, \quad (1)$$

where \hbar - Planck's constant, E_n^e and E_n^h - the proper values of energy in the potential wells for an electron and a hole respectively, $n=1,2,3 \dots$ - an integer number, ΔE_C and ΔE_V - the discontinuities in the conduction and valence bands. The values of electron and hole effective masses have been chosen as $m_{1e}^*=0.28m_0$ and $m_{1h}^*=1.8m_0$ for the active layer ZnO [13] and $m_{2e}^*=0.4m_0$ and $m_{2h}^*=2m_0$ for the barrier layers $Mg_{0.27}Zn_{0.73}O$ [14]. Within the limits of the given model the light holes were not considered.

The resulting exciton energy in a quantum well at $n=1$ will be defined by the expression:

$$E(L_w) = E_g(ZnO) + E_1^e(L_w) + E_1^h(L_w) \quad (2)$$

Fig.3 illustrates the dependence of energy position of photoluminescence MQW exciton peak on the well width L_w is presented. The relation between the discontinuities of the conduction band ΔE_C and valence band ΔE_V was used as a fitting parameter. The best coincidence of the numerical and experimental data has been obtained at the ratio $\Delta E_C/\Delta E_V=0.65/0.35$ that is in a good agreement with the results of the work [15].

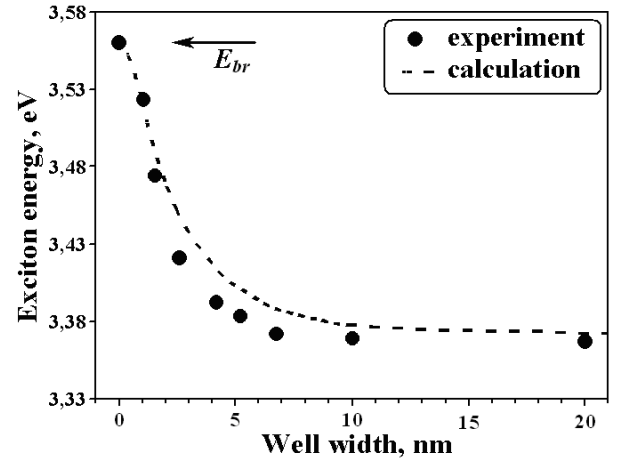


Fig.3. The dependence of position of MQW $Mg_{0.27}Zn_{0.73}O/ZnO$ photoluminescence exciton peak on quantum well width L_w .

The full width at half maximum (FWHM) of the exciton peak in MQW also increased with reduction of the quantum well width L_w that can be explained by random fluctuation of the width $L_w \pm \delta L_w$ of quantum wells, which leads to non-uniform broadening of the photoluminescence spectrum. The smaller is the width of a well L_w , the higher is the influence of this fluctuation δL_w on half width of an UV peak in the photoluminescence spectra of MQW [6,16].

The nonlinear growth of exciton peak intensity I_{ex} was observed in PL spectra of MQW $Mg_{0.27}Zn_{0.73}O/ZnO$ at the quantum well width L_w reducing (Fig.4). The maximum PL intensity value I_{ex} was evidenced in MQW with the well width $L_w=2.6$ nm, at further reduction of L_w the PL intensity was sharply decreased.

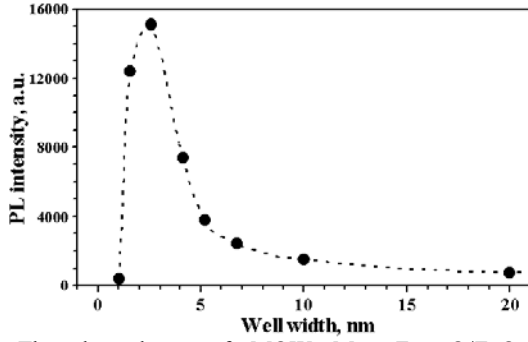


Fig.4. The dependence of MQW $Mg_{0.27}Zn_{0.73}O/ZnO$ photoluminescence intensity on quantum well width L_w .

According to Boze-Einstein model the exciton energy in a quantum is expected to vary with temperature under the following law [10]:

$$E(T) = E(0) - \frac{2\alpha_E}{\exp\left(\frac{\Theta_E}{T}\right) - 1}, \quad (3)$$

where α_E – a constant corresponding to exciton-phonon interaction, $\Theta_E = hf/k$ – Einstein's characteristic temperature, and $E = k\Theta_E$ – the averaged phonon energy, h – Planck's constant, k – Boltzmann constant, f – the frequency of phonon fluctuations.

To define the character of Einstein temperature Θ_E to power density of exciting radiation under pumping with excimer KrF laser. Fig.7(a) presents on a logarithmic scale the photoluminescence spectra of MQW $Mg_{0.27}Zn_{0.73}O/ZnO$ with well width $L_w = 5.2$ nm, measured at a room temperature on pumping with the excimer KrF laser with intensity from 50 to 850 kW/cm^2 . For comparison, the PL spectrum of the same structure excited by a continuous He-Cd laser is shown.

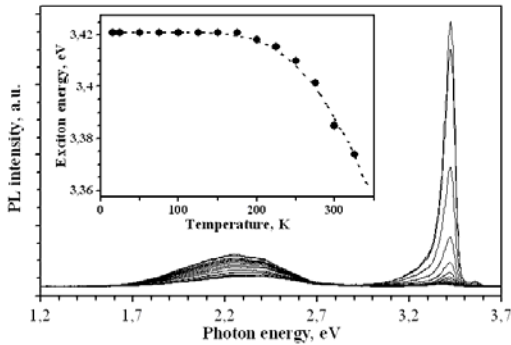


Fig.5. The PL dynamics of MQW $Mg_{0.27}Zn_{0.73}O/ZnO$ (6 nm/2.6 nm) on temperature in the range 8-325 K. An insert illustrates the temperature dependence of exciton energy in MQW.

Einstein's characteristic temperature Θ_E was defined for all the samples MQW $Mg_{0.27}Zn_{0.73}O/ZnO$ by similar approximation of equation (3). Fig.6 presents the dependence of Einstein's characteristic temperature Θ_E on quantum well width L_w . It is seen that Θ_E increases as the quantum well width reduces up to $L_w = 2.6$ nm, and then sharply decreases. The dependences shown on Fig.4 and Fig.6 very well correlate among themselves and have, on our opinion, the common nature. The exciton peak intensity I_{ex} and Einstein's characteristic temperature Θ_E growth with reduction of quantum well width L_w can be explained by an increase in

characteristic exciton binding energy in a quantum well that has been demonstrated in works [15,17].

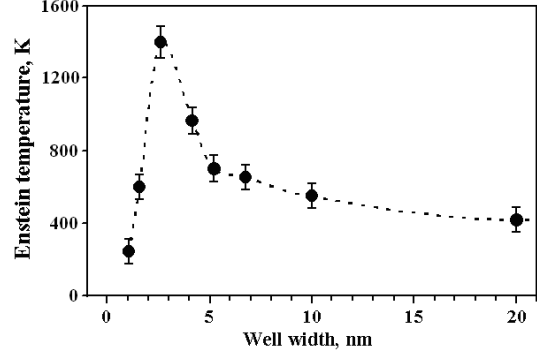


Fig.6. The dependence of Einstein's characteristic temperature Θ_E of MQW $Mg_{0.27}Zn_{0.73}O/ZnO$ on quantum well width L_w .

The abrupt decrease of I_{ex} and Θ_E for $L_w < 2.6$ nm can follow from the quantum well width L_w getting comparable with the value of interface roughness which is ~ 1 nm and excitons undergo scattering on these irregularities, which leads to quenching of photoluminescence.

As noted above, the excitons are expected to play an important role in stimulated radiation [6]. For studying a possibility of stimulated radiation in MQW the photoluminescence spectra have been investigated in relation to power density of exciting radiation under pumping with excimer KrF laser. Fig.7(a) presents on a logarithmic scale the photoluminescence spectra of MQW $Mg_{0.27}Zn_{0.73}O/ZnO$ with well width $L_w = 5.2$ nm, measured at a room temperature on pumping with the excimer KrF laser with intensity from 50 to 850 kW/cm^2 . For comparison, the PL spectrum of the same structure excited by a continuous He-Cd laser is shown.

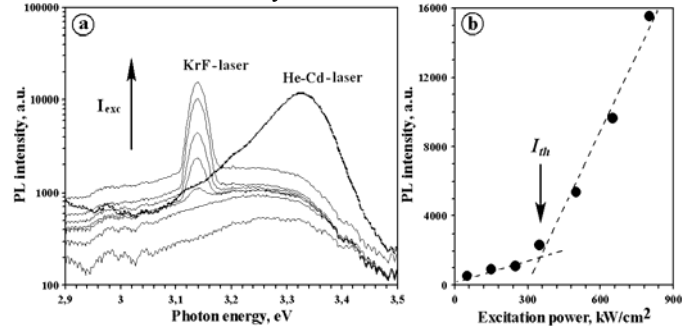


Fig.7. The PL spectra of a line 3.14 eV of MQW $Mg_{0.27}Zn_{0.73}O/ZnO$ with a well width $L_w = 5.2$ nm: (a) excitation by the He-Cd laser and the excimer KrF laser with pump power variation from 50 to 850 kW/cm^2 ; (b) dependence of PL amplitude of a line 3.14 eV of MQW $Mg_{0.27}Zn_{0.73}O/ZnO$ on excimer KrF laser pump power.

At optical pump power densities ~ 350 kW/cm^2 , the PL spectra produced a wide FWHM peak of 112.4 meV corresponding to the exciton line inside the quantum well of 3.34 eV. Further increase of pulsed pump power resulted in predomination of a narrow line with FWHM equal to 31.3 meV, shifted to the red region by 0.2 eV, its intensity rising sharply. As this took place, a characteristic bend corresponding to the threshold of stimulated radiation excitation was observed on the plot of PL line intensity dependence at 3.14 eV on KrF laser pump power. The intensity of this line, unlike the exciton peak of 3.34 eV in the

quantum well, was practically not varied. The similar result was observed in works [6,17].

Fig.8 shows the cross-section image of 20 quantum wells $Mg_{0.27}Zn_{0.73}O/ZnO$ produced by a scan electron microscope.

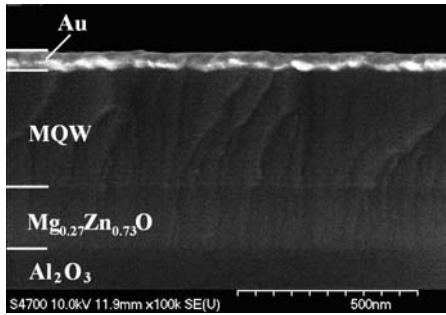


Fig.8. A SEM-image of cross-section of 20 quantum wells $Mg_{0.27}Zn_{0.73}O/ZnO$ grown on a sapphire substrate (00.1) with a buffer layer $Mg_{0.27}Zn_{0.73}O$. For contrast the structure was covered by a gold film.

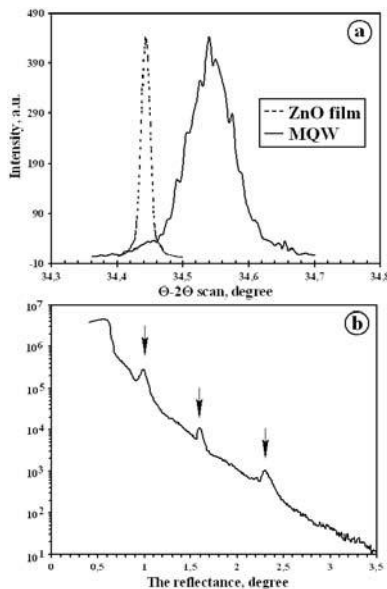


Fig.9. Θ - 2Θ scans of a ZnO film and MQW $Mg_{0.27}Zn_{0.73}O/ZnO$ with the well width $L_w=2.6$ nm (a). A curve of mirror reflection of MQW $Mg_{0.27}Zn_{0.73}O/ZnO$ with the well width $L_w=5.2$ nm.

The structural properties of MQW $Mg_{0.27}Zn_{0.73}O/ZnO$ were examined by X-ray reflectometry method. The width of

the X-ray beam was 0.2 mm, the collect slot in front of the detector also had the size of 0.2 mm. On Fig.9(a) are shown Θ - 2Θ the scans of a ZnO film and MQW $Mg_{0.27}Zn_{0.73}O/ZnO$. The characteristic period of signal modulation and a special software package LEPTOS were used to define the width $L_w=2.6$ nm of a single well that agrees nicely with the expected thicknesses set by the growth speed [18].

To evaluate the quality of interfaces, the chart of reciprocal space has been measured in the vicinity of point 000 of the reciprocal lattices (a curve of mirror reflection). Fig.9(b) presents the curve of mirror reflection of MQW $Mg_{0.27}Zn_{0.73}O/ZnO$ presented in Fig.8, which has been obtained by subtraction of diffusion scattering distribution from the experimental Θ - 2Θ curve. The presence of the resonant diffusion scattering effect indicates to correlation in interface morphology in the whole structure, i.e. roughnesses of the top layers are inherited from the bottom ones and do not exceed 1 nm.

4. CONCLUSION

The multiple quantum wells $Mg_{0.27}Zn_{0.73}O/ZnO$ grown by the pulsed laser deposition method have shown high structural quality and sharp interfaces. We observed the quantum confinement effect in multiple quantum wells $Mg_{0.27}Zn_{0.73}O/ZnO$ showing up in a blue shift of exciton energy at the well width reduction. This reduction caused a nonlinear rise of PL exciton peak intensity I_{ex} and Einstein's characteristic temperature Θ_E which also characterizes the quantum confinement effect in two-dimensional structures. It was found that the ratio of energy zone discontinuity values in the conduction and valence bands is 0.65/0.35. The effect of stimulated exciton radiation in MQW was revealed with the excitation threshold of ~ 350 kW/cm². The effects mentioned above have a fundamental character, but can be applied in designing light emitting diodes and lasers with the tunable wavelength and high temperature stability based on heterostructures $Mg_xZn_{1-x}O/ZnO$.

5. ACKNOWLEDGMENTS

We gratefully acknowledge Dr. C. Wenzel and K.D. Scherbachev for technical and analytical support. This work was supported by RFBR grants: № 09-08-00291, 09-02-12108, 09-08-01053, 09-02-01298, 09-07-12151.

- [1]. Freed E. Shubert. Light-emitting diodes (Troy, New York, 2008).
- [2]. S.E. Nikitin, Yu.A. Nikolaev, I.K. Polushina, V.Yu. Rud, Yu.V. Rud, E.I. Terukov. *Semicond.*, **37**, 11 (2003)
- [3]. A.V. Sacharov, V.V. Lundin, V.A. Semenov, A.S. Usikov. *Tech. Phys.*, **25**, 12, (1999)
- [4]. V. Kuryatkov, G. Kipshidze, S.N.G. Chu, M. Holtz, Yu. Kudryavtsev. *Appl. Phys. Lett.*, **83**, 7 (2003)
- [5]. Y. Ryu, J.A. Lubguban, Y.S. Park, C.J. Youn et al. *Appl. Phys. Lett.* **88**, 241108 (2006)
- [6]. T. Makino, Y. Segava, M. Kawasaki, H. Koinuma. *Semicond. Sci. Technol.* **20**, (2005)
- [7]. U. Üzgür, Ya.I. Alivov, C. Liu, A. Teke et al., *J. Appl. Phys.* **98**, 041301 (2005)
- [8]. O.A. Novodvorsky, L.S. Gorbatenko, V.Ya. Panchenko, O.D. Khramova, Ye.A. Cherebilo, C.Wenzel, J.W. Bartha, N. Trumpaicka, V.T. Bublik, K.D. Scherbachev, *Semicond.*, **43**, 4 (2009)
- [9]. Zg.I. Alpherov, *Semicond.*, **32**, 1 (1998).
- [10]. X.Q. Gu, F. Liu, W. Jaeger et al. *Appl. Phys. Lett.* **91**, 022103 (2007)
- [11]. Peter Y. Yu, Manuel Cardona, *Fundamentals of semiconductors*, (Springer, 2002).
- [12]. Paul A. Tipler, Ralph A. Llewellyn. *Modern Physics*, (W.H. Freeman and company, New York, 2007).
- [13]. Won Il Park, Gyu-Chul Yi, Miyoung Kim, and Stephen J. Pennycook, *Adv. Mater.*, **15**, 6, (2003)

THE OPTICAL AND STRUCTURAL PROPERTIES OF QUANTUM WELLS $Mg_{0.27}Zn_{0.73}O/ZnO$ PRODUCED BY PULSED LASER DEPOSITION

- [14]. *J. G. Lu, S. Fujita, T. Kawaharamura, H. Nishinaka, Y. Kamada, and T. Ohshima*, Appl. Phys. Lett. **89**, 262107 (2006)
- [15]. *G. Coli and K.K. Bajaj*, Appl. Phys. Lett. **78** (2001) p.2861
- [16]. *O. L. Lazarenkova, A. N. Pihtin*, Semicond., **32**, 9 (1998)
- [17]. *H. D. Sun, T. Makino, Y. Segawa, M. Kawasaki, A. Ohtomo, K. Tamura, H. Koinuma*. J. Appl. Phys. **91**, (2002)
- [18]. *L.S. Gorbatenko, O.A. Novodvorsky, V.Ya. Panchenko, O.D. Khramova, Ye.A. Cherebilo, A.A. Lotin, C.Wenzel, N. Trumpaicka, J.W. Bartha*, Laser Phys., **16**, (2009)

COMPACT RAMAN (CLS) SPECTROMETER FOR ACTIVE TEST OF LIQUID AND SOLID SAMPLES

K. R. ALLAKHVERDIEV^{1,3}, T. K. BAYKARA¹, A. M. SECGIN¹, S. OZBEK¹,
A. M. ULUBEY⁴, Z. Yu. SALAEVA¹, M. F. HUSEYINOGLU¹,
S. L. DRUZHININ², K. A. KONOVALOV², V. Y. SHCHAGIN²,
O. N. SMIRNOV², S. Yu. STRAKHOV^{2**}, E.V. PERKHINA²,

¹TÜBITAK, Marmara Research Center, Materials Institute, P.K. 21, 41470 Gebze/Kocaeli, Turkey

²Laser Systems Ltd., Krasnoarmeyskaya str., 1, 190005, Saint-Petersburg, Russia

³Institute of Physics ANAS, 370143, Baku, Azerbaijan

⁴University of Thrace, Faculty of Art and Science, Department of Physics, 22030 Edirne, Turkey

Raman (CLS- Combinational Light Scattering) spectroscopy is a technique used to study vibrational, rotational, other low-frequency modes in a system and takes advantage of the inelastic scattering of laser light by molecules. The laser light interacts with phonons or other excitations in the system, resulting in the energy of the laser photons being shifted up or down. The shift in energy gives information about the phonon modes in the system. Since different molecules show different energy changes, the Raman (CLS) effect have found a wide application as a qualitative or quantitative analysis method.

In this article the results of homemade compact Raman (CLS) spectrometer for remote detection of liquid and solid samples are presented. The spectrometer is intended for active analyses of liquid and solid samples in different environmental conditions, including food samples checking, narcotics and explosives spreading.

The spectrometer consists of the block for spectral analysis, two lasers, two fiber-optical sensors and sampling probe and can work with two types of laser sources without reconfiguration the optics and lasers. ($\lambda_1 = 532 \text{ nm}$; $\lambda_2 = 785 \text{ nm}$)

Scattered radiation via fiber enters the spectral block. Raman (CLS) spectrum is separated in 4096 receiver components (pixels) by help of the TEC- regulated CCD array. Developed spectrometer can operate also by accumulator battery and is considered as portable. The spectrometer is capable to detect the spectral coverage in the range between 150 and 4000 cm^{-1} and may be used for liquids (including water solution, alcohol, different types of gasoline) and solids (including pills, powders, explosives and drugs) analysis. The spectral resolution of developed system is not worse than 8 cm^{-1} .

Range of applications of the developed Raman system includes: forensics; pharmaceuticals; gemotology; recycling; semiconductors; microwave assisted synthesis and other.

1. INTRODUCTION

There are many analytical technologies available for chemical identification in the field situations, particularly. Fourier transform infrared spectroscopy (FTIR) using attenuated total reflection (ATR) [1], gas chromatography/mass spectrometry and Raman (or combinational light scattering - CLS) spectroscopy, ion mobility spectroscopy, Laser Induced Breakdown Spectroscopy (LIBS), colorimetric tests (reaction of specific chemicals with an unknown compound), Raman spectroscopy (RS) and other [2]. Some of these methods are very effective tools for the analysis of unknown materials but can be used in the laboratory settings only because of large dimensions, big mass, long time of analysis and other disadvantages.

Detection techniques based on optical methods possess a reasonable resolution, high quality and purity, easily movable. Moreover several methods such as Raman (CLS) analysis have radiation that penetrates the walls of glass and clear plastic, eliminating necessity to open containers and greatly reducing the risk of exposure.

In this work we present compact homemade Raman (CLS) spectrometer for active test of liquid and solid samples.

Raman (CLS) scattering of light (see fig. 1) [3,4] represents inelastic scattering of radiation by molecules of substance, being the combination of frequencies of incident radiation and own frequencies of a molecule (vibration and rotational).

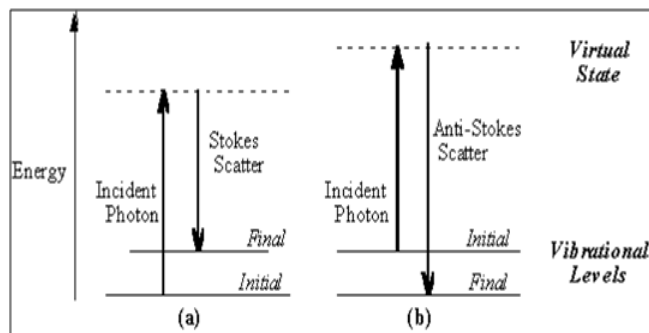


Fig.1. Energy level diagram for Raman (CLS) scattering; (a) Stokes Raman (CLS) scattering (b) anti-Stokes Raman (CLS) scattering.

Frequencies of molecular fluctuations depend on weights of the atoms constituting a molecule, and normally is one order of magnitude less than frequency of visible light. Molecules of the substance, which are taking place in various excited conditions, scatter the photons with addition or subtraction of energy, forming Stokes and anti-Stokes components of a spectrum, respectively.

Advantages of Raman spectroscopy are as follow:

- non-destructive check and research of samples;
- quick inspection;
- no frequency-tuned radiation source is required for revealing of spectral lines of vibration-rotational spectrum for observation of whole spectrum of substance, as in a case of absorption spectroscopy. Practically whole vibration-

rotational spectrum of a researched molecule is observed in a narrow site of a visible range, where there are maxima of sensitivity of photo detectors of optical radiation;

- water does not cause the troubles for Raman spectra measurements, when comparing with IR spectra;
- for packing the samples it is possible to use the glass and quartz, which are transparent for exciting and scattered radiations.

Disadvantages of Raman (CLS) spectroscopy:

- RS spectra have rather small intensity of signals (scattering section 10^{-31} - 10^{-29} $\text{cm}^2\text{molec}^{-1}$), therefore the additional measurements on increasing of energy potential of the device are required for detection of displaying substances with sensitivity on a level of threshold concentration, and even lethal, for some substances with weak lines of radiation;
- frequently meeting unpredictable fluorescence with size of some orders of magnitude higher than Raman (CLS) signal. Fluorescence is observed, when the virtual energy level blocks an external electronic level so, that laser energy becomes higher (shorter wave length). Latter results to increase the probability of fluorescence;
- a problem of suppression of elastically scattered light (Rayleigh scattering). The use of the selective filter blocking the wave length of the exciting laser is possible for its elimination.

Differently, there is a rigid connection between the structure of a molecule and the frequency of the spectral components appearing in scattering. Therefore the number of such components and their position in a spectrum allow to determine a composition and structure of molecules. Thus, not frequencies of emission lines but their shift relative to frequency of exciting light are the major characteristic of RS-spectra.

Since different molecules show different energy changes, the Raman (CLS) effect have found a wide application as a qualitative or quantitative analysis method. In general in Raman (CLS) spectrometer a registration of spectra is carried out in Stokes band (positive Raman (CLS) shift).

Raman (CLS) spectrometers are widely used in criminalities, for detection of drugs and explosives, for analysis of contents of mail items, and also at the control of burning temperature.

The main aim of the present work is to develop and build a portable Raman (CLS) spectrometer for active tests of liquid and solid samples.

2. EXPERIMENT

In Fig. 2 the overview of our compact Raman (CLS) spectrometer for active test of liquid and solid samples is represented. The spectrometer consists of exciting laser, fiber-optics sensor, probe cavity, block for spectral analysis and exploitation packing.

Radiation of exciting laser (535 or 785 nm, 0, 5 W) goes through a fiber-optical sensor to the sampling probe where passes through the notch filter and is focused by lenses on a sample. The sampling probe (SP) has several endings - to be able to focus on different depth from the sample surface, and to calibrate the spectrum with known material.

Light scattered from the sample is collected and passed to the spectral block. Then it is reflected by the mirror 1 and directed onto the diffraction grating and on the receiver (registration system) CCD passing optical system - mirror 3 and cylinder 4.



Fig 2 Pictures of the Raman spectrometer

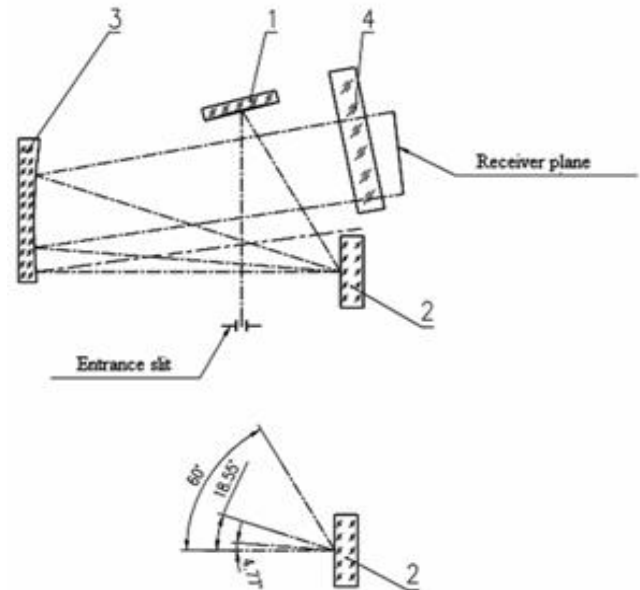


Fig.3. Optical scheme of developed system.(upper scheme) Maximal grating turning angle (below scheme). For details see text.

Continuous spectrum in the range of sensitivity of CCD 4...50 μm is separated in 1000 receiver components (pixels). Data reading from detector to computer is produced through the USB cable. If spectrometer operates on accumulator battery and notebook is used then device is considered to be portable.

In accordance with basis of Raman(CLS) spectroscopy each chemical compound has the specific spectrum of scattering. Relevant different wave numbers pixels register changes of intensity that correspond to displayed spectra.

Further comparison of received spectra and spectral database is carried out.

Detected spectrum is observed in working interface window of special program software. Using special program it is possible to set control parameters of spectrometer (integration time, laser power, smoothing passes etc.). After recording the spectrum, it is possible to find spectral peaks and modify spectrum in other programs (Excel etc.).

It is very important for Raman (CLS) spectrometer to have high resolution. Latter allows to distinguish certain spectral features required to be fully resolved with the aim for identifying the components in an organic liquid samples.

3. RESULTS AND DISCUSSION

In Figure 4 the spectrum of three grades of gasoline are depicted. One can clearly see the aromatic fraction in the 1000 cm⁻¹ region fully distinguishable from the olefinic background of the fuels indicated by the 1450 cm⁻¹ band. With increasing of fuel grades (from 87 to 93) these lines shift to high frequency side (see Fig.5).

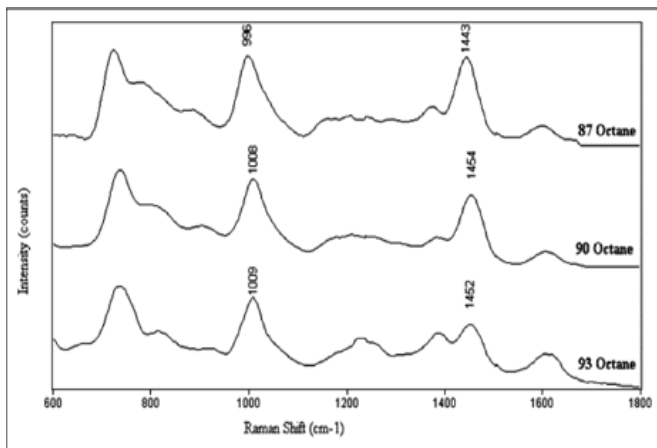


Fig 4 Raman (CLS) spectra of commercial gasoline's.

Fig 5 shows differences between gasoline grades. During the registration of A-92 regular motor gasoline and AI-95 regular motor gasoline definitive Raman (CLS) lines at 725 sm⁻¹, 784 sm⁻¹ and 1000 sm⁻¹ are observed. Depending on gasoline grades different relative intensity of spectral lines 725 sm⁻¹ and 784 sm⁻¹ were detected in our experiments.

The software of the Raman (CLS) spectrometer allows to determine composition of many component mixtures. For these aims the modified algorithm of registration analysis is used [5].

The basic algorithm of the regression analysis for processing a signal consists of the following. There are measurements of spectral curve $x_i(t_j)$ known substances (t_j -frequency or energy, $i = \overline{1, k+1}$); the spectrum of the researched sample containing 1st,...,k+1 substances, is measured, however the percentage of it is unknown. Then the spectrum of a sample $x(t_j)$ supposes representation

$$x(t_j) = \theta_1 x_1(t_j) + \dots + \theta_k x_k(t_j) + \theta_{k+1} x_{k+1}(t_j),$$

and $\theta_1 + \dots + \theta_{k+1} = 1$, $\theta_i \geq 0$, $i = \overline{1, k+1}$, where θ - vector of unknown parameters $\theta_1 \dots \theta_k$.

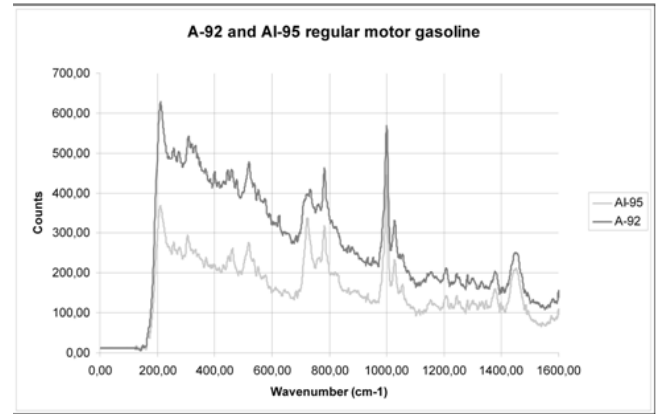


Fig.5. Spectra of A-92 and AI-95 regular motor gasoline.

Thus, the task of definition of a percentage of a mix leads to a model

$$\bar{\varphi} = X\bar{\theta}, \quad (1)$$

where $\bar{\theta} = (\theta_1, \dots, \theta_k)^T$ - vector of parameters (factors of regress), X - matrix (n×k), j-th column of which represents values of j-th controllable variable in 1-st..., n-th measurements, $\bar{\varphi} = (\varphi_1, \dots, \varphi_n)^T$ - vector of math waiting of observable value y (response) in 1-st..., n-th measurements.

Nonlinear model

$$\bar{y} = \bar{\varphi}(x, \bar{\theta}) + \bar{\varepsilon}, \quad (2)$$

where ε - the random error, sometimes is reduced to linear by suitable functional transformation.

So, if

$$\varphi(\bar{x}_i, \bar{\theta}) = \prod_{j=1}^k \exp\{\theta_j x_{ij}\},$$

then transition to (1) is carried out by taking the logarithm. Generally definition of parameters of nonlinear model reduces to the decision of sequence of linear tasks, linearising function φ in (2) and using iterative.

So, let

$$y = X * \theta + \varepsilon \quad (3)$$

If the law of distribution of mistakes is random (but is known), optimum on efficiency (at big n) estimations among all unbiased can be found on a method MP. These estimations $\bar{\theta} = \bar{\theta}(\bar{y})$ will not be linear on \bar{y} , despite of linearity (3). If to be limited by a class of linear estimations $\bar{\theta} = A\bar{y}$, irrespective on the law of distribution of mistakes of an estimation with optimum properties turns out at the set kind of a matrix.

Let's search for such estimation $\bar{\theta}$ of a vector of parameters that at its substitution in (3) sum of squares of

deviation experimental \bar{y} from predictable $\bar{y} = X * \bar{\theta}$ was minimal. Thus we assume that:

1. $E\bar{\varepsilon} = \bar{0}$;
2. $cov(\bar{\varepsilon}, \bar{\varepsilon}) = \sigma I_n$;
3. $rank X = k$;
4. Mistakes ε_i are independent.

Minimization on $\bar{\theta}$ of expression

$$Q = \sum_{i=1}^n (y_i - \sum_{j=1}^k X_{ij}\theta_j)^2 = (\bar{y} - X\bar{\theta})^T (\bar{y} - X\bar{\theta}) \quad (4)$$

leads to research of decisions of system

$$X^T X \bar{\theta} - X^T \bar{y} = 0 \quad (5)$$

By virtue of a condition 3 determinant of matrix $X^T X$ not equal to 0, so the system of the normal equations (5) has the unique decision

$$\bar{\theta} = (X^T X)^{-1} X^T \bar{y} \quad (6)$$

It is obvious, that it corresponds to a minimum (4), as at $\theta_i \rightarrow \pm\infty$ Q grows unlimited. The way of a finding of an estimation of a vector of parameters from a condition of a minimum (4) refers to *as a method of the minimal squares* (MMS), and an estimation (6) - *an estimation of a method of the minimal squares* (MMS estimation).

Let's consider geometrical interpretation of a method of the minimal squares. Let E_n - n-dimensional Euclid's space. Supervision of y_1, \dots, y_n determine in E_n end of a vector \bar{y} , which has been lead from the beginning of coordinates. Columns of matrix X, being by virtue of a condition 3 independent n-dimensional vectors x_1, \dots, x_k , generates in E_n linear variety E_k of vectors $\bar{y} = \bar{\theta}_1 \bar{x}_1 + \dots + \bar{\theta}_k \bar{x}_k$. In general, \bar{y} does not belong to this variety. Vector $\bar{\varepsilon} = \bar{y} - X\bar{\theta}$ represents a line from the end of \bar{y} to a point $X\bar{\theta}$ of variety. Minimizing

$$\bar{\varepsilon}^T \bar{\varepsilon} = (\bar{y} - X\bar{\theta})^T (\bar{y} - X\bar{\theta}) \quad (7)$$

in (4), we solve a task of finding a line with minimal length, i.e. construction of a perpendicular from \bar{y} on a plane E_k . At a corresponding choice of $\bar{\theta}$ vector $\bar{\varepsilon}$ is perpendicular to E_k , i.e., it is orthogonal to any of \bar{x}_j , $j = \bar{1}, \bar{k}$, : $\bar{x}_j^T (\bar{y} - X\bar{\theta}) = 0$, therefore $X^T (\bar{y} - X\bar{\theta}) = 0$, i.e. we received the normal equations (5). By virtue of linear independence $\bar{x}_j rank(X^T X) = k$, follows (6).

At essential noise level in a signal the method of direct regression analysis leads to essential mistakes, especially at definition of substances with small concentration. Such substances can be not recognized on a background of noise.

For their reliable definition and verification it is offered to use algorithm with artificial noise.

Essence of algorithm is an artificial adding of noise to initial signal and definition after that structure of a diagnosed mix with definition of concentration. This procedure is carried out repeatedly and as a result those components from a database which appear steady against brought hindrances are defined. Stability to hindrances can be defined as the attitude of the minimal and maximal concentration of the given substance for all cycle of calculations. If this attitude is great, that is during casual adding of noise the level of determined concentration strongly varies, most likely, that the given substance in a mix is absent. If the attitude is close to 1 the given substance is steady against hindrances and is considered present in a mix. Other components which at the direct analysis have been determined as present in a mix, but eliminated as a result of artificial adding of noise are considered false.

The common algorithm of this method is shown in Fig. 6.

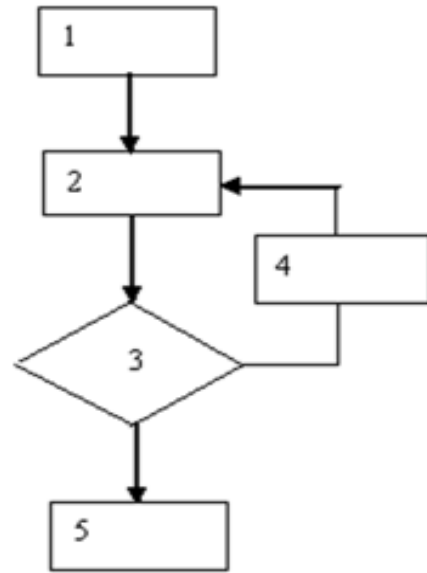


Fig. 6. Algorithm of a method of regression analysis with artificial noise: 1 – depicts the input of the received signal; 2 – calculation of a vector of concentration of substances by using equation (6); 3 – the conditional operator of an exit from a cycle of calculations with artificial noise (the counter of cycles); 4 – generation of random noise and its imposing on a spectrum of a signal; 5 - output of results of calculation of structure of a mix and concentration of the certain substances, definition of calculated value of a signal / noise ratio, a calculated error of calculations.

4. CONCLUSION

We developed and produced compact Raman (CLS) spectrometer for active test of liquid and solid samples as gasoline, drug, explosives and other. The range of practical applications of this device is wide.

5. ACKNOWLEDGMENTS

Turkish co-authors are thankful for the State Planning Committee of Turkey (DPT) for financial support. Russian co-authors are thankful for Institute of Laser Technique and Technologies of Baltic State Technical University.

- [1]. *A. S. Boreisho, E. V. Bertceva, S. Yu. Strakhov, V. S. Korepanov, A. V. Morosov, A. V. Savin*, Detection of explosives traces on documents by attenuated total reflection method, Proceedings of SPIE, 6733, 67331W.1 (2007).
- [2]. Committee on the Review of Existing and Potential Standoff Explosives Detection Techniques, National Research Council, Existing and Potential Standoff Explosive Detection Techniques (National Academies Press, N.W. Washington, DC, 2004).
- [3]. *C. M. Hodges, J. Akhavan*. The use of Fourier Transform Raman spectroscopy in the forensic identification of illicit drugs and explosives, Spectrochimica Acta, 40A, 303 (1990).
- [4]. *Patrick Hendra*, Sampling for FT Raman Spectrometry, Int. J. Vib. Spect., 1, 1.4, (1996).
- [5]. *E.V.Bertceva, S.L. Druzhinin, S.Yu.Strakhov, N.I.Pahomkova*. The analysis of techniques of processing a LIDAR signal based on the algorithms of correlation and regression analysis, Proceedings of SPIE, 6594, 65940G (2006).

SYNTHESIS BY PULSED LASER ABLATION IN Ar AND SERS ACTIVITY OF SILVER THIN FILMS WITH CONTROLLED NANOSTRUCURE

C. D'ANDREA

*Dipartimento di Fisica della Materia e Tecnologie Fisiche Avanzate, Università di Messina,
Salita Sperone 31, 98166 Messina, Italy*

P.M. OSSI

*Dipartimento di Energia & Centre for NanoEngineered MAterials and Surface & NEMAS Politecnico di Milano Via Ponzio,
34-3, 20133 Milano, Italy*

N. SANTO

*Centro Interdipartimentale di Microscopia Avanzata, Università degli Studi di Milano,
Via Celoria 26, 20133 Milano Italy*

S. TRUSSO

*Istituto per i Processi Chimico-Fisici del CNR, S.ta Sperone, C.da Papardo,
Faro Superiore, 98158, Messina, Italy.*

Thin silver films were deposited by pulsed laser ablation in a controlled Ar atmosphere and their SERS activity was investigated. The samples were grown at Ar pressures between 10 and 70 Pa and at different laser pulse number. Other deposition parameters such as laser fluence, target to substrate distance and substrate temperature were kept fixed at 2.0 J/cm², 35 mm and 297 K. Film morphologies were investigated by scanning and transmission electron microscopies (SEM, TEM). Surface features range from isolated nearly spherical nanoparticles to larger islands with smoothed edges. Cluster growth is favored by plume confinement induced by background gas. After landing on the substrate clusters start to aggregate giving rise to larger structures as long as the deposition goes on. Such a path of film growth allows controlling the surface morphology as a function of laser pulse number and Ar pressure. These two easy-to-manage process parameters control the number density and the average size of the as-deposited nanoparticles. Surface enhanced Raman scattering measurements were performed by soaking the samples in rhodamine 6G aqueous solutions over the concentration range between 1.0x10⁻⁴ M and 5.0x10⁻⁸ M. The dependence of the film SERS activity on their surface morphology is discussed.

1. INTRODUCTION

There is a growing interest toward metal nanoparticles (NPs), owing to their peculiar optical, structural and electronic properties, which depend on their size, shape and their mutual aggregation properties [1]. As a consequence metal nanoparticles have been the object of intensive theoretical and experimental research. In particular the search for production methods able to control their structural properties was extended to physical deposition methods usually adopted for the growth of bulk materials. This is the case of the pulsed laser ablation (PLA) technique. PLA is nowadays widely employed to grow a large class of materials, especially when such materials cannot be produced by alternative methods, or when PLA gives superior results in terms of material quality [2]. In conventional PLA the use of an ambient gas during the deposition process is usually required to correct an incongruent stoichiometry transfer from the target to the deposited films, as in the case of superconductor oxides [3]; or when a foreign specie, not included in the target material, is desired in the resulting material, as, for example, in the case of carbon nitride thin films produced by ablating graphite in a nitrogen atmosphere [4]. The pressure values at which deposition takes place are determined by the need to incorporate in the growing films the desired quantity of the gaseous specie, yet avoiding to lower excessively the kinetic energies of the ablated species. Concerning this it was observed that the properties of the PLA deposited materials depend in a non trivial way on the pressure of an ambient gas. The presence of a ambient gas, in fact, leads to a radical modification of the laser generated plasma expansion dynamics. In vacuum a plasma free expansion is observed while in presence of an ambient gas

plasma slowing down, plasma confinement and shock wave formation can be observed, depending on the adopted deposition conditions [5-7]. As a consequence, increasing the pressure of the ambient gas do not lead simply to a compositional change but strongly influences the film morphological properties. From this point of view inert gases can be used to control the energies of the plasma species in order to modify the morphological properties of the films without altering their stoichiometry with respect to the target one. In this work we exploit the presence of an Ar gas atmosphere to grow silver thin films by means of PLA with controlled morphology, and hence controlled optical properties. We found that controlling two experimental parameters, namely the Ar gas pressure and the number of laser shots, markedly different morphologies are obtained. In this work Ag thin films were used as active layer in surface enhanced Raman spectroscopy experiments to detect the presence of a dye molecule in aqueous solutions at concentration levels so low as 2.0x10⁻⁷ M. The morphology influence on the observed SERS activity is presented and discussed.

2. EXPERIMENT

Silver thin films were grown by means of pulsed laser ablation using a KrF excimer laser ($\lambda=248$ nm, pulse width 25 ns). The laser pulse is focused onto the target surface using a quartz lens, a pure silver target is positioned inside a vacuum chamber on a rotating holder in order to avoid craterization phenomena. In front of the target is positioned the substrate holder. The system is equipped with a mass flow controller which allows for the controlled introduction of gaseous species into the chamber. Different substrates

were used depending on the characterization technique used to study the samples: c-Si for scanning electron microscopy (SEM), 7059 Corning glass for Raman and UV-vis absorption spectroscopy and a-C covered copper grids for transmission electron microscopy analysis. A set of samples was grown at the Ar gas pressure between 10 and 70 Pa using 15000 laser shots. All the other relevant deposition parameters were kept fixed: the laser fluence to 2.0 Jcm^{-2} , the target to substrates distance to 35 mm and the substrate temperature at room temperature (RT). TEM images were acquired with a Zeiss Leo 912AB microscope while SEM imaging was performed using a Zeiss Supra 40 field ion scanning microscope. In order to test the SERS activity of the samples they were soaked into rhodamine 6G aqueous (R6G) solutions at different concentrations for 1 h and then rinsed with deionized water. Four different R6G concentrations were tested in the range between 0.1 mM and 50 nM. Raman characterization was performed using a HR-800 Jobin-Yvon micro-Raman apparatus, using the 632.8 nm line of a He-Ne laser as the exciting source. The laser power at the samples surface was kept low, about $100 \mu\text{W}$, in order to avoid R6G degradation. Raman spectra were acquired using a 10x microscope objective resulting in a probed area of about $3.2 \mu\text{m}^2$, while integration times were varied between 1 s up to 240 s depending on the signal to noise ratio. UV-vis spectra were acquired using a Lambda 900 Perkin Elmer spectrophotometer.

3. RESULTS AND DISCUSSION

In Fig.1 are reported the SEM images of the surface of the samples grown at the Ar pressures of 10 and 100 Pa. The surfaces are characterized by the presence of silver nanoparticles whose size and shape depend on the adopted Ar pressure. In particular in Fig.1 the surface of the sample deposited at 10 Pa of Ar is shown. Large nanoparticles with size larger than 35 nm are surrounded by a *depletion region* where the presence of smaller NPs can be observed. The scenario is quite different for the samples deposited at 40 and 70 Pa of Ar (Fig.2 and Fig.3). For those samples the surface is characterized by the presence of the nearly spherical NPs with typical dimensions of 10 nm at 40 Pa and of 5 nm at 70 Pa. In previous works [7,8] we studied the growth mechanism of silver thin films at deposition conditions similar to the ones adopted in this study. In particular we investigated the Ar range pressure between 10 and 100 Pa and we used different laser shot numbers in order to follow the thin film formation mechanism. Our experiments gave evidence for a two step mechanism of film formation: in the first step the presence of the Ar atmosphere induces the aggregation between the silver atoms during the plasma expansion leading to the formation of NPs; in the second step NPs landing on the substrates and having very low kinetic energies start to aggregate giving rise to larger NPs and finally to a coalesced structure characterized by the presence of an interconnected network of silver island with smooth rounded edges. The dimensions of the NPs, which form *in flight*, are determined by the Ar pressure: the higher the Ar pressure the higher the collisional rate inside the plasma which results in larger NPs [9]. The laser shot number, on the other side, drives the aggregation process *on the substrates* (at a fixed Ar pressure). At low laser shot number, isolated NPs are observed on the sample surface, at increasing laser

shot number the NP number density on the surface increases and NPs start to aggregate, initially giving rise to bigger NPs, then to even larger islands with rounded edges, until, for high enough laser shot number, a totally covered surface is achieved. The morphologies observed for the samples grown at different Ar pressures, as shown in Figs.1-3, thus refer to different stages of film formation. The sample grown at 10 Pa of Ar shows the initial stage of aggregation among several NPs which result in the large NPs observed in Fig.1. The process produces the depletion area where are evident smaller NPs: the latter formed at a later time with respect to the bigger ones that underwent a more extended aggregation process. Also the surface of the sample grown at 40 Pa of Ar shows evidence for an aggregation process; in this case all the NPs seem to have nearly the same size. A different scenario is showed by the surface of the sample grown at 70 Pa of Ar. In this case a random distribution of nearly spherical NPs is observed on the surface, without any evidence of aggregation processes.

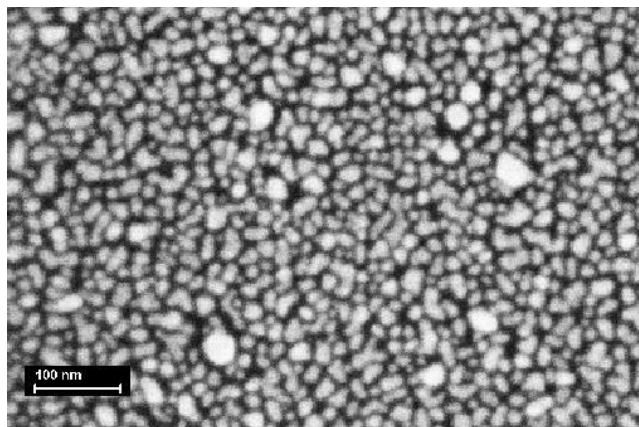


Fig.1. SEM picture of the surface of the sample grown in Ar at 10 Pa using 15000 laser shots. A magnified portion of the original SEM image is shown for a better comparison with the other images.

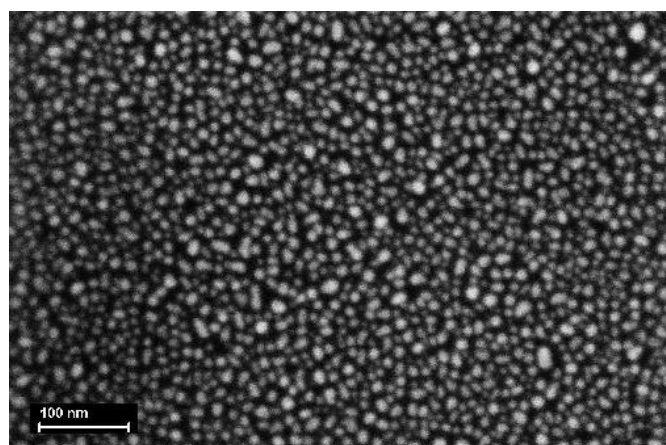


Fig.2. SEM picture of the surface of the sample grown in Ar at 40 Pa using 15000 laser shots.

The different observed morphologies lead to different optical properties. Bulk silver shows an absorption peak in the near-UV, due to the coherent oscillations of surface

electrons interacting with an external electromagnetic radiation, called surface plasmon resonance (SPR).

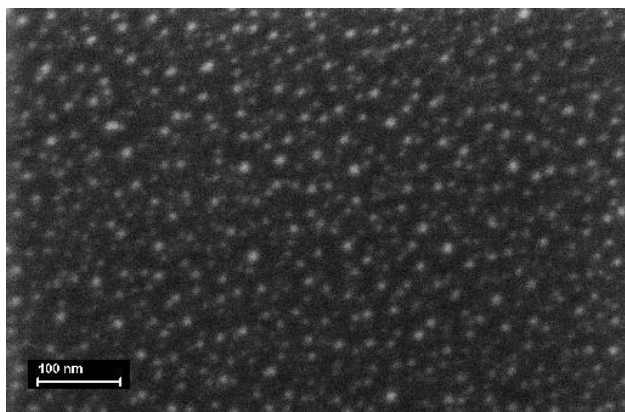


Fig.3. SEM picture of the surface of the sample grown in Ar at 70 Pa using 15000 laser shots.

When typical sizes are reduced to the nanoscale range, the SPR peak shifts to the visible region of the spectrum at about 390 nm. The position and shape of the SPR peak depend on size, shape and mutual aggregation properties of the nanostructures. In Fig.4 are shown the UV-vis absorption spectra of the samples grown at the Ar pressures of 10, 40 and 70 Pa. It can be observed that, keeping fixed the number of laser shots at 15000 and decreasing the Ar pressure from 70 Pa down to 10 Pa, the SPR position red-shifts from 482 to 558 nm while its width progressively increases from 280 nm up to more than 350 nm. As reported above, silver NPs of few nm in size show the SPR peak position near 390 nm and increasing NP size a red shift of the SPR is expected. However the shift is smaller than the observed one; on the contrary the peak position and its width markedly depend on the deviations of NP shape from spherical and on the interaction among closely spaced or aggregated NPs [1]. The SERS activity of the deposited films was tested soaking the samples in aqueous rhodamine 6G solutions at different concentrations for 1 h. In Fig.5 are reported the Raman spectra of the samples soaked in the 2.0×10^{-6} M R6G solution. The spectra are normalized to their own integration times. R6G dye Raman features can be observed at 615, 777, 1189, 1314, 1366 1513 and 1651 cm^{-1} in the spectrum of the samples deposited at 10 Pa of Ar. The 615 cm^{-1} Raman peak is due to the C–C in plane bending mode, the peak at 777 cm^{-1} is attributed to the C–H out of plane bending mode, the remaining peaks refer to aromatic stretching vibrations of C atoms. Less evident, but still visible, are the R6G Raman features in the spectra of the samples deposited at higher Ar pressures. Moreover in Fig. 5 these spectra are multiplied by a factor of 2 for the sake of clarity. Similar results were obtained from the samples soaked in the other R6G concentration solutions, with the exception of the 5×10^{-8} M one, for which no Raman activity could be detected even increasing the integration times up to 240 s.

It must be mentioned that no Raman signal can be detected from uncovered substrates, even if soaked in R6G solution at concentration of 0.1 mM.

We can compare the different SERS activity of the samples looking at the intensity of the 615 cm^{-1} peak which is discernible in all Raman spectra. The peak intensities, reported in the inset of Fig.5, are the higher, the lower the

adopted Ar pressure. In SERS experiments the observed enhancement of Raman signals depends on the excitation wavelength, the nanoparticle size and the interparticle spacing.

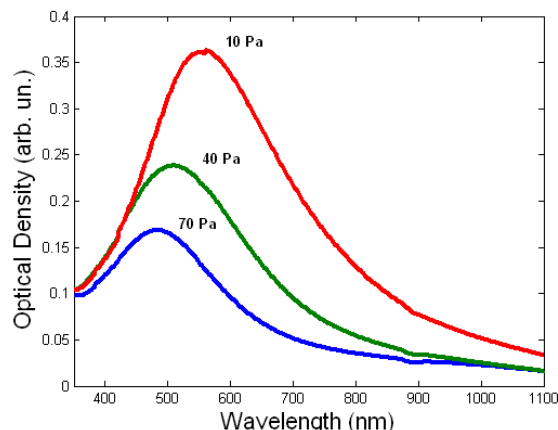


Fig.4. Absorption spectra of the samples deposited at different Ar pressures and with 15000 laser shots.

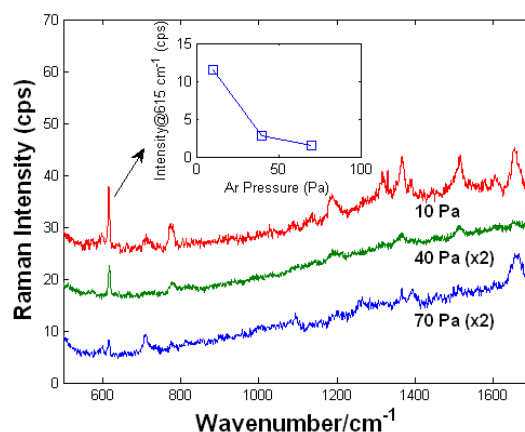


Fig.5. Raman spectra of the samples deposited at different Ar pressures with 15000 laser shots. Spectra collected from the 70 and 40 Pa deposited samples are multiplied by a factor of 2. In the inset the intensity of the Raman peak at 615 cm^{-1} vs the Ar pressure.

The increase of the average NP number density and size observed as the Ar pressure is decreased from 70 Pa down to 10 Pa corresponds to a decrease of the mean interparticle distance and can lead to mutual contact of adjacent NPs. The formation of ‘hot spots’ at the junction site between NPs [10-11] can result in very high enhancement factors. Alternatively, coupling of the excitation wavelength to the surface plasmon resonance of the two samples can explain their different activity. The SPR peak position, in fact, shifts from 482 to 558 nm so that a higher enhancement factor is expected for the samples showing a stronger absorption at the laser excitation wavelength of 633.8 nm .

4. CONCLUSIONS

In conclusion we described a method to grow arrays of silver NPs whose optical properties can be controlled through an easily accessible deposition parameter such as the Ar gas pressure. The deposited thin films present a clear SERS activity that depends on their optical and morphological properties: the detection of R6G molecules can be performed

in aqueous solution at concentration level as low as 5.0×10^{-7} M. The growth method is attractive because the deposition takes place at room temperature without imposing any restriction to the chemical nature of the substrates.

Noticeably, it can be further improved owing to the fact that only a limited range of deposition parameters was explored till now.

-
- [1]. *K. L. Kelly, T. A. Jensen, A. A. Lazarides, G. C. Schatz* in *Metal Nanoparticles: Synthesis, Characterization and Applications*, D. L. Feldheim, C. A. Foss Jr. eds., 2002, (Dekker, New York).
- [2]. *G.K. Hubler* in *Pulsed laser deposition of thin films*, chapt. 13, D.B. Chrisey, H.K. Hubler eds., 1994 (Wiley, New York).
- [3]. *A. Gupta*, *J. Appl. Phys.*, 73, 7877 (1993).
- [4]. *S. Trusso, C. Vasi, F. Neri*, *Thin Solid Films*, 355, 219 (1999).
- [5]. *D. B. Geohegan*, *Appl. Phys. Lett.* 60, 2732 (1992).
- [6]. *J. Gonzalo, C. N. Afonso, I. Madariaga*, *J. Appl. Phys.*, 81, 951 (1997).
- [7]. *E. Fazio, F. Neri, P. M. Ossi, N. Santo, S. Trusso*, *Laser Part. Beams*, 27, 281, (2009).
- [8]. *E. Fazio, F. Neri, P. M. Ossi, N. Santo, S. Trusso*, *Appl. Surf. Sci.*, 255, 9676 (2009).
- [9]. *A. Bailini, P.M. Ossi*, *Europhys. Lett.* 79, 35002-1 (2007).
- [10]. *H. Xu, J. Aizpurua, M. Kall, P. Apell*, *Phys. Rev. E*, 62, 4318 (2002).
- [11]. *A. M. Michels, J. Jiang, L. E. Brus*, *J. Phys. Chem. B*, 104, 11965 (2000).
- [12]. *E. C. Le Ru, P. G. Etchegoin*, *Chem. Phys. Lett.*, 396, 393 (2004).

GROWTH FEATURES AND STRUCTURE OF THE EPITAXIAL FILMS OF GaSe, InSe COMPOUNDS IN CORRELATION WITH PHYSICAL PROPERTIES

E.Yu. SALAYEV, H.R. NURIYEV

*Institute of Physics of the Azerbaijan National Academy of Sciences,
AZ-1143, H.Javid av. 33, Baku, Azerbaijan*

Research of growth features and structure of the epitaxial films of GaSe, InSe compounds have been carried out in correlation with their physical properties. The films were obtained by the molecular beam condensation method on various substrates. Optimum conditions of reception amorphous, polycrystalline, oriented and epitaxial films of the specified compounds have been determined. Correlation between structural perfection and electrophysical parameters for received epitaxial films has been established. It is shown that depending on temperature of a source and a substrate it is possible to receive a film with various crystal structure and electrophysical parameters.

Layered GaSe, InSe semiconductors widely attract attention of researchers. Numerous works [1-10] are devoted to research of physical properties of these compounds. Interest to studying physical properties of the specified layered semiconductors is caused by features of their crystal structure.

The elementary cell contains two and more number of identical layers with various atoms in them. Inside the layers bonds between atoms is carried through the forces of ionic-covalent character, at the same time bond between the next layers – by the Van-der-Vaals forces. It is necessary to note that physical properties of A^3B^6 compounds since 1960 were investigated in the Institute of Physics of the Azerbaijan NAS together with a number of other research centers. In 1963 in GaSe compound induced radiation is revealed and in 1972 effective nonlinear optical properties, effects of switching and memory, etc. have been revealed. It is of big interest the found out by authors of the work [9] quantum oscillations in gallium selenide and results on exciton dynamics. Effective nonlinear optical properties of the селенида gallium selenide have been found out [2]. In [10] attempt of generalization of a material available in the literature devoted to researches of the dynamic and static nonlinear effects observed at interaction of coherent radiation with layered crystals of gallium selenide type was carried out.

These researches were carried out on massive single crystals of the specified compounds. For modern electronics

more perspective are their epitaxial films. In this connection, in the given work research of features of growth and structure of epitaxial films of GaSe, InSe compounds received on various substrates are carried out in correlations with their physical properties.

The structure of the films were controlled by the electron-diffraction method. Samples for electron-diffraction researches in thin film type were prepared in vacuum 10^{-4} Pa by the molecular beam condensation method from beforehand synthesized GaSe, InSe alloys.

Evaporator source was Knudsen cell, the cylinder made of especially pure graphite with two fuses heated by a current and with an aperture in the center in diameter of 0.1 mm. The temperature of the evaporator and a substrate was controlled using chromel-copel thermocouples. As substrates celluloid films and fresh chips of BaF_2 single crystals, as well as mica were used

Samples for research of physical properties have been received by use of a special mask during the growth process, made of stainless steel.

Electron-diffraction researches have shown that condensation of GaSe, InSe on the celluloid substrates which are taking place at room temperature was invariable accompanied by formation their amorphous пленок (Fig. 1, a, b).

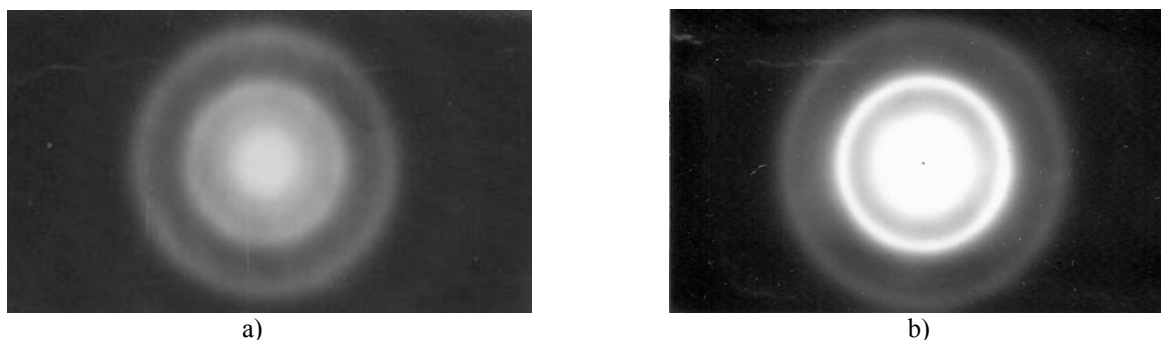


Fig. 1. Electron-diffraction pattern of the amorphous films: a) GaSe, b) InSe.

To avoid oriented influence of single crystal substrates BaF_2 substrates and mica, as well as possible reflection of molecules from their hot surface during sublimation, the special condition was created and substrates was supported at room temperature. By this way on the specified single

crystalline substrates also possible to prepare above-stated amorphous films of the researched compounds.

Annealing of the received films within 1 hour at $t \approx 200^\circ C$ has not changed a pattern, they remained amorphous. This result is in the consent with the data [11].

It is established by as that amorphous GaSe phase in conformity with [11] extremely stable at room temperature. By the authors of work [12] the structure of this phase is determined and it was shown that in the first coordination spheres at amorphous GaSe there is no conformity with a lattice of the crystal phase. At the same time their physical properties, i.e. conductivity, energy of activation, thermoe.m.f. and others are characteristic for crystal substances.

Thin films of GaSe, InSe compounds, received on BaF₂ single crystalline substrates and mica taking place at $\geq 200^{\circ}\text{C}$ have polycrystalline structure. On fig. 2, a, b electron-diffraction pattern of the films received on BaF₂ single crystalline substrates are presented. The received films crystallize in hexagonal lattice with parameters:

$$a=3,74 \text{ \AA}; c=15,89 \text{ \AA} \text{ for GaSe in conformity [11],}$$

$$a=4,04 \text{ \AA}; c=16,90 \text{ \AA} \text{ for InSe in conformity [13].}$$

Calculation of the presented electron-diffraction pattern shows that small crystals of these compounds on the specified substrates grow by (001) plane and partial off-orientation of small crystals is observed, therefore only lines with hk0 indexes appear on electron-diffraction patterns.

It is shown that at annealing temperatures higher $\geq 300^{\circ}\text{C}$ with enough fair speed a crystallization of amorphous films of the above-stated compounds occurs. Thus depending on annealing temperature for the films, more or less fast transformation of an amorphous phase into an oriented crystal phase is observed in them.

Rise in temperature of substrates to $\geq 350^{\circ}\text{C}$ results in growth of epitaxial films of the specified compounds (Fig. 3, a, b). On this electron-diffraction patterns as against above-stated ones, vertically located reflexes with hexagonal the symmetry are observed, testifying reception of structurally perfect epitaxial films of the specified compounds.

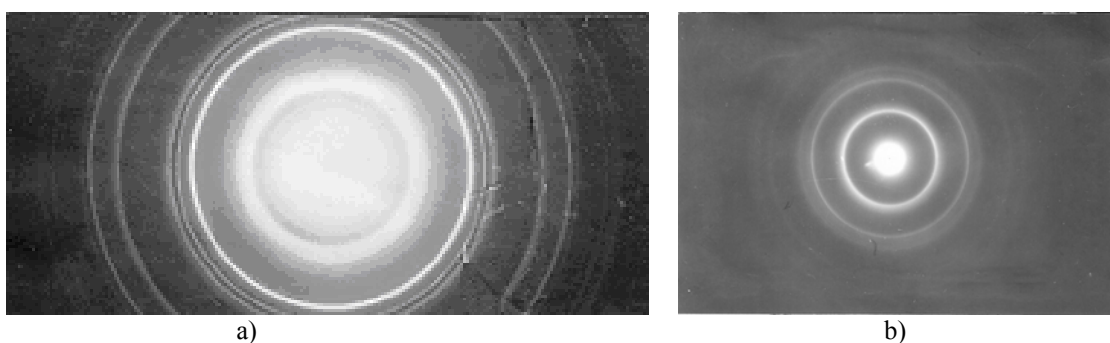


Fig. 2. Electron-diffraction pattern of the polycrystalline films: a) GaSe, b) InSe.

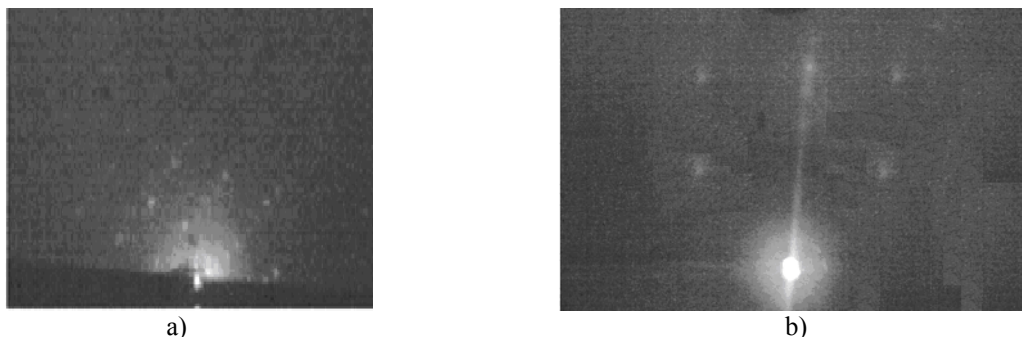


Fig. 3. Electron-diffraction pattern of the epitaxial films: a) GaSe, b) InSe.

Structurally perfect epitaxial GaSe film are received at temperatures of source $T_{\text{source}} = 950 \div 980^{\circ}\text{C}$ and substrates $T_{\text{substrate}} = 350 \div 380^{\circ}\text{C}$; InSe at $T_{\text{source}} = 980 \div 1100^{\circ}\text{C}$ and $T_{\text{substrate}} = 200 \div 300^{\circ}\text{C}$. It is shown that with increase of condensation speed and substrate temperature, thickness of the epitaxial layer grows and perfection of the film structure improves.

It is necessary to note that the samples received in such a way differed from each other by the color: the some samples had a brown shade, and the some samples - grey -steel shine. Samples with a brown shade give diffuse electron-diffraction patterns. Electron-diffraction patterns for samples of grey-steel color have shown presence of the oriented layer. Such distinction of samples is connected, probably, with non-

uniform evaporation of the initial material, resulting in other arrangement of packages in this structure.

Thus, optimum conditions of reception of the epitaxial films with high crystal perfection are determined, and it is shown that depending on temperature of the source and the substrate it is possible to receive films of GaSe and InSe compounds with various crystal structure.

From Hall measurements for received epitaxial films values of electrophysical parameters have been calculated.

The calculated values of these parameters: at $T=77 \text{ K}$ for InSe films $n=(1 \div 1,2) \cdot 10^{12} \text{ cm}^{-3}$, $\mu=(4,6 \div 4,7) \cdot 10^2 \text{ cm}^2 \text{V}^{-1} \text{s}^{-1}$ and for GaSe films $p=(0,9 \div 1,0) \cdot 10^{12} \text{ cm}^{-3}$, $\mu=(5 \div 6) \cdot 10^2 \text{ cm}^2 \text{V}^{-1} \text{s}^{-1}$, are in a good agreement with the literary data.

-
- [1]. *G.A. Akhundov*. Electro-luminescence in GaSe // Optics and spectroscopy, 1965, v.18, No. 4, p. 747.
- [2]. *G.B. Abdullayev, E.Yu. Salayev et al.* GaSe - a new effective material for nonlinear optics // JETP Letters, 1972, v.16, No.3, p. 130-133.
- [3]. *V.P. Mushinsky, M.I. Karaman*. Optical properties of gallium and indium chalcogenides // Kishinev, 1973, p. 213.
- [4]. *G.B. Abdullayev, G.L. Belenkiy, E.Yu. Salayev, R.A. Suleymanov, V.H. Khalilov*. Research of the edge luminescence in GaSe single crystals // FTT, 1974, v.16, No. 1, p. 19-24.
- [5]. *G.B. Abdullayev, E.Yu. Salayev, V.M. Salmanov*. Interaction of the laser radiation with A³B⁶ type semiconductors. Baku: Elm, 1979. 137 p.
- [6]. *G. Gouskov, J. Camassel, L. Gouskov*. Growth and characterization of 3-6 layered crystals like GaSe, GaTe, InSe, GaSe_{1-x}Tex and Ga_xIn_{1-x}Se // Progr. Crystal Growth and Charact, 1982, v.5, pp.323-413.
- [7]. *M.S. Brodin, I.V. Blonsky*. Exciton processes in layered crystals. Kiyev: Naukova Dumka, 1986, 256 p.
- [8]. *G.L. Belenkiy, E.Yu. Salayev, R.A. Suleymanov*. Deformation phenomena in layered semiconductors // UFN, 1988, v.155, No. 1, pp. 89-127.
- [9]. *K.R. Allahverdiyev, E.Yu. Salayev et al.* Quantum oscillations under influence of laser pulses in layered ε - GaSe // JETP Letters, 1990, v.51, No.3, pp. 145-147.
- [10]. *K.R. Allahverdiyev, E.Yu. Salayev* Dynamic and static nonlinear effects in layered gallium selenide type crystals. Baku: Elm, 1993, 230 p.
- [11]. *L.I. Tatarinova, A.A. Auleytner, Z.G. Pinsker* Electron-diffraction research of GaSe crystal structure // Crystallography, v. I, No. 5, 1956.
- [12]. *L.I. Tatarinova*. Electron-diffraction research of amorphous GaSe// Crystallography, 1956, v. I, No. 5.
- [13]. *S.A. Semiletov* Electron-diffraction definition of InSe structure // Crystallography, 1958, v.3, No.3, pp. 288-292

SPECIFIC CHARACTER OF THE ^{119}Sn THIN FILMS GROWTH ON AMORPHOUS Si BY THE CBPLD METHOD

V.V. ROCHEVA, E.V. KHAYDUKOV, O.A. NOVODVORSKY,
O.D. KHRAMOVA, V.Ya. PANCHENKO

*Institute on Laser and Information Technologies of the Russian Academy of Sciences (ILIT RAS),
1 Svyatoozerskaya St., 140700 Shatura, Moscow Region, Russia*

The research of the ^{119}Sn thin films growth on amorphous Si that is important for the multilayer periodical spin-tunnel nanostructures creation have been investigated in this paper. The ^{119}Sn mono-isotopic thin films on the silicon substrates (100) had been received by crossed-beam pulsed laser deposition method (CBPLD). Similarly the [Fe/Si/Sn/Si] multilayered periodical structures have been deposited. The received samples were investigated by atomic-force microscopy, electronic microscopy and X-ray reflectometry methods. It has been established that at ^{119}Sn film thickness up to 3 nm it is possible to received atomic-smooth surfaces with 0.5 nm roughness.

1. INTRODUCTION

Using an electron spin properties in data transmission devices and storage devices is rather actual for one of the important directions of the materials nanotechnology – spintronics [1-3]. From the fundamental physics point of view main problems here are electron polarization mechanisms, polarized electrons injection from ferromagnetic in semiconductors through interface border, electron mean free path with conservation of spin polarization (polarization dispersion), relaxation time of domains magnetization. One of precision research methods of such processes is Mossbauer spectroscopy which allows registering spatial distribution of spin polarization via a superfine interaction by the introduction of the probe isotopes (^{57}Fe , ^{119}Sn , ^{151}Eu , etc.) as an interlayer or directly in a semiconductor layer [4]. As control samples the [Fe/Si/Sn/Si] multilayer films of type ferromagnetic metal – the semiconductor with ^{57}Fe and ^{119}Sn Mossbauer isotopes are

used. It is possible to measure an ultrathin field and to define degree of electron polarization and its penetration depth placing Mossbauer atoms-probes (for example diamagnetic ^{119}Sn) on distance from interface border.

For the qualitative multilayer structures production (with distinguished and smooth interface border) research of the specific character of the ^{119}Sn thin films growth on amorphous Si has been done. The crossed-beam pulsed laser deposition method (CBPLD) in the high vacuum conditions was used for the thin films deposition [5-8].

2. EXPERIMENTAL SETUP

Experimental setup scheme is presented on fig. 1. Deposition was performed in the vacuum chamber 9 at 10^{-6} Torr residual pressure received by turbo-molecular pump 11, the ^{119}Sn targets 4 were ablated by $\lambda=1.06 \mu\text{m}$ laser radiation 1 at $5 \cdot 10^8 \text{ W/cm}^2$ power density on the targets. Pulse repetition frequency was equal 10 Hz.

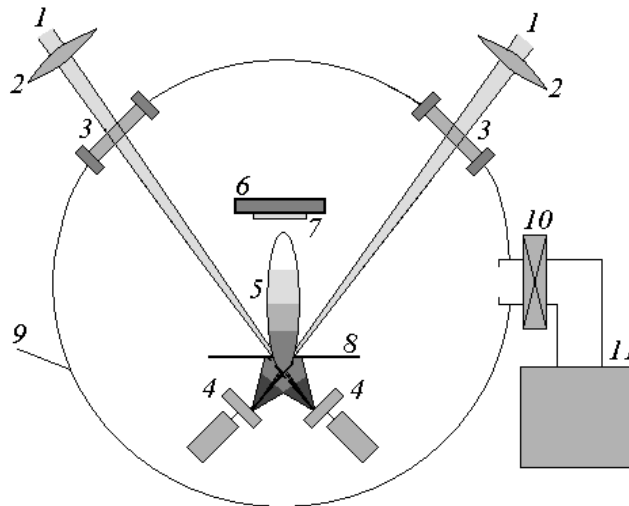


Fig. 1.1. YAG:Nd³⁺ laser radiation, 2 – focusing lenses, 3 – window of the vacuum chamber, 4 - targets, 5 – plasma plume, 6 – substrate heater, 7 – substrate, 8 - diaphragm, 9 - vacuum chamber, 10 - vacuum seal, 11 – turbo-molecular pump.

3. RESULTS AND DISCUSSION

The (100) silicon for microelectronics was used as substrates. The roughness of the substrates surface was 1 nm. Preliminary on the silicon substrate (from which the layer of natural oxide did not remove) the 40 nm amorphous silicon film was deposited. After the amorphous silicon deposition the surface roughness made 0.5 nm [9]. Surface quality was

defined by the atomic-force microscope (AFM). Various thickness ^{119}Sn films were deposited on received amorphous Si surface without of unvacuumization procedure.

It has been established that at ^{119}Sn film thickness up to 3 nm were received atomic-smooth surfaces with 0.3-0.5 nm roughness (fig. 2).

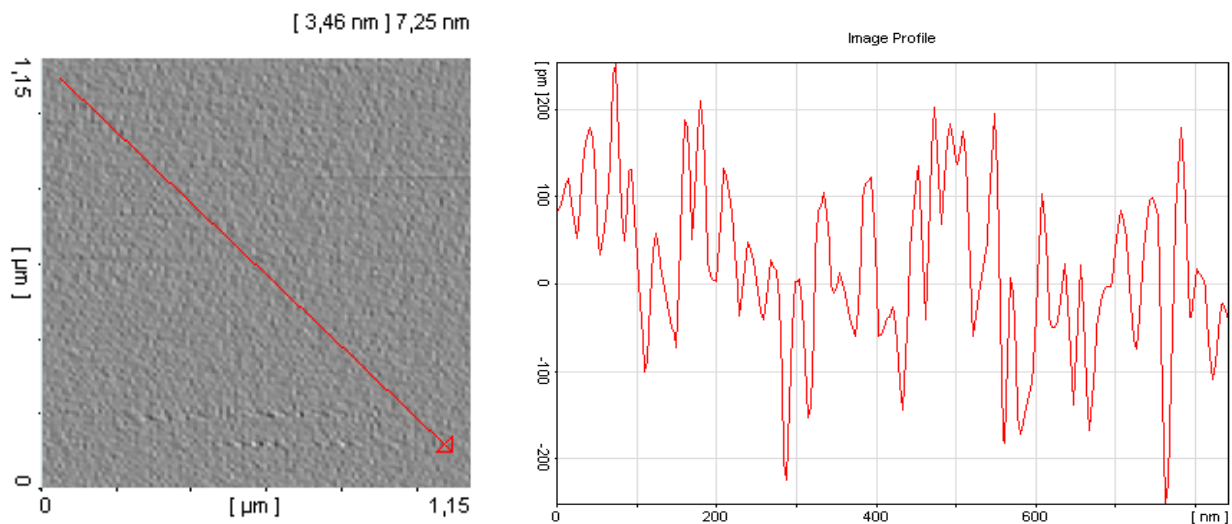


Fig. 2. AFM image and surface profile of the 3 nm thickness ^{119}Sn film.

At the thickness increase of the ^{119}Sn deposited films to 6 nm qualitative change of the surface morphology was observed. In fig. 3 it is visible that on the film surface start to be formed small local mountainous formations by separate groups with the lateral sizes about 50 nm and height to 20 nm. Thus the flat surface roughness of the film remained unchanged. At thickness increase of the deposited films to 9

nm groups started to unite and their height increased to 50 nm.

It is possible to connect the appearance of such changes with films flaking but film surface observation with the course of time hasn't revealed morphology changes though in the films flaking case such changes should increase.

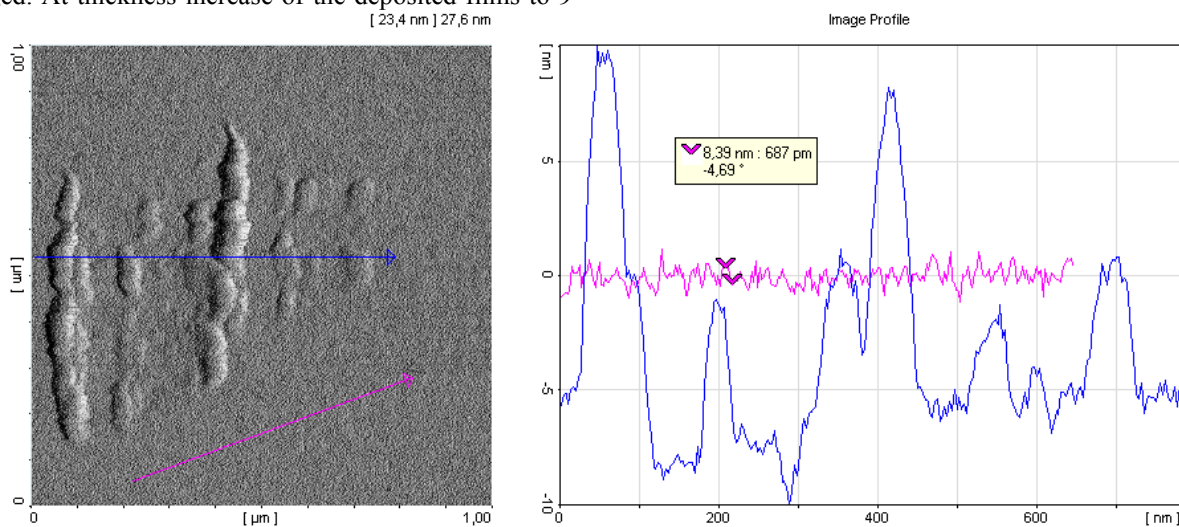


Fig. 3. AFM image and surface profile of the 6 nm thickness ^{119}Sn film.

In the 20 nm thickness films surface quantitative and qualitative changes increase even more. In fig. 4 it is visible that quantity of the mountainous formations increase and the height of some from them reaches 80 nm at 20 nm film thickness on flat areas.

At the films thickness increase to 40 nm all surface got close-packed granules character. In fig. 5 it is visible that granules height makes from 20 to 30 nm and lateral sizes makes 80-90 nm.

At the films thickness increase to 100 nm the granules size increases and on the average makes 100 nm. Fig. 6 shows scanning electronic microscope image of such film surface. On fig. 6 insert demonstrates high resolution SEM image of the film area etched to the substrate on which separate granules are clearly visible.

Similar research of the film surface morphology change with the thickness increase has been conducted at the amorphous silicon thin films deposition. Research hasn't revealed specific character of the films growth with increase in the film thickness. The surface roughness of the received amorphous silicon films of on the average improved to 0.5 nm at the 1 nm initial roughness of the single-crystalline silicon (100) substrate surface. In fig. 7 demonstrated AFM research results of 20 nm thickness amorphous silicon film. Research of the Fe thin films surface morphology change with the thickness increase also hasn't demonstrated specific character of the films growth with increase in the film thickness.

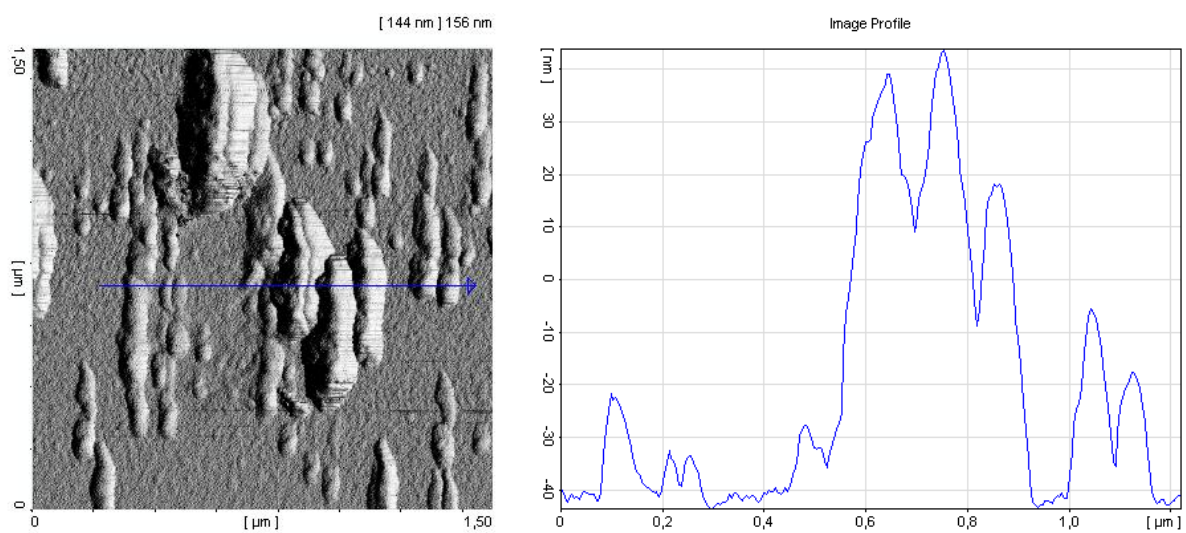


Fig. 4. AFM image and surface profile of the 20 nm thickness ^{119}Sn film.

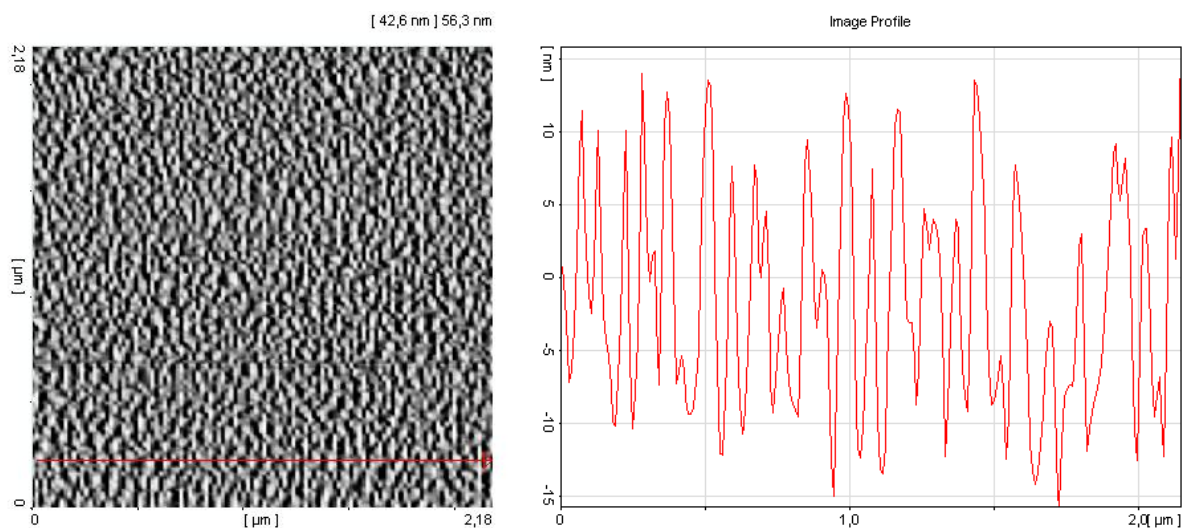


Fig. 5. AFM image and surface profile of the 40 nm thickness ^{119}Sn film.

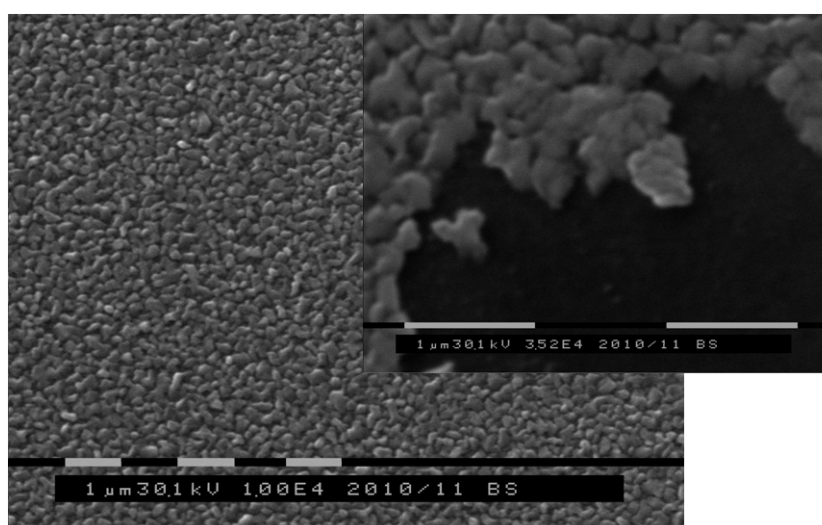


Fig. 6. SEM image of the 100 nm thickness ^{119}Sn film. On insert demonstrates the film area etched to the substrate on which separate granules are clearly visible.

SPECIFIC CHARACTER OF THE ^{119}Sn THIN FILMS GROWTH ON AMORPHOUS Si BY THE CBPLD METHOD

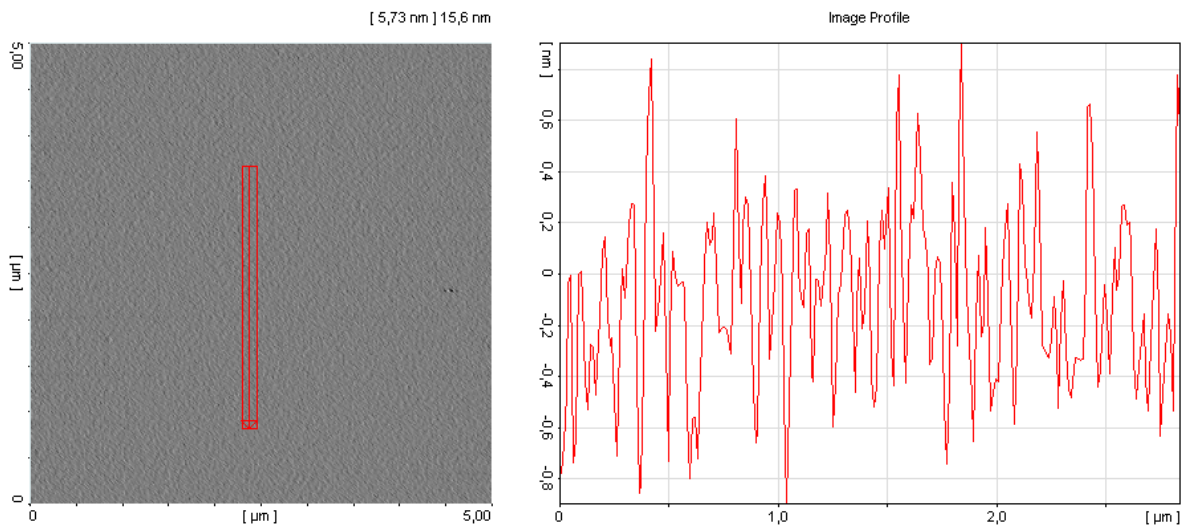


Fig. 7. AFM image and surface profile of the 20 nm thickness amorphous silicon film.

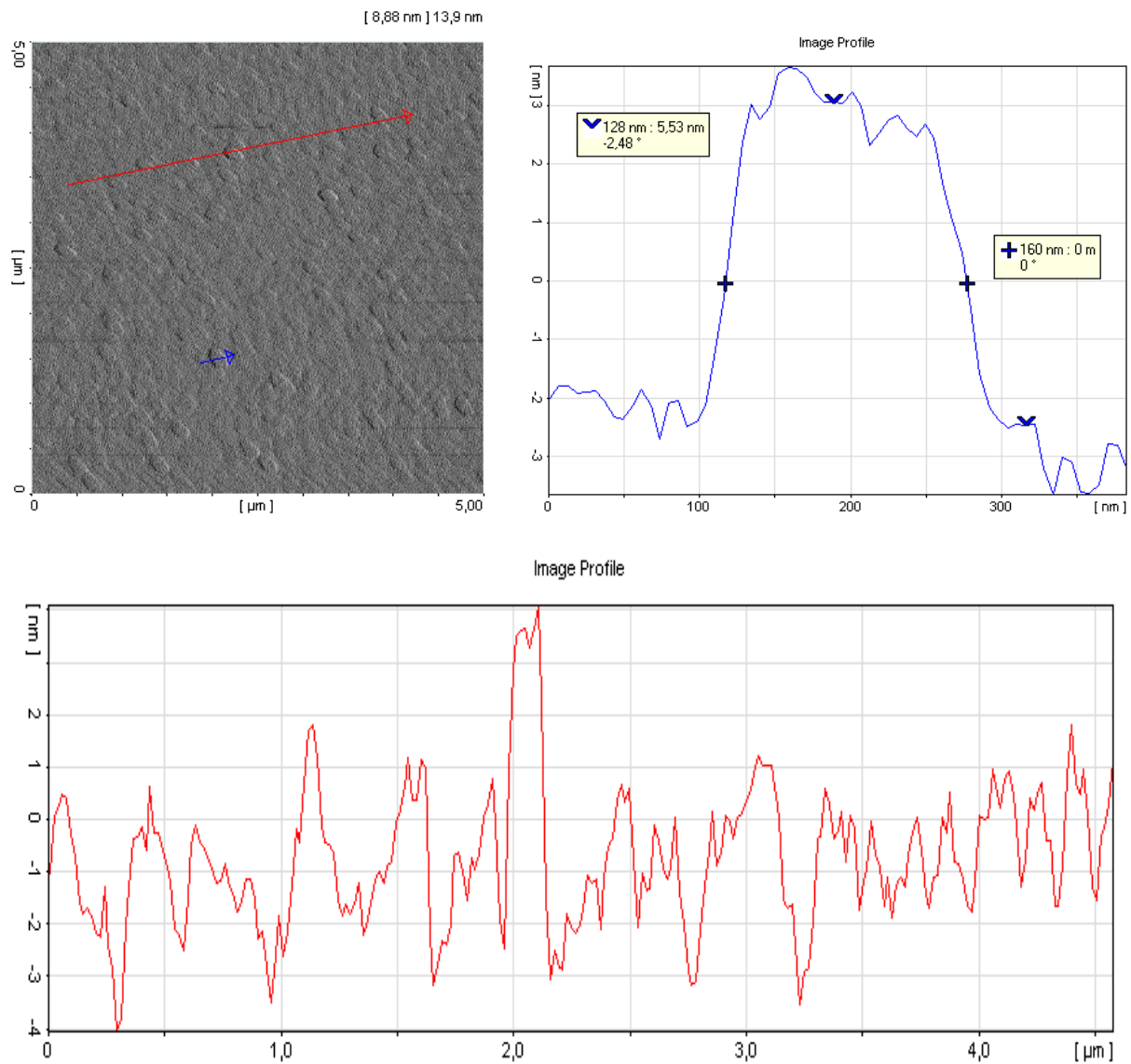


Fig. 8. AFM image and surface profile of the [Fe/Si/Sn/Si] multilayer periodical structure (Fe-10 nm, Si-5 nm, Sn-5 nm, Si-5 nm (3 periods)).

The [Fe/Si/Sn/Si] multilayer periodical structures with various layers thickness have been deposited subject to results of the specific character of the Fe, Si and ¹¹⁹Sn films growth research

Fig. 8 shows the structure with Fe-10 nm, Si-5 nm, Sn-5 nm, Si-5 nm (3 periods) layers thickness. It is visible that the surface is covered by areas with lateral sizes about 5 nm and width to 160 nm. As Si and Fe don't show surface morphology changes at the deposition observation of such structures on the surface can be connected only with the specific character of the ¹¹⁹Sn thin films growth.

At the multilayered structure deposition with Fe - 9 nm, Si - 3 nm, Sn - 3 nm, Si - 3 nm (6 periods) layers thickness

the surface was smooth without presence of any formations (fig. 9), the average roughness the surface according to AFM data made 0.5 nm. It has been established that the interface layers roughness also made from 0.2 to 0.5 nm at research of the given sample by the X-ray reflectometry method.

According to the X-ray reflectometry data at the entering into multilayer structure layers thickness decrease to Fe – 3 nm, Si – 2 nm, Sn – 1 nm, Si – 2 nm (6 periods) the interface between Fe and Si appears indistinct that is possibly caused by the Fe and Si interaction with formation of iron silicide (fig. 10). It is confirmed by agreement theoretical reflectometrical curve shape with experimental curve shape at replacement pure iron on the FeSi₃ silicide in calculations.

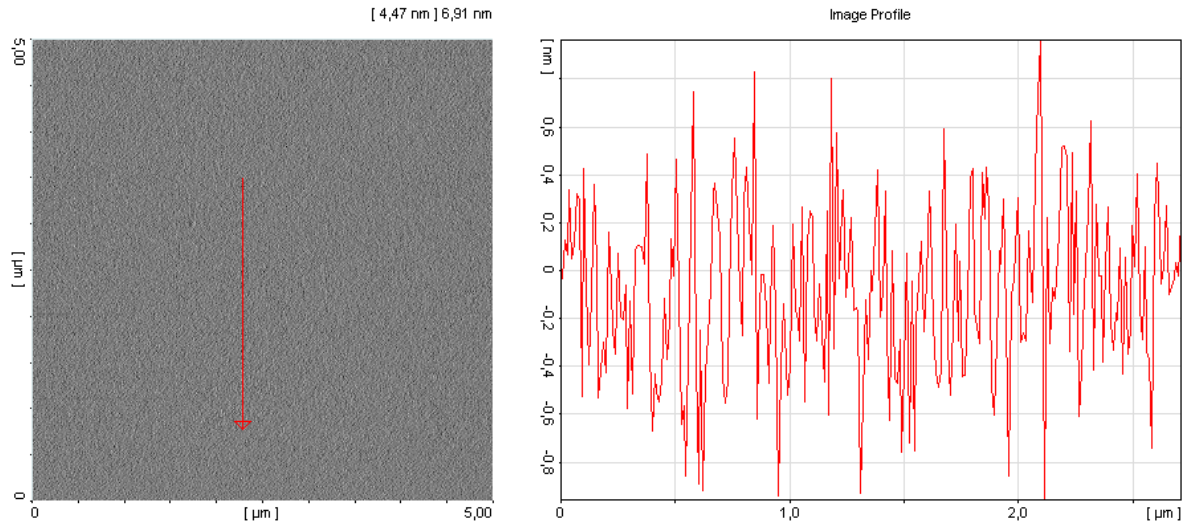


Fig. 9. AFM image and surface profile of the [Fe/Si/Sn/Si] multilayer periodical structure (Fe - 9 nm, Si - 3 nm, Sn - 3 nm, Si - 3 nm (6 periods)).

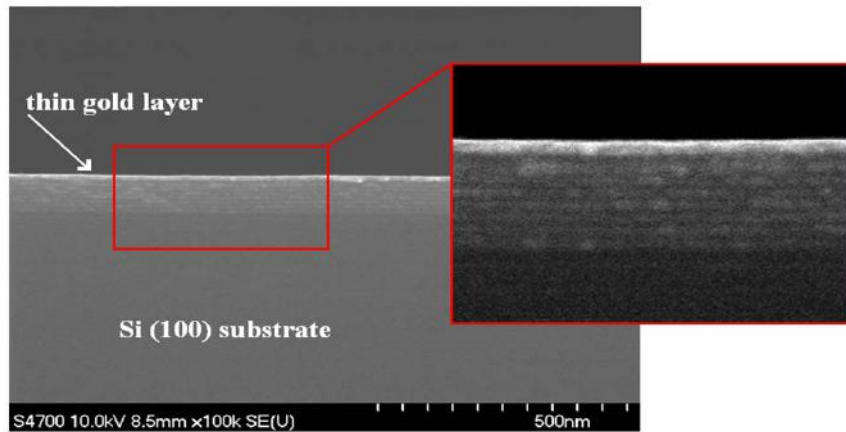


Fig. 10. SEM cross-section image of the [Fe/Si/Sn/Si] multilayer periodical structure (Fe – 3 nm, Si – 2 nm, Sn – 1 nm, Si – 2 nm (6 periods)).

The received samples of spin-tunnel nanostructures with various layers thickness will be used for the further studying by the magnetometry and Mossbauer spectroscopy methods with attraction of the electric, x-ray and other measurements results in the wide temperature and magnetic field ranges. By these results the specific nanodimensional systems properties information such as degree of electron polarization and its penetration depth through interface border, size and energy of anisotropy nanoparticles distributions, relaxation time of magnetization will be received.

4. CONCLUSIONS

The research of the specific character of the ¹¹⁹Sn thin films growth on amorphous Si by the CBPLD method has been done for the [Fe/Si/Sn/Si] multilayer periodical spin-tunnel nanostructures of type ferromagnetic metal – the semiconductor with the ¹¹⁹Sn Mossbauer isotope production.

It is established that at ¹¹⁹Sn film thickness up to 3 nm were received atomic-smooth surfaces with 0.3-0.5 nm roughness. At the thickness increase of the ¹¹⁹Sn deposited films to 6 nm qualitative change of the surface morphology not connected with films flaking was observed. On the film surface were formed small local mountainous formations by separate groups with the lateral sizes about 50 nm and height

to 20 nm. At the films thickness increase to 100 nm all surface got close-packed granules character with 100 nm on the average granules size.

The [Fe/Si/Sn/Si] multilayered periodical structures with various layers thickness are demonstrated. It is established that at the ¹¹⁹Sn layers thickness from 1 to 5 nm it is possible to receive qualitative multilayered structures (with

distinguished and smooth interface borders) suitable for Mossbauer spectroscopy as control samples.

5. ACKNOWLEDGMENTS

Work is executed with support of RFBR grants 09-02-01298, 09-08-00291, 09-02-12108, 09-07-12151.

-
- [1]. *T. Dietl*, Lecture Notes. **712**, 1 (2007).
- [2]. *J.F. Gregg, I. Petej, E. Jouguelet, C. Dennis*, J. Phys. D: Appl. Phys. **35**, R 121 (2002).
- [3]. *A.V.Ognev, A.S.Samardak*, FEB RAS bulletin. **4**, 70 (2006).
- [4]. *M. A. Chuev*, JETP Letters. **83**, 572 (2006).
- [5]. *A. Gorbunov, A. Tselev, W. Pompe*, Proceedings of SPIE. **3688**, 351 (1999).
- [6]. *A. Gorbunov*, Proceedings of SPIE. **6106**, 61060U (2006).
- [7]. *R. Eason*, Pulsed laser deposition of thin films: Applications-LED growth of functional materials (Hoboken. N.J.:Wiley-Interscience, 2007).
- [8]. *M.D. Strikovskiy, E.B. Klyuenkov, S.V. Gaponov, J. Schubert, C.A. Copetti*, Appl. Phys. Lett. **63** (8), 1146 (1993).
- [9]. *V.V. Rocheva, E.V. Khaydukov, O.A. Novodvorsky, V.Ya. Panchenko*, Proceedings of II All-Russian scientific school of young scientists «The concentrated energy streams in the nanosystem, materiel and living system industry», Moscow, Russia, 2009 (MIEM), pp. 290-294.

ULTRAFAST SINGLE-PHOTON IMAGE DIAGNOSTICS SENSORS WITH APD ARRAYS FOR INDUSTRIAL AND BIO APPLICATIONS

EDOARDO CHARBON^{1,2} AND SILVANO DONATI³

¹ *Quantum Architecture Group (AQUA), EPFL, 1015 Lausanne, Switzerland*

edoardo.charbon@epfl.ch

² *Circuits and Systems Group, TU Delft, 2600 AA Delft, The Netherlands*

³ *Dipartimento di Elettronica, Università di Pavia, 27100 Pavia, Italy*

silvano.donati@unipv.it

We review recent advances in the field of ultrafast imagers with single-photon detection capability. These sensors in general are capable of photon counting and time-of-arrival analysis, thus enabling an increasingly broad range of diagnostics techniques. The current trend is to migrate the designs to increasingly smaller feature sizes and to push integration to new highs, so as to enable placing more functionality and more processing at the pixel level. Examples of these new trends are given in the context of industrial and bio applications.

1. INTRODUCTION

In recent years, there has been increasing activity in the acceleration of acquisition and readout speed in imaging technology [1]. Among the reasons for this trend, there has been the creation of new biomedical and/or improved diagnostics techniques based on optical imaging. The emergence of more powerful and faster light sources has only accelerated this trend and placed an increasing burden on conventional image sensors.

Image sensors capable of one million frames-per-second (fps) in bursts of over 100 subsequent frames have been proposed for charge-coupled devices (CCDs) [2],[3]. CMOS active pixel sensor (APS) chips have achieved over 10,000fps in continuous mode in sub-megapixel format and more recently up to 100Mfps but only on small line sensors [4].

Time-correlated imaging has become one of the most influential techniques currently available to scientists and doctors for research and diagnostics purposes. In order to take advantage of the potential of this technique at its best, it is necessary to detect photons in small quantities and at high time correlations, typically of the order of tens or hundreds of picoseconds. Thus, image sensors for time-resolved applications should in principle exceed 10Gfps. To our knowledge, imagers with this speed, especially in continuous mode, do not exist and are not likely to be developed in the next few years.

As an alternative, scientists have developed sensors capable of detecting the arrival of single or multiple photons with picosecond resolution within a longer frame of perhaps a few tens of microseconds. There exist many non-solid-state implementations of such sensors, most notably photomultiplier tubes (PMTs) and microchannel or multichannel plates (MCPs).

The operating principle of a PMT is well known [5]. Photoelectrons emitted by the input sensitive surface – the photocathode – are accelerated to a first dynode where they are multiplied by secondary emission. Secondary electrons become the primary of next stage and multiplication through a number of stages of the dynode chain allows the gain go up to 10^8 , so that single detected photon gives a sizeable current spike at the anode, easily counted.

The main limitation of PMTs is their size and the high voltage required - up to a few thousand volts. In addition, they are basic single-point detector not easily partitioned to multi-point operation.

A solution to this problem is the use of a MCP, a device in which photoelectron multiplication is achieved inside a micro-channel [5], much more compact than a dynode chain and already sectioned in a large number of individual pixels. Photoelectrons emitted by the photocathode are multiplied by the MCP and then readout by a CCD used in place of a normal anode.

Unfortunately, MCPs are still not solid-state devices and require deep vacuum as well as high bias voltages. In addition, though the sensitivity to single-photons may be achieved, the speed of detection is limited by the reaction time of the phosphor screen and of the CCD. Nonetheless over the years, PMTs and MCPs have become the sensors of choice in many biomedical applications [6].

Solid-state alternatives to these sensors have been known for some time. For instance, silicon avalanche photodiodes (SiAPDs) have been studied since the 1960s [7] and have recently become a serious competitor to MCPs and PMTs. In SiAPDs, carriers generated by the absorption of a photon in the p-n junction, are multiplied by impact ionization in the lattice thus producing an avalanche. The resulting optical gain is usually in the hundreds. The main drawback of these devices however, is a relatively complex amplification scheme and/or complex ancillary electronics. In addition, specific technologies are often required. Nevertheless, these devices offer flexible, versatile, and relatively low-cost solutions to imaging where sensitivity, low noise, and high time resolution are needed.

More recently, new CMOS compatible APDs have emerged, with lower operating voltages and a high potential of integration. CMOS APDs can operate in linear or proportional mode as well as in Geiger mode. In the latter mode of operation they are known as single-photon avalanche diodes (SPADs). In a SPAD the optical gain is virtually infinite, thus it enables the detection of single photons. The time resolution is generally in excess of 100ps while the detection cycle, dominated by the dead time of the

device, is generally of the order of 10 to 100ns. Thanks to the high level of integration possible in these devices, large arrays of single-photon detectors may be built while unprecedented levels of parallelism may be achieved.

In this paper, we focus on these devices and we review some of the latest results achieved using SPADs and SPAD arrays.

2. SINGLE-PHOTON DETECTION IN CMOS

If biased above breakdown, a p-n junction can operate in so-called Geiger mode. In Geiger mode of operation, SPADs exhibit a virtually infinite optical gain, however a mechanism must be provided to quench the avalanche. There exist several techniques to accomplish quenching, classified in active and passive quenching. The simplest approach is the use of a ballast resistance. The avalanche current causes the diode reverse bias voltage to drop below breakdown, thus pushing the junction to linear avalanching and even pure accumulation mode. After quenching, the device requires a certain recovery time, to return to the initial state. The quenching and recovery times are collectively known as *dead time*.

SPADs have been integrated in CMOS achieving large arrays of pixels that operate independently with noise and timing resolutions comparable to those of PMTs and MCPs [8]. Current developments in more advanced CMOS technologies have demonstrated full scalability of SPAD devices, a 25 μ m pitch, and dead time as low as 32ns [9],[10],[11],[12]. The sensitivity, characterized in SPADs as photon detection probability (PDP), can exceed 25-50%. The noise, measured in SPADs as dark count rate (DCR), can be as low as a few Hertz [9]. Thanks to these properties, CMOS SPAD arrays have been proposed for imaging where speed and/or event timing accuracy are critical. Such applications range from fluorescence-based imaging, such as Förster Resonance Energy Transfer (FRET), fluorescence lifetime imaging microscopy (FLIM) [13], and fluorescence correlation spectroscopy (FCS) [14], to voltage sensitive dye (VSD) based imaging [15],[16], particle image velocimetry (PIV) [17], instantaneous gas imaging, [18],[19], etc.

Recently, the first fully integrated single-photon sensor with on-chip deep sub-nanosecond time-discriminators has appeared [20]. This sensor enabled to determine photon time-of-arrival upon detection at the chip level for the first time. The EC project MEGAFRAME has gone even further, creating a new family of SPADs implemented in 130nm CMOS technology [21]. These new devices, coupled with deep sub-nanosecond time-to-amplitude (TAC) and time-to-digital (TDC) converters, have yielded a new generation of ultrafast imagers capable of sustained speeds of 1Mfps [22],[23],[24]. These speeds could be achieved thanks to the implementation of pixel-level time discrimination and ultrafast readout schemes, capable of sustained of over 10Gb/s.

The development of architectures that support time-correlated modes with some degree of resource sharing is currently underway in many research groups. The main trade-off is at the architectural level, due to the nature of the signal

generated by SPADs. Application-specific optimal architectures are possible, provided a model of the application is built to characterize the performance of the sensor *a priori*. The sharing of resources may involve a number of pixels, say 4 or 16, or on-demand sharing based upon the reaction of SPADs may be used. Other trade-offs may include the complexity of the time discriminator itself.

3. APPLICATIONS

Fluorescence Correlation Spectroscopy

FCS is often used to measure transitional diffusion coefficients of macromolecules, to count fluorescent transient molecules, or to determine the molecular composition of a fluid being forced through a bottleneck or a gap. In FCS a femtoliter volume, is exposed to a highly focused laser beam that causes the molecules in it to emit light in a well-defined spectrum and with a time-response that depends on the modality of the movement of the molecules to and from the detection volume. The photon time-dependent response is quantified by means of the autocorrelation function $G(\tau)$

$$G(\tau) = \frac{\langle I(t+\tau)I(t) \rangle}{\langle I(t) \rangle^2},$$

where $I(t)$ represents the intensity of fluorescence emission and $\langle \rangle$ denotes time average. To be give useful results $G(\tau)$ is generally evaluated for a total range of several microseconds [25].

The average molecular concentration C and radial diffusion time τ_D through the illumination region may be derived from $G(\tau)$ by fitting standard analytical models of the molecular processes involved in a given experimental setup. Such models are generally single or multi-exponential, as well as rational functions of C , τ_D , and of the geometry of the gap [26]. Thus, for normal gap sizes, and most molecules, sub-nanosecond time resolutions are necessary. In addition, the availability of multi-pixel sensors with simultaneous, parallel operation allows one to better characterize the diffusion processes underlying the experimental setup.

Lifetime imaging

Among time-correlated imaging methods, time-correlated single photon counting (TCSPC) is perhaps one of the most used in bioimaging. Multiple exposures are employed to reconstruct the statistical response of matter to sharp and powerful light pulses. The study of calcium at the cellular level has made intensive use of fluorescent Ca^{2+} indicator dyes. Examples of heavily used dyes or fluorophores are Oregon Green Bapta-1 (OGB-1), Green Fluorescent Protein (GFP) and many others. Calcium concentration can be determined precisely by measuring the lifetime of the response of the corresponding fluorophore, when excited at a given wavelength. Lifetime is generally characterized using FLIM. There exist several flavors of FLIM based on how lifetime is characterized or based on the excitation mode.

In [27] a two-photon FLIM setup was employed based on a SPAD array capable of a time resolution of 79ps at a system level. The sensor made it possible to fit the lifetime

dependency of OGB-1 on Ca^{2+} using a triple exponential fit. Unlike previous approaches that exploit detector with lower resolutions [13], our model required no calibration factors, nor corrections of any kind, thus proving the robustness of the measurement system.

$$I_k = \frac{1}{2} \left[\frac{1 + e^{-T/\tau_k}}{1 - e^{-T/\tau_k}} - \text{erf} \left(\frac{\sigma_{IRF}}{\sqrt{2}\tau_k} - \frac{t}{\sqrt{2}\sigma_{IRF}} \right) \right] \times \exp \left(-\frac{t}{\tau_k} + \frac{\sigma_{IRF}^2}{2\tau_k^2} \right), k = \{f, i, s\}.$$

I_k represents the intensity of fluorescence emission, where k denotes the fast ‘f’, intermediate ‘i’ and slow ‘s’ components

of it. Terms σ_{IRF}^2 and τ_k denote the variance of the instrument response function (IRF) and the corresponding lifetime time constants, respectively.

Time-of-flight Imaging

Time-of-flight (TOF) is the time a light ray takes to propagate between two points in the three-dimensional space. There exist several applications requiring a precise measurement of TOF to image particular properties of targets and environments. In TOF based 3D imaging, for example, pulsed or continuously modulated light is used to determine the distance between the sensor and a reflecting target (Fig.1).

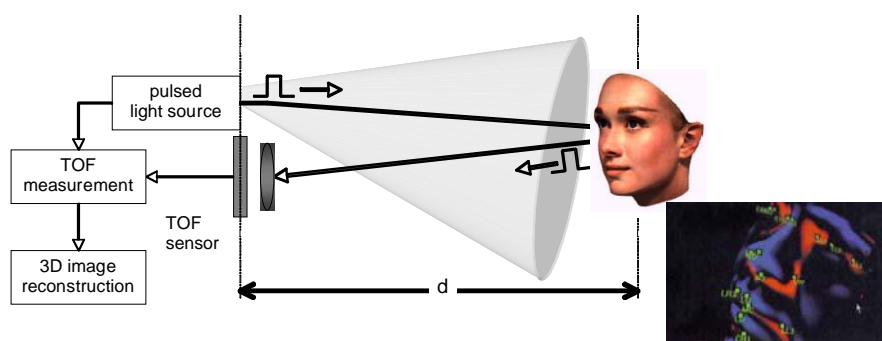


Fig. 1. Time-of-flight based imaging setup (left); resulting 3D image (right). The distance is computed in every pixel using the relation $d = c/2 \text{ TOF}$, where c is the speed of light. Again, for a resolution of 1mm, time resolutions of at least 6.6ps are necessary, whereas statistical methods may be used to relax the resolution of a single measurement.

In positron emission tomography, the exact location of positron emission is found by monitoring all gamma radiation reaching a pair of detectors on an axis at exactly the same time and then cross-correlate all estimated arrival times. The emission loci may be derived by measuring the TOF of the particle with respect to a reference point of known coordinates.

4. CONCLUSIONS

With the introduction of CMOS single-photon avalanche diodes, it is possible today to achieve great levels of miniaturization without compromising time resolution and overall speed. Not only large arrays of photon counters are

now possible, but also very high dynamic range and timing accuracy have become feasible. Thanks to these advances, applications requiring time-resolved single photon detection are now possible using low-cost CMOS detectors. We have outlined some of these applications and we have discussed system issues related to these and novel applications in the field of bio- and medical imaging.

5. ACKNOWLEDGEMENTS

The authors are grateful to their graduate students, Dmitri L. Boiko, and to the members of the MEGAFRAME consortium.

- [1] E. Charbon, “Will CMOS Imagers Ever Need Ultra-High Speed?”, *IEEE International Conference on Solid-State and Integrated-Circuit Technology*, pp. 1975-1980, Oct. 2004
- [2] T. G. Etoh, “Specifications of High-Speed Image Sensors based on Requirements of Multiscientific Fields”, *Proc. of SPIE*, Vol. 3173, pp. 57-66, Aug. 1997.
- [3] T. G. Etoh et al., An Image Sensor Which Captures 100 Consecutive Frames at 1,000,000 Frames/s, *IEEE Trans. on Electron Devices*, pp. 144-151, Vol. 50, N. 1, pp. 144-151, Jan. 2003.
- [4] S. Kleinfelder, S. Lim, X. Liu, A. El Gamal, “A 10000 Frames/s CMOS Digital Pixel Sensor”, *Journal of Solid-State Circuits*, pp. 2049 – 2059, Vol. 36, N. 12, Dec. 2001; see also S. Kleinfelder, et al., “High-speed, High Dynamic-Range Optical Sensor Arrays”, *Trans. Nuc. Sci.*, Vol. 56, N. 3, pp. 1069-1075, June 2009
- [5] S. Donati: “Photodetectors”, Prentice Hall, Upper Saddle River, 1999, Chapter 4.
- [6] J. McPhate, J. Vallerga, A. Tremsin, O. Siegmund, B. Mikulec, A. Clark, “Noiseless KiloHertz-frame-rate Imaging Detector based on Microchannel Plates Readout with Medipix2 CMOS Pixel Chip”, *Proc. SPIE*, Vol. 5881, pp. 88-97, 2004.

- [7] R.H. Haitz, "Studies on Optical Coupling between Silicon p-n Junctions", *Solid-State Electronics*, Vol.8, pp.417-425, 1965.
- [8] C. Niclass, A. Rochas, P.A. Besse, E. Charbon, "Design and Characterization of a CMOS 3-D Image Sensor Based on Single Photon Avalanche Diodes", *IEEE Journal of Solid-State Circuits*, Vol. 40, N. 9, pp 1847-1854, Sept. 2005.
- [9] C. Niclass, M. Sergio, E. Charbon, "A Single Photon Avalanche Diode Array Fabricated on Deep-Submicron CMOS Technology", *Design and Test in Europe (DATE)*, Mar. 2006.
- [10] D. Mosconi, D. Stoppa, L. Pacheri, L. Gonzo, A. Simoni, "CMOS Single-Photon Avalanche Diode Array for Time-Resolved Fluorescence Detection", *Proc. ESSCIRC*, Oct. 2006.
- [11] C. Niclass, M. Sergio, E. Charbon, "A CMOS 64x48 Single Photon Avalanche Diode Array with Event-Driven Readout", *Proc. ESSCIRC*, Oct. 2006.
- [12] M. Sergio, C. Niclass, E. Charbon, "A 128x2 CMOS Single-Photon Streak Camera with Timing-Preserving Latchless Pipeline Readout", *Proc. ISSCC*, pp. 120-121, Feb. 2007.
- [13] A. V. Agronskaia, L. Tertoolen, H. C. Gerritsen, "Fast Fluorescence Lifetime Imaging of Calcium in Living Cells", *Journal of Biomedical Optics*, Vol. 9, N. 6, pp. 1230-1237, Nov./Dec. 2004.
- [14] P. Schwille, U. Haupts, S. Maiti, W. W. Webb, "Molecular Dynamics in Living Cells Observed by Fluorescence Correlation Spectroscopy with One- and Two-Photon Excitation", *Biophysics Journal*, Vol. 77, pp. 2251-2265, 1999.
- [15] A. Grinvald *et al.*, "In-Vivo Optical Imaging of Cortical Architecture and Dynamics", *Modern Techniques in Neuroscience Research*, U. Windhorst and H. Johansson (Eds), Springer, 2001.
- [16] J. Fisher *et al.*, "In Vivo Fluorescence Microscopy of Neuronal Activity in Three Dimensions by Use of Voltage-Sensitive Dyes", *Optics Letters*, Vol. 29, N. 1, pp 71-73, Jan. 2004.
- [17] S. Eisenberg *et al.*, "Visualization and PIV Measurements of High-Speed Flows and Other Phenomena with Novel Ultra-High-Speed CCD Camera", *Proc. of SPIE*, Vol. 4948, pp. 671-676, 2002.
- [18] S. V. Tipinis *et al.*, "High-Speed X-ray Imaging Camera for Time-Resolved Diffraction Studies", *IEEE Trans. on Nuclear Science*, Vol. 49, N. 5, Oct. 2002.
- [19] W. Reckers *et al.*, "Investigation of Flame Propagation and Cyclic Combustion Variations in a DISI Engine using Synchronous High-Speed Visualization and Cylinder Pressure Analysis", *Proc. Intl. Symposium für Verbrennungdiagnostik*, pp. 27-32, 2002.
- [20] C. Niclass, C. Favi, T. Kluter, M. Gersbach, and E. Charbon, "A 128x128 Single-Photon Imager with on-Chip Column-Level 10b Time-to-Digital Converter Array Capable of 97ps Resolution", *IEEE Journal of Solid-State Circuits*, Vol. 43, N. 12, pp. 2977-2989, Dec. 2008.
- [21] M. Gersbach, J. Richardson, C. Niclass, L. Grant, R. Henderson, E. Charbon, "Low-Noise Single-Photon Detectors in 130-nm CMOS Technology", to appear, *Solid-State Electronics*, Aug. 2009
- [22] J. Richardson, R. Walker, L. Grant, D. Stoppa, F. Borghetti, E. Charbon, M. Gersbach, R. K. Henderson, "A 32x32 50ps Resolution 10 bit Time to Digital Converter Array in 130nm CMOS for time Correlated Imaging", to appear, *Custom Integrated Circuits Conference*, Sep. 2009.
- [23] M. Gersbach, Y. Maruyama, E. Labonne, J. Richardson, R. Walker, L. Grant, R. K. Henderson, F. Borghetti, D. Stoppa, E. Charbon, "A Parallel 32x32 Time-to-Digital Converter Array Fabricated in a 130nm Imaging CMOS Technology", to appear, *IEEE European Solid-State Device Conference (ESSDERC)*, Sep. 2009.
- [24] D. Stoppa, F. Borghetti, J. Richardson, R. Walker, L. Grant, R.K. Henderson, M. Gersbach, E. Charbon, "A 32x32-Pixel Array with In-Pixel Photon Counting and Arrival Time Measurement in the Analog Domain", to appear, *IEEE European Solid-State Device Conference (ESSDERC)*, Sep. 2009.
- [25] K. J. Moore, S. Turconi, S. Ashman, M. Ruediger, U. Haupts, V. Emerick, A. J. Pope, "Single Molecule Detection Technologies in Miniaturized High Throughput Screening: Fluorescence "
- [26] M. Gösch, *et al.*, "Parallel Single Molecule Detection with a Fully Integrated Single-photon 2x2 CMOS Detector Array", *J. Biomed. Optics*, Vol. 9, N. 5, pp. 913-921, Sep./Oct. 2004.
- [27] M. Gersbach, D. L. Boiko, C. Niclass, C. Petersen, E. Charbon, "Fast Fluorescence Dynamics in Non-ratiometric Calcium Indicators", *Optics Letters*, Vol. 34, N. 3, pp. 362-364, Feb. 2009.

EFFECT OF USING DISSOLVED AIR FLOTATION SYSTEM ON INDUSTRIAL WASTEWATER TREATMENT IN PILOT SCALE

YAHYA HABIBZADEH*, K.B.GURBANOV**

*University of Applied Sciences & Technology Tabriz (Iran)

**Institute of Physics of Azerbaijan National Academy of Sciences
Baku, Az-1143, H. Javid ave.,33

In the present paper the application of Dissolved Air Flotation (DAF) system for wastewater treatment, especially for industrial wastewater on a designed pilot system has been investigated. It is for the first time in dissolved air flotation system that instead of air dissolving tube, hydro cyclone technology is used to dissolve air in water with ratio of 1:1 (almost 100%) in the form of small air bubbles and a circular flotation tank instead of rectangular tank. The advantage of usage of circular tank in DAF system is the capability of being treated in higher rate of mass, so less space is needed. Although application of hydro cyclone with different diameters of holes for producing mixing energy which also has the capability of direct injection of chemical coagulant and polymeric materials leads to the higher efficiency of treatment and so reduces the cost of pump and consumed air.

Investigations on the efficiency of this system was done by providing and analyzing samples of wastewater with and without adding of PAC (Poly Aluminum Chloride). Sampling and analyzing was done according to standard methods. The results of the analyses show that pilot system has high efficiency, especially for oil removal.

1. INTRODUCTION

Nowadays importance of environmental problems has increased which leads to establishment of stricter environmental standards and according to these standards more limits are applied on pollution caused by wastewater of industrial units. Considering the large amount of these wastes, it is necessary to find new technologies with higher efficiency for treatment of wastewater to satisfy new standards. These new systems in spite of their

high technology and efficiency should need less space and have lower cost, so even small industrial units can take advantage of these systems [1].

Because of the existence of suspended solids and stable fats emulsion in industrial wastewater, its treatment is technically difficult. Conventional treatment process consists of physical, chemical and biological steps. In the first step of treatment process which is physical treatment, floating or settled materials are removed by screening or sedimentation. Chemical and biological treatments are carried out as second step of treatment process which removes most kinds of the organic material from waste water. As the last and third step of treatment some other processes such as adsorption and electro coagulation (EC) units are used to reduce the amount of pollutants like nitrogen, phosphorus, metals and so on.

In physico-chemical treatment for more, fast and better removal of suspended organics, minerals and oily materials and forming larger flocs, coagulants and polymers (flocculents) are used and then these flocs can be separated and removed from waste water by applying sedimentation, filtering or flotation methods [1,2].

DAF (Dissolved air flotation) system is known as an economic and efficient system compared to other conventional clarification systems in the field of treating industrial and recently municipal wastewater during the last 35 years. Solid particles, fat and oily materials in DAF system are removed very fast and sludge obtained from this system is of high consistency. DAF system can be used as a process for removing finest suspended particles. Air dissolved in water forms small bubbles that contact suspended particles in water so by decreasing their density these particles gain enough energy to be floated. For increasing the efficiency of flotation system chemical

additives (coagulants) are used, these additives form flocs which leads to better flotation due to collisions of these flocs and small bubbles [1,3].

The results of a case study done by S. M. J. Hoseyni on wastewater of paper mill (wastewater with fibers, hot press and mixed wastewater) using DAF system for flotation with rectangular tank and air dissolving tube, shows that the best efficiency for treatment of wastewater with fibers is reached at pressure of 3 bar and retention time of 15 min. In this situation the results of treatment is 40% for suspended particles, 10% for TSS (Total suspended solid) and 16.6% for COD (Chemical oxygen demand). In the wastewater of hot press at pressure of 5 bar and retention time of 15 min, the results of treatment is 45% for suspended particles, 6.5% for TSS and 29.75% for COD and in the wastewater of mixed at pressure of 4 bar and retention time of 15 min, the results of treatment is 38% for suspended particles, 10% for TSS and 17.3% for COD. In this study the effect of adding lime and alum was investigated which shows removal of 28% of COD from mixed wastewater and 23-28% from wastewater with fiber and without any effect on wastewater of hot press [3].

In a research done by Miller, Morse and Colic in spite of investigating on different flotation methods there are acceptable results approving the efficiency of hydro cyclone with rectangular flotation tank in different wastewaters [4].

TSS and COD of several different kinds of wastewaters treated by DAF system are compared in table1.

Table1: Comparison of TSS and COD [4]

	TSS before (ppm)	TSS after (ppm)	COD before (ppm)	COD after (ppm)
Seafood processor	28000	150	62000	12000
Rendering plant	25000	80	67000	13000
Food processing	1500	35	12000	3000
Laundry	5500	5	24000	3500
Municipal	285	50	320	180

Papageorgiou and et al in wastewater treatment of an olive oil extraction factory, gained 10.8% efficiency in COD

removal without using any chemical additive but by adding sulfuric acid (PH=2) and lime (PH=11) efficiency increased to 30% and 24.5% respectively [5]. Parker used DAF for oil industry's wastewater treatment and get to 58% and 57% efficiency in TSS and TVSS (Total volatile suspended solid) removal respectively, he also removed 74% of oil and grease from wastewater using this system [6]. Jarsarayi using physical and chemical (Aluminum sulfate and lime) processes for treatment of wastewater with fibers in paper mill got to 45-55 percent in COD and 75-95 percent in color removal efficiency, he also got to 45-55 percent in COD and 75-95 percent in color removal efficiency in the case of alkaline wastewater. Adding 2.5 g/lit of lime or 0.4 g/lit Alum to these wastewaters leaded to 55% in COD and 90% in color removal efficiencies [2].

2. DISSOLVED AIR FLOTATION SYSTEM BY HYDRO CYCLONE

An important matter in flotation method, is the introduction of air bubbles into water. In early flotation machines larger air bubbles (2-5mm) are formed by blowing air through a canvas or other porous medias. In some impller-based machines, air enters system directly from atmosphere and no compressor or blower is necessary, bubbles produced by this method are coarse, so this method is not suitable for flotation in wastewater treatment and oil extraction.

DAF is another method for flotation, which usually is used for oily wastewater treatment. In DAF system, stream of wastewater is saturated with air at elevated pressures up to 5 atm. Small bubbles which are formed in DAF system, are brought into contact with continuously flowing particles. Having such small bubbles (up to 20 microns) may cause some problems. Bubbles formed in DAF system rise very slowly to the surface of the

tank, this is the reason of using tanks with large dimitions in DAF system. Air-to-water ratio even at high pressures is very low, air-to-water ratios of 0.15:1 by volume are common in DAF systems and it is difficult to achieve higher ratios. Some of these problems are solved by new higher technologies like air sparged hydro cyclone coupled with a porous cylinder. Inffluent enters hydro cyclone from side of it and in the entrance a spiral flow forms which causes a centrifugal acceleration. Air enters hydro cyclone from its top, gas entering the pipe produces bubbles in it which are floated in centrifugal flow field due to radial acceleration gradient that affects vortex caused by hydro cyclone. Bubbles accelerate towards inner surfaces of spiral layer. Centrifugal flow field in spite of forming angular acceleration, assists the classification of particles with different density in water. Although retention time of liquid in bubble chamber is only a few cent seconds but for its high acceleration, bubbles cover this short distance in vortexes in a few milliseconds. In this short time bubbles contacting particles moving towards porous cylinder form flocs of particle/bubble (colloids).

Another advantage of air sparged is cleaning of porous cylinder and preventing its malformation and sedimentation. Velocity of gas transmission in this system is very high and formed bubbles are fine and floated, this improves separation of volatile organic and aeration of water. The last step of treatment takes place in the flotation tank, flocs of polymer/particle/bubble are formed in bubble

chamber of hydro cyclone before being fed to flotation tank. This tank is a place for separation of particles from wastewater, not for collision of bubbles and particles. Hydro cyclone system responds very fast to chemical reactions (seconds against hours). This becomes more useful when the entering water has variable compound and needs to be adjusted fast. Regarding high efficiency of hydro cyclone in pilot system that provides needed energy for mixing under the influence of centrifugal forces, this system (hydro cyclone system) is used for adding coagulants and flocculants to wastewater too, leading to formation of flocs. As it was mentioned, bubbles formed in hydro cyclones are more finer and smaller than bubbles of conventional DAF systems, that is due to shear force applied on bubbles by centrifugal force. Smaller bubbles and more mixing energy in hydro cyclones makes the mixing process more effective and shortens its time compared to conventional DAF systems. Desired chemicals are added to wastewater in the entrance of cylinders because mixing takes place in these columns. Chemical materials are prepared and agitated in special tanks and each material is added in a separate hydro cyclone unit, so the number of hydro cyclones should be the same as the number of chemical materials. To have the best operation, each chemical needs definite mixing energy depending on its molecular configuration so the nozzles of hydro cyclone have holes with different diameters.

With varying the diameter of holes, the velocity of fluid entering to hydro cyclone changes which leads to the variation of mixing energy. The number of holes can be changed by using a filled bush. Gaining the best mixing energy is possible by try and error [4].

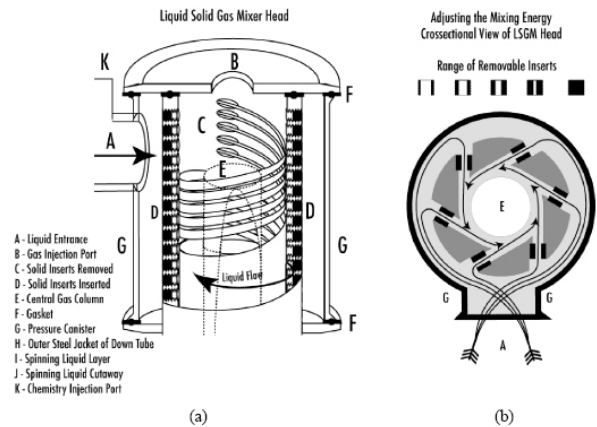


Fig.1. Cut-away view of (a) liquid solid gas mixer head (b)cross-sectional view of a liquid solid gas mixer head [4]

3. RESEARCH METHOD

3.1. Description of process

Pilot system was designed after initial studies to provide needed equipments for taking necessary samples. The schematic of the designed system is demonstrated at figure2.

In the pilot system wastewater enters equalization tank after passing through screen and then it is pumped to hydro cyclone where air and chemicals are added to it, this wastewater containing particles/air/chemicals is fed to flotation tank and in this tank, floating solids are scraped by a spiral scoop. Wastewater leaving this tank enters level

control tank by two pipes, in this tank the level of treated wastewater in flotation tank and the thickness of scraped sludge form flotation tank can be adjusted. There is a tank in the bottom of flotation tank for gathering settled sludge, finally the sludge of this part is discharged to sludge storage tank.

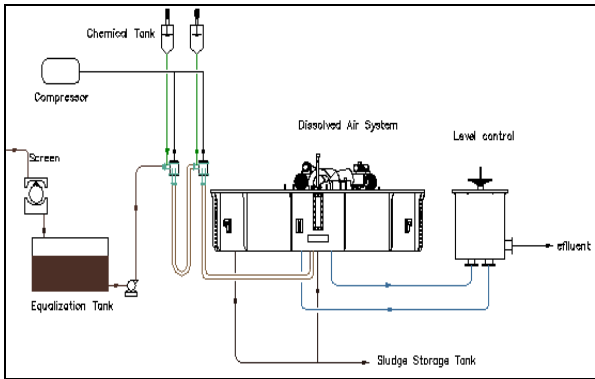


Fig. 2. Schematic of the designed equipment

3.2. Design of systems used in pilot

Designed pilot consists of DAF, electro coagulation, ozonation and excess chrome separation units. Figure3 shows three dimensional view of the arrangement of designed pilot system containing all above mentioned units.

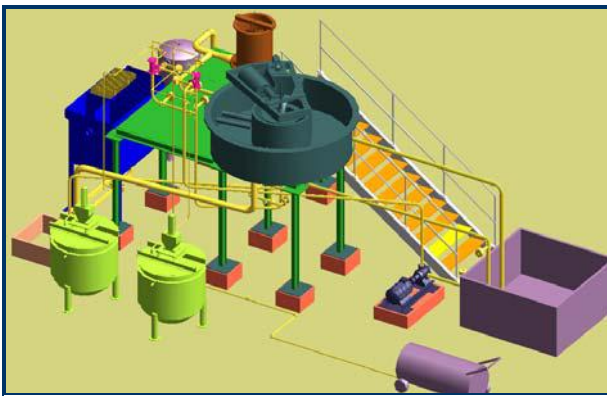


Fig.3. Three dimensional view of the arrangement of pilot

The assemblage process of pilot system in SPS Co. is shown at figure4.

In this study we have focused on the effect of DAF system with circular flotation tank and one hydro cyclone unit, the effect of adding PAC (Poly Aluminum Chloride) is investigated too. Other units and their effect on industrial wastewater treatment will be analyzed in future studies.

Pilot system is designed according to the DAF system of reference 4, but we have used circular flotation tank (figure 5) in our pilot system instead of rectangular one that is used in reference 4.

Some advantages of circular flotation tanks are:

- Retention time: Minimum
- Purchase cost: Lower than other systems of comparable performance
- Installation cost: Low, heavy support not needed
- Space requirement: Minimal
- Cleaning: Easy, bottom is self cleaning



Fig.4. Assemblage process of pilot system

Finally the most important advantage of circular tanks is their capability of handling more influent flow compared with rectangular tanks.



Fig.5. Circular flotation tank of pilot system

Different parts of pilot system, used in recent research are explained in the following.

3.2.1. Screen

To protect systems placed in downstream of flow like pumps and other accessories and also to prevent clogging of holes of hydro cyclone system a screen is used to remove big solids.

3.2.2. Volume of equalization tank

To have an equalized, steady flow of wastewater, it is fed to a tank with the name of equalization tank and after spending retention time, it is send to main parts of DAF system. The volume of this tank is calculated as following.

$$V (m^3) = Q (m^3/hr) \times T (hr) \quad (1)$$

Where Q is the flow rate of entering wastewater ($Q = 2 m^3/hr$) and T is retention time of wastewater in the tank ($T = 2.5 hr$).

So the volume of tank is:

$$V = 2 m^3/hr \times 2.5 hr = 5 m^3$$

To prevent sepsis of wastewater it should be aerated and for better mixing and keeping aerobic condition, surface aeration in the form of agitation is used.

3.2.3. Rotating clarification unit of DAF

To separate flocs of solids/air/coagulants formed in hydro cyclone from wastewater, it enters a tank. This tank is known as floatation tank and like conventional DAF systems of this company, is designed in circular form (figure6). Wastewater send to floatation tank contains solids and flocs that after scraping of them by spiral spoon, floated wastewater is send to next step. In the pilot system designed for this investigation to have the best efficiency circular tank combined with spiral spoon is used. Sludge of floatation tank that consists of scraped floated solids and settled material enters sludge storage tank.

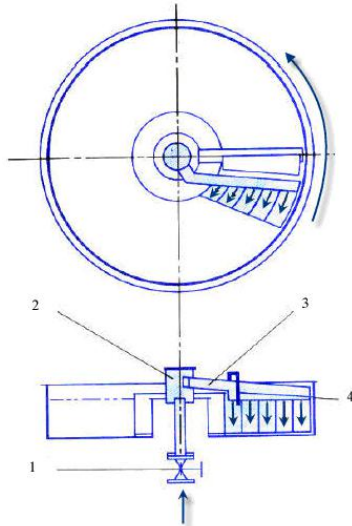


Fig.6. Schematic of floatation tank

Treated water discharged from floatation tank, is fed to level control tank. In this section fluid flows by gravity and no pump is needed. In conventional non rotating systems fluid flows from inlet to outlet but in DAF system inlet and outlet are centrally rotating so during clarification the velocity of water becomes zero. This means that the efficiency of clarification increases to theoretically maximum efficiency level. According to figure6 non clarified wastewater passes through valve (1) and then gets to central cylinder (2) which plays the roll of a collector, after this part wastewater is fed to inlet head box (3). Excess air is discharged from wastewater by a pipe (4).

The volume of floatation tank can be calculated using relation1 with Q of $2\text{m}^3/\text{hr}$ and retention time of 4min.

$$V = 2 \text{ m}^3/\text{hr} \times 4 \text{ min} = 0.133 \text{ m}^3$$

The floatation tank of pilot system after starting_the system is shown at figure7.

For calculating the volume of needed air per hour, we should know that the maximum efficiency of dissolved air flotation systems can be reached when the percentage of injected air volume is about 2-3 percent of wastewater's volume. So for Q of $2\text{m}^3/\text{hr}$ we have:

$$V_{\text{air}} = 2 \text{ m}^3/\text{hr} \times 0.03 = 0.06 \text{ m}^3/\text{hr}$$

$$V_{\text{air}} = 2 \text{ m}^3/\text{hr} \times 0.02 = 0.04 \text{ m}^3/\text{hr}$$

3.2.4. Hydro cyclone

Air enters hydro cyclone from gas injection port on the top of hydro cyclone and wastewater enters tangentially from side of it marked with (a) in figure8. Cross section of hydro cyclone is shown at figure8. Tangential entrance

forms a spiral fluid flow causing a centrifugal acceleration (figure9).

Compressed air passes through central gas column of hydro cyclone and produces fine bubbles under the influence of radial acceleration gradient. All parts of hydro cyclone are made from stainless steel. To control mixing energy of wastewater and chemicals, nozzles with different diameters are used, one of these nozzles is marked with (b) in figure8. Hydro cyclone designed for installation on pilot system can be seen in figure10.



Fig.7. Floatation tank of pilot system after starting the system

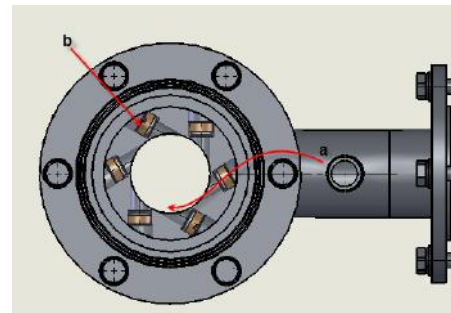


Fig.8. Cross section of hydro cyclone

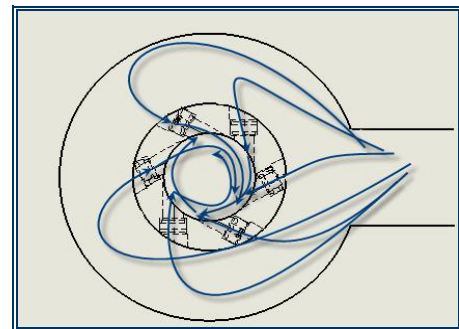


Fig.9. Schematic of tangential flows entering hydro cyclone



Fig.10. Hydro cyclone installed on pilot system

For calculating the diameter of nozzles of hydro cyclone, relations of mixing energy and equations of continuity are used. Diameters are calculated for velocity gradients (G) in range of 250 1/s to 1500 1/s which is suitable for fast mixing operation according to reference1. For G of 1500 1/s nozzle diameter is calculated as following:

$$\text{Maximum mixing energy} \Rightarrow G = 1500 \frac{1}{s}$$

$$\text{Vol. of hydro cyclone's cylinder: } \bar{V} = \frac{\pi}{4} \times (D)^2 \times L \quad (2)$$

Where D is diameter of hydro cyclone's cylinder and L is its height. Replacing these values in relation2, volume of cylinder becomes:

$$\bar{V} = \frac{\pi}{4} \times (0.15)^2 \times 0.25 \Rightarrow \bar{V} = 4.4 \times 10^{-3} m^3$$

$$\text{Mixing energy: } G = \sqrt{\frac{P}{\mu \times \bar{V}}} \quad (3)$$

In relation3, μ is dynamic viscosity ($N.s/m^2$), \bar{V} is the volume of cylinder calculated before and P is the power lost of effluent leaving nozzle that should be calculated in this relation, replacing known parameters in relation3 we have:

$$\Rightarrow 1500 = \sqrt{\frac{P}{10^{-3} \times 4.4 \times 10^{-3}}} \Rightarrow P = 10W$$

The relation among P (W), γ (kN/m^3), Q (m^3/hr) and h (m) is demonstrated in relation4:

$$P = \gamma \times Q \times h \quad (4)$$

Where h is the head lost of effluent passing through nozzle and can be calculated using relation5:

$$h = \frac{kV^2}{2} \quad (5)$$

In relation above k is constant and in this case it equals 1 and V is the velocity of effluent leaving nozzle that is unknown and should be calculated using relations 4 and 5 as following:

$$\Rightarrow 10 = 10000 \times \frac{2}{3600} \times 1 \times \frac{V^2}{2} \Rightarrow V = 1.9 m/s$$

Now we can find diameter of nozzle (d) by using relation6, knowing velocity of leaving effluent ($V=1.9$ m/s), effluent flow rate ($Q= 2$ m^3/hr) and the number of nozzles ($n= 48$):

$$Q = n \times \frac{\pi d^2}{4} \times V \quad (6)$$

$$\Rightarrow \frac{2}{3600} = 48 \times \frac{\pi d^2}{4} \times 1.9 \Rightarrow d = 2.8mm$$

For minimum mixing energy (with G of 250 1/s) and the same volume of cylinder, μ and number of nozzles, new value of P can be calculated using relation3:

$$\Rightarrow 250 = \sqrt{\frac{P}{10^{-3} \times 4.4 \times 10^{-3}}} \Rightarrow P = 0.275W$$

Now V can be calculated by means of relations 4 and 5:

$$\Rightarrow 0.275 = 10000 \times \frac{2}{3600} \times \frac{V^2}{2} \Rightarrow V = 0.32 m/s$$

Finally the diameter of nozzle (d) is calculated using relation6:

$$\Rightarrow \frac{2}{3600} = 48 \times \frac{\pi d^2}{4} \times 0.32 \Rightarrow d = 7.0mm$$

Diameters of nozzles of hydro cyclone for fast mixing, according to previous calculation vary among 2.8 and 7 mm, and five nozzles of different diameters are demonstrated in figure11, but only two size of nozzles are used in this paper. These nozzles can easily be installed on and uninstalled from hydro cyclone. The material of these nozzles is phosphorous brass.



Fig.11.Nozzles of hydro cyclone with different diameters

4. RESULTS

Industrial wastewater used in this study has been taken from food processing industry, samples of wastewater were treated during steps explained before. Used coagulant was Poly Aluminum Chloride (PAC), prepared with necessary consistency in tank of chemical materials and then is pumped by a dosing pump. According to executed jar test the best doze of PAC with PH of 6.95 is 30 ppm for the wastewater used in this study.

In usage of additive chemicals in spite of their effect on coagulation, the effect of them on flocculation should be considered too, those chemicals with lower molecular weight like PAC are mostly used as coagulant and need more mixing energy (smaller diameter of nozzles of hydro cyclone) but chemicals with higher molecular weight like long chained polymers that are suitable for flocculation need less mixing energy (bigger diameter of nozzles of hydro cyclone).

In this study just one hydro cyclone is used for adding PAC and for future researches another hydro cyclone is considered for adding polymer as flocculent. Although we have used only PAC as coagulant, considering its little effect on flocculation, the results are acceptable.

For detailed analysis, sampling was done in two steps with and without adding PAC and each time with two different diameters of nozzles. Sampling and analyzing was carried out according to standard methods for measuring the amount of COD, TSS, Oil and PH in wastewater.

The results of analyses are presented in tables2 and 3 respectively for steps without and with adding PAC.

Table2: Results of samples analyses without adding PAC

Sample No.	Sample 1	Sample 2	Sample 3
PH	6.95	6.80	6.40
COD	23470	17784	14046
TSS	830	460	380
Oil	272.7	174.6	167.2

Table3: Results of samples analyses with adding PAC

Sample No.	Sample 1	Sample 4	Sample 5
PH	6.95	6.45	6.20
COD	23470	10940	7820
TSS	830	320	160
Oil	272.7	85.4	81.2

Sample1 is the wastewater being fed to pilot system which is taken from equalization tank. In Samples 2 and 3, no PAC is added and diameters of nozzles are respectively 7 and 3 mm. The effect of adding PAC is investigated by taking samples 4 and 5 with nozzle diameters of 7 and 3 mm respectively. Samples 2, 3, 4 and 5 are taken from level control tank.

It should be mentioned that these diameters are selected to search on the effect of mixing energy on efficiency of treatment. According to presented calculations with diameter of 7 mm the mixing energy is minimum and it is maximum for diameter of 2.8 mm, but because of machinery problems nozzle with diameter of 3 mm is used instead of 2.8 mm.

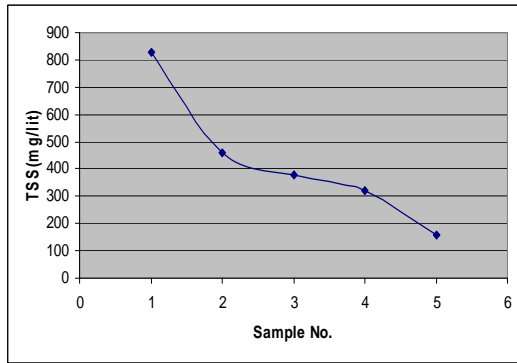


Diagram 1: TSS value of samples

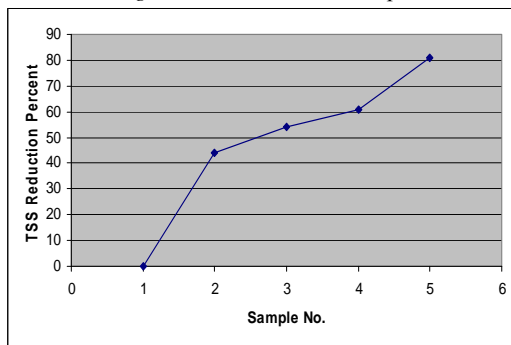


Diagram 2: TSS reduction percent

As shown in diagram1, TSS has decreased from 830 mg/lit to 380 mg/lit in sample3 and adding PAC makes its value 160 mg/lit in sample5. In diagram2, reduction percent of TSS is demonstrated, which is 81% in sample5. Diagram3 shows COD value before and after adding PAC. Diagram4 shows COD reduction percent, its value is 67% in sample5. According to diagram5 oil content of samples has decreased from 272.6 mg/lit in sample1 to 167.2 mg/lit in sample3 and it decreases to 81.2 mg/lit in sample5 by adding PAC. Diagram 6 demonstrates that oil reduces to 70.2% in sample5, this means that adding PAC is very effective for reducing oil. Adding PAC hasn't a

considerable effect on PH reduction, according to diagram7.

Finally according to the results this system can be offered for pre treatment of industrial wastewater.

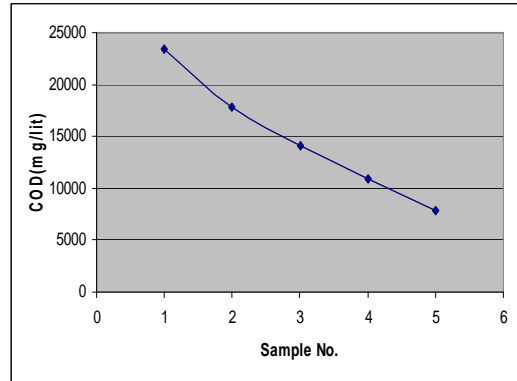


Diagram 3: COD value of samples

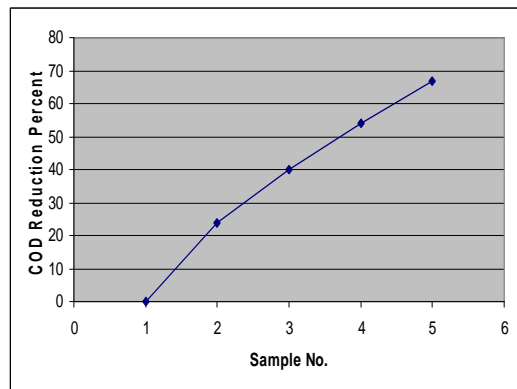


Diagram 4: COD reduction percent

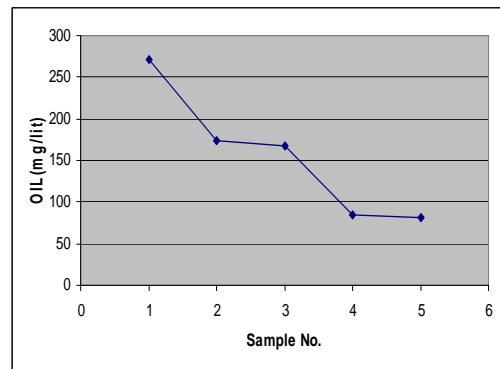


Diagram 5: Oil content of each case

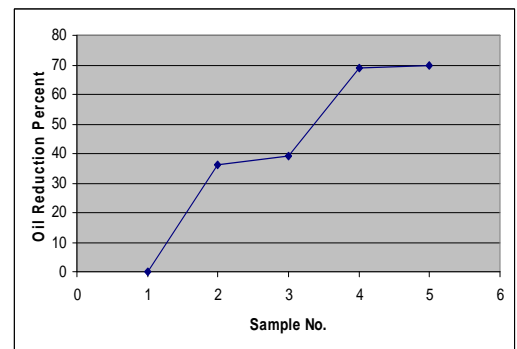


Diagram 6: Oil reduction percent

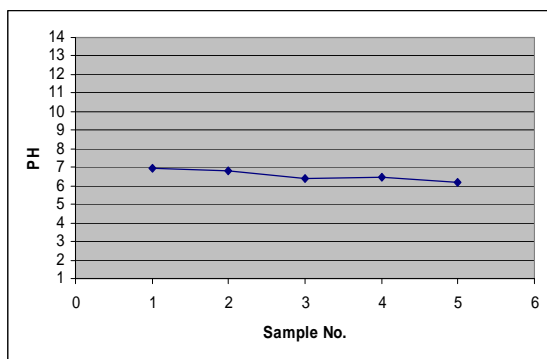


Diagram 7: PH values in each case

5. CONCLUSION

According to the results of this study we get to the following conclusion:

1. Results of samples 4 and 5 shows that adding PAC is effective in flotation process.

2. Compared to sample2, sample 3 has better characteristics that is because of usage of nozzles with smaller diameters, leading to higher mixing energy.

3. Compared to sample4 and two other samples, sample5 has better characteristics that is because of usage of nozzles with smaller diameters combined with adding PAC, resulting in higher mixing energy and more effective flotation.

4. Usage of advanced DAF system (with circular tanks and hydro cyclone) combined with adding PAC reduces TSS to 81%, COD to 67% and oil to 70.1% but has no considerable effect on PH.

5. Using hydro cyclone leads to lower costs by reducing volume of needed air and so a cheaper compressor would be enough and also the number of necessary pumps decreases too.

-
- [1]. Tchobanoglous, g. et al, "Wastewater Engineering", Metcalf & eddy Inc, McGraw Hill, New York, 1991.
- [2]. A. Jarsarayi Talar, "Identification of Design Parameters of Wastewater Treatment in Wood and Paper Manufacturing in Iran Using Physical, Chemical and Biological Pilot", Mse. thesis, Civil eng. Environmental eng., Tarbiyat Modarres University, Engineering faculty, 1377.
- [3]. S. M. J. Hoseyni, "Physucal and Chemical Treatment of Iran's Fiber Factory's Wastewater Using DAF System", Mse. thesis, Civil eng. Environmental eng., Tarbiyat Modarres University, Engineering faculty, 1378.
- [4]. Colic, M., Morse, D.E., Morse, W.O., Matherly, T.G., Carty, S. and Miller, J.D., "From air-sparged hydrocyclone to bubble accelerated flotation", 2001.
- [5]. Mitraker, M., Papageorgiou, G., Docoslis, A., Sakell aropoulos, G. "Evaluation of various pretreatment methods for olive oil Mill wastewater" European water pollution control V6 n6 1996 p10-16.
- [6]. Parker, W. J., Monteith, H. D. "Stripping of Voc's from Dissolved air flotation ", environmental progress V15 n2 1996 P73-81.
- [7]. Bratby, J., Jones, G. and Uhte, W., "State- of-practice of DAFT technology – is there still a place for it?", 77th Annual Conference of the Water Environ. Federation, L CD-ROM Conference Proceedings, WEFTEC, New Orleans, 2004.

COMPARISON OF EXPERIMENTAL AND THEORETICAL RESULTS TO DEFINE CENTRALITY OF HEAVY ION COLLISIONS

Z.WAZIR¹, M.K. SULEYMANOV^{1,2,3}, O.B. ABDINOV³, E.U. KHAN¹,
MAHNAZ Q. HASEEB¹, M. AJAZ¹, K. H. KHAN¹, SH. GANBAROVA³

¹CIIT, Islamabad (Pakistan),

²JINR, Dubna (Russia),

³Institute of Physics NAS Azerbaijan Republic

Using the simulation data coming from the DCM, we have studied the behavior of Number of events as a function of impact parameter b and the number of charged particles N_{ch} for light and heavy nuclei at different energies. We have seen that for light nuclei, the number of charged particles N_{ch} could be used to fix the centrality. But for heavy nuclei we have got strong initial energy and mass dependences therefore the results for impact parameter b and the number of charged particles N_{ch} differ. So for heavy nuclei, a number of charged particles N_{ch} could not be use to fix the centrality.

Используя данные моделирования по Дубненской Каскадной Модели было рассмотрено поведение числа событий в зависимости от функции параметра столкновения b и числа заряженных частиц N_{ch} для легких и тяжелых ядер при различных энергиях. Видно, что для легких ядер, число заряженных частиц N_{ch} можно использовать для определения центральности. Но для тяжелых ядер, где мы имеем очень большую массу и большую начальную энергию зависимости результатов для параметра столкновения b и числа заряженных частиц N_{ch} отличаются. Таким образом, для тяжелых ядер число заряженных частиц N_{ch} не может быть использовано для определения центральности.

Yüngül və ağır ionların toqquşmalarında müxtəlif enerjilərdə Dubna Kaskad Modelindən istifadə edərək hadisələrin sayı təsir parametri b -nin və yüklü zərrəciklərin sayı N_{ch} funksiyası kimi asılılığını öyrənilib. Görünür ki, yüngül nüvələr üçün yüklü zərrəciklərin sayı N_{ch} mərkəzləşməyinin müəyyən etmək olar. Ancaq ağır nüvələr üçün biz güclü ilk enerjiyə və böyük kütləyə malik olduqumuz halda parametri b -i və yüklü zərrəciklərin sayı N_{ch} təsirlərin asılılığı fərqlənir. Beləliklə ağır nüvələr üçün yüklü zərrəciklərin sayı N_{ch} mərkəzləşməyinin təyin etmək üçün istifadə edilə bilməz.

1. INTRODUCTION

To fix the baryon density of nuclear matter, the centrality experiments are usually used. It is considered as best tool to reach the Quark Gluon Phase (QGP) [1] of nuclear matter under extreme conditions. Studying the different characteristics of events as a function of the centrality [2] in JINR (Dubna), CERN (Geneva), BNL (New-York), and SIS (Darmstadt) could give new information about the properties of nuclear matter which could appear under extreme conditions. On the other hand the centrality of collisions cannot be defined directly in the experiment. In different experiments the values of the centrality are defined [3-5] as a number of identified protons, projectiles' and targets' fragments, slow particles, all particles, as the energy flow of the particles with emission angles $\theta = 0^\circ$ or with $\theta = 90^\circ$. Apparently, it is not simple to compare quantitatively the results on centrality-dependences obtained in literature while on the other hand the definition of centrality could significantly influence the final results. May be this is a reason, why we could not get a clear signal on new phases of strongly interacting matter, though a lot of interesting information has been given in those experiments. During last several years some results of the central experiments are discussed which demonstrate the point of regime change and saturation on the behavior of some characteristics of the events as a function of the centrality [6]. It is supposed that these phenomena could be connected with fundamental properties of the strongly interacting mater and could reflect the changes of its states (phases).

2. DUBNA CASCADE MODEL

Among the host of models which are proposed to explain the general features of relativistic nucleus-nucleus collisions,

Dubna Cascade Model (DCM) is the most popular model. It is an approach based on simulation (Monte-Carlo techniques) and applied to situation where multiple scattering is important. In the simplest approach it is assumed [7-12] that due to the interaction of a projectile hadron with one of the target nucleons the creation of a new particle takes place. The participating target nucleon accepts momentum and begins to move in the nucleus. All moving (cascade) particles can interact with other nuclear nucleons to produce new particles or suffer elastic rescattering. Therefore, cascade reproduction of moving particles is assumed. The interactions between cascade particles are omitted as a rule. The process continues until all moving particles either leave the nucleus or are absorbed. In the case of (A+A) collisions, it is assumed that cascade particles can interact with projectile and target nucleons. Due to analysis fast particles and correlations between slow and fast particles DCM [13] was recognized as the best model applied in the intermediate energy physics [14].

3. RESULTS FROM CENTRAL EXPERIMENTS

In paper [15] the results from BNL experiment E910 on pion production and stopping in proton-Be, Cu, and Au collisions as a function of centrality at a beam momentum of 18 GeV/c are presented. The centrality of the collisions is characterized using the measured number of «grey» tracks, N_{grey} , and a derived quantity ν , the number of inelastic nucleon-nucleon scatterings suffered by the projectile during the collision. In Fig. 1, the values of average multiplicity for π^- -mesons ($\langle \pi^- \text{ multiplicity} \rangle$) as a function of N_{grey} and ν is plotted for the three different targets. One can observe that $\langle \pi^- \text{ multiplicity} \rangle$ increases approximately proportionally to N_{grey} and ν for all three targets at small values of N_{grey} or ν .

and saturates with increasing N_{grey} and v in the region of more high values of N_{grey} and v . Fig. 2 is a plot of multiplicity of grey particles - N_g -dependences verses $\langle N_b \rangle$ average multiplicity of b-particles for different reactions taken from [16]. One can see that the values of $\langle N_b \rangle$ increase with N_g in the region of the values of $N_g < 8$. Than the values of the $\langle N_b \rangle$ saturate in the region $N_g \geq 8$ as well as in Ref.[17].

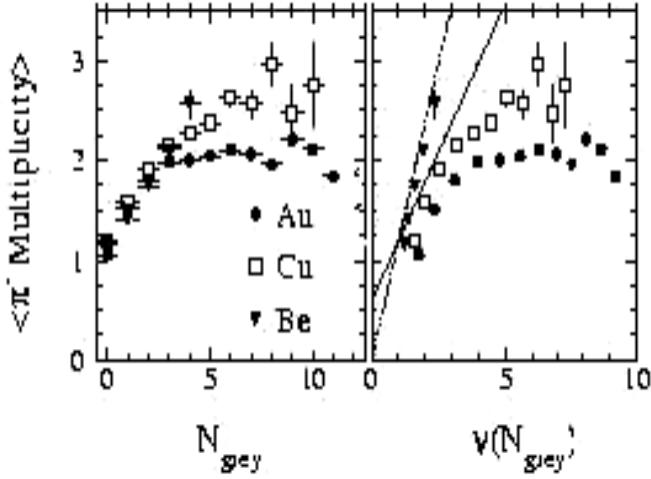


Fig.1. The average multiplicity of the π^- -mesons produced in proton-Be, Cu, and Au collisions as a function of centrality at a beam momentum of 18 GeV/c. Solid line demonstrates the results coming from the WN-model [15].

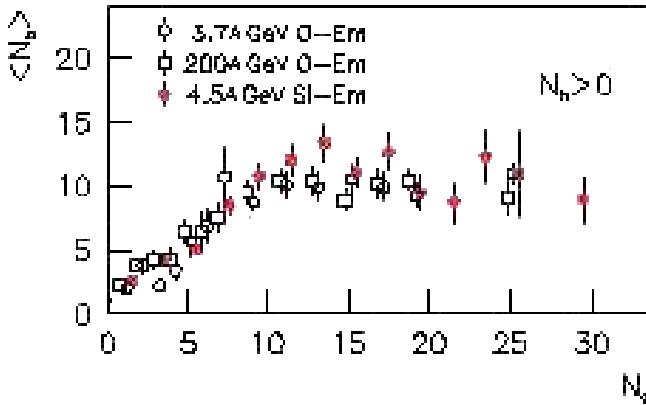


Fig.2. N_g -dependences of $\langle N_b \rangle$ for different reactions [16]

The main results of these central experiments are: The regime change has been observed: at some values of centrality (as critical phenomena); for hadrons-nucleus, nucleus-nucleus and even in ultra relativistic heavy ion collisions; in the energy ranges from SIS energy up to RHIC; almost for all particles; after the point of regime change, saturation is observed; the existing simple models cannot explain the effect. If the regime change takes place unambiguously two times, this would surely be the most direct experimental evidence seen to observe the QCD critical point and phase transition. But the central experiments could not confirm it. One of its reasons may be the incorrect definition of the centrality. So it is very important to study the connections between the different methods for fixing the centrality and looking for the new possibilities to fix the centrality especially in heavy ion

collisions where the formation of QGP is expected. The main goal of our paper is to study the connections between different methods offered to fix the centrality and search for new methods to fix the centrality.

4. METHOD

To reach our goal, we use the simulation data coming from the DCM. DCM is usually used for a chosen variable to fix centrality. It is supposed that its values have to increase linearly with a number of colliding nucleons or baryon density of the nuclear matter. The simplest mechanism that could give this dependence is the cascade approach. So, we have used DCM to simulate events at different energies and mass colliding hadrons and nuclei. This code [18] is written by F.G. Geregy and J.J. Musulmanbekov and was modified by S.Yu. Shmakov and V.V. Uzhinskii in 1993. The DCM is used for calculation of nucleus-nucleus inelastic interactions at energies up to 20 A GeV. We considered the following reactions: He+He; C+C; Au+Au at the energies; 1; 6; 12; 18 A GeV/c for 200 events. Two variables were used to fix the centrality: a) impact factor b , which could not be define experimentally; b) charged particles N_{ch} , which could be defined experimentally.

5. DUBNA CASCADE MODEL RESULTS

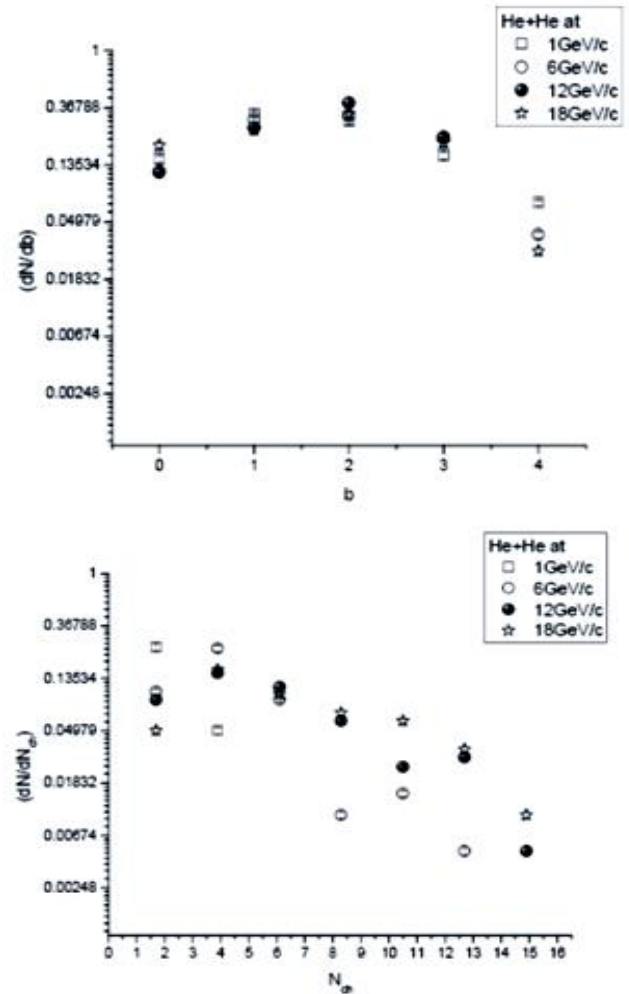


Fig.3. The b and N_{ch} dependences of normalized event numbers for He+He interactions coming from DCM

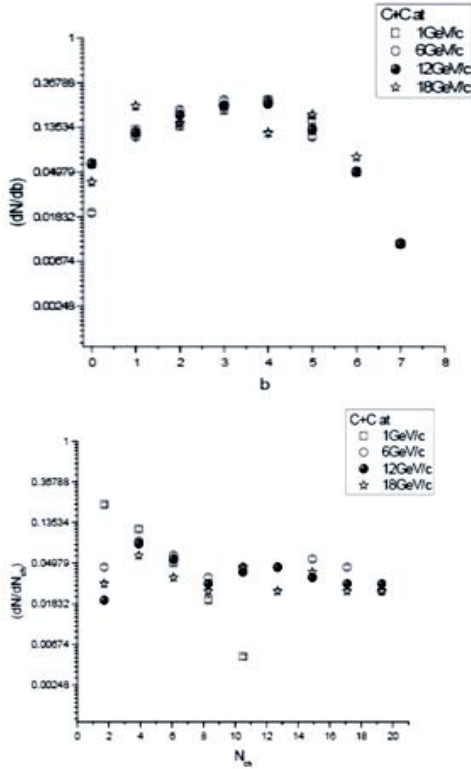


Fig.4. The b and N_{ch} dependences of normalized event numbers for $C+C$ interactions coming from DCM

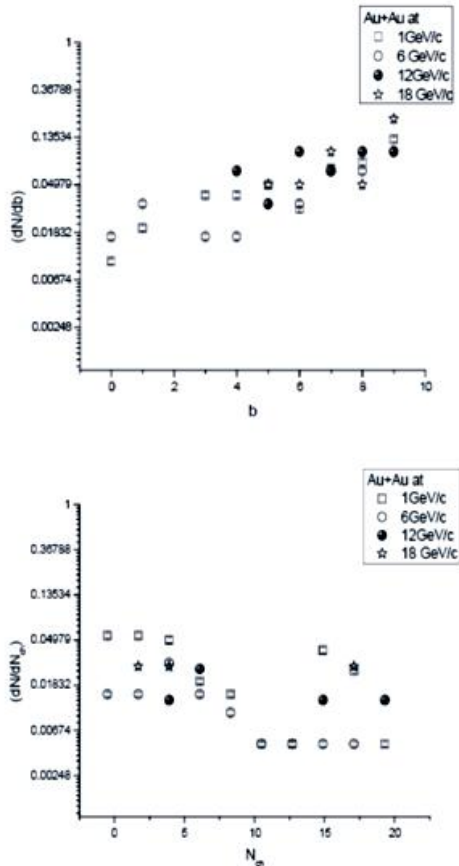


Fig.5. The b and N_{ch} dependences of normalized event numbers for $Au+Au$ interactions coming from DCM.

6. DISCUSSION

The behavior of the normalized event number dN/db as a function of b and the dN/dN_{ch} as a function of N_{ch} for $He+He$ reactions at different initial energies are shown in fig.3. One can see that the behavior of the impact parameter distributions don't depend on the energy of the colliding nuclei for most central ($b=0$), central and semi central collisions ($0 < b < 3$). We can see some mass dependence for the peripheral collisions ($b > 3$). We can also say that there are 2 regions on the behavior of the dN/db as a function of the b . In first region $b < 3$, the values of dN/db greater than in region with $b > 3$. The behavior of the event number as a function of N_{ch} has the stronger energy dependences. We can say that at energies equal and great than 6 GeV we can find some analogies between the behavior of the distribution of the events as a function of the b and N_{ch} . It means in these cases the N_{ch} could be use to fix the centrality instead of b . In fig. 4 ,the behavior of the normalized event number as a function of b and N_{ch} for CC reactions at different energies is shown. There is some energy dependence for the behavior of dN/db as a function of the b in the region of momentum great that 12 AGeV/c. For these reactions there are 3 regions on the behavior of the N as a function of the b : $b=0$ most central collisions; $0 < b < 5$ central and semi central collisions and $b > 5$ peripheral collisions. So one can say that with increasing the mass of the colliding particles, DCM give some energy dependence for the behavior event number as a function of b . Again we can say that the behavior of the event number as a function of N_{ch} has the stronger energy dependences. The fluctuation in the behavior of the event number as a function of N_{ch} increase and it is very difficult to find some analogies between the behavior of the distribution of the events as a function of the b and N_{ch} . So it means that it will be very difficult to use the last to fix the centrality instead of b . The same result we can get for the heavy ion collisions. For $Au+Au$ reactions at different energies the b and N_{ch} dependences of normalized event number dN/db and dN/dN_{ch} are shown in the Fig.5. We can see the strong dependence for the behavior of event numbers as a function of the impact parameter b . This picture also indicates different regions for the behavior of event numbers as a function of the b but N_{ch} has strong energy dependence. We cannot find any analogy for the behavior of the distributions with b and N_{ch} . It means that for heavy nuclear interactions N_{ch} is not good variable to fix the centrality.

7. CONCLUSION

The behavior of the normalized event number as a function of impact parameter b and charged particles N_{ch} for $He+He$, $C+C$ and $Au+Au$ reactions at different initial energies coming from DCM are point that for the light nuclei charged particles N_{ch} could be used to fix the centrality. For heavy nuclei we have got strong initial energy and mass dependences and the results for impact factor b and charged particles N_{ch} differ. So in this case charged particles N_{ch} could not be use to fix the centrality.

-
- [1]. *Collins, J.C., Perry, M.J.*, 1975. Super dense Matter: Neutrons or Asymptotically Free Quarks? *Phys.Rev.Lett.*34, 1353-1356
- [2]. *Kotoku, A. P., Gorenstein, M. I., Stöcker, H., Greiner, W.*, 2003 .Charm coalescence at relativistic energies. *Phys. Rev. C* 68, 041902
- [3]. *M.K.Suleymanov et al*, 2007.Multiplicity and angular distribution of particles emitted in relativistic nuclear-nuclear interactions. ArXiv: 0712.0062v1 [nucl-ex]
- [4]. *Mohanty, B., et al*, 2003. Indication of a coexisting phase of quarks and hadrons in nucleus nucleus collisions.*Phys.Rev. C* 68, 021901
- [5]. *Suleimanov, M.K., et al.*, 1998. Single-particle correlations in events with total disintegration of nuclei. *Phys. Rev. C*58, 351
- [6]. *Suleymanov ,M. K., et al.*2008. Search for deconfinement in the cluster at ultra relativistic heavy ion Collisions. *Nuclear Physics B (Proc. Suppl.)*, vol. 177–178, pp. 341–342
- [7]. *Barashenkov V.S. and Toneev V.D.* “Interaction of high energy particles and atomic nuclei with nuclei”, Moscow, Atomizadt, 1972.
- [8]. *Bertini N.W. et al.* *Phys. Rev. C*9 (1974) 522.
- [9]. *Bertini N.W. et al.* *Phys. Rev. C*14 (1976) 590.
- [10]. *Bondorf J.P. et al.* *Phys. Lett.* 65B (1976) 217.
- [11]. *Bondorf J.P. et al.* *Zeit. Phys.* A279 (1976) 385.
- [12]. *Toneev V.D., Gudima K.K.* *Nucl. Phys.* A400 (1983) 173.
- [13]. *Mashnik S.G.* In “Proceedings of a Specialists Meeting - Intermediate Energy Nuclear Data: Models and Codes”. Paris, 1994, P.107.
- [14]. *Blann M.B., Gruppelaar H., Nagel P., Rodens J.* Report “International Code Comparison for Intermediate Energy Nuclear Data”, NEA, OECD, Paris, 1994.
- [15]. *Chemakin I., et al.* Centrality dependence of Production and Stopping in p-A Collisions at 18 GeV/c .The BNL E910 Collaboration, 1999, E-print: nucl-ex/9902009
- [16]. *Liu ,Fu-Hu., Abd Allah ,N. Nabil .,Zhang,Dong-Hai.,Duan,Mai-Ying.,2003.* Particle multiplicity distributions in silicon-emulsion collisions at 4.5A GeV/c.*Phys. Rev. C*, 67, p. 047603
- [17]. *Abduzhamilov, A., etal.*1988. Multiplicity in proton-nucleus interactions in emulsion at 800 GeV. *Z. Phys. C*, vol. 40, p. 223-229
- [18]. *Barashenkov V.S., Zheregry F.G., Musulmanbekov Zh.Zh.* Preprint JINR P2-83-117, 1983, Dubna.

PHONON SYMMETRIES AND PHASE TRANSITION IN TlSe AND TlInSe₂

NAZIM MAMEDOV^{1*}, GUSEYN ORUDZHEV¹, KOJIRO MIMURA², KAZUKI WAKITA³,
YONG GU SHIM⁴, SUSAN SCHORR⁵, MUNIRA NIZAMETDINOVA⁶, VUSALA JAFAROVA¹,
SADIG HAMIDOV¹ AND FIRUDIN HASHIMZADE¹

¹ *Institute of Physics, Azerbaijan National Academy of Sciences,
H. Javid ave. 33, Baku AZ-1143, Azerbaijan*

² *Osaka Prefecture University, Department of Mathematical Sciences,
Graduate School of Engineering, Sakai 599-8531, Japan*

³ *Chiba Institute of Technology, Department of Electrical, Electronics and
Computer Engineering, Narashino, Chiba 275-0016, Japan*

⁴ *Osaka Prefecture University, Department of Physics and Electronics,
Graduate School of Engineering, Sakai 599-8531, Japan*

⁵ *Free University, Department of GeoSciences, Malteser str., 74-100, D-12259 Berlin, Germany*

⁶ *University of Architecture and Construction, Department of Physics,
A. Sultanova str. 5, Baku AZ1143, Azerbaijan*

The symmetry and atomic displacements corresponding to each phonon have been derived from the calculations of the phonon band structure of TlSe and TlInSe₂ chain compounds, which belong to the same family of materials. It is shown that at least acoustic branches along Δ -symmetry line are, for the most part, Einstein-like and their frequency is a weak function of the wave-vector. Anti-crossing between acoustic and low-frequency optic modes along Γ -T direction of the Brillouin zone is found to be similar to that observed in thermoelectric Ba-Ni-Ge clathrates. The found symmetry-forbidden crossing on A-symmetry line between the two-fold degenerated low-frequency phonon modes with A₅ symmetry is vanishing in TlInSe₂ in the point with the wave vector of 0.67Å⁻¹ along the Γ -H-T direction of the Brillouin zone. On the other hand, a kink transforming into a gap-like structure with decreasing temperature has been observed at the same wave-vector for the uppermost valence band of TlInSe₂, accessed by angle-resolved photo-emission spectroscopy at SPRING-8 facility (Japan). Both theoretical and experimental data obtained are evident of an incommensurate phase transition due to pseudo-Jahn-Teller effect in TlInSe₂.

1. INTRODUCTION

The ternary Tl-contained compounds, TlMeX₂, crystallize either into a tetragonal chain structure (MeX = TlSe, InSe, InTe, GaTe) with space group D_{4h}¹⁸ [1] or into a monoclinic layered structure (MeX= GaSe, GaS, InS) with space group C_{2h}⁶ [2]. In either case the main building blocks are the MeX₄ tetrahedrons arranged into the chains or layers and the Tl-atoms positioned between these chains or layers. Both structures are low-dimensional and can transform into one another under the proper conditions such as, for example, 2Gpa and 873K for TlGaSe₂ [2].

The most interesting properties, which promise novel applications in MEMS (micro-electro- mechanical systems) and other devices are giant thermoelectric power [3] and giant thermoelastic effect [4], both are believed to be an attribute of a wide-range incommensurate (modulated) phase emerging in TlMeX₂ in the course of the subsequent phase transitions.

Our attention has been attracted to TlInSe₂ whose superior thermoelectric and thermoelastic properties have already been verified in an experimental way [3,4]. Concerning the nature of phase transitions, which eventually lead to these properties, the situation is not completely clear. According to the angle-resolved electron photoemission spectroscopy (ARPES) of TlInSe₂ [5,6], in a certain arbitrary point on the A-line of the Brillouin zone (BZ) the uppermost valence band exhibits a kink structure that transforms into a gap-like structure upon farther temperature decrease. On the other hand, the available experimental data on heat capacity of TlInSe₂ [7-10] are rather ambiguous regarding the clear manifestations of phase transition. The heat effects (if any), accompanying the transition, are small and indicative of the

dependence of the obtained results on the thermal history of the measured samples [8, 10]. In connection with this, we consider it important to mention that memory effects are inherent in incommensurate phases and that our very recent studies of the negative differential resistance, reported earlier for all chain TlMeX₂ [11-13], have disclosed its strong history dependence that was not mentioned before. According to the works [11-13], non-linear electric properties of all chain TlMeX₂ (including TlInSe₂) have thermal nature.

In this work we report the symmetry and dispersion of the phonons, as well as atomic displacements leading to the low-frequency phonons near 0.67Å⁻¹ wave vector along the BZ direction parallel to the chains of TlSe and TlInSe₂. We also discuss the possible nature of incommensurate phase transition in TlInSe₂. All details concerning the calculations of the phonon band structure of TlSe and TlInSe₂ can be found in our recent work [14].

2. PHONON SPECTRA AND SYMMETRIES

In TlSe or TlInSe₂ the full vibration representation consists of 24 modes and is given, depending on the position (Γ -point, T-point, Δ -line, A-line etc.) of the wave-vector in the BZ, as

$$\begin{aligned}\Gamma_{\text{vib}} &= \Gamma_1 + 2\Gamma_2 + \Gamma_3 + 2\Gamma_4 + 3\Gamma_5 + \Gamma_6 + 3\Gamma_9 + 4\Gamma_{10} \\ T_{\text{vib}} &= \Gamma_1 + \Gamma_2 + \Gamma_3 + 3\Gamma_4 + 3\Gamma_5 + \Gamma_6 + \Gamma_7 + 2\Gamma_9 + 4\Gamma_{10} \\ \Delta_{\text{vib}} &= 6\Delta_1 + 8\Delta_2 + 4\Delta_3 + 6\Delta_4 \\ A_{\text{vib}} &= 4A_1 + 2A_2 + A_3 + 3A_4 + 7A_5\end{aligned}$$

Here the irreducible representations Γ_5 , Γ_{10} , T_5 , T_{10} , and A_5 are two-dimensional, while the others are one-dimensional.

Since phonon symmetries in the obtained phonon band structures of TlSe and TlInSe₂ [15] were not specified, here we give these symmetries for each phonon branch shown in

Fig.1 for normal (non-modulated) phases of TlSe (Fig.1a) and TlInSe₂ (Fig.1b). For TlSe (Tl¹⁺Tl³⁺Se₂) and TlInSe₂ the pictures of phonon dispersion and symmetries are very similar. This is seen from Fig.2a (TlSe) and Fig.2b (TlInSe₂), which reproduce the results for low-frequency part of the phonon spectra along the BZ –directions, Δ and A. Note that the results of calculations of phonon dispersion across the BZ of TlSe are in a good agreement with the inelastic neutron scattering (INS) data [15], as we have shown previously [14]. Therefore we believe that phonon band structures we obtained for TlSe and TlInSe₂ are quite reliable.

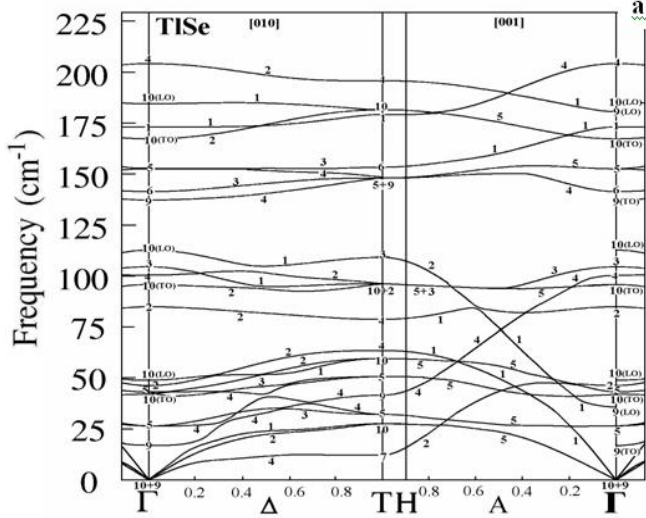


Fig.1 Band structure of TlSe (a) and TlInSe₂ (b) in the directions perpendicular (Δ) and parallel (A) to the chains. Numbers on phonon curves show phonon symmetries.

Comparison shows consistence between the phonon symmetries obtained in this work and the phonon symmetries given by Vakhrushev et al [15] for low-frequency part of the phonon spectra of TlSe. The only exception is the mode A₂ (Fig. 2a) compatible with T₇ symmetry in T-point. Although INS data [15] in the relevant frequency range are not detailed enough for unambiguous conclusions, one may think that, in fact, above mode has A₄ rather than A₂ symmetry. Since A₄-symmetry is also compatible with T₇ symmetry in T-point, we leave the matter for more detailed experimental examination.

While acoustic phonons along Δ -line, which is perpendicular to the chains and connects the centre (Γ) of the BZ and surface point T, correspond to one-dimensional irreducible representations (A₁ to Δ_4 , A₂ to Δ_2 , and A₃ to Δ_1), only LA- mode along A-line, which is parallel to the chains, connects Γ and surface point T' equivalent to T [6], and includes edge point H of the BZ, is described by one-dimensional representation (A₁). In the later case the TA-mode is two-fold degenerated and corresponds to the two-dimensional irreducible representation A₅ (Fig. 2). Especially for the acoustic modes A₁ and A₂, the slopes of the linear sections in the neighbourhood of the BZ centre is small and so would be sound velocities and rates of heat transfer along the direction perpendicular to the chains. Besides, all acoustic branches along Δ -direction are for the most part Einstein-like in both TlSe and TlInSe₂, which may lead to negative Gruneisen parameter for these modes and negative linear expansion coefficient. Note that anti-crossing between acoustic and low-frequency optic branches is similar to that

observed in thermoelectric Ba-Ni-Ge clathrates, pointing on both the strong scattering and low velocity of the acoustic waves responsible for heat transport. The last fact, along with giant thermoelectric power [3], puts TlInSe₂ in a row with promising thermoelectric materials.

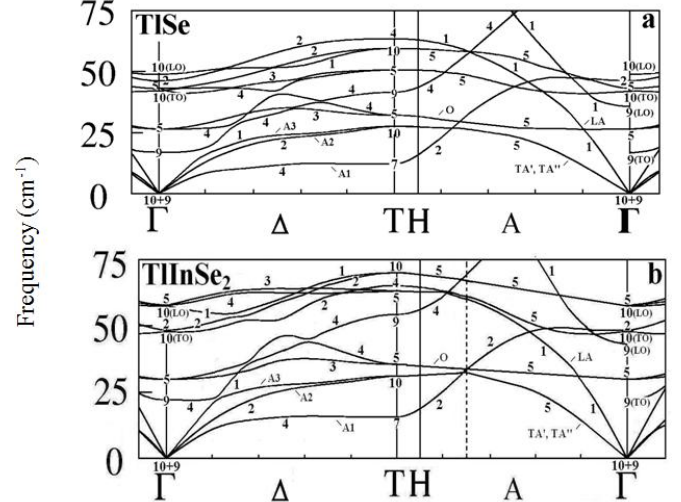


Fig. 2 Low frequency phonon branches along Δ - and A-directions of the Brillouin zone of TlSe (a) and TlInSe₂ (b). Vertical broken line shows the wave vector position at which transversal acoustic branch (TA', TA'') and upper phonon branch (O) that has the same A₅ symmetry come too close to each other in TlInSe₂.

3. POSSIBLE REASON OF INCOMMENSURATE PHASE TRANSITION

A peculiarity of the phonon band structures of TlSe and TlInSe₂ along A-symmetry line is that TA and low frequency optic modes are superimposed, as it is apparent from Fig.2 in which acoustic modes along A-line are indicated as TA', TA'', and LA. Another peculiarity is rather specific and manifests itself in nearly closed-up frequency gap between the transversal acoustic branch (Fig.2, TA', TA'') and upper optic branch (Fig.2, O) at the wave-vector value given by vertical broken line (Fig.1).

Still observable in TlSe (Fig.2a), this gap, however, vanishes upon passing to TlInSe₂ (Fig. 2b) and the modes TA and O, having the same A₅-symmetry, tend to touch each other, which is symmetry-forbidden. It is, therefore, natural to assume that there will develop a structural instability that will lead to the phase transition changing the above-situation to the one allowed by symmetry. As a whole, this might be considered as pseudo- Jahn-Teller effect, proposed earlier for driving force of phase transition in TlGaTe₂ from nuclear-magnetic-resonance studies [16].

In Fig. 3a the position of the above closing-up on the wave-vector scale is shown by vertical broken arrow and is denoted as I. Exactly the same I-point is found to be peculiar from ARPES of TlInSe₂ [6].

Fig. 3b displays the uppermost valence band along A-line of the BZ of TlInSe₂ at low temperature (50K) and the excitation photon energy, 11.4eV, necessary to observe the valence band along Γ -H-T direction. The large dots show the experimental data-points at the accessed wave numbers. The full, dotted, and dashed-dotted curves are the results of simulation. (For more details on the simulation results please refer to our work [6].)

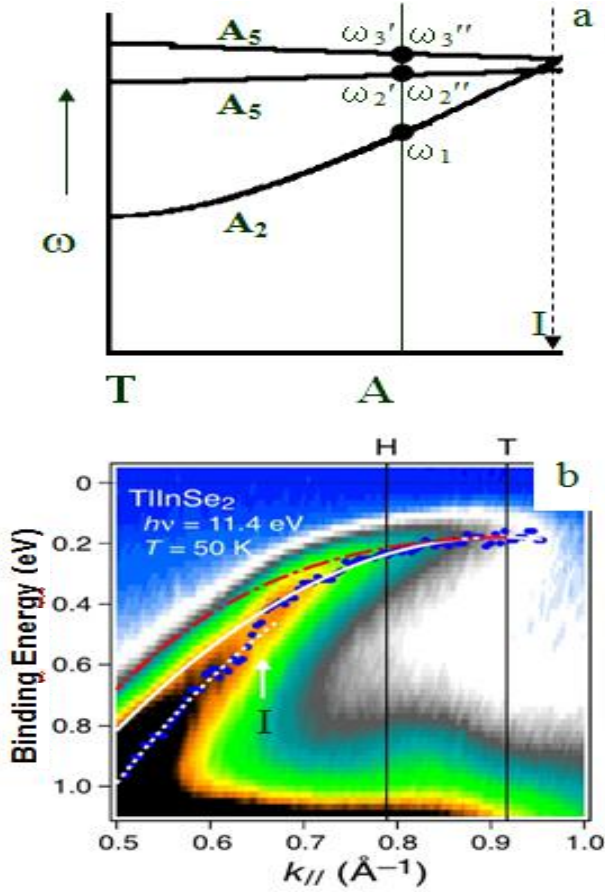


Fig.3 The point (I) related to incommensurate phase transition in TlInSe₂: (a) schematic fragment of the phonon band structure of TlInSe₂; the cross-points (dots) between the vertical lines and phonon dispersion curves are labelled by ω with subscripted integers increasing with increasing phonon frequency, superscripts ' and '' mean that for a given phonon there are two components with the same frequency, vertical broken arrow show the wave-vector position (I) that corresponds to the incommensurate phase; (b) experimental wave-vector dependence of electron binding energy (E) in TlInSe₂, as obtained by angle resolved photoemission spectroscopy [6], the gap-like structure at the wave-vector corresponding to the incommensurate phase is indicated by arrow; large dots – experimental points, full, dotted, and dashed –dotted curves – results of simulation .

There is a gap-like structure shown by vertical arrow in Fig.3b, which is impossible for an electronic band of a non-modulated phase and indicates on phase transition in TlInSe₂ into modulated phase. Since I-point is an arbitrary point on A-line the phase transition is supposed to occur through intermediate incommensurate phase.

Following our reasoning regarding the nature of the I-point peculiarities, evident from both phonon and electron spectra of TlInSe₂, we shall conclude that a possible reason of the incommensurate phase transitions in TlInSe₂ might be lattice instability that develops in I-point (0.67\AA^{-1} [6]) of the BZ with temperature and generates the observed phase transition. If this is true, examination of the valence band of TlSe should bring the evidence that the phase transition (if any) and its manifestation in the form of kink- or gap-like structure are less pronounceable for this material since the closed-up gap between the already-specified phonons slightly opens upon passing from TlInSe₂ to TSe (compare Fig2a and

Fig. 2b). Otherwise, one shall consider the observed phase transition is related to purely electron subsystem.

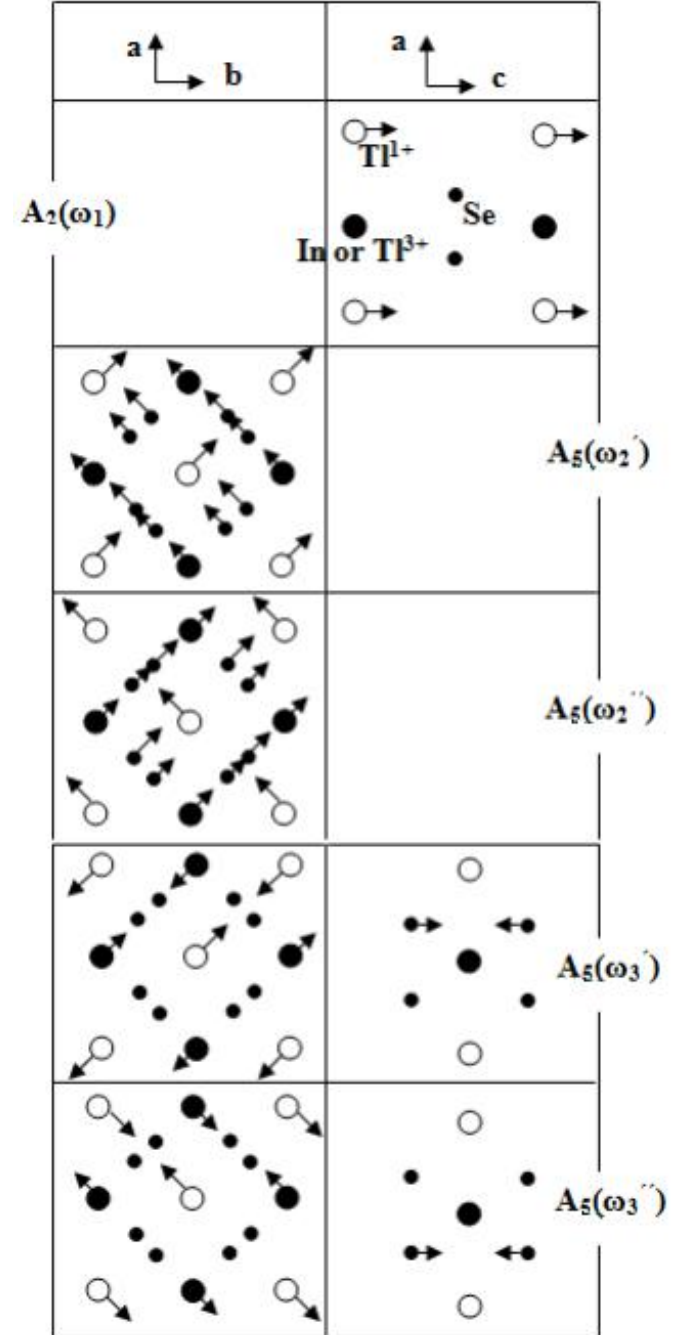


Fig. 4 Atomic displacements in a-b and a-c planes (a,b,c- unit cell vectors) for the phonons along A direction of the Brillouin zone of TlInSe₂; the frequency notation of each phonon is given in brackets after phonon's symmetry, all notations are the same as in Fig. 3.

4. ATOMIC DISPLACEMENTS NEAR I-POINT OF BRULLOUIN ZONE

In Fig.3a in the proximity of the closed-up gap in I-point we have selected a set of the phonon frequencies given by dots and denoted as ω_i ($i=1,2,\dots$). The frequencies of the two-fold degenerated modes are denoted as ω_i' and ω_i'' . The atomic displacements corresponding to the selected set are shown in Fig.4. Only univalent Tl^I atoms are moving along c-direction to form the low frequency A₂ mode with ω_1 frequency. Displacements of all atoms in a-b plane lead to the

phonon with A_5 symmetry, two fold degenerated (ω_2' and ω_2'') in a-b plane. Finally, anti-phase displacements of Tl and In (or threevalent Tl^{III} atoms) in a-b plane, accompanied by anti-phase displacements of Se along c-direction form the optic phonon, O which also have A_5 symmetry and is two-fold degenerated in a-b plane. We would like to mention that the above-picture of atomic displacements is changing while moving along T-H- Γ or T- Γ trajectory. Pure acoustic-type atomic displacements in the neighborhood of Γ point are no longer remaining acoustic away from this point, as it is seen for phonons with ω_2 frequency (Fig. 4).

5. CONCLUSIONS

We have assigned the proper symmetries to all phonons of TlSe and TlInSe₂. We have shown that the crossover observed in TlInSe₂ between low frequency modes with the same symmetry occurs just in the BZ -point that was earlier identified in ARPES studies in relation to incommensurate phase transition. We have proposed that the driving force of this transition in centre-symmetric TlInSe₂ might be pseudo-Jahn-Teller effect. Symmetry considerations related to phase transition are under way.

-
- [1]. D. Müller, G. Eulenberger, and H. Hahn, *Z. Anorg. Allg. Chem.* 398, 207 (1973).
- [2]. D. Muller and H. Hahn: *Z. Anorg. Allg. Chem.* 438, 258 (1978).
- [3]. N. Mamedov, K. Wakita, A. Ashida, T. Matsui, and K. Mori, *Thin Solid Films* 499, 275 (2006).
- [4]. N. Mamedov, K. Wakita, Y. Shim, K. Abe, and N. Ogushi, *Thin Solid Films* 517, 1434 (2008).
- [5]. K. Mimura, K. Wakita, M. Arita, N. Mamedov, G. Orudzhev, Y. Taguchi, K. Ichikawa, H. Namatame, and M. Taniguchi, *J. Electron Spectrosc. Relat. Phenom.* 156-158, 379 (2007).
- [6]. K. Mimura, T. Nogami, K. Abe, K. Wakita, M. Arita, N. Mamedov, G. Orudzhev, H. Namatame, M. Taniguchi, Y. Taguchi, and K. Ichikawa, *Jpn. J. Appl. Phys.* 47, 8188 (2008).
- [7]. K. K. Mamedov, A.M. Abdullayev, and E.M. Kerimova, *Phys. Stat. Sol. A* 44, 115 (1976).
- [8]. M. A. Aldzhanov, N. G. Guseinov, and Z. N. Mamedov *Phys. Sol. State* 30, 332 (1988).
- [9]. A. M. Abdullaev, E. M. Kerimova, and A. K. Zamanova, *Inorganic Materials* 30, 824 (1994).
- [10]. V. A. Aliev and M. A. Aldzhanov, *Inorganic Materials* 34, 207 (1998).
- [11]. M. Halias, A. N. Anagnostopoulos, K. Kambas, and J. Spyridelis, *Phys. Rev. B* 43, 4135 (1991).
- [12]. M. P. Halias and A. N. Anagnostopoulos, *Phys. Rev. B* 47, 4261 (1993).
- [13]. M. P. Halias, J. A. Kalomiros, Ch. Karakotsou, A. N. Anagnostopoulos, and J. Spyridelis, *Phys. Rev. B* 49, 16994 (1994).
- [14]. G. Orudzhev, V. Jafarova, S. Schorr, K. Mimura, K. Wakita, Y. Shim, N. Mamedov, F. Hashimzade, *Jpn. J. Appl. Phys.* 47, 8193 (2008).
- [15]. S. B. Vakhrushev, B. E. Kvyatkovskii, N. M. Okuneva, K. R. Allakhverdiev, R. M. Sardarly, N. A. Bakhyshev, A. Vasilkevich, N. G. Ivanitskii, V. T. Krotenko, and V. I. Slisenko, *Phys. Sol. State* 26, 746 (1984).
- [16]. N. T. Mamedov and A. M. Panich, *Phys. Stat. Sol. A* 117, K15 (1990).

THE CURRENT OSCILLATIONS IN SEMICONDUCTORS IN EXTERNAL ELECTRIC AND MAGNETIC FIELDS.

E.R.GASANOV^{1,2}, T.R.MEHDIYEV¹

¹*G.M. Abdullayev Institute of Physics of Azerbaijan National Academy of Sciences
AZ-1143, G.Javid ave., 33, Baku, Azerbaijan*

²*Baku State University,
AZ-1148, Z.Khalilova str. 23, Baku, Azerbaijan*

The theory of current oscillation in impurity semiconductors in external electric and magnetic fields is given. The strength values of electric and magnetic fields under different experimental conditions, at which instabilities leading to current oscillations in crystal are observed, are obtained. The frequencies of current oscillations are obtained. The theory of oscillation appearance in two-valley semiconductors of GaAs type in strong external electric and magnetic fields is constructed.

INTRODUCTION

The charge carriers: electrons and holes in internal electric field at acceleration by electric field have the additional energy the average value of which in a unit of time on unit of volume is defined as \vec{jE} [1], where \vec{j} is current density and \vec{E} is electric field strength. In stationary state this energy should be equal to energy in average lost in a unit of time by charge carriers at collisions. Let's designate $\dot{\epsilon}$ the energy change in a unit of time of charge carriers because of collisions. It is obvious that $\dot{\epsilon}$ depends on ϵ energy which the charge carrier has. Averaging it on ϵ values we obtain $(\dot{\epsilon})_{cm}$. The condition of energy balance of stationary state under consideration will have the following form:

$$(\vec{jE}) = n(\dot{\epsilon})_{cm} \quad (1)$$

where n is concentration of charge carriers. In thermodynamic equilibrium state the charge carriers give energy in a unit of time upon the average to lattice as much as they receive from one, i.e.

$$(\dot{\epsilon})_{cm} = 0 \quad (2)$$

If in the case of external fields the condition (2) is realized then such fields are considered as weak ones. However, the situation essentially changes at presence of external fields at which the energy obtained by charge carriers from the field increases and the value $(\dot{\epsilon})_{cm}$ calculated for states close to thermodynamic equilibrium ones can be less than (\vec{jE}) .

Then the average energy of charge carriers begins to increase with respect to its equilibrium value. At small equilibrium disturbance the right part of equation (1) can be expanded into series over difference between average energy and its equilibrium value $\frac{3}{2}kT$ by the following expression:

$$(\vec{jE}) = \sum \frac{\frac{3}{2}(\dot{\epsilon}) - kT}{\tau_e} n \quad (3)$$

Here τ_e^{-1} are the expansion coefficients, moreover τ_e is called the average time of energy relaxation, has the time dimension, depends on temperature and scattering

mechanism of charge carriers. The average energy of charge carriers in electric field can exceed its thermodynamic equilibrium value because of comparative slowness of energy exchange process between charge carriers and their surroundings in lattice. If only electrons are charge carriers then this effect will lead to the electron gas heating.

For effect description let's introduce the conception of electron temperature T_e which differs from lattice temperature T .

Let's define T_e by the following expression:

$$(\epsilon) = \frac{3}{2}kT_e \quad (4)$$

Note that average energy (ϵ) should contain the summand connected with kinetic energy of charge carrier system as a whole.

Taking into account the drift of charge carriers the equation (4) is rewritten in the following form:

$$(\epsilon) = \frac{3}{2}kT_e + \epsilon_d \quad (5)$$

Taking into consideration (4) we obtain from (3) the following expression:

$$(\dot{\epsilon}) = \frac{k(T_e - T)}{\tau_e} \quad (6)$$

From (6) it follows that "temperature" T_e depends on electric field strength and the scattering mechanism.

The "heating" of charge carriers leads to the series of consequences observed on the experiment being technical interest. Note that Ohm's law is broken under conditions of charge carrier "heating", the mobility and electric conduction depend on field strength, and charge-drift velocity becomes the non-linear function of field strength.

In general, the flow density is the tensor value and depends on external field direction. Therefore it follows that \vec{j} and \vec{E} vectors can be not parallel to each other. The angle between them depends on \vec{j} vector orientation with respect of crystal crystallographic axes. This effect is called Sasaki effect [2].

The presence of external fields leads to the change of conduction charge carrier number and their mobility. The dependence of charge carrier concentration on field strength is connected with specifics of recombination process. Under

the condition of thermodynamic equilibrium the free electron concentration is only defined by position of Fermi level and temperature. The last one is the result of that the probability of charge carrier capture by recombination centers and probability of reversal emission connect with each other by principle of detail equilibrium.

At system deviation from thermodynamic equilibrium the free charge carrier concentration will depend not only on lattice temperature but on relation between probabilities of processes of capture and reversal emission of charge carriers. The electric conduction decrease will connect with change of charge carrier number and mobility.

GUNN EFFECT

For simpleness let's consider the spatially homogeneous crystal [2-8]. In this case the current density is described by the expression:

$$j = \sigma E; \sigma = en\mu = \sigma(T_e) \tag{7}$$

and equation $j = j(E)$ defines the volt-ampere characteristic of considered sample the graphic picture of which is usually given in coordinates (j, E) . At condition at which Ohm's law is applied, the plot of function $j(E)$ is the direct line passing through origin of coordinates with angular coefficient σ_0 which is equal to conduction value in weak field

As a result of heating of electron gas the volt-ampere characteristic becomes the non-linear one and for its description it is comfortable to introduce the concept of differential conduction σ_d .

When σ is scalar the σ_d value is defined by equation:

$$\sigma_d(E) = \frac{dj}{dE} = \sigma + E \frac{d\sigma}{dE} \tag{8}$$

Using the equilibrium equation:

$$\sigma E^2 = n \frac{T_e - T}{\tau_e} \tag{9}$$

and introducing the variable $R = \left(\frac{T_e - T}{\tau_e}\right)$ we obtain $\sigma E^2 = nR$. The nR value is energy given by current carriers in the lattice in unit of volume. As μ is mobility, n is concentration and τ_e is time depend on temperature T_e then:

$$\sigma_d = \sigma + E \frac{d\sigma}{dT_e} \frac{dT_e}{dE} \tag{10}$$

Differentiating over E the expression (9)

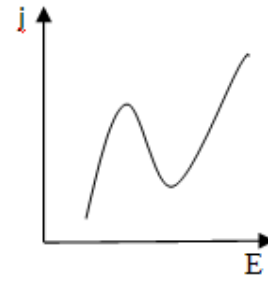
$$\frac{dT_e}{dE} = \frac{2\sigma E}{\frac{d(nR)}{dT_e} - E^2 \frac{d\sigma}{dT_e}}, \tag{11}$$

substituting (11) into (10) and changing E^2 on $\frac{nR}{\sigma}$ we obtain:

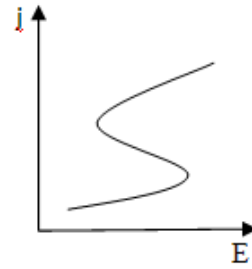
$$\sigma_d = \sigma \frac{\frac{d(nR)}{dT_e} + \frac{nR}{\sigma} \frac{d\sigma}{dT_e}}{\frac{d(nR)}{dT_e} - \frac{nR}{\sigma} \frac{d\sigma}{dT_e}} \tag{12}$$

In dependence on the fact that the formula (12) increases or decreases on field strength, the plot of volt-ampere characteristic $j(E)$ will be inclined up or down from direct

line $j = \sigma_0 E$. The corresponding volt-ampere characteristics of both types have the following form:



N – type characteristics



S – type characteristics

In case of N-type characteristic the differential conduction changes the sign passing zero (the numerator in (12) changes the sign). In case of S-type characteristic the differential conduction changes the sign passing the singular point in which the denominator in (12) takes zero value.

The formation conditions of characteristics of both types are easily found from formula (12):

for N – type characteristics

$$\frac{n^2\mu}{\tau_e} + (T_e - T) \frac{d}{dT_e} \left(\frac{n^2\mu}{\tau_e} \right) = 0 \tag{13}$$

for S – type characteristics

$$1 - \left(\frac{T_e - T}{\tau_e\mu} \right) \frac{d(\tau_e\mu)}{dT_e} = 0 \tag{14}$$

From formula (13) it follows that with increase of electron temperature the product of mobility on concentration of charge carriers should rapidly decrease, moreover T_e should enough exceed the T lattice temperature. In second case (condition (14)), the energy given by electrons in unit of time should rapidly decrease with increase of electron temperature, moreover the overheating $(T_e - T)$ shouldn't be very small one.

One can consider the following facts:

- In homogeneous *n-GaAs* the appearance of N-type characteristic is expected at room temperature. The negative differential conductivity should appear at field strength $E \approx 2300 \text{ V/cm}$ and disappear at $E \approx 10000 \text{ V/cm}$.
- In *n-Ge* doped by aurum or cuprum at lattice temperature 30-35K also should appear the characteristic of N-type.

It is obvious that conception on spatial inhomogeneity in average doesn't exclude the local deviations of physical

values from their average ones. The fluctuations of charge carrier concentrations and electric field strength are caused by random heat motion of charge carriers by other hand and by spontaneous homogeneities in distribution of impurity atoms and other structural defects of crystal lattice. In the case when charge carriers are in the state of thermodynamic balance or close to it the presence of these fluctuations weakly influences on transfer phenomenon. However, the situation can change if charge carriers are strongly "heated". Then at fluctuation of electric field ΔE the fluctuation of charge carrier density should appear and according to Poisson equation it equals to following expression:

$$\Delta \rho = \frac{\epsilon}{4\pi D} \text{div } \Delta E \quad (15)$$

and the current fluctuation has the following form:

$$\Delta j = \sigma_d \Delta E \quad (16)$$

From this it follows that for $\sigma_d > 0$ and $\sigma_d < 0$ cases the charge inflow into fluctuation region changes and fluctuations can either damp or increase, correspondingly.

Thus, in homogeneous crystal the regions of strong and weak fields can appear, moreover, the distribution of electric fields and charge carriers will be fluctuationally instable, correspondingly. These regions so-called domains can form in any point of homogeneous crystal under influence of heat fluctuations and transfer along crystal until they disappear in one of contact electrodes. The domain path velocity essentially depends on mechanism responsible for their appearance in detail for appearance of negative differential conduction and it is possible the observance of such types of non-linear processes as drift and recombination ones.

Note that multi-valley semiconductors in the mechanism of drift nonlinearity the field dependence of mobility plays the main role. In this case the domain path velocity is drift one of majority carriers in weak field. In the mechanism of recombination nonlinearity the processes of capture and generation of charge carriers play the main role. In the dependence on field strength values the relation of concentrations of free and bound charge carrier changes. The domain movement is caused by redistribution of charge carriers between band and capture levels. This process limits the domain path velocity which as a result can be essentially less than drift one.

So in *n-Ge* doped by aurum the domain path velocity at $T=20K$ varies in interval $10^{-5} - 10^{-2}$ cm/sec.

During domain movement along technologically homogeneous sample, the current doesn't change. Achieving to electrode the domain destroys that leads to current increase in the electric circuit. The appearance of new domain on another electrode leads to new current decrease in the electric circuit. This cyclic process of origin, motion and destroy of domains leads to periodic current oscillations in electric circuit load. The current oscillation frequency ω is easily evaluated. If v_d is domain path velocity, L is sample length in current direction, then domain time of flight through sample is equal to $t = \frac{L}{v_d}$. From this it follows that

$$\omega = 2\pi \frac{v_d}{L} \quad (17)$$

In *n-GaAs* the oscillation frequency varies in interval $5 \cdot 10^8 \div 5 \cdot 10^9$ Hz.

The oscillation appearance in *n-GaAs* and in similar materials was firstly observed by Gunn and nowadays is widely used in micro-semiconductor electronics at development of microwave generators.

CURRENT OSCILLATIONS IN IMPURITY SEMICONDUCTORS.

In impurity semiconductors the number of electrons and holes changes because of capture and generation of charge carriers by impurity centers [9-14]. It is possible to experimentally reveal the current oscillations in semiconductors with deep centers (traps) studying the impedance change appearing at introducing of the given semiconductor in electric circuit. Under the given conditions in some frequency region the active resistance introducing by semiconductor into electric circuit and consequently the value of impedance real part can be negative one. The last one means that current oscillations should appear and consequently the instability on impedance can be observed.

There are two types of instabilities. If the oscillations of charge carriers take place only inside the semiconductor, but aren't observed in external electric circuit then such type of instability is called internal instability. If the oscillations of charge carriers are observed in external circuit then such type of instability is called external instability.

In the present paper the external instability has analyzed for semiconductors with certain impurities.

Let's consider the impurity semiconductor with deep negatively charged traps and charge carriers of both signs, i.e. the electrons and holes with n_- and n_+ concentrations. Let's suppose that concentration of deep traps is N_0 , N of them is concentration of once negatively charged traps and N is concentration of doubly negatively charged traps. Then:

$$N_0 = N + N.$$

Note that such model is to germanium doped by aurum impurities. The continuity equation for electrons and holes has the following form [15]:

$$\frac{\partial n_-}{\partial t} + \text{div } j_- = \left(\frac{\partial n_-}{\partial t} \right)_{rec.} \quad (18)$$

$$\frac{\partial n_+}{\partial t} + \text{div } j_+ = \left(\frac{\partial n_+}{\partial t} \right)_{rec.}$$

$$\left(\frac{\partial n_-}{\partial t} \right)_{rec.} = \gamma_-(0)n_{1-}N_- - \gamma_-(E)n_-N \quad (19)$$

$$\left(\frac{\partial n_+}{\partial t} \right)_{rec.} = \gamma_+(E)n_{1+}N_+ - \gamma_+(0)n_+N$$

Here $\gamma_-(E)$ and $\gamma_+(E)$ are coefficients of trapping and ejection of electrons by once negatively charged traps at presence of electric field, correspondingly.

$$\text{At } E=0; \gamma_-(E) = \gamma_-(0) \text{ u } \gamma_+(E) = \gamma_+(0)$$

$$n_{1-} = \frac{n_0^0 N_0}{N_0^0}; \quad n_{1+} = \frac{n_+^0 N_0^0}{N_0} \quad (20)$$

The equation describing the concentration variation of charged traps on time in current carrier recombination and generation processes has the form:

$$\frac{\partial N_{\pm}}{\partial t} = \left(\frac{\partial n_{\pm}}{\partial t} \right)_{rec.} - \left(\frac{\partial n_{\pm}}{\partial t} \right)_{rec.} \quad (21)$$

The quasineutrality condition at presence of recombination and generation of charge carriers means that total current doesn't depend on coordinates but depends on time. Thus

$$\begin{aligned} \text{div } \mathbf{J} &= e \cdot \text{div}(j_+ - j_-) = 0; \\ j_+ &= n_+ \mu_+(E) E - D_+ \nabla n_+; \\ j_- &= -n_- \mu_-(E) E - D_- \nabla n_-; \end{aligned} \quad (22)$$

It is easily proved that taking into account of dependence of electron and hole mobilities on electric field doesn't lead to essential corrections to mobility values. For example, linearized mobility of electrons and holes will have the form:

$$\mu_{\mp} = \mu_{\mp}^0 \left(1 + \frac{d(\ln \mu_{\mp})}{d(\ln E_0^2)} \right) \text{ и } \frac{d(\ln \mu_{\mp})}{d(\ln E_0^2)} \sim 1. \text{ In the case of dispersion lattice acoustic oscillations have } \mu_{\mp} \sim E^{-\frac{1}{2}} \text{ и } \frac{d(\ln \mu_{\mp})}{d(\ln E_0^2)} = -\frac{1}{r} \text{ and in the case of dispersion on lattice optic oscillations we obtain: } \frac{d(\ln \mu_{\mp})}{d(\ln E_0^2)} = 1$$

Let's suppose that concentration of electrons and holes is big enough, so diffusion coefficient satisfy to Einstein relation $D_{\pm} = \frac{k_0 T}{e} \mu_{\pm}$. Supposing

$$n_{\pm} = n_{\pm}^0 + \Delta n_{\pm}; \quad N_{\pm} = N_{\pm}^0 + \Delta N_{\pm}; \quad E = E_0 + \Delta E \quad (23)$$

we linearize the equation (19-22) on small inclinations. The oscillating current $\Delta \mathbf{J}$ is proportional to $\sim e^{-i\omega t}$ and each of rest variables n_{\pm} , N_{\pm} и E are the sum of two members the one of which is proportional to $\sim e^{-i\omega t}$, and other one is proportional to $\sim e^{i(kx - \omega t)}$, where κ is wave vector, ω is oscillation frequency. For example

$$\Delta n_{\pm} = \Delta n'_{\pm} e^{-i\omega t} + \Delta n''_{\pm} e^{i(kx - \omega t)} \quad (24)$$

Let's confine ourselves by the solving plan because of calculation inconvenience. Excluding $\Delta N'_{\pm}$, $\Delta N''_{\pm}$, $\Delta E'$, $\Delta E''$ we obtain the equation systems for obtaining of $\Delta n'_{\pm}$, $\Delta n''_{\pm}$ and wave vector κ :

$$\begin{cases} U_{-}(k) \Delta n''_{-} + U_{+}(k) \Delta n''_{+} = 0 \\ C_{-}(k) \Delta n''_{-} + C_{+}(k) \Delta n''_{+} = 0 \end{cases} \quad (25)$$

$$\begin{cases} U_{-}(0) \Delta n''_{-} + U_{+}(0) \Delta n''_{+} + U \Delta J = 0 \\ C_{-}(0) \Delta n''_{-} + C_{+}(0) \Delta n''_{+} + C \Delta J = 0 \end{cases}$$

Coefficients $U_{\pm}(k, 0)$ and $C_{\pm}(k, 0)$ depend on character frequency and constant electric field.

To find κ wave vector we solve the dispersion equation obtained from determinant of U_{\mp} and C_{\mp} coefficients, i.e.

$$U_{-} C_{+} - U_{+} C_{-} = 0 \quad (26)$$

Let's consider solutions of (26) in two limit cases:

- 1) high-frequency limit: $\omega \gg \nu_{\mp}$, ν_t^E ;
- 2) low-frequency limit: $\omega \ll \nu_{\mp}$, ν_t^E

$\nu_{-} = \gamma_{-}(E_0) N_0$ is frequency of electron capture by once charged traps;

$\nu_{+}^E = \gamma_{+}(E_0) N_0$ is frequency of ejection of holes doubly charged traps;

$\nu_{+} = \gamma_{+}(0) N_0^0$ is frequency of hole capture by doubly charged traps.

To obtain κ wave vector values we take into consideration the following condition: $k_0 T \ll l E_0$ at $k_0 T \sim 10^{-14}$ erg, $L \sim 1$ cm, $E_0 \gg 6 \cdot 10^{-2}$ V/cm (l is sample length).

Neglecting small values we obtain:

$$\Delta n_{\pm}(x, t) = D_{1}^{\pm} e^{i k_1 x} + D_{2}^{\pm} e^{i k_2 x} + D^{\pm} \Delta J \quad (27)$$

$D_{1,2}^{\pm}$ contacts are found from boundary conditions. The contacts are always in some degree "straightening" ones. Thus, so-called ohmic contacts present themselves limit cases. One can difference two types of boundary conditions in dependence on filter directions of both contacts:

- the particles of similar signs inject on both contacts

$$\Delta n_{+}(0) = \delta_{+}^0 \Delta J, \quad \Delta n_{+}(L) = \delta_{+}^L \Delta J$$

or

$$\Delta n_{-}(0) = \delta_{-}^0 \Delta J, \quad \Delta n_{-}(L) = \delta_{-}^L \Delta J$$

- the particles of opposite signs inject on both contacts

$$\Delta n_{+}(0) = \delta_{+}^0 \Delta J, \quad \Delta n_{-}(L) = \delta_{-}^L \Delta J$$

or

$$\Delta n_{-}(0) = \delta_{-}^0 \Delta J, \quad \Delta n_{+}(L) = \delta_{+}^L \Delta J$$

Here $\delta_{\pm}^{0,L}$ are injection rates.

Thus, defining constants $D_{1,2}^{\pm}$ one can calculate the crystal impedance using the following expression:

$$\Delta E(x,t) = \frac{1}{\sigma} [\Delta J - ev_- \Delta n_-(x,t) - ev_+ \Delta n_+(x,t) + \frac{T}{e} \mu_+ \nabla n_+(x,t) - \frac{T}{e} \mu_- \nabla n_-(x,t)] \quad (28)$$

$$z = \frac{1}{\Delta JS} \int_0^L \Delta E(x,t) dx$$

Here L is crystal length, S is crystal cross-sectional area, $v_{\pm} = \mu_{\pm} E_0$ are drift velocities of electrons and holes, correspondingly, T is temperature in erg.

The impedance will depend on injection rates $\delta_{\pm}^{0,L}$ различным образом in dependence on straightening on contacts.

The expression (28) for impedance in general case is very complex and unwieldy. Thus, let's analyze it for following cases:

$$\left\{ \begin{array}{l} 1. n_-^0 \gg n_+^0, \text{ is given } \delta_+^0 \\ 2. n_-^0 \gg n_+^0, \text{ is given } \delta_-^0 \\ 3. n_-^0 \ll n_+^0, \text{ is given } \delta_-^L \\ 4. n_-^0 \ll n_+^0, \text{ is given } \delta_+^L \end{array} \right. \quad (29)$$

Note that the following equation is taken into consideration before analyzing (28) with help of (29) at linearization of corresponding equation:

$$\beta_{\pm}^{\gamma} = \frac{d(\ln(\nu_{\pm}(E_0)))}{d(\ln(E_0^2))} \gg 1 \quad (30)$$

Taking into consideration (30) and $ev_{\pm} \delta_{\pm}^{0,L} \ll 1$, let's write for all cases (29) for real and imaginary impedance parts the following expression:

A. High-frequency limit: $\omega \gg v_{\mp}, v_t^E$

Case 1: $n_-^0 \gg n_+^0$, is given δ_+^0

$$\left\{ \begin{array}{l} \frac{Re(z)}{z_0} = -\frac{v_+}{L\omega}, z_0 = \frac{1}{\sigma_0 S}, \sigma_0 = e(n_-^0 \mu_-^0 + n_+^0 \mu_+^0) \\ \frac{Im(z)}{z_0} = 0, ev_+ \delta_+^0 = \frac{\mu_+}{2\mu_-} \ll 1, \beta_1^{\gamma} = \frac{\omega}{2v_-} \gg 1 \\ \beta_1^{\gamma} = \frac{1}{2} \cdot \frac{n_-^0}{n_+^0} \cdot \frac{v_-}{v_+} \gg 1 \end{array} \right.$$

The oscillation frequency is found from $\left(-\frac{Re(z)}{z_0} + R\right) = 0$ equation, where R is electrical resistance. From this it follows:

$$\omega = \frac{z_0}{R} \cdot \frac{v_+}{L} \quad (31)$$

Electric field at frequency (31) changes in region

$$v_+ \gg \frac{L\omega}{2} \quad (32)$$

Case 2: $n_-^0 \gg n_+^0$, is given δ_-^0 ;

$$\omega = 2v_- \cdot \frac{R}{z_0} \cdot \frac{1}{ev_- \delta_-^0}, E \gg \left(\frac{Lv_- R}{z_0 \mu_- \mu_+ e \delta_-^0}\right)^{1/2}$$

Case 3: $n_-^0 \ll n_+^0$, is given δ_-^L ;

In this case the impedance can be negative by only oscillation method.

Case 4: $n_-^0 \ll n_+^0$, is given δ_+^L ;

B. Low-frequency limit: $\omega \ll v_{\mp}, v_t^E$

1 case: $n_-^0 \gg n_+^0$, is given δ_+^0

In this case $Im(z) > 0$ и $Re(z)$ can be negative as the function of $\sin \alpha$ \ and $\cos \alpha$, $\alpha = \frac{L\omega}{v_{\mp}}$

2 case: $n_-^0 \gg n_+^0$, задано δ_-^0

The current oscillations can appear in external electric circuit by oscillation form.

3 case: $n_-^0 \ll n_+^0$, is given δ_-^L ;

4 case: $n_-^0 \ll n_+^0$, is given δ_+^L

In cases 3 and 4 the oscillations don't appear at all.

The analysis of above mentioned results shows that current oscillations in considered impurity semiconductors mainly take place because of change of electron concentration. The electron capture by impurity centers leads to bigger current oscillation than hole capture. Note that in this process the contacts are inject ones, but not ohmic ones.

For impedance analysis at presence of external magnetic field it is necessary to take into consideration the dependence of current density on magnetic field.

$$\vec{j}_{\pm} = \pm n_{\pm} \mu_{\pm}(E, H) \vec{E} + n_{\pm} \mu_{1\pm}(E, H) [\vec{E}, \vec{h}] \pm \pm n_{\pm} \mu_{2\pm}(E, H) \vec{h} (\vec{E} \vec{h}) - D_{\pm} \nabla n_{\pm} \mp D_{1\pm} [\nabla n_{\pm} \vec{h}] - D_{2\pm} (\nabla n_{\pm} \vec{h}) \quad (33)$$

Here \vec{h} is unit vector on magnetic field; $\mu_{\pm}(E, H)$, $\mu_{1\pm}(E, H)$, $\mu_{2\pm}(E, H)$ are ohmic, Hall and focusing mobilities of holes and electrons, correspondingly; D_{\pm} , $D_{1\pm}$, $D_{2\pm}$ are ohmic, Hall and focusing coefficients of diffusion charge carriers, correspondingly.

For impedance calculation at the presence of external magnetic field let's consider the case when charge carrier has the effective temperature:

$$D_{\pm} = \frac{T_{eff}}{e} \mu_{\pm}, T_{eff} = \frac{T}{3} \left(\frac{cE_0}{SH}\right)^2 \quad (34)$$

where S is sound speed, c is light speed, T is temperature in erg. Note that the given task is related to three-dimensional ones at the presence of magnetic field and consequently, the

crystal sizes play the essential role. Let's consider the crystal the sizes of which satisfy to following conditions $L_y \ll L_x, L_y \ll L_x$. Let's external electric field is directed along x axis, but magnetic one is directed to Z axis. Let's calculate the impedance for high-frequency $\omega \gg \nu_{\mp}, \nu_{\pm}^E$ and low-frequency $\omega \ll \nu_{\mp}, \nu_{\pm}^E$ cases.

The frequency of current oscillations at the presence of magnetic field besides the physical values very strongly depends on injection rates. At small values of magnetic field ($\mu_{\pm}H \ll c$) the variation interval of electric field in which the instabilities on impedance appear, practically doesn't change. Let's consider the classically strong magnetic field ($\mu_{\pm}H \gg c, H \gg H_{char.} = \frac{c}{\mu_{\pm}}$) and after complex algebraic calculations for real and imaginary impedance parts we obtain the following expressions:

$$1) \quad \omega \gg \nu_{\mp}, \nu_{\pm}^E$$

$$\frac{Re z}{z_0} = \left(\frac{H}{H_{char.}} \right)^2 \left(1 - \frac{H_1}{H} + \frac{H_2}{H} - \frac{H^2}{H_{char.}H_3} \theta \right);$$

$$\mu_- H \theta \ll c$$

$$\frac{Im z}{z_0} = \left(\frac{H}{H_4} \right)^4 (v_{\mp}^E H_2' - v_- H_1') \frac{1}{\omega H};$$

$$\theta = \frac{2L_x v_- (n_+ v_{\mp}^E \beta_{\mp}^{\gamma} + n_- v_- \beta_{\mp}^{\gamma})}{n_0 k_y u_0^2} \quad (35)$$

Here

$$H_1 = a H_{char.} \left(1 + \frac{\beta_{\mp}^{\gamma}}{\beta_{\mp}^{\gamma}} \cdot \frac{v_{\mp}^E}{v_-} \cdot \frac{n_+}{n_-} \cdot \frac{\mu_{\mp}}{\mu_-} \right) =$$

$$= a H_{char.} \left(1 + b \frac{v_{\mp}}{v_-} \right)$$

$$a = \frac{2v_- n_- \beta_{\mp}^{\gamma}}{n_0 \omega \theta}; \quad b = \frac{\beta_{\mp}^{\gamma}}{\beta_{\mp}^{\gamma}} \cdot \frac{n_+}{n_-} \cdot \frac{\mu_{\mp}}{\mu_-};$$

$$H_4 = \left[\frac{c}{\mu_-} \cdot \frac{2T k_y}{3e E_0} \left(\frac{v_-}{S} \right)^2 \right]^{1/4};$$

$$H_2 = a H_{char.} \left(1 + b \frac{v_{\mp}}{v_-} \right); \quad H_1' = H_{char.} a;$$

$$H_2' = H_{char.} a \cdot \frac{n_+}{n_-} \cdot \frac{\beta_{\mp}^{\gamma}}{\beta_{\mp}^{\gamma}};$$

$$H_3 = H_{char.} \cdot \frac{\mu_-}{\mu_+} \cdot \frac{\theta}{e u_- \delta}; \quad \delta = \delta_-^0 + \delta_+^0 + \delta_-^L + \delta_+^L$$

At $Re z$ current oscillations passing through zero becomes negative value and moreover, $Im z$ can take any sign. From (35) it follows that there are different variation intervals of magnetic field in which $Re z$ and $Im z$ can change the signs. For simpleness we confine ourselves by following case:

$Re z = 0$ и $Im z = 0$.

From (35) one can easily find that at $\frac{\beta_{\mp}^{\gamma}}{\beta_{\mp}^{\gamma}} = \frac{v_-}{v_+}$. $\frac{n_-}{n_+}$ $Im z = 0$ and at $H_1 = H_2$, i.e. when hole radiation

frequency ν_{\mp}^E will be equal to hole capture frequency $\nu_{\mp}^E = \nu_{\mp}$, at following values of external magnetic field,

$$H = H_{char.} \left(\frac{1}{e v_- \delta} \right)^{1/2} \quad (36)$$

the impedance real part $Re z = 0$, the current oscillations appear and take place.

2) $\omega \ll \nu_{\mp}, \nu_{\pm}^E$

$$\frac{Re z}{z_0} = \left(\frac{H}{H_x} \right)^2 \left[1 - \left(\frac{v_{\mp}^E H_2'}{v_{\mp} H} + \frac{H}{H_3} \right) \frac{\mu_- H \theta}{c} \right];$$

$$Im z = 0; \quad \frac{\beta_{\mp}^{\gamma}}{\beta_{\mp}^{\gamma}} = \frac{v_-}{v_{\mp}^E} \cdot \frac{n_-}{n_+}$$

$Re z = 0$ at $H = (H_{char.} H_3)^{1/2}$ when the condition is carried out:

$$\frac{v_{\mp}^E}{v_{\mp}} < \frac{1}{2} \frac{n_0}{n_+} \cdot \frac{1}{\beta_{\mp}^{\gamma}}$$

Thus at the presence of external magnetic field the capture and radiation of holes play the essential role.

CURRENT OSCILLATIONS IN TWO-VALLEY SEMICONDUCTORS.

The current oscillations in external magnetic field in two-valley semiconductors of GaAs type had been firstly studied by Gunn. Beginning from given value of electric field, the current oscillations with microwave frequency $\omega \sim 10^9 \div 10^{11} Hz$ appear. This effect is studied in many theoretical works only near threshold, i.e. when differential conductivity $\sigma_d = \frac{dj}{dE} = 0$ (N -type characteristics).

When conductivity becomes negative one, i.e. $\sigma_d < 0$ the distribution of electric field E in crystal becomes inhomogeneous one, the strongly expressed electric field regions, i.e. domains form. Moreover, the amplitude of current oscillations from some moment begins to depend on time, the task becomes nonlinear one and its theoretical solving becomes the complex one. In this part the some results of theoretical investigations of nonlinear Gunn effect in region $\sigma_d < 0$ at presence of constant electric field will be discussed [16-18].

Let's total concentration of charge carriers is as follows $N = n + n'$, the mobilities of charge carriers μ and μ' , diffusion coefficients D and D' satisfy the following conditions:

$$D \gg D'; \quad \mu \gg \mu'; \quad n \gg n'; \quad n = fN = f(E)N(E) \quad (37)$$

$$f(E) = (m-1) \left[m-1 + \left(\frac{E}{E_a} \right)^m \right]^{-1}$$

Parameter m is calculated from experimental data as the relation of ohmic current to actual one in point $E_0 = E_a$ ($\sigma_d \neq 0$).

The rate of σ dynamic conductivity to conductivity in weak field σ_0 has the form:

$$S_0 = \frac{\sigma}{\sigma_0} = \frac{1}{\sigma_0 E_a} \frac{df_0}{dx_a} = \left(f_0 + x_0 \frac{df_0}{dx_a} \right) \quad (38)$$

Since $x_0 = \frac{E_0}{E_a}$ then in the point of zero inclination we have $x_0 = 1$; $f_0 = -\frac{df_0}{dx_a}$ and static current in it is as follows:

$$J_p = \frac{m-1}{m} \sigma_0 E_a; \quad m = \frac{1}{1 - \frac{J_p}{\sigma_0 E_a}} \quad (39)$$

The dynamics of current passage through sample is described by following equations:

$$J = e f N \mu E + D e \frac{\partial(fN)}{\partial x}; \quad \frac{\partial J}{\partial x} = e \frac{\partial N}{\partial t} \quad (40)$$

$$J_1 + \varepsilon \frac{\partial E_1}{\partial t} = 0; \quad u_0 = -\mu E_0$$

Supposing $J = J_0 + J_1$; $E = E_0 + E_1$; $N = N_0 + N_1$ and all inclinations from equilibrium values have the following form: $(E_1, J_1, N_1) \sim e^{i\omega t}$. From equation (40) for all values $(E_1, J_1, N_1) \leq (E_0, J_0, N_0)$ and $y = \frac{N_1}{N_0}$ we obtain:

$$\frac{\partial^2 y}{\partial t^2} + \omega_0^2 y = \frac{\sigma_0 f_0}{\varepsilon \omega_0} \Phi \left(y, \frac{dy}{dt}, \frac{d^2 y}{dt^2} \right) \quad (41)$$

Here $\omega_0^2 = \frac{\sigma_0 f_0}{\varepsilon} (k u_0 + D k^2)$. Let's introduce the designations: $r = \frac{\sigma_0 f_0}{\varepsilon \omega_0}$ and $\tau = \omega_0 t$. From this it follows that equation (41) is to equations of Van-der-Pole type

$$\frac{\partial^2 y}{\partial \tau^2} + \omega_0^2 y = r F \left(y, \frac{dy}{d\tau}, \frac{d^2 y}{d\tau^2} \right) \quad (42)$$

For crystal GaAs r is small parameter ($r \ll 1$), $D = 130 \frac{sm^2}{s}$, $u_0 \approx 10^7 \frac{sm}{s}$, $\omega_c = \frac{\sigma_0}{\varepsilon} \approx 10^{12} s^{-1}$.

The solution (42) at $r=0$ has the form $y = a(0) \cos(\tau + \theta) = a \cos \psi$. To solve the differential equation (42) at value $r \neq 0$ let's use Bogolubov-Mitropolsky's method:

$$\frac{da}{d\tau} = r A_1(a) + r^2 A_2(a);$$

$$\frac{d\psi}{d\tau} = \omega_0 + r B_1(a) + r^2 B_2(a) + \dots; \quad (43)$$

$$A_1(a) = -\frac{\omega_0}{2\pi} \int_0^{2\pi} F \left(y, \frac{dy}{d\tau}, \frac{d^2 y}{d\tau^2} \right) \sin \psi d\psi;$$

$$B_1(a) = -\frac{\omega_0}{2\pi a} \int_0^{2\pi} F \left(y, \frac{dy}{d\tau}, \frac{d^2 y}{d\tau^2} \right) \cos \psi d\psi$$

Let's confine ourselves by second approximation and after easy calculations we obtain:

$$a_1 = a_0 \exp \left(\frac{r}{2} \left[\frac{m(1-f_0) D k \varepsilon}{u_0} \right] \omega t \right) \quad (44)$$

$$a_2 = \frac{a_0}{\left[\exp \left(-\frac{m D k \sigma_0 f_0 t}{2 u_0} \right) + \frac{m \omega_0 D k \varepsilon}{48 k u_0 u_0} a_0^2 \right]} \quad (45)$$

From (44) it follows that when external field satisfies to condition $E_0 > E_a \left(\frac{2u_0}{3Dk\varepsilon} \right)^{1/2}$ then the amplitude increases in first approximation and in second approximation $a_2 \rightarrow \left(\frac{48ku_0}{m\omega_0} \cdot \frac{u_0}{Dk\varepsilon} \right)^{1/2}$ tends to constant (limiting) value.

For current density propagating in crystal in external electric \vec{E}_0 and magnetic \vec{H}_0 fields let's write the following equation:

$$\vec{J} = en\mu\vec{E} + en\mu'[\vec{E}\vec{H}] + eD\nabla\vec{n} + eD'[\nabla\vec{n}\vec{H}] \quad (46)$$

One can chose the following geometry for electric and magnetic fields: $\vec{H}_0 = H_{0z}\vec{h}$, $\vec{E}_0 = E_{0x}\vec{l}$ where \vec{h} and \vec{l} are unit vectors along z and x axes. Van-der-Pole equation at presence of magnetic field has the following form:

$$\frac{\partial^2 R}{\partial t^2} + \omega_0^2 R = r\Phi \left(R, \frac{\partial R}{\partial t} \right); \quad R = \frac{n'}{n_0}$$

$$r = \frac{\omega_0}{k_x u_0} \ll 1; \quad \omega_0 = \left[\frac{\sigma_0 f_0 (k u_0 + k_x^2 D^+)}{\varepsilon} \right]^{1/2}; \quad (47)$$

$$\Phi = \omega \frac{\partial R}{\partial t} \left[\frac{f_0 m (1-f_0) \sigma_0 D' k_x (1+R)}{u_0 \omega_0} + mR(f_0 - 1) - m - 1 \right] + \left(\frac{\partial R}{\partial t} \right)^2 \frac{m(1-f_0)+R+2}{k u_0 \omega_0}$$

From (47) we find the amplitude:

$$A = A_0 e^{-\frac{r\omega_0 y t}{2}} \quad (48)$$

$$\gamma = 2r + \frac{\sqrt{2}}{f_0^2} \cdot \frac{H_0}{H_{char.}} + \frac{k_x D}{f_0 u_0} + \frac{\sqrt{2k_x D'}}{f_0^2 u_0} \left(\frac{L_x}{L_y} - 1 \right)$$

The crystal is in instable state at appearance of current oscillations and at definite magnetic field strength \vec{H}_0 the wave the frequency of which can be defined in nonlinear approximation from the solution of following equation

$$\frac{\partial^2 R}{\partial t^2} + \omega_1 \frac{\partial R}{\partial t} + \omega_2^2 R = 0 \quad (49)$$

where ω_1 and ω_2 are character frequencies

From equation solution it follows that the external magnetic field strength varies in interval

$$H_1 < H_0 < H_2$$

where

$$H_1 = \frac{\sqrt{2m}}{m-1} H_{char.};$$

$$H_2 = H_{char.} \cdot \frac{u_0 L_x}{D} \left[\frac{m u_0}{2\pi L_x \sigma_0 (m-1)} \right]^{1/2}$$

The wave frequencies

$$\omega_0 = \frac{H_{char.}}{H_0} \left[\frac{\sigma_0 k_x u_0 (m-1)}{m} \right]^{1/2}$$

decrease with magnetic field increase.

1. *E.Konuyel*. The kinetic properties of semiconductors in strong electric fields, "World", Moscow, 1970.
2. *J.R.Gunn*. Solid State Communication, 1, 88, 1963.
3. *B.K.Ridley, T.B.Watkins*, Proc.PhysSoc.78, 293, (1961).
4. *C.Hilsum*. Proc IRE. 50, 185 (1962).
5. *A.G.Chynoweth, W.L.Feldman, D.E.McCumber*. Proc. Int. Conf. Phys. Semicond. Kyoto, 1966, p 514.
6. *R.W.H.Engelmann, C.F.Quate*, IEEE Trans. ED-13, 14 (1966)
7. *E.R.Hasanov, R.K.Gasimova, A.Z.Panahov, A.H.Demirel* Progress of Theoretical Physics, vol.121, № 3, March 2009.
8. *E.R.Hasanov, R.K.Qasimova, A.Z.Panahov and A.H.Demirel* Adv. Studies Theor. Phys., vol.3, 2009, №8, 293-298.
9. *L.E.Gurevich and E.R.Gasanov*, PhTT, 11, 1433, 1969.
10. *I.A.Kurova, S.G.Kalashnikov*, PhTT, 5, 3224, 1963.
11. *M.S.Kachan, S.G.Kalashnikov, N.G.Jdanov* Phys.Stat.Sol. 24, 551 (1967)
12. *V.I.Stafeyev*, PhTT, 5, 3095.
13. *E.R.Gasanov, K.B.Gurbanov, Rasoul Nezhad Hossein*, International Journal for knowledge, science and technology, October 2009, № 1, vol.1, pp.114-120.
14. *E.R.Hasanov, K.B.Gurbanov*, Azerbaijan National Academy of Sciences Transacctionic, volume XXIX, №5, 2009, pp.108-111.
15. *V.L.Bonch-Bruyevich, P.S.Serebrennikov*, "The radio engineering and electronics", vol.XIV, 1648, 1969.
16. *N.N.Bogolubov, U.A.Mitropolskii* "Asymtotic methods in theory of non-linear oscillations", Gosizdat, 1963.
17. *E.R.Gasanov, R.K.Gasimova*. ANA of Sciences Transactions, vol.XXV, №5, 2005, 139-143.
18. *J.Copeland* IEEE, Trans., ED.13., 189, 1966.

CONTENT

1.	Laser crystallization induced multicrystalline silicon thin film solar cells on glass: European High-EF project.....A.Antoni, E. Fogarassy, A. Slaoui, Y. Leroy, Z. Said-Bacar, F. Falk, E. Ose, S. Christiansen, G. Sarau, J. Schneider, N. Lichtenstein, B. Valk, M. Leclercq, R. Lewandowska, J. Michler, X. Maeder, A.-S. Dehlinger, J. Lábár, G. Sáfrán	3
2.	Turkish accelerator complex, fel resonator system Hatice Duran Yildiz	7
3.	M^2 qualify laser beam propagation.....Abdelhalim Bencheikh, Mohamed Bouafia	11
4.	Effect of CO ₂ Laser Focusing on Groove Cutting into Steel Surfaces.....Suleyman Biyikli and Jale Yilmazkaya Sungu	16
5.	Preliminary Results From The New Multiwavelength Aerosol Lidar In Turkey.....K.R. Allakhverdiev, T. Baykara, M. Bekbolet, M. F. Huseyinoglu, S. Ozbek, Z. Salaeva, A. Secgin, S. Vartapetov, I. Veselovskii, M. Korenskii	22
6.	Near ir laser light visualizers using nonlinear GaSe and other layered crystallites.....K. R. Allakhverdiev, M. Ö. Yetis, T. B. Baykara, S. Özbek, E. Yu. Salaev	26
7.	The erosive laser plume ions component researches at the silicon ablation in vacuumE.V. Khaydukov, V.V.Rocheva, A.A. Lotin, O.A. Novodvorsky, V.Ya. Panchenko	29
8.	Experimental investigation of different refining stages influences on optical and ultrasonic signals in paper pulp suspensions..... Jan Niemi	33
9.	Tree Mapping Using a Time-of-Flight 3D Camera..... Arttu V.H. Ollikkala, Anssi J. Mäkynen	37
10.	The optical and structural properties of quantum wells Mg _{0.27} Zn _{0.73} O/ZnO produced by pulsed laser deposition.....A.A. Lotin, O.A. Novodvorsky, L.S. Parshina, E.V. Khaydukov, O.D. Khramova, V.Ya. Panchenko	41
11.	Compact Raman (CLS) spectrometer for active test of liquid and solid samples.....K.R.Allakhverdiev,T.K.Baykara,A.M.Secgin,S.Ozbek,A.M.Ulubey,Z.Yu.Salaeva, M.F.Huseyinoglu, S. L. Druzhinin, K.A. Konovalov, V. Y. Shchagin, O.N. Smirnov, S.Yu. Strakhov, E.V. Perkhina	46
12.	Synthesis by pulsed laser ablation in Ar and SERS activity of silver thin films with controlled nanostructure.....C. D’Andrea, F. Neri, P.M. Ossi, N. Santo, S. Trusso	51
13.	Growth features and structure of the epitaxial films of GaSe, InSe compounds in correlation with physical properties..... E.Yu. Salayev, H.R. Nuriyev	55
14.	Specific character of the ¹¹⁹ Sn thin films growth on amorphous Si by the CBPLD method..... V.V.Rocheva, E.V.Khaydukov, O.A.Novodvorsky, O.D Khramova., V.Ya Panchenko.	58
15.	Ultrafast single-photon image diagnostics sensors with apd arrays for industrial and bio applications.....Edoardo Charbon and Silvano Donati	64
16.	Effect of using dissolved air flotation system on industrial wastewater treatment in pilot scaleYahya Habibzadeh, K.B.Gurbanov	68
17.	Comparison of experimental and theoretical results to define centrality of heavy ion collisions..... Z.Wazir, M.K.Suleymanov, O.B.Abdinov, E.U.Khan, Mahnaz Q. Haseeb, M.Ajaz, K.H. Khan, Sh.Ganbarova	75
18.	Phonon symmetries and phase transition in TlSe and TlInSe ₂Nazim Mamedov, Guseyn Orudzhev, Kojiro Mimura, Kazuki Wakita, Yong Gu Shim, Susan Schorr, Munira Nizametdinova, Vusala Jafarova, Sadig Hamidov and Firudin Hashimzade	79
19.	The current oscillations in semiconductors in external electric and magnetic fields.....E.R.Gasanov, T.R.Mehdiyev	83

CONTENT



Laser crystallization induced multicrystalline silicon thin film solar cells on glass: European High-EF project	3
. . . . A.Antoni, E. Fogarassy, A. Slaoui, Y. Leroy, Z. Said-Bacar, F. Falk, E. Ose, S. Christiansen, G. Sarau, J. Schneider, N. Lichtenstein, B. Valk, M. Leclercq, R. Lewandowska, J.Michler, X. Maeder, A.-S. Dehlinger, J. Lábár, G. Sáfrán	
Turkish accelerator complex, fel resonator system	7
. Hatice Duran Yildiz	
M ² qualify laser beam propagation	11
. Abdelhalim Bencheikh, Mohamed Bouafia	
Effect of CO ₂ Laser Focusing on Groove Cutting into Steel Surfaces	16
. Suleyman Biyikli and Jale Yilmazkaya Sungu	
Preliminary Results From The New Multiwavelength Aerosol Lidar In Turkey	22
. K.R. Allakhverdiev, T. Baykara, M. Bekbolet, M. F. Huseyinoglu, S. Ozbek, Z.Salaeva, A.Secgin , S.Vartapetov, I.Veselovskii, M.Korenskii	
Near ir laser light visualizers using nonlinear GaSe and other layered crystallites	26
. K. R. Allakhverdiev, M. Ö. Yetis, T. B. Baykara, S. Özbek, E. Yu. Salaev	
The erosive laser plume ions component researches at the silicon ablation in vacuum	29
. Khaydukov, V.V.Rocheva, A.A. Lotin, O.A. Novodvorsky, V.Ya. Panchenko	
Experimental investigation of different refining stages influences on optical and ultrasonic signals in paper pulp suspensions	33
. Jan Niemi	
Tree Mapping Using a Time-of-Flight 3D Camera.	37
. Arttu V.H. Ollikkala, Anssi J. Mäkynen	
The optical and structural properties of quantum wells Mg _{0.27} Zn _{0.73} O/ZnO produced by pulsed laser deposition.	41
. A.A. Lotin, O.A. Novodvorsky, L.S. Parshina, E.V. Khaydukov, O.D. Khramova, V.Ya. Panchenko	
Compact Raman (CLS) spectrometer for active test of liquid and solid samples	46
. K.R.Allakhverdiev, T.K.Baykara, A.M.Secgin,S.Ozbek,A.M.Ulubey,Z.Yu.Salaeva, M.F.Huseyinoglu, S. L. Druzhinin, K.A. Konovalov, V. Y. Shchagin, O.N. Smirnov, S.Yu. Strakhov, E.V. Perkhina	
Synthesis by pulsed laser ablation in Ar and SERS activity of silver thin films with controlled nanostructure	51
. C. D’Andrea, F. Neri, P.M. Ossi, N. Santo, S. Trusso	
Growth features and structure of the epitaxial films of GaSe, InSe compounds in correlation with physical properties.	55
. E.Yu. Salayev, H.R. Nuriyev	
Specific character of the 119Sn thin films growth on amorphous Si by the CBPLD method	58
. V.V.Rocheva, E.V.Khaydukov, O.A.Novodvorsky, O.D Khramova., V.Ya Panchenko	
Ultrafast single-photon image diagnostics sensors with apd arrays for industrial and bio applications.	64
. Edoardo Charbon and Silvano Donati	
Effect of using dissolved air flotation system on industrial wastewater treatment in pilot scale	68
. Yahya Habibzadeh, K.B.Gurbanov	
Comparison of experimental and theoretical results to define centrality of heavy ion collisions	75
. Z.Wazir, M.K.Suleymanov, O.B.Abdinov, E.U.Khan, Mahnaz Q. Haseeb, M.Ajaz, K.H. Khan, Sh.Ganbarova	
Phonon symmetries and phase transition in TlSe and TlInSe ₂	79
. Nazim Mamedov, Guseyn Orudzhev, Kojiro Mimura, Kazuki Wakita, Yong Gu Shim, Susan Schorr, Munira Nizametdinova, Vusala Jafarova, Sadig Hamidov and Firudin Hashimzade	
The current oscillations in semiconductors in external electric and magnetic fields	83
. E.R.Gasanov, T.R.Mehdiyev	